A Numerical and Mechanistic Study of Residual Stress Relaxation in Laser Powder Bed Fused Materials during Hot Isostatic Pressing

by

Rasool Mokhtari Homami

A thesis submitted to the Faculty of Graduate and Postdoctoral Studies of
The University of Manitoba
in partial fulfillment of the requirements for the degree of

DOCTOR OF PHILOSOPHY

Department of Mechanical Engineering,
University of Manitoba
Winnipeg, Manitoba, Canada

ABSTRACT

Laser powder bed fusion (LPBF) is an additive manufacturing process capable of producing complex metallic components; however, the rapid thermal cycles inherent to the process generate residual stresses and porosity. These residual stresses can cause part distortion, micro-cracking, and reduced fatigue life, particularly in safety-critical applications such as aerospace and energy systems. Therefore, understanding the mechanisms governing residual stress formation and developing effective stress-relief strategies are essential for the reliable application of LPBF components.

Hot isostatic pressing (HIP) is widely used to eliminate internal porosity and improve mechanical performance in additively manufactured materials. Although HIP has occasionally been reported to reduce residual stress, the specific role of externally applied hydrostatic pressure remains poorly understood. Under purely hydrostatic loading, the equivalent von Mises stress is theoretically zero, suggesting that hydrostatic pressure alone should not induce plastic deformation or enhance residual stress relaxation. This apparent contradiction forms the central motivation of this research.

This thesis presents a mechanistic and qualitative investigation of residual stress relaxation using combined analytical and numerical approaches. Analytical investigations established the conditions under which hydrostatic pressure can contribute to stress relaxation. A computationally efficient thermo-mechanical finite element framework was also developed to generate LPBF-induced residual-stress fields with reduced computational time while maintaining sufficient accuracy. This framework provides a fast tool for generating different initial residual-stress states that can subsequently be transferred to furnace and HIP simulations for systematic investigation of stress relaxation.

The results indicate that temperature is the primary driving force for residual stress relaxation through creep deformation, whereas the contribution of hydrostatic pressure depends strongly on internal defects. In void-free geometries, HIP and furnace treatment produced nearly identical stress-relaxation responses because hydrostatic pressure did not generate deviatoric stresses. In contrast, internal voids converted the otherwise hydrostatic loading condition into a locally deviatoric stress state, generating a non-zero local equivalent stress around the void. This localized stress state promotes dislocation motion and the associated creep and plastic deformation, which contribute to residual-stress relaxation during HIP. Furthermore, elongated and irregular

voids produced greater stress reduction than near-spherical pores due to higher local stress concentrations.

ACKNOWLEDGMENT

I wish to express my profound gratitude to **Dr. Olanrewaju Ojo** for granting me the opportunity to pursue my Ph.D. and his invaluable scientific and technical guidance throughout my doctoral journey. His expertise, timely advice, and constructive feedback have been instrumental in shaping my research and inspiring me to achieve my full potential. His mentorship has guided me academically and encouraged me to grow as both a researcher and an individual.

I am sincerely grateful to my advisory committee members, **Dr. Xihui Liang** and **Dr. Ahmad Z. Naser**, as well as my former committee member, **Dr. Matt Khoshdarregi**, for their insightful comments, thoughtful suggestions, and critical evaluations, which have greatly enhanced the quality of this research work.

I am thankful to the **University of Manitoba** for its financial support through the International Graduate Student Entrance Scholarship (IGSES), International Graduate Student Scholarship (IGSS), University of Manitoba Fellowship for Education Purposes, University of Manitoba Graduate Fellowship (UMGF), Faculty of Graduate Studies Research Completion Scholarship, and University of Manitoba General Bursary. These scholarships and bursaries were vital in supporting my academic progress.

I acknowledge the **National Research Council Canada** and the **Natural Sciences and Engineering Research Council (NSERC)** under grant ALLRP 560378-20 for their financial support. I am also thankful to **Precision ADM** for providing the samples used in this study.

Finally, I would like to express my sincere gratitude to my colleagues and friends — **Dr. Priti Wanjara, Dr. Gbenga Asala, Dr. Javad Gholipour, Dr. Bamidele Akinrinlola, Dr. Ehsan Jalayeri, Dr. Lina Zhang, and Mr. Mike Boskwick** — for their support, collaboration, and encouragement, which have made this journey more fulfilling and memorable.

DEDICATION

First and foremost, I am deeply thankful to God for granting me the strength, patience, and opportunity to complete this journey. In His name, this dissertation is dedicated with heartfelt gratitude to my beloved parents, **Afsaneh Mokhtari Homami** and **Fereidoon Mokhtari Homami**, and my dear sister, **Masoomeh (Golnaz) Mokhtari Homami**. Your unwavering love, encouragement, and sacrifices have been the foundation of my academic path and the source of my perseverance.

The constant support, patience, and prayers of my parents have guided me through every stage of this academic journey. Their unwavering belief in my abilities has inspired me to overcome challenges and continue to strive for excellence. I am deeply grateful for their endless encouragement and the values that they have instilled in me.

To my sister, Masoomeh (Golnaz), thank you for your love, understanding, and encouragement, which have always lifted my spirits. Your confidence in me has been a constant source of motivation.

This achievement would not have been possible without the love and support of my family. I am profoundly grateful for everything you have done for me, and I dedicate this work to you with my deepest appreciation.

Table of Contents

List of Tables

List of Figures

Copyrighted Materials

Chapters 2 through 4 of this thesis include material that has been reproduced, adapted, or developed from the author's previously published and currently under-review works. Parts of Chapters 3 and 4 are based on the following two previously published journal articles authored by the candidate:

R. Mokhtari Homami, O. Ojo, "*Residual Stress Analysis through Numerical Simulation in Powder Bed Additive Manufacturing Using the Representative Volume Approach*," The International Journal of Advanced Manufacturing Technology, vol. 129, pp. 5581–5599, 2023.

R. Mokhtari Homami, P. Wanjara, J. Gholipour, G. Asala, B. Akinrinlola, O. Ojo, "*Numerical Analysis of Residual Stress in a Material Produced by Additive Manufacturing and Hot Isostatic Pressing*," Journal of Manufacturing Processes, vol. 150, pp. 1018–1039, 2025.

The applicable publisher copyright requirements for reuse of these two published articles in this thesis have been addressed. Permission/license for thesis/dissertation reuse was obtained where required, and the original journal articles are appropriately cited.

Figures 2.1–2.7 include figures that were adapted or reproduced from previously published sources, as identified in their corresponding figure captions. Where required, permission to reproduce or adapt these materials was obtained from the respective copyright holders/publishers. Materials available under Creative Commons licenses were used in accordance with the applicable license terms, with appropriate attribution.

Parts of Chapters 3 and 4 also contain material developed as part of two additional manuscripts that are currently under review for publication. These manuscripts arise from the present PhD research and address the analytical and numerical investigation of pressure-assisted residual-stress relaxation during HIP and the influence of internal void characteristics on this behavior.

All reproduced or adapted materials are identified and appropriately acknowledged in the thesis through their corresponding citations, figure captions, and applicable copyright or licensing statements.

NOMENCLATURE AND ABBREVIATIONS

Symbol / Abbreviation	Description
AM	Additive Manufacturing
LPBF	Laser Powder Bed Fusion
HIP	Hot Isostatic Pressing
FE	Finite Element
FEM	Finite Element Method
RV	Representative Volume
LOF	Lack of Fusion
CAD	Computer-Aided Design
GUI	Graphical User Interface
NSERC	Natural Sciences and Engineering Research Council
IGSES	International Graduate Student Entrance Scholarship
IGSS	International Graduate Student Scholarship
UMGF	University of Manitoba Graduate Fellowship
σ	Stress
$\Delta\sigma$	Stress reduction
ε	Strain
ε^e	Elastic strain
ε^p	Plastic strain
ε^c	Creep strain
ε^t	Thermal strain
CEEQ	Equivalent creep strain
PEEQ	Equivalent plastic strain
S_{11}, S_{22}, S_{33}	Normal stress components in principal directions
τ	Shear stress
T	Temperature
P	Pressure
t	Time
Q	Heat input / Activation energy
k	Thermal conductivity

Cp	Specific heat capacity
A, n, α	Material constants in hyperbolic-sine creep law
R	Universal gas constant
$\boldsymbol{\sigma_e}$	Equivalent deviatoric stress
$\dot{\boldsymbol{\varepsilon}}$	Strain rate
x, y, z	Cartesian coordinates
r, θ, φ	Spherical coordinates
E	Young's modulus
ν	Poisson's ratio
$\boldsymbol{\sigma_\gamma}$	Yield stress
H	Hardening modulus

CHAPTER ONE: INTRODUCTION

1.1 Background

Additive manufacturing (AM), commonly known as three-dimensional (3D) printing, has expanded the capabilities for fabricating complex metal parts by providing greater design flexibility, reducing material waste, and producing near-net-shape components directly from digital models. Among the various AM techniques, laser powder bed fusion (LPBF), which is also known as selective laser melting, is one of the most mature and widely adopted processes for manufacturing high-performance metallic components. LPBF is carried out by selectively melting successive layers of metal powder with a focused laser beam in an inert atmosphere, thereby consolidating the powder into fully dense structures and enabling the production of intricate geometries, such as internal cooling channels and lightweight lattices, that are difficult to produce using traditional subtractive or casting methods or cannot be produced using such methods. The layer-by-layer fabrication approach offers precise control over the geometry of the part and local material distribution, thereby making LPBF a highly attractive technique for aerospace, biomedical, and energy applications. Consequently, the process is now widely used to produce high-performance alloys, including nickel (Ni)-based superalloys, in complex shapes that meet the stringent requirements of gas turbines, biomedical implants, and other advanced engineering systems[1–3].

Despite its advantages, LPBF has a number of technical challenges that must be rectified to unlock its full industrial potential. One such challenge is its melt pool instability, which refers to the unpredictable behavior of the molten region due to fluctuations in energy input, powder distribution, or thermal gradients. These instabilities can lead to uneven fusion, keyholing, or balling, thus ultimately degrading the quality of the part. Another concern is splattering, where molten particles are ejected from the melt pool and redeposited on the part or surrounding powder bed, thus introducing surface roughness and increasing the likelihood of defects. Additionally, laser powder bed fused parts exhibit anisotropic mechanical behavior due to the directional solidification patterns and thermal histories imposed by the laser scanning strategy. This anisotropy can reduce reliability in structural applications, as mechanical properties vary significantly with loading direction. Therefore, although LPBF offers many advantages, these intrinsic process challenges require careful control and post-processing[4–6].

A further critical issue inherent to LPBF is the formation of internal porosity. These pores can originate from the lack of fusion—where insufficient laser energy or inadequate scan overlap leaves unmelted regions—or from keyholing and vaporization, in which excessive energy creates unstable melt pools that entrain gas. Additionally, gas porosity may develop when evaporated metal or shielding gas becomes trapped within the rapidly solidifying melt pool. Although careful optimization of the parameters can significantly reduce such defects, which often achieves >99% density in many LPBF builds, completely eliminating porosity remains challenging, and even then, the issue can re-emerge and persist. Even when nominally identical processing conditions are used, variations in melt pool behavior, powder flow, and thermal gradients can lead to non-negligible differences in defect formation. The resulting pore morphologies range from near-spherical gas pores to irregular, crack-like lack-of-fusion (LOF) voids with high aspect ratios. Both types of defects are detrimental: internal pores act as stress concentrators that may initiate cracks under service loads, and clusters of defects can reduce fatigue life and the ductility of additively manufactured components. For safety-critical parts—such as turbine blades or pressure-retaining components—even a small number of defects can be unacceptable. Consequently, internal porosity is widely recognized as one of the fundamental technical limitations of LPBF-produced parts[7,8].

In addition to porosity, residual stress is another major challenge inherent to the LPBF process. From a mechanical integrity perspective, residual stress represents an important challenge to the reliable use of laser powder bed fused components, particularly in fatigue-sensitive applications. Not only do residual stresses undermine structural soundness but also obscure the true material performance, thus making it difficult to evaluate the behavior of parts during service. The layer-by-layer melting process and rapid solidification of LPBF impose steep thermal gradients within a part. As each new layer is fused, the underlying material undergoes localized heating followed by rapid cooling. These repeated thermal cycles produce non-uniform expansion and contraction throughout the build. Newly solidified, hotter regions are mechanically constrained by the cooler, surrounding material, thus leading to thermally induced residual stresses that remain in the component after it is cooled to an ambient temperature. LPBF-induced residual stresses often approach the yield strength of a material and can be manifested across the entire part, thus causing geometric distortion (e.g., warping) or even cracking if local stresses exceed material ductility. Moreover, these internal stresses may degrade mechanical performance—reducing fatigue life, stiffness, or load-bearing capacity—if left untreated in the as-built condition. Researchers have shown that in situ approaches, such as preheating the build platform, can mitigate residual stress by moderating thermal gradients; for example, elevated base-plate temperatures have been shown to significantly reduce the magnitude of stress. Nonetheless, even with optimized scanning strategies and high build-plate temperatures, substantial residual stresses typically persist, especially in high-strength alloys. As a result, post-processing stress-relief treatments remain essential for most LPBF components. This PhD research primarily focuses on understanding the mechanisms of residual stress formation and developing strategies to mitigate them by using advanced simulation tools and targeted post-processing methods[9–11].

To overcome these challenges, researchers and manufacturers in the AM field increasingly rely on post-processing techniques. One of the most common approaches is thermal stress-relief annealing in a furnace. This method involves heating the laser powder bed fused part to a sub-critical temperature (typically between 600°C and 900°C for metallic systems) and holding it for several hours, thus allowing residual stresses to relax via creep and microplasticity. While furnace annealing can reduce residual stresses by as much as 60–90%, the process suffers from inherent limitations. Most notably, furnace annealing is carried out at an ambient pressure and thus has little effect on the internal porosity, which is unlikely to shrink appreciably without applied pressure. Furthermore, improper or non-uniform cooling after the annealing cycle may reintroduce residual stresses, especially if quenching is used. Consequently, furnace annealing alone is not sufficient to produce pore-free, stress-relieved parts suitable for critical applications[12–14].

Hot isostatic pressing (HIP) provides an alternative to conventional furnace treatment by combining elevated temperature and hydrostatic pressure, which can contribute to both stress relaxation and pore closure under controlled conditions. During HIP, the component is exposed to a uniform hydrostatic pressure—typically argon at 100–200 MPa—while being held at elevated temperatures for an extended duration of time. The combined influence of high temperature and hydrostatic pressure promotes time-dependent plastic deformation, thus enabling the material to plastically flow, collapse internal voids, and heal defects through metallurgical bonding. Unlike standard furnace annealing, HIP not only reduces residual stresses but also reduces internal porosity, thus addressing two of the most critical limitations of laser powder bed fused components. A number of studies have shown that HIP can reduce porosity to near-zero levels and transform tensile residual stresses, which are detrimental to fatigue life, into compressive stresses, which are less likely to cause cracking. These changes can contribute to improved mechanical performance, including fatigue resistance, ductility, and fracture toughness. Given these advantages, HIP is increasingly being adopted as a standard post-processing technique for additively manufactured parts, particularly in aerospace and medical applications where structural reliability is essential. This PhD research specifically focuses on HIP as the primary post-processing method for mitigating residual stresses and improving the integrity of laser powder bed fused components[3,14–16].

1.2 Research Motivation

While the benefits of HIP for defect removal in additively manufactured components are well documented, relatively few studies have examined the specific role of externally applied pressure in residual stress relaxation. In particular, important knowledge gaps remain regarding how and to what extent HIP improves the residual stress state of laser powder bed fused components when compared directly with conventional furnace-based stress-relief treatments.

Residual stress relaxation is critical for ensuring the structural integrity and dimensional stability of LPBF components, particularly in high-performance applications such as aerospace and energy systems[17]. Although furnace annealing is widely used for stress relief, it relies primarily on temperature-driven mechanisms and does not effectively eliminate internal porosity. In contrast, HIP introduces an additional driving force through hydrostatic pressure, with the potential to enhance both stress relaxation and defect healing[12–14].

Despite this potential, the mechanisms through which hydrostatic pressure contributes to residual stress relaxation remain poorly understood. It is unclear whether the improved relaxation arises primarily from enhanced plastic deformation under hydrostatic pressure, whether creep mechanisms dominate, or how internal defects influence the evolution of stress during HIP. Furthermore, because of the experimental challenges associated with measuring residual stress under high-temperature and high-pressure conditions, the time-dependent mechanisms governing stress relaxation remain insufficiently explored.

Overall, the limited understanding of pressure-assisted stress relaxation and the lack of mechanistic insight into the role of internal defects highlight the need for a systematic investigation of residual stress evolution during HIP. Addressing these knowledge gaps is essential for improving post-processing strategies and supporting the safe implementation of LPBF components in demanding engineering applications.

1.3 Research Objectives

The primary objective of this PhD research is to develop a mechanistic understanding of how hydrostatic pressure can contribute to residual stress relaxation during HIP beyond the relaxation achieved by temperature alone during conventional furnace treatment, particularly by identifying the conditions under which hydrostatic pressure can generate the non-zero local equivalent stress required to promote creep and plastic deformation. To achieve this objective, the following specific objectives were pursued:

- To develop a computationally efficient finite element framework capable of predicting residual stress generation during LPBF.
- To compare the effectiveness of HIP and conventional furnace treatment in reducing residual stress under controlled thermal conditions and thereby isolating the contribution of externally applied hydrostatic pressure.
- To investigate, through analytical and numerical approaches, whether hydrostatic pressure can promote residual stress relaxation in fully dense materials and under different geometrical configurations.
- To establish the mechanism by which enclosed internal voids influence pressure-assisted residual stress relaxation during HIP.
- To systematically examine the effects of void characteristics, including morphology, aspect ratio, irregularity, and porosity volume fraction, on residual stress evolution during HIP.

1.4 Research Contributions

The original contributions of this PhD research are summarized as follows:

First, a computationally efficient thermo-mechanical finite element framework based on the representative volume (RV) approach was developed to predict residual stress evolution during LPBF. The proposed framework significantly reduced computational time while maintaining good agreement with experimental data reported in the literature. Beyond reducing computational time, the framework provides a fast and routinely applicable tool for generating different levels and distributions of initial residual stress. These residual-stress fields can subsequently be transferred as initial conditions to the furnace and HIP simulations, enabling systematic investigation of post-processing stress-relaxation behavior without repeatedly performing computationally expensive LPBF simulations. This work was published in *The International Journal of Advanced Manufacturing Technology* (2023).

Second, a coupled simulation strategy was established to investigate the evolution of residual stress from the as-built LPBF condition through subsequent post-processing treatments. Using this framework, the interactions between additive manufacturing-induced residual stress and HIP-induced stress redistribution were systematically examined. This coupled approach enabled direct comparison of residual-stress relaxation during HIP and equivalent furnace treatments under consistent numerical conditions. This contribution established a fundamental question addressed by the subsequent analysis: how can hydrostatic pressure generate the non-zero equivalent stress necessary to drive dislocation motion and the associated creep and plastic deformation that contribute to residual-stress relaxation, when pure hydrostatic pressure acting on a defect-free solid does not itself generate equivalent stress? The numerical findings associated with this contribution were published in the *Journal of Manufacturing Processes* (2025).

Third, a combined analytical and numerical investigation was conducted to address this fundamental question by comparing defect-free materials with various geometrical configurations and materials containing internal voids under externally applied hydrostatic pressure. The results demonstrated that, in defect-free configurations, purely hydrostatic loading does not generate a non-zero equivalent von Mises stress and therefore cannot independently promote additional plastic deformation and residual-stress relaxation. In contrast, the presence of internal voids generates a non-zero local equivalent stress in the surrounding material, providing the shear stress required to promote dislocation motion and the associated creep and plastic deformation. Together, these analyses establish the mechanistic basis for explaining how internal voids enable pressure-assisted residual-stress relaxation during HIP. The analytical and numerical findings associated with this contribution form part of a manuscript currently under review.

Fourth, a systematic analytical and numerical investigation was conducted to evaluate the influence of void characteristics, including morphology, aspect ratio, irregularity, and porosity volume fraction, on residual stress relaxation during HIP. The results demonstrated that elongated and irregular defects promote higher localized deformation, faster pore closure, and greater stress reduction than near-spherical pores. These findings provide new insights into the relationship between defect characteristics and the effectiveness of HIP and form part of a second manuscript currently under review.

The scientific significance of these contributions has been recognized through publications in reputable peer-reviewed journals and presentations at national conferences. In particular, the work received the *Best Presentation Award* at the 36th Canadian Materials Science Conference (CMSC) held at the University of Waterloo, reflecting the novelty and impact of the research findings.

1.5 Summary of Major Findings

This PhD research provides a mechanistic understanding of residual stress generation during LPBF and its subsequent relaxation during post-processing treatments, particularly HIP. A reliable finite element framework based on the representative volume approach was developed to simulate residual stress evolution during LPBF. The simulations showed that residual stresses generated during LPBF are not uniformly distributed. High tensile stresses develop near the top surface, whereas lower and sometimes compressive stresses are found in the interior regions. A systematic investigation of LPBF processing parameters further showed that laser power, scanning speed, and build plate preheating influence the final stress state, with preheating exhibiting the greatest potential for reducing residual stresses through the reduction of thermal gradients during fabrication. Nevertheless, significant residual stresses remained even under optimized processing conditions, highlighting the need for effective post-processing strategies.

To establish the theoretical basis for stress relaxation, an analytical investigation was performed to identify the conditions required for irreversible deformation. The analysis confirmed that residual stress relaxation requires non-zero equivalent stress to activate creep or plastic deformation and demonstrated that purely hydrostatic pressure cannot induce such deformation in fully dense materials. This finding provided the foundation for understanding the role of hydrostatic pressure during HIP. The analytical results further showed that the presence of enclosed internal voids can disrupt the hydrostatic stress state and generate localized deviatoric stresses, thereby promoting plastic and creep deformation around the void surfaces. Consequently, internal defects can create the conditions necessary for pressure-assisted residual stress relaxation.

Building upon these findings, conventional furnace treatment simulations showed that temperature-driven creep could partially relieve residual stress; however, the extent of relaxation remained limited by the initial LPBF stress field, and internal porosity remained unaffected. HIP simulations further revealed that the effectiveness of hydrostatic pressure depends strongly on the presence and nature of internal defects. In fully dense materials and in components containing only surface-connected defects, HIP produced stress-relaxation responses that were nearly identical to those observed during furnace treatment. In contrast, the introduction of enclosed internal voids altered the stress state by generating localized deviatoric stresses around the void surfaces. These stresses promoted creep and plastic deformation, contributing to pore collapse and greater residual stress relaxation. This observation confirmed that the beneficial effect of HIP is not universal but arises specifically from the interaction between externally applied hydrostatic pressure and enclosed internal defects.

The influence of HIP processing conditions was further examined by independently varying temperature and hydrostatic pressure. The results demonstrated that temperature is the primary factor controlling the kinetics of stress relaxation through its effect on creep deformation, whereas hydrostatic pressure serves as an enabling factor that intensifies localized deformation around internal voids. Furthermore, the effectiveness of HIP was found to depend strongly on the characteristics of the initial porosity. Elongated and irregular defects generated higher local stress concentrations and experienced faster closure and greater stress reduction than near-spherical pores. Increasing the porosity level initially enhanced stress relaxation by providing additional sites for localized deformation; however, excessive porosity reduced this benefit because of mechanical constraints between neighboring defects.

Overall, this research advances the fundamental understanding of pressure-assisted residual stress relaxation in LPBF materials during HIP. The study demonstrates that hydrostatic pressure contributes to stress relaxation only under specific conditions associated with enclosed internal defects and establishes the mechanisms by which temperature, hydrostatic pressure, and defect characteristics influence the post-processing response. By integrating LPBF simulations with post-treatment analyses, this work provides a unified understanding of residual stress evolution throughout the additive manufacturing process chain and establishes a scientific basis for the effective application of HIP to additively manufactured components.

1.6 Thesis Structure

The research follows a sequential analytical and numerical approach. First, a thermo-mechanical FE framework based on the representative volume (RV) approach is used to generate LPBF-induced residual-stress fields. These stress fields are then transferred as initial conditions to furnace and HIP simulations. Analytical stress-state formulations are used to examine the mechanical effect of hydrostatic pressure and the conditions required to generate non-zero equivalent stress. Controlled numerical comparisons are subsequently performed for defect-free geometries, surface-connected defects, and internal voids. Finally, parametric simulations are used to investigate the effects of temperature, pressure, and void characteristics on residual-stress relaxation during HIP. This overall research approach is reflected in the organization of the thesis chapters, as outlined below.

Chapter 1 introduces the research problem by providing the background, motivation, research objectives, and contributions. The chapter also presents a summary of the major findings and outlines the overall structure of the thesis.

Chapter 2 presents a detailed literature review related to AM and post-processing heat treatments. The chapter summarizes existing knowledge on LPBF-induced residual stress, mechanisms of stress changes during AM, and post-processing pathways—particularly furnace heat treatment and HIP—that are relevant to understanding stress relaxation and evolution of defects in additively manufactured components.

Chapter 3 describes the numerical and analytical methods and the governing equations adopted in this study. The first part of the chapter explains the numerical implementation of the LPBF and post-processing simulations, including thermomechanical modeling, heat-source representation, residual stress initialization, and FE model configuration. The second part introduces the fundamental mechanical principles that govern stress generation, redistribution, and relaxation. This section covers the underlying physics of plastic deformation, hydrostatic loading, stress states around voids, void-geometry-dependent stress amplification, and the analytical relationships among stress relaxation, PEEQ, and applied hydrostatic pressure, thereby providing the theoretical foundation for interpreting the simulation results.

Chapter 4 presents and discusses the numerical results. The first section focuses on the LPBF simulations, including temperature changes, in-process stress development, stress components, and the influence of laser parameters and preheating on residual stress. The second section examines the post-processing results through controlled comparisons between furnace treatment and HIP, including cases without internal voids, with surface-connected defects, and with enclosed internal voids. The effects of temperature, pressure, void morphology, aspect ratio, irregularity, size, and porosity volume fraction are then examined to clarify their influence on localized deformation and residual-stress relaxation during HIP.

Chapter 5 summarizes the major findings of the research and highlights the key conclusions drawn from the numerical analysis and theoretical framework.

Chapter 6 offers recommendations for future work by outlining both experimental and computational directions to build upon the thesis findings. The chapter emphasizes advanced characterization and modeling approaches to overcome current limitations and guide subsequent research efforts.

Appendix A provides supplementary details of the numerical framework, including material definitions and constitutive inputs, the sequential LPBF-to-post-processing workflow, solver implementation, boundary conditions and pressure application, and the treatment of void deformation and contact assumptions.

CHAPTER TWO: LITERATURE REVIEW

This chapter provides a review of the literature on the effect of the HIP process in reducing residual stresses generated during AM. Residual stresses are a critical issue in AM, as they significantly influence the mechanical performance, dimensional accuracy, and service life of manufactured components. To provide a structured context, the chapter first examines research conducted in the field of AM, with a particular focus on the LPBF process, which is one of the most widely studied and industrially relevant AM techniques for metals. In this chapter, the mechanisms of residual stress formation during LPBF, influence of processing parameters, and resulting microstructural characteristics are highlighted. Following this, attention is directed toward the HIP process to explore its role as a post-processing technique to alleviate the residual stresses, close the internal pores, and enhance the overall mechanical properties of additively manufactured parts. The review covers both experimental investigations, which provide direct evidence of the effectiveness of HIP through measurements and characterization, and simulation-based studies, which offer valuable insights into the fundamental mechanisms that govern stress relaxation, densification, and changes to the microstructure during HIP. By integrating the findings from these two domains, the chapter establishes a clear understanding of the current state of knowledge and identifies areas where further research is needed to optimize HIP as a post-processing treatment for additively manufactured components.

2.1 Laser Powder Bed Fusion: Process Overview

AM is a manufacturing process that fabricates 3D components by sequentially depositing layers of materials based on a computer-aided design (CAD) model[18]. Among the various AM technologies, LPBF has emerged as one of the most widely used metal additive manufacturing processes in the aerospace, medical, and automotive industries because of its capability to produce near-net-shape components with complex geometries and high dimensional accuracy. In addition to reducing material waste, LPBF enables the fabrication of customized components and intricate features that are difficult to manufacture using conventional subtractive methods. Although AM has the potential to improve resource efficiency, its energy consumption relative to traditional manufacturing processes depends on factors such as material type, component geometry, and processing conditions[1–3,18–21]. Figure 2.1 illustrates the applications of AM in various industries.

Figure 2.1 Applications of AM in various industries, Adapted from Ref. [22], under the Creative Commons CC-BY license.

LPBF employs a high-power laser to selectively melt metallic powder in an inert atmosphere to produce near-net-shape components. The fabrication process involves the repeated deposition and selective melting of thin powder layers until the desired geometry is achieved, as schematically illustrated in Figure 2.2.

Figure 2-3 schematically illustrates the fabrication sequence of cubic specimens produced by the LPBF process. Figure 2-3(a) presents the fabrication of the initial layers[23]. Figure 2-3(b) illustrates the final stage of printing, where multiple cubic specimens remain attached to the base plate. Figure 2-3(c) shows one of these metallic specimens after being separated from the base plate using wire cutting. As observed in this figure, on the XZ surface—where the Z-axis represents the build direction—my name (Rasool), along with the build number, is printed, which shows the capability of this process to fabricate parts with complex and customized geometries.

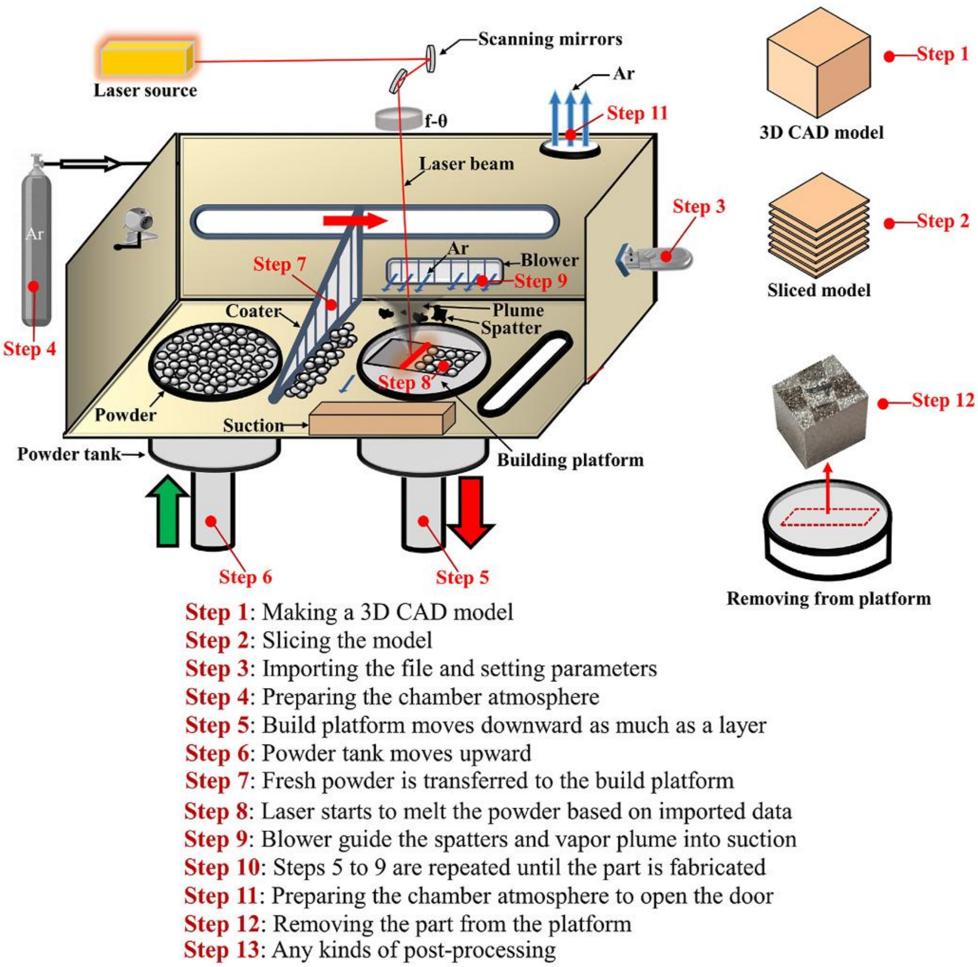

Figure 2.2 Thirteen sequential steps to fabricate an industrial additively manufactured part with LPBF process, reprinted from Ref. [3]. Used with permission.

When the laser interacts with the powder bed during LPBF, complex thermophysical phenomena occur within the melt pool, including conduction, convection, radiation, and possible chemical reactions at elevated temperatures[5,24], as illustrated in Figure 2.4(a). Owing to the short interaction time between the laser and powder particles, melting and solidification occur rapidly, resulting in small melt pools[17]. The melting behavior and solidification characteristics are strongly influenced by processing parameters such as energy density, scanning strategy, and powder characteristic[4,6,7,25]. The energy density (E), which represents the laser energy delivered per unit volume of material, is defined as[26]

$$E = \frac{P}{v \times h \times t} \tag{2.1}$$

where P is the laser power, v is the scanning speed, h is the hatch spacing, and t is the layer thickness. During LPBF, the laser beam scans the powder bed at velocities of up to 3.0 m/s, while the layer thickness typically ranges from 20 to 100 μm depending on the particle size distribution and flowability of the feedstock powder[8,27–30].

(a)

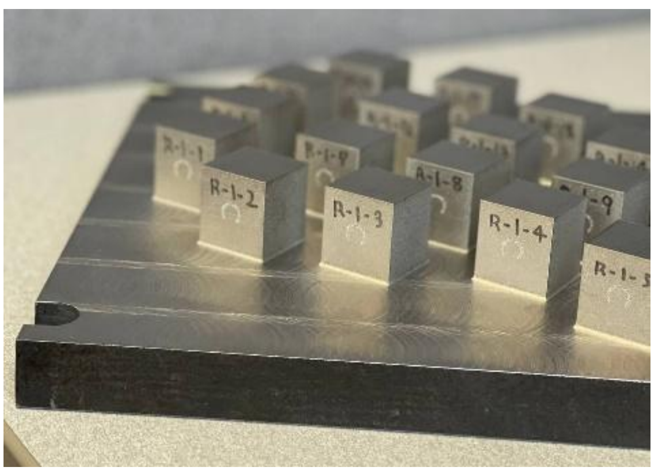

(b)

(c)

Figure 2.3 Fabrication sequence of cubic specimens using LPBF: (a) initial layers, reprinted from Ref. [14]. Used with permission, (b) final build attached to the base plate, and (c) separated cube.

2.2 Defect Formation in LPBF Components

If the applied energy density is insufficient, the powder particles do not fully melt, thus resulting in LOF porosity. This defect is further aggravated by entrapped shielding gases or residual air present between the powder particles, which remain trapped during solidification[31–33], as shown in Figure 2.4(b). In certain alloys such as stainless steel, nitrogen can even dissolve into the molten pool and subsequently form pores during resolidification[34]. On the other hand, excessive energy input leads to unstable melt pool dynamics. High recoil pressure and localized overheating can expel molten droplets from the pool, which produces spatter that redeposits onto previously solidified layers. This causes uneven thicknesses of the layers, thereby promoting the so-called balling phenomenon[9–11]. Balling is manifested as bead-like solidified tracks that increase surface roughness, reduce dimensional accuracy, and degrade the wettability of the interlayers. The result is poor metallurgical bonding and the formation of incomplete fusion defects[35–37]. Another important porosity mechanism arises from keyhole formation, which occurs when the applied energy density is so high that metal vaporization creates a deep and unstable cavity within the melt pool[12], as illustrated in Figure 2.4(c). Keyhole collapse can entrap gas, which leaves behind spherical pores that compromise the density and mechanical strength of the part. Furthermore, inadequate melting at the track boundaries or contour edges causes partially sintered particles to adhere to the surface, which leads to a poor surface finish and irregularities in the part.

Another defect is the formation of elongated, columnar grains that grow along the build direction, as illustrated in Figure 2.4(d). These grains develop because of the steep thermal gradients and directional heat flow inherent to the LPBF process: the laser induces rapid localized melting followed by directional solidification, which promotes epitaxial grain growth from the underlying solidified layers. As a result, grains tend to elongate along the build direction instead of forming an equiaxed structure. This microstructural feature introduces significant anisotropy, which leads to directional dependence in the mechanical response of the material. This anisotropy reduces the overall strength uniformity and markedly shortens the fatigue life of laser powder bed fused components under cyclic loading[13].

2.3 Residual Stress Formation in LPBF

Additionally, this method inherently leads to the development of significant internal residual stresses. During the LPBF process, the material is subjected to rapid and localized heating and cooling cycles as the focused laser selectively melts the layer of powder. These cycles create steep thermal gradients between the newly solidified regions and surrounding cooler material, which, in turn, generate substantial thermal stresses. Upon cooling, these thermal stresses may no longer relax fully and are transformed into residual stresses that remain locked within the part. If the magnitude of these stresses exceeds the yield strength of the material, localized plastic deformation occurs, thereby producing permanent defects. Such defects can be manifested in the form of micro-cracking, warpage, distortion of the overall geometry, or even delamination between successive layers. These stress-induced imperfections not only compromise dimensional accuracy but can also deteriorate the mechanical performance and reliability of the final component, thus making residual stress management a critical aspect of optimizing the LPBF process, as illustrated in Figure 2.5[10,14–16,38–46].

This behavior originates from the highly localized and intense heating caused by the laser during the LPBF process. As the laser irradiates a region, the material rapidly absorbs the energy, thus leading to thermal expansion. However, this expansion is constrained by the adjacent, cooler material that has not yet been exposed to the laser, which produces significant compressive stress within the heated zone. When these compressive stresses exceed the compressive yield strength of the material, the deformation transitions from being purely elastic to a combination of elastic and plastic deformation. Once the laser moves forward and the heated region begins to cool, the material undergoes thermal contraction. This contraction, however, is hindered by both the previously induced plastic deformation and resistance of the surrounding solidified material, thus resulting in the development of residual tensile stresses in the irradiated region. To preserve mechanical equilibrium, the neighboring zones experience compensating compressive stresses, which leads to a complex distribution of residual stresses, as depicted in Figure 2.6. Furthermore, as successive layers are deposited and solidified, they also appear to contract upon cooling, but this shrinkage is constrained by the underlying layers that are already solidified. Consequently, additional tensile stresses are introduced into the newly formed layers, thereby amplifying the overall residual stress accumulation in the part and increasing the risk of cracking, distortion, or delamination[47].

To investigate the parameters that influence the formation of residual stresses in LPBF and identify the factors that can either increase or mitigate them, both experimental approaches and numerical simulations can be used. Residual stresses can, in principle, be reduced through several methods. For instance, post-processing heat treatments are commonly employed to relieve stresses; however, such treatments add both cost and production time. Alternatively, controlling the thermal gradients and cooling rates during the LPBF process itself can also mitigate residual stresses. These in-situ stress relief strategies include optimizing processing parameters such as the laser speed, laser power, hatch distance, interlayer dwell time, and preheating temperature, as well as modifying the scanning strategies. Nevertheless, experimentally determining the optimal conditions is not straightforward, since such trials are time-consuming, require specialized equipment, and are associated with high costs. For this reason, FE simulation is widely recommended as an efficient alternative method, as it enables systematic investigation of the influence of the processing parameters on residual stress development with greater flexibility and at a significantly lower cost. Moreover, the primary objective of this research is to study the HIP process as an effective post-treatment for reducing residual stress generated during LPBF. Since HIP experiments are very expensive and the number of feasible trials is limited, numerical modeling becomes an essential approach. In this work, FE modeling is employed to both analyze the changes in residual stresses during LPBF and evaluate the effectiveness of HIP in mitigating these stresses.

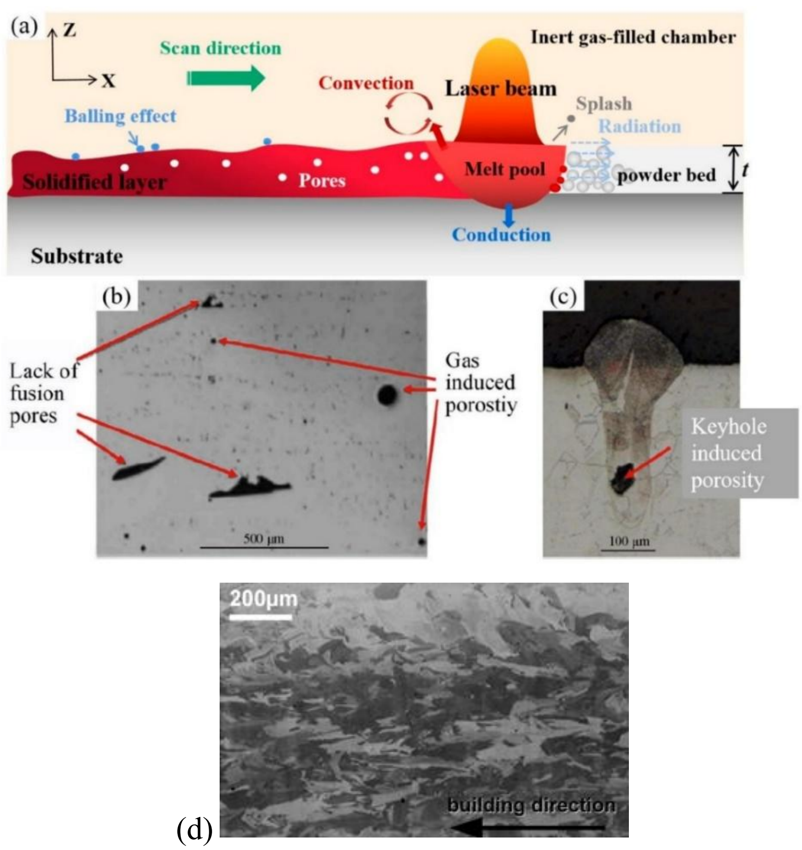

Figure 2.4 (a) Schematic overview of interaction zone between laser and powder bed; (b) lack-of-fusion and gas-induced porosity; (c) keyhole-induced porosity; and (d) formation of elongated grains, reprinted from Refs. [24,36,39,48]. Used with permission.

(a)

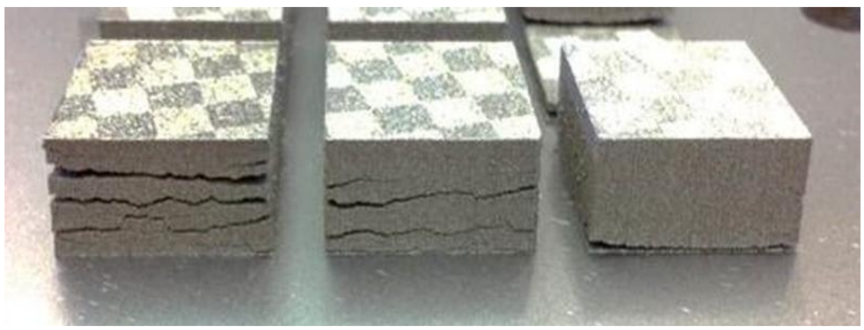

(b)

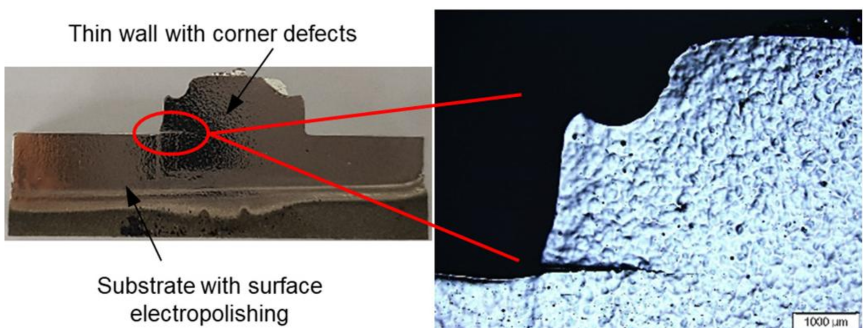

(c)

Figure 2.5 Examples of defects commonly observed in LPBF-manufactured components, including layer delamination and cracking due to thermal stresses (a), cracking and distortion in bulk samples (b), and localized defects such as thin-wall corner cracking (c), reprinted from Refs. [38,39,41]. Used with permission.

The FEM is a powerful numerical technique that has become the most widely adopted tool for modeling residual stress distribution in additively manufactured components. Unlike analytical models, FEM provides the flexibility to incorporate complex geometries, transient loading conditions, and coupled thermal–mechanical interactions, which make it particularly effective for simulating the LPBF process. This computational approach explicitly accounts for both the external loading history and intricate temperature variations that arise during the layer-by-layer fabrication process, thereby offering an efficient means to predict residual stress changes and their influence on the quality of the final part[49,50]. As a result, FEM has been the subject of extensive research, and a large number of models have been developed to simulate the LPBF process under various assumptions and levels of fidelity.

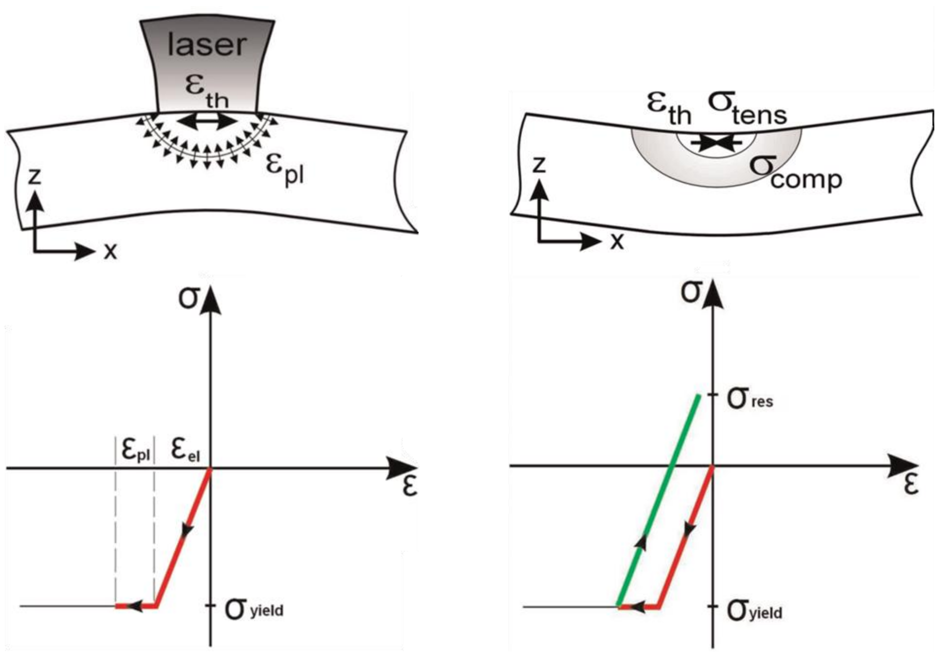

(a) **(b)**

Figure 2.6 Stress and strain changes during LPBF: (a) thermal expansion during laser heating induces elastic–plastic deformation, (b) cooling and contraction generate residual tensile stresses in the irradiated zone and compensate compressive stresses in surrounding regions, reprinted from Ref. [38]. Used with permission.

Early attempts to develop models for LPBF were predominantly based on simplified two-dimensional (2D) simulations[51,52]. These models provided initial insights into the thermal cycles and stress development but could not capture the inherent 3D complexity of the process. With advancements in computational resources and modeling techniques, researchers began to employ more sophisticated 3D simulations to gain a better understanding of the mechanisms that govern residual stress. For example, Hussein et al.[53] investigated single-layer components fabricated without substrate bonding to isolate and analyze the stress states in overhanging structures. While such direct modeling approaches provide detailed physical insights, they suffer from critical limitations. Specifically, they require fine mesh densities and very small time increments to accurately capture the moving laser heat source. Consequently, these models often involve millions of nodes and elements, which lead to computational times that can extend to hundreds of hours for relatively small domains. As a result, direct modeling becomes impractical for simulating large-scale components or conducting parametric studies[54–56].

To address these computational challenges, indirect modeling strategies have been introduced. These approaches simplify the interaction between the laser and material, and reduce the required number of elements and increments, thereby reducing calculation time without entirely sacrificing accuracy. Among these strategies, four principal methods are commonly reported in the literature: flash heating, lumped laser passes, line heating, and the inherent strain approach[55]. In the flash heating method[23], individual laser scans are neglected, and instead, groups of layers are assumed to be heated uniformly and simultaneously. While this drastically reduces the simulation time and provides approximate average values of residual stresses, the method neglects localized plasticity effects induced by the moving laser. Since these localized effects are the primary drivers of residual stress in LPBF, the accuracy of the flash heating approach is limited. Additionally, the approach fails to capture the influence of the scanning speed, as the entire layer is treated as a single heating event.

Lumped laser models are another simplified modeling method, in which multiple discrete laser passes are consolidated into a single larger laser track. This approach further accelerates simulations and provides a general picture of the distortion and stress fields; however, lumped laser models reduce accuracy and are incapable of evaluating the effect of different scanning patterns or hatch strategies[57]. The line heating model offers an intermediate solution by treating the moving laser as a continuous line source, which improves accuracy in representing thermal gradients and allows for the study of scanning strategies. Although faster than beam-scale models, the line heating model still struggles with representing large build volumes, and its predictions of cooling rates are often less reliable[58,59]. Finally, the inherent strain model assumes that the PEEQ accumulated during fabrication is spatially uniform and independent of geometry[60,61]. While computationally efficient, this assumption neglects nonuniform distortions that arise in parts with complex geometries. Furthermore, the model ignores the detailed thermal history of the build, so that it is not suitable for studying transient effects or accurately predicting stress changes in geometrically intricate components.

Despite the simplifications offered by these indirect methods, the simulation of large-scale parts remains computationally demanding, and important details such as geometric influences and different scanning strategies are often overlooked. Therefore, thermo-mechanical FE modeling of the LPBF process is typically restricted to relatively small domains or RVs rather than full-scale parts. To extend the applicability of the FEM, researchers have increasingly relied on user-defined subroutines such as USDFLD, UMATHT, and DFLUX, which are implemented within commercial software packages like Simufact.Additive, Ansys, and Abaqus to model custom heat inputs, material behavior, or boundary conditions[62–64]. However, the effective use of such subroutines not only requires a strong grasp of thermomechanical theory but also advanced programming skills in languages such as Fortran, which constitute a significant barrier to entry for many users.

To address these challenges, the Abaqus AM Modeler plugin has been recently introduced as a solution, which integrates many of these complex subroutines into a user-friendly interface. This tool significantly reduces the difficulty of model development and accelerates the simulation setup for LPBF processes. Although there are few studies that have applied the AM Modeler[41,65], the tool has shown promise in bridging the gap between computational efficiency and modeling accuracy. In the first stage of this study, a coupled thermo-mechanical FE model is developed by using the Abaqus AM Modeler, which incorporates the RV approach. This method evaluates a smaller domain that is statistically representative of the overall part, thus minimizing the calculation time while still maintaining sufficient accuracy to study the influence of the processing parameters. Using this approach, the effects of key variables such as laser power, laser speed, and preheating temperature are systematically investigated. The resulting predictions of the residual stress are compared against experimental data reported in the literature to validate the model and provide confidence in its applicability to real-world scenarios. More importantly, the ability to predict residual stress with high fidelity offers valuable insights into fatigue performance, dimensional accuracy, and distortion control, all of which are critical considerations for the reliable deployment of LPBF-manufactured components in demanding industries such as the aerospace and energy industries.

2.4 Post-processing of LPBF Components

The preceding section described how the steep thermal gradients and layer-wise solidification with LPBF generate residual stresses, along with process-specific defects (e.g., LOF pores and micro-cracks) and microstructural anisotropy. These issues can reduce dimensional stability and fatigue performance if left unmitigated. To relax the AM-induced stresses, two industrial post-processing routes are commonly employed: (i) conventional furnace heat treatments (at an ambient pressure) for stress relief and (ii) HIP, which combines elevated temperature with hydrostatic gas pressure. Both treatments reduce the residual stresses accumulated during AM; however, HIP additionally collapses internal voids and heals sub-surface defects, thereby lowering local stress concentrations beyond the use of solely thermal exposure. In this section, a detailed review of previous studies on HIP is presented, which specifically focuses on the effect of HIP on residual stress mitigation in additively manufactured components. This review not only highlights the mechanisms by which hydrostatic pressure contributes to stress reduction but also provides context for the modeling approach adopted in this research. Additionally, HIP and conventional furnace heat treatments are compared, and the effects of processing parameters, including temperature, hold time, cooling rate, and hydrostatic pressure, on residual stress reduction are systematically evaluated using finite element simulations and validated against experimental data reported in the literature.

Conventional furnace heat treatment is the most widely used and straightforward post-processing route for stress relief, as the method relies solely on elevated temperature under ambient pressure to relax internal stresses. Conventional annealing in a furnace at an ambient pressure typically involves heating the part to an appropriate temperature (often 550–650°C for stress relief in steel or higher for superalloys/titanium), holding for 1–2 hours or more, then cooling at a controlled rate. This process allows recovery and recrystallization: dislocations rearrange and new strain-free grains form, thereby relieving internal stresses. For laser powder bed fused parts, a well-chosen stress-relief anneal can eliminate a large portion of the residual stresses – for example, reducing the tensile residual stress from ~466 MPa (as-built) down to ~16 MPa[66]. Furnace annealing does not involve applied external pressure; stress relaxation occurs purely from thermal mechanisms (thermal expansion, creep, and recrystallization) during the hold and slow cooling.

In contrast, HIP is a post-processing technique extensively employed across a wide range of manufacturing sectors to produce components with superior quality and performance. Industries such as the aerospace, automotive, chemical, petrochemical, and medical industries rely heavily on HIP because of its ability to significantly enhance the structural integrity and reliability of critical parts. The process involves subjecting a material to a high hydrostatic inert-gas pressure—typically in the range of 100–200 MPa—while simultaneously exposing the material to elevated temperatures within a hermetically sealed hydrostatic pressure vessel. At such elevated temperatures, the applied hydrostatic pressure often exceeds the yield strength of the material, thus inducing plastic flow and creep that collapse the internal voids, reduce porosity, improve overall density, and trigger microstructural changes beyond those of a simple anneal[67–71]. High temperatures (usually 70–90% of the melting point of the alloy) further accelerates diffusion and recrystallization, thereby enhancing stress relief. The hold time is carefully selected to ensure that even the thickest sections of the part reach thermal equilibrium and sufficient diffusion occurs for stress relaxation, while longer holds can compensate for the use of lower temperatures or hydrostatic pressure. Following the hold stage, the cooling rate is controlled to avoid the introduction of new thermal stresses. As a result, HIP-treated parts exhibit superior mechanical properties, including enhanced strength, improved ductility, and longer fatigue life, all without altering the external geometry of the component. Beyond these general benefits, HIP has been used in a number of specialized applications: to repair shrinkage defects and microporosity in castings; consolidate powders into fully dense solids in powder metallurgy; and enable diffusion bonding between dissimilar materials that are otherwise difficult to join through conventional methods[48,72–74]. The versatility of HIP makes it indispensable for producing high-performance parts that must meet stringent safety and durability requirements. Figure 2.7 presents a schematic illustration of a typical pressure vessel set-up, while Figure 2.8 shows a representative HIP schedule in the form of a T–P–t profile: temperature (T) and hydrostatic pressure (P) ramp concurrently to the setpoints T_1 and P_1, followed by an isothermal–isobaric hold at T_1 and P_1 for a dwell time that drives creep-assisted residual stress relaxation and pore collapse; finally, T and P are reduced at the same time in a coordinated cool-down/depressurization to prevent the reintroduction of thermal stresses.

In AM, HIP is increasingly recognized as one of the most effective post-processing techniques[3,45,75–83]. Its importance is particularly evident in LPBF, a process widely employed for fabricating a broad range of metallic materials[84–87], including high-performance alloys such as Ni-based superalloys[18,20,43,88–91] which are extensively used in aerospace and energy applications. As discussed earlier, laser powder bed fused components often suffer from two critical issues: the accumulation of high residual stresses due to steep thermal gradients and rapid solidification, and the presence of porosity-related defects such as gas pores, LOF voids, and microcracks. HIP directly addresses these challenges by subjecting the material to a combination of elevated temperature and hydrostatic pressure. Under these conditions, several mechanisms are activated simultaneously: the plastic deformation of the pore walls, time-dependent creep deformation, and atomic diffusion. Together, these mechanisms promote the collapse and elimination of internal voids while enabling the redistribution and relaxation of residual stresses that originated during the printing process. The outcome is a component with enhanced density, reduced stress concentrations, and improved mechanical properties, thus making HIP an indispensable step for ensuring the reliability of additively manufactured parts[3,13,22,92,93].

Recently, increasing attention has been directed toward studies that investigate the densification of additively manufactured parts and elimination of porosity through HIP[3,94–98]. Unlike conventional thermal annealing, which operates at an ambient pressure, HIP applies high temperature and hydrostatic pressure simultaneously to collapse voids, heal micro-cracks, and promote microstructural homogenization. This capability makes HIP particularly effective in addressing defects that remain largely unaffected by standard heat treatments. For instance, LPBF-processed Inconel 718 subjected to HIP at 1393 K and 100 MPa for 4 h exhibits nearly complete porosity elimination, with the porosity reduced from ~0.15% to <0.01%. Alongside this densification, HIP dissolved the as-built cellular microstructure, thus resulting in more than 60% increase in ductility. These findings highlight the limitations of heat treatments performed without external pressure, as the pores cannot be closed or microstructural heterogeneities that act as stress concentrators are not fully eliminated. As the HIP process both closes pores and removes dendritic or cellular structures, the technology not only improves density but also reduces stress concentration within the bulk material[99]. Williams et al.[100] reported that HIP of electron beam melted Ti-6Al-4V effectively reduces all internal pores to below the detection limit of X-ray computed tomography (~5 μm), thus resulting in nearly complete densification, apart from a few surface-connected defects. Following HIP, the characteristic defect size is significantly reduced, which in turn increases the fatigue crack initiation threshold and extends the overall fatigue life of the material.

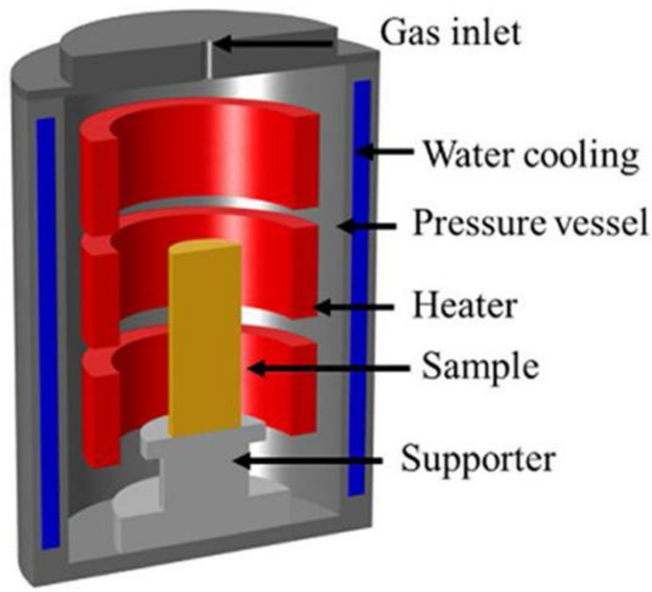

Figure 2.7 Schematic illustration of HIP process, reprinted from Ref. [83]. Used with permission.

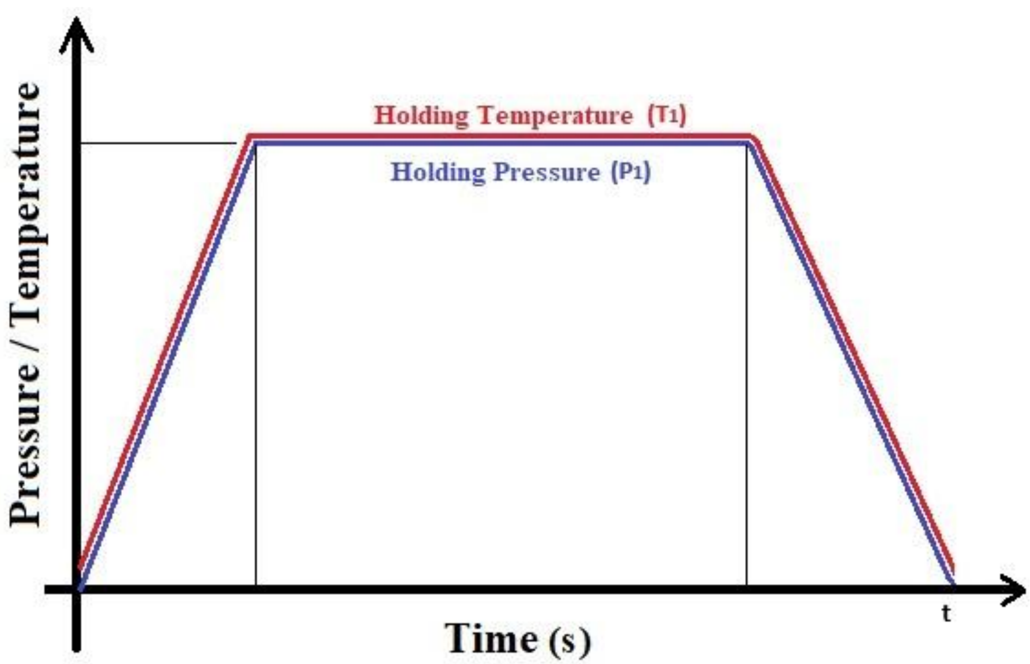

Figure 2.8 Typical HIP schedule (T and P versus time).

Extensive research has also been devoted to optimizing HIP conditions for specific alloys. For example, Lee et al.[101] identified an optimal HIP process temperature of 1180°C for Inconel 718, which resulted in significant reductions in porosity, improvements in segregation behavior, and enhanced tensile and bending strength. In a subsequent study[102], they confirmed that using this processing temperature with a pressure of 1750 bars resulted in a remarkable 78.5% reduction in porosity and additional mechanical improvements, including increased tensile and bending strengths as well as improved elongation in tension tests. Similarly, Plessis et al.[103] used x-ray microcomputed tomography, which is a non-destructive method, to track porosity changes in cast Ti-6Al-4V rods before and after HIP, which revealed that the pores are effectively sealed under HIP conditions through a combination of plastic deformation and atomic diffusion. In addition to its role in defect healing and stress relief, HIP can also reduce the overall LPBF processing time. This is because higher scanning speeds or larger hatch distances can be employed during printing, even though such parameters often increase the risk of porosity. The subsequent HIP cycle effectively eliminates much of this porosity through densification, thereby enabling a faster and more cost-effective build without sacrificing the quality of the final part. Moreover, post-densification through HIP not only decreases the pore content but also homogenizes the as-built microstructure, thus leading to significant improvements in fatigue strength and reliability. In this way, HIP serves as both a corrective and an enabling technology: the process mitigates the shortcomings of accelerated LPBF processing while still delivering components with high density and mechanical integrity[79]. Beyond densification, HIP has also been consistently linked to improvements in fatigue performance[104–110], primarily due to its ability to eliminate gas pores[107,111] that otherwise act as crack initiation sites. Poulin et al.[110] reported that the smaller, healed defects generated by HIP substantially increase the threshold for fatigue crack growth in LPBF-processed materials. However, it is important to note that residual defects—sometimes up to 150 μm in depth—may persist in even high-density laser powder bed fused parts following HIP[107], thus indicating that the process, while highly effective, is not universally capable of eliminating all imperfections.

Both annealing and HIP alleviate internal stresses and improve homogeneity, which enhance ductility and reduce distortion by removing dislocations or pores that serve as stress concentrators. In many industrial contexts, the two processes are employed in sequence or combination: critical laser powder bed fused parts often receive a thermal stress-relief or solution heat treatment in addition to a HIP cycle, which ensure stress mitigation. Nevertheless, comparative studies have consistently indicated that HIP provides superior overall improvements in mechanical performance relative to annealing alone. For instance, in laser powder bed fused Ni-based alloys, conventional solution plus aging treatments improve the fatigue life by approximately twofold compared to as-built samples, whereas HIP extends fatigue life by a factor of four to five. This significant improvement is due to the unique ability of HIP to combine stress relief with defect elimination and microstructural homogenization[99]. Similarly, HIP-treated Ti-6Al-4V and Inconel alloys consistently show higher fatigue endurance compared to the annealed alloys, largely due to the removal of internal porosity and development of beneficial compressive residual stresses at the surface of the materials[112].

It is worth noting, however, that the benefits of HIP can be marginal in terms of static strength if a part is already nearly fully dense and optimized. For a well-processed Hastelloy-X (Ni-superalloy) with ~99.85% density, HIP carried out at a temperature of 1160°C and pressure of 100 MPa for 4 h only reduces porosity from 0.15% to <0.01% – a negligible change that does not translate to a strength increase. The HIP cycle in that case primarily coarsens the grains and anneals out the residual stresses, thus compromising some of the yield strength for more ductility and higher isotropy (yield strength declines from ~680 MPa as-built to ~315 MPa after HIP, while the elongation is increased from ~17% to ~40%). This underscores that the main benefits of HIP for high-quality laser powder bed fused parts lie in residual stress relief and defect healing rather than increasing the yield strength[99].

By contrast, research specifically focused on the role of HIP in managing residual stresses in additively manufactured components remains relatively limited compared to the extensive body of work on porosity elimination and microstructural homogenization. The available studies, however, demonstrate that HIP can have a significant effect on the residual stress state. For example, Qin et al.[82] reported that HIP not only reduces the magnitude of surface residual stresses but also converts them from tensile to slightly compressive—an important improvement over conventional heat treatment, which generally leaves the surface in tension. In their study, the application of inert gas pressure during quenching promotes a more uniform contraction, thus resulting in a slight compressive stress (~−11 MPa) at the surface, whereas a conventional quench produces tensile stress (+48 MPa). Such compressive surface stresses are typically beneficial for fatigue life. Thus, applying pressure during heat treatment can, in some cases, reverse the sign of the residual stresses—transforming detrimental tensile stresses into beneficial compressive ones at critical locations. Similarly, Zhang et al.[113] observed that HIP effectively relieves tensile residual stresses in as-built samples and, in some cases, induces compressive stresses. This transformation is particularly advantageous for fatigue performance, as compressive stresses act to suppress crack initiation and slow down crack propagation, thereby extending the service life of additively manufactured parts. Moreover, several studies indicate that higher HIP temperatures further enhance this effect: the larger thermal gradients generated during the cooling phase encourage the development of compressive residual stresses.

The peak temperature in either an annealing or HIP cycle is the dominant factor for stress relief. Higher temperatures promote greater stress relaxation by enabling recovery and recrystallization of the microstructure. For instance, laser powder bed fused Ti–6Al–4V has an as-built elongated microstructure and high residual stresses; heating this alloy near the β-transus temperature (~950°C) facilitates recrystallization which substantially reduces the residual stress[112]. In general, a heat treatment must reach a sufficient fraction of the melting point of a material to relieve most stress – commonly around 0.5–0.8 Tm. Ni-base superalloys, for example, often require a solution treatment in the order of 1100–1200°C to fully relieve thermal stresses and dissolve strengthening precipitates[99]. If the temperature is too low, the residual stresses may only partially relax. Chen et al.[66] conducted an experimental study on laser powder bed fused titanium alloy and reported that increasing the temperature from 280 °C to 380 °C under thermo-vibratory stress relief conditions significantly enhanced residual stress relief, with the axial stress reduction increasing from 62.89% to 72.91% under the same dynamic stress of 300 MPa. Thus, elevating the temperature generally increases the fraction of residual stress relieved (up to the point of complete stress relaxation). High temperatures also accelerate creep and diffusional relaxation mechanisms, thus enabling stresses to relax at a given pressure in a shorter period of time.

The holding time also influences stress relief, although to a lesser extent than temperature. A minimum duration (often ~1–4 hours) is required to allow stress relaxation mechanisms such as creep and dislocation recovery to reach equilibrium. Extending the holding time can further reduce residual stresses, but may also promote grain growth. In practice, the required hold depends on the size of the part, thickness of the section, and diffusion kinetics. Thick components or materials with slow diffusion rates may require extended holds to ensure that the core is fully heated and stress is relaxed. The HIP process inherently allows for trade-offs among time, temperature, and pressure; for example, a lower-temperature cycle held for a longer duration can achieve comparable densification and stress relief as those with a hotter and shorter cycle. In many cases, HIP treatments of laser powder bed fused alloys use holding times of approximately 2–4 hours as a practical compromise, which experimental evidence shows is sufficient to relieve the majority of the residual stresses[99].

The cooling stage is critical to avoid reintroducing residual stresses. After annealing or HIP, if a part is cooled too quickly, thermal gradients can generate new stresses. Slow cooling (furnace cooling) is often recommended for stress-relief treatments so that the part cools uniformly. Studies indicate that a more rapid cooling rate that exceeds approximately 20°C/min can introduce new residual stresses, whereas very slow rates of cooling (<5°C/min) minimizes thermal stress but may allow excessive grain growth. For example, a HIP-treated Ni-based alloy that is rapidly quenched (>20°C/min) has measurable residual stress due to differential contraction, whereas the same treated part cooled slowly is essentially stress-free[99]. In steels or titanium alloys that undergo phase changes, the cooling rate also affects the residual stress via transformation strains. A conventional quench can leave significant tensile stresses due to the volume expansion of martensite that forms in the cooler regions. In fact, Qin et al.[82] found that in AISI M50 tool steel, vacuum furnace quenching after austenitization introduces tensile residual stresses at a pressure of 150 MPa, which even subsequent tempering cannot fully remove. By contrast, the same steel quenched under HIP conditions (high-pressure gas quenching) shows much lower residual stress. High-pressure gas allows rapid yet more uniform cooling and can suppress some of the phase transformation stress by shifting the transformation kinetics. The integrated HIP + quenching approach has been shown to reduce quench-induced warping or cracking. In essence, controlled cooling (moderate cooling rates or high-pressure gas cooling) helps to ensure that once residual stresses are relieved at high temperature, they do not return upon cooling. Many HIP systems now include precision cooling control: for instance, quenching in argon under a pressure of 150 MPa can cool parts quickly and uniformly, thus alleviating thermal gradients and resulting in significantly lower residual stress than an atmospheric quench[82].

The application of hydrostatic pressure fundamentally distinguishes HIP from a regular furnace treatment. Under high hydrostatic pressure at elevated temperatures, internal pores collapse via the plastic deformation of the surrounding material. This not only densifies the part but can also relieve localized residual stresses around those voids. In laser powder bed fused parts that contain LOF pores or micro-cracks, the hydrostatic pressure forces those defects to close, which reduces stress concentration and can relax tensile residual stresses that are locked in around the voids. Essentially, if voids are present, pressure is an extra driving force for stress relief by eliminating the void volume that internal stresses might be trying to expand. Experimental evidence shows that HIP can reduce porosity to near-zero (e.g. $<0.1\%$) and thereby remove one of the causes of internal stress hotspots[99,114].

At high temperatures during HIP, the yield strength of the material is greatly reduced, and the von Mises yield criterion is not directly pressure-dependent, as it is governed by the shear stress. Hydrostatic pressure contributes meaningfully to yielding only with the presence of voids to collapse. In a fully dense part with no pores, purely hydrostatic external pressure does not generate the shear deformation required to relieve residual stresses—unless the internal residual stresses combine with the external pressure to trigger localized yielding.

Finite element simulations indicate that, in the absence of initial porosity, the extent of residual stress relaxation during HIP is approximately comparable to that achieved through thermal annealing alone. This observation is further supported by our published work[114], which demonstrates that fully dense LPBF components exhibit similar levels of stress relaxation following high-temperature annealing and HIP treatment. By contrast, when voids are present, the pressure-induced plastic flow enhances stress relief substantially. The collapse of the pores allows the material to plastically redistribute and release the stored elastic strains that a thermal treatment at ambient pressure may not be able to fully alleviate[66,114]. It has also been observed that increasing the applied hydrostatic pressure in HIP can amplify these effects: for example, Maj et al.[99] conducted a study on an Ni-based superalloy and applied a hydrostatic pressure of 175 MPa rather than 100 MPa (at the same temperature and dwell time) which produced a more uniform grain structure and improved the tensile properties, thus suggesting more complete stress relief and defect closure at a higher hydrostatic pressure. Standard HIP practices for laser powder bed fused alloys, such as hydrostatic pressure of ~100 MPa for Ti-6Al-4V and 100–150 MPa for Inconel 718—are already highly effective; however, moving toward the upper range of hydrostatic pressure (e.g., ~200 MPa) may yield only marginal additional stress reduction while imposing higher equipment and cost demands[82].

Optimizing the HIP process has traditionally relied on trial-and-error approaches, which are both time-consuming and costly due to the high expense of experimental HIP cycles and the limited number of trials that can be realistically conducted. Consequently, the development of FE models for the HIP of LPBF-built parts is an attractive alternative option, which offers a powerful numerical tool to simulate the process without the need for extensive physical experimentation[96,97,115]. FE modeling can be used to predict the dimensional evolution of components, monitor the development and relaxation of residual stresses, assess the closure of pores, and optimize the processing parameters. These capabilities enable better control over the quality of the final part and improve the overall industrial efficiency of HIP-treated components. In particular, the FEM has emerged as a valuable method for understanding and predicting the changes in residual stresses during post-processing. However, simulating a complete HIP cycle is highly complex, as it requires accounting for thermo-mechanical coupling, time-dependent creep deformation, and, in some cases, phase transformations under hydrostatic pressure. To address these challenges, recent studies have incorporated advanced constitutive laws, such as viscoplastic creep formulations, into FE models, thus enabling more accurate predictions of residual stress relaxation and microstructural changes during HIP.

FE modeling of HIP generally falls into three categories, based on the captured material constitutive behavior. Many studies use time-independent plasticity models (often adapted from soil or porous metal mechanics) to describe powder densification under hydrostatic pressure[116–121]. For example, cap plasticity models like Cam-Clay and the modified Drucker–Prager Cap (DPC) model are widely applied to the HIP of metal powders[116,117,121]. The accuracy of these models can be increased by combining them with a creep law[116,122]. These models relate yield strength to density, thereby capturing how the powder yields and compacts as the void volume decreases. Studies such as Abdelhafeez and Essa[116] demonstrate the use of Cam-Clay and Drucker–Prager formulations in simulations of HIP with 316L steel powder, while Buljak et al.[117] focus on calibrating a DPC model for ceramic powder compaction. Plasticity-only models can predict final shapes reasonably well but may neglect time-dependent deformation. Other works incorporate time-dependent deformation laws (creep or viscoplastic flow) to simulate the slow densification that occurs over the holding time during HIP[123,124]. In these models (which often employ a Norton power-law or hyperbolic-sine creep), densification is driven by thermal activation and sustained pressure, which are analogous to high-temperature creep in metals[98]. For instance, Abouaf et al.[123] developed an early HIP model that treats powder consolidation like a viscoplastic flow. Similarly, Abena et al.[124] implemented a creep law (with coefficients fitted from high-temperature compression tests) in their HIP simulation of Ti-6Al-4V, by using an ABAQUS creep subroutine. Xu et al.[98] explicitly used a Norton creep equation to model the densification of Ti-6Al-4V castings during HIP, which resulted in a good agreement with experimental data reported in the literature. Creep-based models capture the time-sensitive pore shrinkage well but might need enhancements with an initial yield criterion for early densification. The most advanced simulations combine both instantaneous plastic yielding and time-dependent creep to cover all stages of HIP densification[97,125–128]. During a typical HIP cycle, the powder particles undergo initial plastic rearrangement and yield under hydrostatic pressure, followed by slow creep deformation as the material approaches full density[125]. To reflect this, researchers have formulated unified models that couple multiple deformation mechanisms. For example, Van Nguyen et al.[127] proposed a combined model that incorporates plasticity along with primary and secondary creep behaviors. Wikman et al.[128] similarly developed a material model that transitions from a plastic compaction response to a creep-dominated response as densification progresses. These hybrid approaches have been shown to improve the prediction accuracy of the final dimensions and density[116,128]. As Abdelhafeez and Essa[116] reported, adding a creep component to a Drucker–Prager model reduces the shape prediction errors to ~1.5–4.8%, compared to 6% or more when using a purely plastic model. Combined models leverage the strength of both plastic yield modeling and viscoplastic flow, which is crucial since HIP involves simultaneous high-temperature plastic deformation and creep over the holding time[125].

For powder consolidation with HIP, one of the most commonly used constitutive laws is the modified DPC model[117]. This yield model was originally adapted from soil mechanics and has a yield surface composed of a shear failure envelope (Drucker–Prager) and a compaction cap that flattens at high hydrostatic pressure. The cap enables modeling of volumetric plastic compaction, which makes it well-suited for porous powders. Studies have shown that the DPC model can effectively capture powder densification under HIP conditions. For example, Essa et al.[120] modeled the HIP of IN718 powder by using a Gurson-type porous plasticity model for the initial stages and a DPC approach for tool design considerations, while Sundaram et al.[121] employed a DPC model to simulate capsule-free HIP of sintered steel gears, which required an initial density ~95% for surface pore closure. Buljak et al.[117] underline the flexibility of the DPC model and noted that it has been applied not only to metal powders but even to other particulate materials.

A limitation of a pure DPC plasticity model is that it does not inherently account for time-dependent deformation at a constant stress (i.e. creep), which occurs during the holding period of HIP. To address this, researchers often combine the DPC model with a creep law for better accuracy. Abdelhafeez and Essa[116] showed that enhancing a modified Drucker–Prager model with a creep component significantly improves predictions of the dimensions of the final part and densification history in the HIP of 316L stainless steel powder. The CEEQ allows continued densification beyond the instant plastic yield, thus mirroring real consolidation. Du et al.[122] provided a clear example of this approach: they simulated the HIP of selective laser sintered (SLS) 304 stainless steel parts by using an ABAQUS DPC model combined with a hyperbolic-sine creep law. Their simulation showed that the relative density of the SLS parts increases from an initial ~0.37 to ~0.90 after HIP. This substantial densification was achieved in the model by accounting for creep-driven pore collapse in addition to instantaneous compaction. The authors reported minimal shape distortion and good agreement between the simulated dimensions and the experimental data reported in the literature, with the discrepancy remaining within 6%. These results confirm that coupling a creep constitutive law with a powder plasticity model can capture gradual pore elimination during the HIP soak, thus enhancing the fidelity of FEM predictions.

Once a powder compact or additively manufactured part reaches a high relative density (e.g. >90–95%), its remaining porosity consists of isolated voids in a nearly fully dense metal matrix. For this regime, a porous metal plasticity model like the Gurson model (or its extensions by Tvergaard and Needleman) can be very effective. The Gurson model, originally developed for ductile voided materials, introduces a yield function that depends on the void volume fraction, thus allowing the function to predict how voids shrink or grow under plastic flow[129]. It is essentially a modified metal plasticity model that incorporates porosity as an internal state variable. This model is most applicable when the material is nearly fully dense, typically above a ~90% relative density[119–121,129]. In fact, the ABAQUS implementation of Gurson's model explicitly notes that it is intended for a dilute concentration of voids (relative density > 0.9). Several HIP simulation studies of high-density powder compacts or as-built parts have adopted Gurson-based models once the densification reaches the final stage. Xue et al.[119] used a hybrid model that interpolated between a low-density cap model and a Gurson-Tvergaard model at ~90% density during the HIP of Ti–6Al–4V powder. Essa et al.[120] similarly applied a modified Gurson model to represent the powder in HIP simulations for IN718, given that the powder was pre-compacted and near full density.

Sundaram et al.[121] noted that for capsule-free HIP to work, the part must initially exceed ~95% density so that surface pores collapse – a condition where Gurson's assumptions (small void volume) hold true. The appeal of the Gurson model is its ability to predict void closure under plastic deformation for dense materials, which makes it a promising choice for simulating HIP as a post-process for laser powder bed fused parts that typically have relative densities around 99% with small residual porosity.

However, it is important to recognize the limitations of using the Gurson model for HIP. By design, Gurson's formulation handles plastic void closure (voids that contract as the surrounding material yields). The model does not inherently include time-dependent creep or diffusion mechanisms. During HIP, especially at high temperatures and with long holding times, creep deformation can significantly contribute to closing pores[125–128]. The Gurson model and classical creep laws are based on different assumptions and mathematical frameworks, which makes it challenging to combine them directly into a single material model. In other words, Gurson's yield function (a function of instantaneous stress and void fraction) is not formulated to incorporate rate-dependent viscoplastic strain accumulation in the same equation. Van Nguyen et al.[127] and Wikman et al.[128] highlighted this issue: only a few formulations exist that couple multiple deformation mechanisms into one unified model[125]. While one could implement a sequential approach (apply plastic collapse then creep in separate steps), a truly simultaneous Gurson+creep model is non-trivial. In practice, researchers either use the Gurson model in the final stage of densification (when creep may be less dominant over plastic flow) or resort to the combined models discussed above. The Gurson model is very useful for high-density porous metals, but if long-term creep effects during HIP need to be captured, a separate viscoplastic modeling approach needs to be considered rather than a straightforward superposition with Gurson's yield criterion. This is why some HIP simulations switch material models at a certain density threshold (e.g. from a creep-based model to Gurson-based plasticity once $D > 0.9$), rather than attempting to merge the two into one set of equations.

Beyond the constitutive modeling of overall densification, a number of studies have specifically examined the closure of internal pores during HIP, through both experiments and simulations. Understanding pore closure is critical for cast or additively manufactured parts that contain trapped pores even at a high overall density. Recent investigations have shed light on the dominant mechanisms of void elimination and influence of HIP parameters. Xu et al.[95] created a controlled internal gas pore in a Ti–6Al–4V casting and monitored its closure during HIP via interrupted experiments and FEM simulation. They found that pore closure is rapidly initiated in the early stages of HIP; that is, during initial pressurization and heat-up, and then significantly slows down in the later holding stage. The simulations and micrographic observations showed that the pore volume is most dramatically reduced at the beginning of the cycle. Notably, even a standard full HIP cycle (920°C, 120 MPa, 150 min in their case) did not completely eliminate the gas pore. A small residual pore remained, thus indicating that typical HIP parameters might be insufficient to entirely close isolated gas-filled voids. These findings suggest that gas pores are harder to close than shrinkage pores, and extended HIP time or a higher hydrostatic pressure may be needed for complete healing.

In an earlier study, Xu et al.[98] examined shrinkage porosity in Ti–6Al–4V castings under different HIP temperatures (750–950°C, at 150 MPa). They observed that there is a temperature threshold at around 920°C, above which void closure is achieved. Specifically, shrinkage cavities in the casting were fully closed after HIP at 920°C and 950°C, whereas lower temperatures (750 and 850°C) left some residual porosity. Increasing the temperature enhances densification up to that threshold, due to higher thermal energy promoting creep deformation. Their simulations with a creep-based model corroborated the experimental trend, thus showing accelerated pore collapse at higher temperatures. From a practical standpoint, they identified 920°C as an optimal HIP temperature for Ti–6Al–4V: high enough to heal voids effectively, but not so high as to cause excessive grain growth. Epishin et al.[96] investigated void closure in a single-crystal Ni-based superalloy (CMSX-4) during HIP by using interrupted tests and crystal-plasticity modeling. They found that two distinct mechanisms contribute to pore elimination. Plastic deformation of the surrounding matrix is one mechanism: under HIP pressure, dislocations move and climb, thus causing the pore to shrink. The second mechanism is diffusion (a vacancy-driven process): at the HIP temperature (1288°C, ~0.9 T_M for Ni-based superalloy), atomic diffusion leads to pore shrinkage through material transport, albeit more slowly. The study noted that plastic collapse of the pores dominates the initial and intermediate stages of HIP (reducing most of the pore volume), while diffusional pore rounding and final elimination become significant at longer times once the driving pressure for plastic flow is reduced. This aligns with the classic understanding that mechanical closure brings pore surfaces into contact, and then diffusion (if time/temperature permit) bonds the interface. Their work highlights the dual nature of pore healing: pressure-induced plasticity and high-temperature diffusion both play roles. Prasad et al.[97] focused on how HIP parameters (hydrostatic pressure, temperature, holding time) affect pore closure in a Ni-based superalloy, by using a simulation-based approach. They employed a model that incorporates void evolution to study various HIP schedules. The simulations indicated that higher hydrostatic pressure and longer holding times promote more complete pore annihilation, as expected, but with diminishing returns beyond a point. For instance, increasing the hydrostatic pressure significantly speeds up pore closure in the early phase, and extending the hold time helps to reduce final pore size, but long holds only have marginal benefits once the diffusion mechanisms plateaued. They thus aimed to optimize the HIP cycle: find a combination of hydrostatic pressure and time that achieves near-complete pore closure without unnecessary overheating or grain growth. Their results, which were consistent with experimental data reported in the literature, suggested that a carefully calibrated HIP cycle can eliminate most micro-pores while preserving the mechanical properties.

FE simulations provide valuable insights into HIP by enabling the visualization of not only densification but also the changes in stress distribution during and after the process, which is critical for predicting distortions and identifying the risk of cracking[130]. Void-containing materials (such as powder metallurgy compacts, castings with shrinkage porosity, or as-built additively manufactured parts with LOF) are a major focus of modeling the HIP process because the primary purpose of HIP in these cases is to eliminate internal porosity. The closure of pores is accompanied by complex material flow and can generate localized PEEQs, which in turn affect the residual stresses. Recent studies have devoted effort to modeling pore closure kinetics and the resulting stress fields in materials like titanium alloys, Ni-based superalloys, and stainless steels[114,131]. An integrated FE framework simulates the layer-by-layer AM (with residual stress build-up), then applies a HIP cycle to the as-built stress state. These studies have found that a post-treatment with HIP can relax most of the as-built residual stresses, even before all of the porosity is eliminated. The implication is that the thermal exposure and creep during HIP are very effective stress-relief mechanisms– sometimes more effective than a standard stress-relief anneal at ambient pressure[131]. Thus, beyond densification, the role of HIP in mitigating residual stress can be explicitly evaluated via numerical modeling. One notable study on Ni-based superalloy residual stresses during HIP is Bassini et al.[73] on Astroloy. They used FEM to analyze how the HIP parameters influence micro-scale residual stress and hardness in HIP-treated Astroloy powder compacts. Their simulations indicated that higher HIP pressures can induce more plastic deformation in prior particle boundary regions, thus potentially reducing residual micro-stresses upon cooling. Experimentally, they measured the hardness and found that HIP at a higher hydrostatic pressure slightly increases the uniformity of hardness, thus indirectly suggesting a more uniform residual stress field (since hardness differentials are often related to residual stress). These findings align with the general simulation result that sufficient HIP pressure (in the order of 100 MPa) is needed for complete pore elimination in Ni alloys, whereas overly low hydrostatic pressure (e.g. 5–10 MPa) has a negligible effect[132]. In other words, modeling and tests concur that there is a threshold pressure below which pores simply deform elastically without collapsing, thus leaving residual voids (and possibly high local stresses around them). Once that threshold is surpassed, plastic yielding around the pores leads to rapid closure and a corresponding drop in internal stresses. For single-crystal Ni-based superalloys (used in turbine blades), internal porosity and residual stresses are also critical. While grains are absent, these castings often have micro-pores from solidification. Creep-based FE models have been applied to simulate the HIP of single-crystal superalloys, which distinguishes the dislocation creep (plastic flow) from diffusion creep (vacancy diffusion driven pore shrinkage) regimes[97]. The studies have noted that in typical HIP conditions, both mechanisms contribute with larger pores closed primarily through dislocation creep (accompanied by local residual stress that can persist after cooling), whereas very fine pores heal by diffusion with minimal stress generation[97,104]. FE studies have reported that a minimum hydrostatic pressure of 100 MPa is required to eliminate LOF pores at typical HIP temperatures. At much lower hydrostatic pressures (50 MPa), simulations indicate that the yield strength of the material at 1561 K is not exceeded, so pores remain essentially intact[97]. This is experimentally confirmed: HIP-treated 316L samples processed at 5 MPa show no porosity improvement, whereas those treated at 100 MPa become fully dense[133]. Such insights have been captured in FE studies by incorporating the creep law of the material: only above a certain stress (from the applied hydrostatic pressure) would the CEEQ rate become sufficient to collapse the voids. After HIP, 316L shows good residual stress results. As the material is ductile, it ends up almost stress-free, with only slight compressive stress at the surface from uniform contraction. Numerical models of laser powder bed fused 316L with HIP also show that nearly all tensile residual stress from printing can be removed. In Dye et al.[134], neutron diffraction was used to measure the internal residual stresses in a HIP-treated superalloy turbine disk, and these were compared to an FE simulation of the HIP + cooling process.

The simulation accurately reproduced the compressive hoop stresses in the disk bore and the slight tensile stresses at the rim that the neutron data indicated, thus bolstering confidence in the creep-plasticity material model used.

While the general benefits of HIP in promoting densification and relieving residual stresses are well established, the influence of the initial void fraction, void morphology, and void distribution in additively manufactured parts on the final HIP outcome remains an important area of investigation. The morphology of voids—specifically their shape and size—plays a crucial role in determining how they deform and close during the HIP process. Non-spherical or irregularly shaped voids tend to concentrate local stresses at protrusions, edges, or sharp corners, which can facilitate localized plastic deformation and accelerate pore collapse under hydrostatic pressure. In contrast, spherical voids experience a uniform pressure distribution on all sides, which lack such stress concentration sites. As a result, they are more resistant to plastic deformation and therefore require higher temperatures, longer holding times, or larger applied hydrostatic pressure to achieve full closure[97,135,136]. Consequently, understanding the combined effects of void shape, size, and initial porosity level is essential for optimizing HIP parameters to ensure complete densification and defect healing in additively manufactured components.

Comparative studies have shown that under the same HIP parameters, spherical pores close more slowly than elliptical or crack-like pores. Prasad et al.[97] observed that large irregular or elliptical shrinkage cavities in a casting heal more readily than nearly round pores, which remain open longer due to the more uniform stress distribution that resist their collapse. Similarly, recent pore tracing experiments on HIP-treated additively manufactured AlSi10Mg found that irregularly shaped pores close faster than spherical ones during the HIP cycle[136]. Pore shape may also change during densification. Even if a pore starts out roughly spherical, the deformation is often not perfectly self-similar – a collapsing spherical void can become slightly ellipsoidal as the material flows inward[135,136]. The classic experiments of Kellett and Lange[137] on ceramic compacts show that surface-connected pores do not close during HIP. However, pores located near the surface can induce significant surface damage during HIP. The observed cratering and puncturing associated with near-surface spherical pores, together with the accompanying changes in pore morphology, suggest that plastic deformation is the dominant mechanism that governs pore collapse[137]. In general, as the pores shrink, they tend to lose any smooth, rounded geometry and may morph into an irregular shape before the final healing. This is because different facets of the void may close at different rates (due to the crystallographic orientation or local microstructural inhomogeneities), which give the final pore (if any remains) a jagged or non-spherical profile[135,136].

Alongside void shape, the size of voids is another critical factor that influences densification during HIP. Smaller pores—typically micro-voids less than 0.1 μm—tend to shrink more rapidly than larger ones under the same conditions. From a thermodynamic perspective, smaller voids have higher internal gas pressure and greater surface curvature, as described by Laplace's law, which together provide a greater driving force for diffusion-controlled shrinkage and creep processes. Numerical simulations have confirmed this effect, which show that pores below a certain critical radius can vanish much faster, whereas larger voids require extended deformation and diffusion times to achieve full closure[97]. The experimental observations in Mishurova et al.[138] are consistent with these findings, and smaller pores with a similar morphology heal faster than the larger pores. This size dependence phenomenon suggests that, after the initial plastic-yielding stage of HIP, any remaining micro-pores can gradually disappear through diffusion and creep, provided that a sufficient holding time and suitable temperature are applied. Void morphology not only dictates the kinetics of pore closure but also the residual stress field left behind once the void has vanished. Sharply irregular pores tend to generate localized PEEQ and may leave strain scars after closure, while spherical pores collapse more uniformly, and produce minimal residual strain in the surrounding matrix. Ultimately, complete elimination of the voids removes stress concentrators and allows the material to equilibrate to a relatively low residual stress state[82,97,135,136]. Conversely, partially closed voids can act as persistent sources of local residual stress and potential initiation sites for subsequent damage or cracking.

The location of pores relative to the free surface is another critical factor that affects HIP efficiency. HIP is generally most effective in closing internal voids deep within the bulk material, while surface-connected pores or cracks often persist even after treatment[31,100,135,137,139,140]. Such surface-connected defects are difficult to heal because the pressurizing gas can penetrate the cavity or the free surface allows the void to expand outward instead of collapsing. Williams et al.[100] reported that, following the HIP of EBM Ti-6Al-4V, all fully internal pores are eliminated, whereas defects connected to the surface by narrow ligaments remain partially open. Similarly, Nudelis and Mayr[135] observed that pores in direct contact with the surface or those that contain oxide films resist complete closure even under aggressive HIP conditions. In such cases, additional measures—such as encapsulation prior to HIP or post-HIP chemical milling—may be necessary to achieve full densification.

The spatial arrangement of pores not only influences densification but also affects the changes in the internal stresses during HIP. Clusters of voids may locally relieve stress as they collapse, owing to concentrated plastic flow in that region, yet this localized compaction can leave behind a residual tensile stress halo that surrounds the densified area relative to the less-deformed surrounding material. In contrast, a uniformly distributed porosity field promotes more homogeneous shrinkage and stress relaxation. Ideally, the aim of using HIP is to obtain uniform densification such that the residual stresses are minimized throughout the part. One of the key advantages of HIP over non-isostatic treatments lies in its ability to equalize internal stress heterogeneities by applying uniform pressure in all directions. For example, in the post-treatment of LPBF-produced steel with HIP, researchers have observed that the process not only nearly eliminates porosity but also significantly reduces both the magnitude and scatter of residual stresses across the component. Any residual stresses that remain after HIP are generally much lower than those in the as-built condition and can even become compressive[82,114]. The proper selection of HIP parameters, in particular sufficient hold time and temperature, is therefore essential to enable full stress relaxation and achieve optimal material uniformity.

Beyond the effects of void morphology and spatial distribution, the initial void volume fraction plays a critical role in determining the overall effectiveness of the HIP process. The initial degree of porosity strongly influences both the kinetics of densification and the processing conditions required to achieve full consolidation. In general, higher void volume fractions require more plastic deformation to eliminate all voids, and if the pores are large or interconnected, HIP might not completely remove them[100,139], thus leaving behind residual stress concentrators that can deteriorate the mechanical performance. Many studies report a characteristic two-stage densification behavior: an initial rapid reduction in porosity dominated by plastic deformation, followed by a slower process toward full density as time-dependent creep and diffusion processes become dominant. This transition occurs because, as the pores shrink and the surrounding material densifies, the local driving stress around the voids decreases, thus reducing the rate of closure[97]. Overall, the healing rate during HIP primarily depends on both the initial void volume fraction and its distribution within the material. When the porosity is high, densification easily starts to occur due to the low initial stiffness of the material; however, excessive clustering of the pores can lead to coalescence or mutual interference which impedes complete elimination. Conversely, at very low porosity levels—where only a few isolated pores remain—prolonged holding times are often required for diffusion-assisted closure. According to Cegan et al.[139] , who investigate the effect of HIP on 316 L stainless steel prepared by using LPBF and characterized by using X-ray computed micro-tomography (XCT), the reduction in the percentage of void volume fraction from the initial state (after LPBF) to the secondary state (after HIP) does not show a direct and monotonic relationship with the initial void volume fraction. In other words, as the porosity generated under different LPBF conditions increases, the percentage of void reduction during HIP does not follow a purely increasing or purely decreasing trend. Specifically, within the initial porosity range of 0.13 to 0.69, the percentage of void reduction first increases and then decreases as the initial void fraction increases from 0.13 toward 0.69. Similarly, Williams et al.[100] who examine the effect of HIP on titanium prepared by selective electron beam melting and analyzed by using XCT, also report non-monotonic behavior. In[100], a 100% void reduction was observed as the initial porosity increased up to 0.202. However, within the higher initial porosity range of 0.225 to 0.625, the percentage of void reduction decreased with increasing initial porosity. This further supports the non-monotonic relationship between initial porosity and HIP densification efficiency.

An additional factor that influences the densification behavior and residual stress changes during HIP is the presence of trapped gas within the voids, such as argon from the build chamber or gaseous reaction products. Gas-filled pores behave differently from vacuum or empty voids: as the pore volume decreases under external hydrostatic pressure, the internal gas pressure rises and increasingly resists further collapse. This back pressure can substantially slow down or even stop the densification process, even if the surrounding material has already yielded plastically[97,100,141–144]. Prasad et al.[97] modeled this phenomenon and showed that small gas-filled pores (<0.1 μm) can develop internal pressure in the order of several gigapascals during HIP. The pressure may diffuse argon into the surrounding matrix, but if the gas remains trapped, the pore may reopen during subsequent heat treatments or in-service thermal exposure once the external hydrostatic pressure is released. Effective elimination of gas porosity during HIP therefore depends on whether the gas can either dissolve into the metal matrix or escape. Extended holding times at elevated temperatures can facilitate this diffusion, and in some cases, getter elements are deliberately added to alloys to chemically trap gases. Nevertheless, residual micro-pores may persist when insoluble gases remain trapped[97,135]. These unclosed pores are not only like small defects but can also generate localized tensile stresses due to the internal gas pressure. Consequently, the chemical composition and gas solubility of the material must be considered alongside void volume fraction, size, shape, and distribution when predicting HIP efficiency and post-treatment material integrity.

This research investigates the generation, changes, and relaxation of residual stresses that arise during the LPBF process, by using advanced FE simulations as the primary analytical tool. Residual stresses can significantly affect dimensional accuracy, mechanical integrity, and fatigue performance, thus making their understanding and mitigation essential for ensuring the reliability of additively manufactured components. In the first stage of this study, a detailed coupled thermo-mechanical FE model is developed to simulate the LPBF process. This model predicts the changes in temperature, strain, and stress fields throughout the build, thereby accounting for the influence of key process parameters such as laser power, scanning speed, and preheating temperature, as well as the temperature-dependent behavior of the material properties. The simulation enables an in-depth examination of how steep temperature gradients and layer-by-layer solidification contribute to the formation of complex tensile and compressive residual stress zones within the part.

In the second stage, the research focuses on the post-processing phase, where these residual stresses are alleviated through thermal and pressure-assisted treatments. Two primary routes are considered: (i) conventional furnace heat treatment under ambient pressure, and (ii) the HIP process, which combines elevated temperatures with high hydrostatic pressure. Using FE simulations, the time-dependent changes of the residual stresses during both treatments are analyzed, thus providing insight into the plastic deformation and creep mechanisms that govern stress relaxation. A comparative investigation is then conducted to examine the specific effect of hydrostatic pressure on HIP relative to the purely thermal effects of furnace annealing. This comparison demonstrates how applied hydrostatic pressure can promote plastic deformation and creep, thereby contributing to stress redistribution and greater residual stress relaxation compared with heat treatment alone.

Finally, the study is extended to explore the void-related factors that influence stress relaxation under HIP conditions. Special attention is given to cases where the internal gas pressure inside the voids is assumed to be zero, to isolate the mechanical effects of the surrounding material. The investigation systematically examines how void morphology (shape and size) and void volume fraction affect local deformation behavior, densification kinetics, and stress redistribution within the matrix. Variations in pore geometry are analyzed to determine their influence on the efficiency of pore closure and the uniformity of residual stress relief. This stage provides critical insight into the pressure-assisted plastic flow and creep mechanisms that dominate during HIP, thus linking microscale void changes to macroscale stress relaxation.

The findings of this research advance current understanding of post-processing optimization for laser powder bed fused components. The study establishes a predictive framework for selecting optimal HIP and heat-treatment parameters—such as temperature and hydrostatic pressure—to achieve maximum residual stress relief and defect elimination. Ultimately, this work contributes to the broader goal of enhancing the structural integrity, mechanical performance, and service life of additively manufactured components used in demanding sectors, such as aerospace, energy, and biomedical engineering.

CHAPTER THREE: SIMULATION FRAMEWORK & GOVERNING EQUATIONS

3.1 Simulation Implementation Framework

This chapter provides a description of the simulation framework, governing equations, and numerical implementation strategies employed throughout this study. The primary objective of this section is to establish the theoretical and computational foundations necessary for constructing the FE models used in both the AM and post-processing phases. The physical mechanisms that underlie heat transfer, mechanical deformation, and residual stress generation are discussed together with their numerical representations to ensure a transparent modeling methodology.

The chapter begins with an overview of the LPBF process, which represents the initial stage of material fabrication. In this section, the key thermal–mechanical phenomena associated with LPBF—such as rapid melting and solidification, cyclic heating and cooling, and the generation of residual stresses—are analyzed. The numerical modeling approach, including assumptions, boundary conditions, material properties, and meshing strategy, is presented in detail to capture the transient temperature and stress changes during the AM process.

In the second part of this section, the attention shifts to the simulations performed during post-processing, including conventional furnace heat treatment and HIP. These simulations aim to characterize the relaxation of residual stresses, onset of plastic deformation, progression of creep, and closure of internal voids under elevated temperatures and hydrostatic pressure. The constitutive models used to represent high-temperature material behavior—including viscoplasticity and creep laws—are introduced and justified to ensure accurate representation of the material response during these high-temperature operations.

3.1.1 Simulation of Laser Powder Bed Fusion Process

Commercial software like Simufact.Additive, Ansys, and Abaqus utilizes FEM to provide accurate assessments of part distortions and residual stresses[62–64]. Typically, various user subroutines like USDFLD, UMATHT, DFLUX, and others are added to the commercial software packages for FEM simulations of the LPBF process. However, usage of these subroutines often needs extensive knowledge of both thermodynamic theory and Fortran programming. The Abaqus plugin AM Modeler recently uses these subroutines as internal user subroutines to reduce the difficulty of simulating the LPBF process and simplify model development. There are very few publications on the use of the Abaqus plugin in AM process modeling[41,65]. In this study, an FE model is developed by using the Abaqus plugin AM Modeler tool to accurately evaluate the residual stress produced during the LPBF process. The model utilizes the RV approach to minimize calculation time, and evaluates the impacts of laser speed, laser power, and pre-heating temperature during AM on the resultant residual stress, which affects the component fatigue life and geometrical distortions. The predicted residual stress is studied and outputs of the FE model are compared with the experimental data reported in the literature.

3.1.1.1 LPBF Thermomechanical Modeling

It has been extensively shown in the literature that thermomechanical modeling is a powerful and suitable approach for predicting residual stresses and geometrical distortions in additively manufactured components. During the LPBF process, a variety of strongly coupled thermal and physical phenomena occur simultaneously—such as the movement of a focused laser heat source, rapid melting and solidification, material deposition, phase transformations, radiation losses, and heat conduction through both the powder bed and solidified material. The combination of these transient and nonlinear phenomena makes LPBF an inherently complex and highly dynamic process, characterized by steep thermal gradients and localized temperature fluctuations.

Accurate prediction of residual stresses and distortions therefore depends critically on the precise determination of the transient temperature field throughout the build. Since the thermal history directly influences the mechanical response of the material—through temperature-dependent elastic–plastic behavior, thermal expansion mismatch, and phase evolution—capturing the temperature distribution with high fidelity is essential. Consequently, the heat transfer analysis serves as the foundation of the entire thermomechanical simulation. Any inaccuracy in modeling thermal behavior, such as incorrect boundary conditions or simplified laser heat input, can be reproduced through a mechanical analysis but leads to significant errors in predicted residual stress and distortion[49,50].

3.1.1.1.1 Governing Equations

The transient heat transfer problem in the LPBF process is resolved by using a 3D heat conduction equation. To determine the temperature field, the heat conduction equation is solved by considering the initial conditions, surface convection boundary conditions, and a heat source model. The equation for 3D heat conduction is:

$$\rho(T)C_p(T)\frac{\partial T}{\partial t} = k\nabla^2 T + q(r,t) \tag{3.1}$$

where Cp, ρ, k, T, and q are the specific heat [J/kg K], density [kg/m^3], thermal conductivity [W/m K], temperature [K], and volumetric heat source [W/m^3], respectively. The variable r can be interchanged with each coordinate as required (i.e. X, Y, Z in the Cartesian coordinates). T stands for temperature, and t represents time. To analyze the effect of the pre-heating temperature, the initial temperature (T_0) at time $t = 0$ was set to 25, 125, and 225℃. As the laser scans the powder, some of the heat dissipates into the environment through radiation and convection. On the scanning surface (XY-plane), the surface convection and surface radiation heat loss during the LPBF process are defined, respectively, by using:

$$q_{Convection} = \tilde{h}(T - T_\infty) \tag{3.2}$$

$$q_{Radiation} = \varepsilon\sigma(T^4 - T_\infty^4) \tag{3.3}$$

where $\tilde{h}$ is the convection heat transfer coefficient (15 W/m^{2}K) at the surface, T_∞ is the ambient chamber temperature which is 25℃, and σ is a Stefan-Boltzmann constant. A radiation boundary condition with an emissivity (ε) of 0.4 was imposed on the top surface of the powder layer. The numerical values of the convection heat transfer coefficient and emissivity utilized in this study closely align with values found in well-established literature sources, specifically referencing[41,145–149]. The thermal results were used as input for the mechanical model to calculate the thermal and total strains:

$$\varepsilon^{th} = \alpha(T - T_0) \tag{3.4}$$

$$\varepsilon = \varepsilon^{e} + \varepsilon^{pl} + \varepsilon^{th} \tag{3.5}$$

The total, elastic, plastic, and thermal strains, and the thermal expansion coefficient in Equations (3.4) and (3.5), are represented by ε, ε^{e}, ε^{pl}, ε^{th}, and α, respectively. The total strain is used for an elastoplastic mechanical analysis to determine the residual stress in the LPBF process by using[50,150–152]:

$$\{\sigma\} = [D]\{\varepsilon\} \tag{3.6}$$

$$D_{ijlm} = \frac{E}{1+\nu}\left[\frac{1}{2}(\delta_{ij}\delta_{lm} + \delta_{il}\delta_{jm})\frac{\nu}{1-2\nu}\delta_{ij}\delta_{lm}\right] \tag{3.7}$$

$$\delta_{ij} = \begin{cases} 1, & i = j \\ 0, & i \neq j \end{cases} \tag{3.8}$$

The fourth-order elastic stiffness matrix for isotropic materials and the Kronecker delta function in Equations (3.6), (3.7), and (3.8), are represented by $[D]$, and δ_{ij}, respectively. Also, E and ν are the Young's modulus and Poisson's ratio, respectively[50,151].

3.1.1.1.2 Modeling of the Heat Source

To predict the nodal temperature and heat distribution, the heat input model must be accurate. The Goldak heat source model[153] is an accurate heat input model which is widely used in welding and AM. The Goldak heat source model utilizes four geometric parameters, namely width (a), depth (b), front length (c_f), and rear length (c_r), as outlined in Equations (3.9), (3.10) and (3.11), to determine the distribution of heat fluxes. Note that the fractional factors of the heat deposited in the rear and front quadrants are $f_r = \frac{2c_r}{(c_r+c_f)}$ and $f_f = \frac{2c_f}{(c_r+c_f)}$, respectively, and their sum is equal to 2. Figure 3.1 shows the Goldak heat source model.

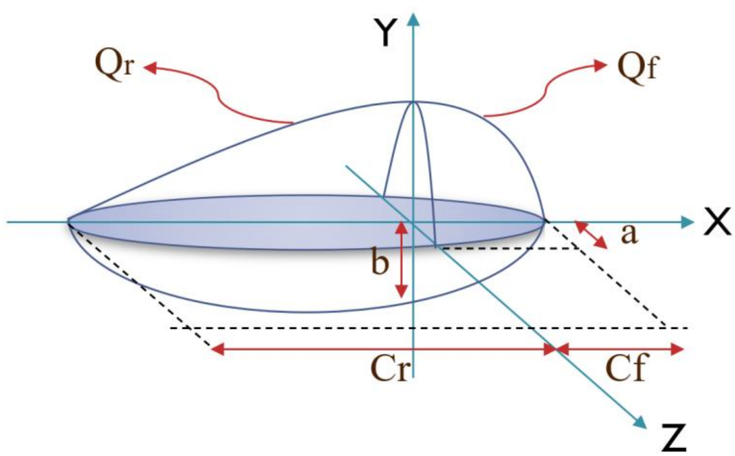

Figure 3.1 Goldak's double ellipsoidal heat source model.

$$Q = \begin{cases} Q_r, & x < 0 \\ Q_f, & x \geq 0 \end{cases} \tag{3.9}$$

$$Q_f(x,y,z) = \frac{6\sqrt{3}\, f_f\ P}{abc\pi\sqrt{\pi}}\, e^{\left(-\frac{3x^2}{c_f^2}\right)} e^{\left(-\frac{3y^2}{b^2}\right)} e^{\left(-\frac{3z^2}{a^2}\right)} \tag{3.10}$$

$$Q_r(x,y,z) = \frac{6\sqrt{3}\, f_r\ P}{abc\pi\sqrt{\pi}}\, e^{(-\frac{3x^2}{c_r^2})} e^{(-\frac{3y^2}{b^2})} e^{(-\frac{3z^2}{a^2})} \tag{3.11}$$

where P and Q are the laser power and power density, respectively. In this study, the Goldak heat source parameters are c_f = 0.05 mm, c_r = 0.1 mm, b = 0.07 mm, and a = 0.07 mm. The numerical values of the four geometrical parameters in this study are derived by following the direction and methodology outlined in[41]. Also, the simulations are carried out with different laser powers and speeds, and pre-heating under a constant layer thickness of 50 μm and a constant hatch distance of 0.1 mm. Table 3.1 shows the identified parameters and their corresponding values.

Table 3.1 Processing parameters of LPBF used in simulations with zigzag pattern

Factor	Unit	Value			
		1	2	3	4
Laser speed, Vs	mm/sec	600	750	900	1050
Laser power, P	W	120	150	180	---
Initial temperatures, T_0	◦C	25	125	225	---

3.1.1.2 Numerical Model

3.1.1.2.1 Representative Volume Approach

The FEM is an efficient method for solving heat transfer problems and can be used as an advanced tool to study residual stress during LPBF[41,65]. Abaqus CAE 2021, an FE solver, is used in this study to create a sequentially coupled thermo-mechanical FE model. The FE model includes two analysis steps. The temperature history produced during LPBF is determined in the thermal analysis by calculating the temperature field at different time steps. Afterward, the results are imported into mechanical equations to solve for the stress state[154,155]. The plugin tool *AM Modeler* and RV approach are employed to simulate these two steps.

In Section 3.1.1, the Abaqus plugin AM Modeler was discussed, which offers enhanced capabilities for simulating AM processes, thus eliminating the need for user-submitted codes. This plugin features a user-friendly graphical user interface (GUI) and maintains compatibility with the user keyword interface and subroutine structure of Abaqus. However, it can be accessed through table collections with string identifiers that start with 'ABQ_AM.'

The plugin effectively represents the physical aspects of AM processes, including dynamic heat flux modeling for laser beams and element activation for simulating raw material deposition. The plugin utilizes two types of data, Event Series and Table Collections, to manage simulation input data. Event Series specifies the timing (t) and spatial coordinates (x, y, and z) of events and is employed in this study to simulate the movements of the powder recoater and laser beam.

On the other hand, Table Collections store essential parameters for each event, including those dependent on the field variables, temperature, and solution-specific state variables. For instance, in the Goldak heat source model, the Table Collections define four geometric parameters as outlined in Equations (3.9), (3.10), and (3.10), along with the heat absorption coefficient used in the modeling of moving laser heat sources.

It is not computationally efficient to simulate the residual stresses of a real-size model accurately with current computational capabilities. Instead, the printing of the RV of an area can be used to estimate the average residual stress in that area[148]. Although the RV is a small volume, it is large enough to be representative of the entire component and used to predict the average residual stress under the same thermal and mechanical boundary conditions. In the RV approach, the aim is to replicate real-world conditions as closely as possible. This encompasses aspects such as environmental temperature, convection conditions, and radiation, which are mirrored to align with real conditions. Additionally, it is ensured that the printing parameters, such as laser speed and power, and hatch spacing, are set to match real conditions. The contact between layer and the base plate, as well as cooling time, are also configured to closely resemble real conditions. To provide a quantitative perspective, Bayat et al.[156] conducted a study that focused on the number of tracks in a layer by refining the stripe widths in sequential flash heating, which vary from 15 mm to 1.5 mm. Their research showed a substantial reduction in deviation between the predicted and measured deflection, with the deviation decreasing from 35.7% to an impressive 1.19% when selecting ten tracks in a layer. Based on the insights derived from their research work, it becomes evident that by having ten tracks in a layer, a layer with minimal deviation between predicted and measured deflections can be constructed. This significantly contributes to enhancing the ability of the model to accurately predict the deflection field. In this work, a hatch distance of 0.1 mm is specifically chosen. Consequently, to accommodate ten tracks in a layer, the minimum width would be 1 mm, thereby adhering to the insights in Bayat et al.[156].

In this study, AM Modeler is implemented by using the RV approach to simulate an actual physical process. The RV approach reduces the calculation time because the real model is not simulated, which includes over 1000 layers and tracks. This approach has a more efficient calculation time with respect to modeling accuracy as a beam-scale heat input model is used. This beam-scale model has the smallest scale for AM simulation and provides a high degree of accuracy and details. This FE model can incorporate the laser speed and power, hatch spacing, layer thickness, and pre-heating. Since the movement of the laser is simulated, it is also possible to analyze the created residual stress and thermal history for different printing patterns, such as zigzag, spiral-in, spiral-out, etc. Also, this FE model can simulate the effect of the cooling rate on the residual stress. Furthermore, this method can model the substrate to apply the boundary conditions according to the real process.

3.1.1.2.2 RV Model Configuration

For computational modeling, an RV of 1 mm × 1 mm × 1 mm (x × y × z) was used with a mesh density of 40 elements per 1 mm maintained throughout the powder layers in the model. This model represents the components with a real size of N×(1×1×1) mm^3 where N is a natural number. The geometrical model of the LPBF process is presented in Figure 3.2, where the yellow line demarcates the powder and substrate. Thermal and mechanical modeling in Abaqus was carried out by using the DC3D8 and C3D8 elements, respectively. C3D8 is a 3D, eight-node continuum element employed in solid modeling. It's sometimes called a 'brick' element because it embodies an eight-node hexahedron, therefore resembling a cube. This element has been highly effective in simulating 3D structures with intricate shapes, thus providing accurate representations of curved and irregular forms. C3D8 elements are commonly used in structural and thermal analyses, as well as simulations that involve solid materials under various loads and boundary conditions. Meanwhile, DC3D8 is a variation of the C3D8 element, which features reduced integration for improved computational efficiency. Mesh sensitivity research was performed to establish the minimal mesh size needed for the thermal and mechanical models, in which the minimal mesh size from the sensitivity analysis was maintained. With high energy intensity and rapid travel speeds, LPBF is expected to have high thermal gradients. Achieving accurate simulations in LPBF requires employing finer meshes along the scanning path to capture the intricacies of the heat-affected zone (HAZ), while coarser meshes can be utilized in regions farther away from it to reduce the calculation time.

The thickness of the layer of powder is 50 μm. One physical layer of powder is represented by two layers of elements. The AM of the layers was simulated with the use of layer-by-layer element activation based on the use of a recoater or roller blade in the layer-by-layer deposition of the powder. The bottom region has an element size of 100 μm × 25 μm × 25 μm. Elements with dimensions of 25 μm in the X, Y, and Z directions were used to mesh the area over which the laser passed. Furthermore, coarser elements were used in areas farthest from the laser heat source. The substrate and printed part have 92,800 linear hexahedral elements and 99,179 nodes. A fixed constraint boundary condition was assigned for the bottom of the substrate which prevented the nodes from moving in all directions.

Each layer of powder was first deposited, and then the layer was selectively melted with a laser beam that followed a predetermined printing pattern. The printing pattern has a major effect on residual stress and part distortion. The local thermal boundaries that surround the melt pool at the time of solidification, as well as the overall limitations imposed by the build plate on the component, determine how the thermal stress changes during the LPBF process. Different scanning patterns can result in different boundary conditions that surround the melt pool, which can change the residual stress and distort the laser powder bed fused components. In this study, a zigzag pattern is used. As shown in Figure 3.3, a specific event series is created to simulate the movement of a laser beam so that the left edge of the layer of powder [position (-0.1 mm, -0.1 mm, 0.05 mm)] is heated by the laser beam first. Afterward, the laser beam travels along the X-axis from the right to the left at a constant speed and laser power amplitude. The next track is scanned in the Y-axis, and then the next track is scanned from the left to the right along the X-axis. This pattern is repeated until all of the layers are completed. Figure 3.3 shows the examined geometry and tool path of the event series for Layers 1, 4, and 20. Scanning is performed on a solid substrate with dimensions of 1 mm × 1 mm × 1 mm (length × width × height). The first layer is added on top of the substrate and the second layer added onto the first layer. Layers of powder are sequentially added. These fill a total volume of 1 mm^3 which comprises 20 layers of powder on the top of the substrate. The length of the tracks is considered to be longer than the top surface to replicate the skywriting process of the LPBF machine.

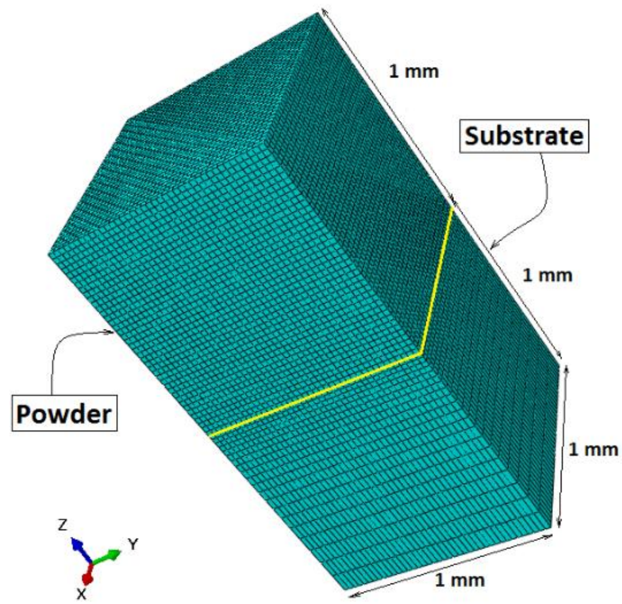

Figure 3.2 Geometrical model of LPBF process.

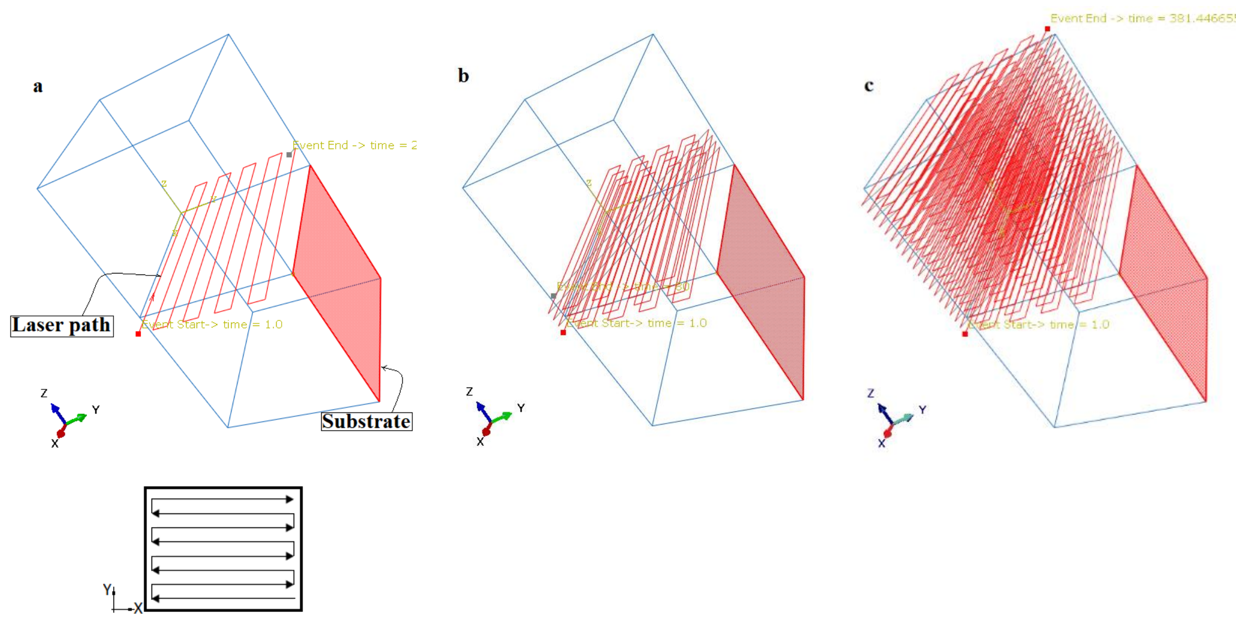

Figure 3.3 Tool path of event series for Layers a) 1, b) 4, and c) 20.

3.1.2 Simulation of Post-processing Heat Treatment

Following the completion of the LPBF simulation, the residual stress field obtained from the previous stage was used as the initial condition for the post-processing simulations. These simulations are designed to analyze how the existing residual stresses change under elevated temperature and hydrostatic pressure, and predict the extent of stress relaxation, plastic deformation, and void closure during the subsequent heat-treatment stages. In this study, two major post-processing techniques are modeled: conventional furnace heat treatment and HIP.

The furnace heat-treatment simulation focuses on the effect of temperature and holding time on stress relaxation in the absence of external hydrostatic pressure. The simulation incorporates the residual stress field from the LPBF process as the initial state, which allows the material to undergo plastic deformation and thermally induced creep according to the temperature-dependent constitutive relations. In contrast, the HIP simulation applies an additional external hydrostatic pressure, which acts in conjunction with high temperature to enhance the plastic flow, accelerate creep, and facilitate void collapse and pore closure. The combined influence of temperature and hydrostatic pressure leads to a more significant reduction in internal stresses compared to conventional heat treatment. As a result, thermomechanical–creep coupling becomes a key element of the numerical framework.

Accordingly, a coupled thermal–stress FE analysis was employed to evaluate the time-dependent changes of stress, strain, and creep behavior during the post-LPBF heat-treatment processes. The governing equations for heat conduction, mechanical equilibrium, and viscoplastic–creep response are presented in the following sections, along with the associated boundary conditions and loading parameters used for both the furnace and HIP simulations.

3.1.2.1 Post-processing Thermomechanical Modeling

Studies have largely shown that thermomechanical modeling is effective for predicting residual stresses in manufacturing processes[49,50,157–160]. Thus, in this study, a coupled thermal-stress analysis is employed during the post-AM heat treatment process. In this work, Abaqus CAE is used to simulate post-AM stress relaxation heat treatments for a part produced by LPBF. A two-part model was developed to simulate stress relief heat treatment. To accurately predict the effects of heat treatment on stresses and strains in the part, the model needs to capture the effect of temperature changes (e.g., heating from room temperature, holding at the desired temperature, and then cooling to room temperature) during the process. For this purpose, the model used in this study consists of thermal and mechanical components. The equations provided in the following sections are used to simulate the post-LPBF stress relaxation heat treatment.

3.1.2.1.1 Thermal Analysis

An accurate prediction of residual stress over time depends on the accurate determination of the temperature field within the model, which makes heat transfer an important consideration in the analysis. A transient heat conduction equation was solved at each increment to obtain the temperature field during the post-AM stress relaxation heat treatment. The governing 3D heat conduction equation has already been introduced in Equation (3.1).

3.1.2.1.2 Mechanical Analysis

HIP causes the material to undergo plastic deformation and creep due to exposure to high temperatures and hydrostatic pressure for long periods of time[127,128,161,162]. Therefore, three constitutive components—the effects of temperature, creep, and plastic deformation—are utilized in this simulation to model residual stress relaxation. Several strain components contribute to the total strain. The total strain (ε) is represented in Equation (3.12):

$$\varepsilon = \varepsilon^{el} + \varepsilon^{th} + \varepsilon^{pl} + \varepsilon^{cr} \tag{3.12}$$

where ε^{el} is the elastic strain, ε^{pl} is the inelastic (plastic) time-independent strain, ε^{th} is the thermal strain, and ε^{cr} is the inelastic (creep) time-dependent strain. The elastic strain (ε^{el}) is calculated by using the generalized Hooke's law, which has already been introduced in Equations. (3.6)–(3.8)[163,164]. As the Young's modulus and Poisson's ratio are temperature-dependent, they vary with the temperature calculated with Equation (3.1). The thermal strain is evaluated using the formulation previously defined in Equation (3.4) and is therefore not repeated here.

For calculating PEEQ, the mechanical analysis employed a bilinear isotropic hardening law, with the yield strength and hardening modulus varying with temperature. The bilinear isotropic hardening model[165], assumes that the stress-strain relationship is linear in both the elastic and plastic phases, with the yield point serving as the inflection point:

$$\sigma = \begin{cases} E \times \varepsilon & \sigma \leq \sigma_Y \\ \sigma_Y + E_1 \times (\varepsilon - \varepsilon_Y) & \sigma > \sigma_Y \end{cases} \tag{3.13}$$

where ε_Y is the yield strain, σ_Y is the yield stress, and E_1 is the hardening modulus.

Studies have successfully demonstrated that the hyperbolic-sine creep law[122,166,167] can be used to describe a long-term stress relaxation heat treatment. Additionally, the hyperbolic-sine creep law shows the exponential dependence of CEEQ rate on stress at high stress levels ($\frac{\sigma}{\sigma_Y} \gg 0$), thus reducing to a power law at low stress levels. This law is commonly used to describe the dislocation creep mechanism at high temperatures and stresses, as it effectively captures the non-linear dependence of the creep rate on stress. This creep equation has been widely implemented in commercial finite element software and has been successfully used in numerous studies involving high-temperature deformation. The hyperbolic-sine creep law is written as:

$$\dot{\varepsilon}^{cr} = A[\sinh(B\sigma^{cr})]^n \exp[-\frac{\Delta H}{R(T - T^Z)}] \tag{3.14}$$

where $\dot{\varepsilon}^{cr}$ is the uniaxial equivalent CEEQ rate, σ^{cr} is the uniaxial equivalent deviatoric stress, T is the temperature which is calculated by using Equation (3.1), T^Z is the user-defined value of absolute zero on the temperature scale used, ΔH is the activation energy, R is a universal gas constant, and A, B, and n are the material constants.

3.1.2.1.3 Initial Residual Stress Field

It is important to have a reliable residual stress field when evaluating the effect of a heat treatment since the amount of stress relaxation depends on the initial residual stress. In this study, the model in[131] is used to obtain the initial residual stress field. This model involves a thermo-mechanical simulation of the LPBF process with the use of the RV approach which reduces calculation time without sacrificing accuracy.

3.1.2.2 Numerical Simulation

The simulation procedure involves several key stages to accurately represent the physical conditions of the post-processing heat treatment. The simulation began with defining the initial loading conditions, which include the residual stress field obtained from the preceding LPBF simulation, as well as the thermal and pressure profiles that correspond to the conventional furnace heat treatment and HIP cycles. Next, specific element and node sets were defined for deactivation, thus enabling the model to realistically capture material behavior, stress redistribution, and pore evolution during the process. Appropriate boundary conditions were then applied to represent the mechanical constraints and thermal interactions between the component and its surroundings. Finally, temperature and pressure loads are imposed according to the actual furnace treatment and HIP schedules, thus ensuring accurate representation of the heating, holding, and cooling phases. These modeling steps are described in detail in the following sections to provide an understanding of the numerical methodology adopted to simulate the post-processing heat treatment and evaluate its effects on stress relaxation, creep deformation, and void or pore closure within the material.

3.1.2.2.1 Stress Relaxation Modeling Procedure

Pure hydrostatic stress does not produce plastic deformation in metals and as such, the yield function is independent of hydrostatic pressure[168]. Figure 3.4(a) shows the von Mises yield surface in the principal stress coordinates. The yield surface is an infinite cylinder that has a radius of $\sqrt{2/3}\sigma_y$ around the hydrostatic stress axis, and plastic deformation in the material can only occur under shear stress. Planar problems, such as plane stress or plane strain, have an elliptic plastic surface, as shown in Figure 3.4(b).

Although plastic deformation does not occur in defect-free materials subjected to hydrostatic pressure, additively manufactured materials often contain defects, such as porosities, which can lead to plastic deformation under such conditions. The presence of porosities in the material contributes to the development of equivalent stress under hydrostatic pressure. This stress, coupled with high temperatures that lower the yield strength of the material, promotes significant plastic deformation and creep. When external hydrostatic pressure is applied to a material, it generates internal stress. In defect-free materials, this stress is typically distributed uniformly. However, when there are defects like porosities present in the material, the stress distribution becomes non-uniform and intensified around the porosities compared to the surrounding material due to the irregular shape of the pores and the inherent stress-raising effect that they create. As a result, stress concentration occurs around these defects, which leads to regions with elevated stress levels compared to the surrounding material. These elevated stress levels create stress gradients, which act as internal forces that attempt to balance the stress around the defects. These gradients cause the adjacent regions to push or pull against each other. When the internal forces that generate shear stress exceed a critical threshold, plastic deformation occurs in the areas that surround the porosities. This enhanced plasticity allows the material to flow into voids and cracks, thus effectively closing them. Furthermore, the increased equivalent stress that acts on the material, especially at elevated temperatures, accelerates creep deformation. As a result, the combined effect of high stress and temperature not only enhances plastic flow but also facilitates the relaxation of residual stresses within the material.

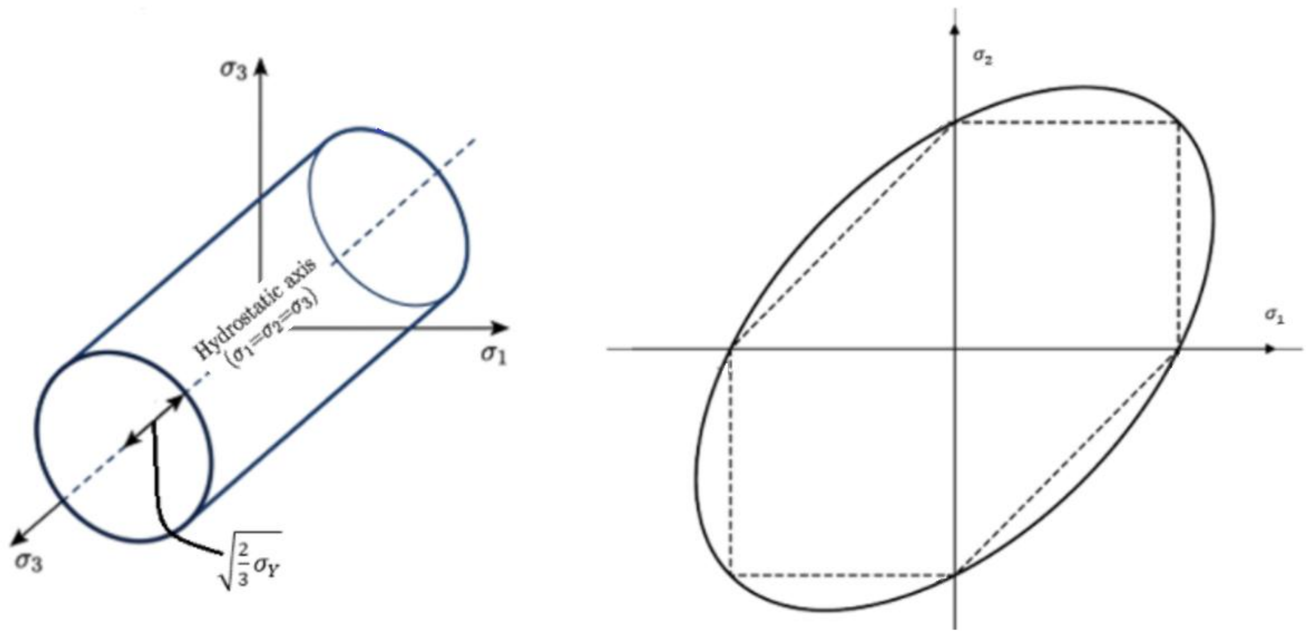

Figure 3.4 Von Mises yield surface in principal stress coordinates: (a) in a 3D problem (b) in a planar problem.

3.1.2.2.2 Finite Element Model Configuration

For the computational modeling, a representative part with dimensions of 1 mm × 1 mm × 2 mm (x × y × z) was used with a brick element. The geometrical model of the HIP process is presented in Figure 3.5, where the section line separates the as-built part from the substrate. Thermal and mechanical modeling in Abaqus/CAE 2023 was implemented by using C3D8T elements. C3D8T is an 8-node thermally coupled brick, trilinear displacement and temperature element employed in solid modeling. This element has shown that it is highly effective in simulating 3D structures with intricate shapes, thus providing accurate representations of curved and irregular forms. C3D8T elements are commonly used in mechanical and thermal analyses, as well as simulations that involve solid materials under various loads and boundary conditions[131].

Using this method, a 3D simulation was performed with the element deactivation method under specific pressure and temperature conditions. To introduce micropores randomly, certain elements were deactivated and effectively removed from the simulation, thereby eliminating their contributions to the stiffness matrix. Consequently, the deactivated elements were no longer used in the analysis. These randomly distributed elements were created by using Python scripting in

Abaqus. The selected elements were deactivated with the model change feature in Abaqus to simulate embedded micropores in the as-built part.

A mesh sensitivity analysis was conducted to determine the minimum mesh size required for the thermomechanical model. Achieving accurate simulations in the HIP process necessitates the use of finer meshes in the as-built section, which contains a number of voids. Elements with dimensions of 25 μm in the X, Y, and Z directions were used to mesh the as-built region. Conversely, coarser meshes can be employed in regions further away from the as-built side to reduce the computational cost. The bottom region consisted of an element size of 100 μm × 25 μm × 25 μm. The substrate and printed part have 92,800 linear hexahedral elements and 99,179 nodes. A fixed constraint boundary condition was assigned to the bottom of the substrate which prevented the nodes from moving in all directions.

Time-step convergence was also verified: several increment schemes were evaluated throughout the HIP cycle, and none produced appreciable changes in the predicted residual stresses or strains, thus demonstrating that the solution is insensitive to time discretization. With both mesh-refinement and time-step studies completed, the FEM results are fully converged.

In this study, simulation of the HIP process is conducted at different hydrostatic pressures and temperatures for an LPBF-built material that contained micropores. Figure 3.6 illustrates the temperature-pressure profile over time. The initial time point, t = 60 min, marks the transition between Stages I and II of the HIP process. The second time point, t = 240 min, denotes the transition from Stages II to III, while the third time point, t = 300 min, marks the end of the entire HIP process. From t = 300 to 366 min, the material is kept at under normal room-temperature and atmospheric-pressure conditions. During the process, the temperature is elevated for 60 min, allowed to reach 400, 500, 600, 650, or 700°C, and then maintained for 180 min. It then takes 60 min for the temperature to return to the normal level, where it is maintained for an additional 66 min. Concurrently, the hydrostatic pressure is raised for 60 min, allowed to reach 100, 200, 300, and 400 MPa, and maintained for 180 min, followed by a return to the normal level for 66 min. Table 3.2 summarizes the stages of the HIP process, along with the corresponding temperatures and hydrostatic pressures.

Table 3.2 Stages of HIP process, along with corresponding temperatures and pressures

Time (s)	Stage	Temperature (°C)	Pressure (MPa)
0 - 3,600	I	Elevated to 500, 600, or 700°C	Elevated to 100 or 200 MPa
3,600 - 14,400	II	Maintained at elevated levels	Maintained at elevated levels
14,400 - 18,000	III	Returned to normal levels	Returned to normal levels
18,000 - 22,000	IV	Maintained at normal levels	Maintained at normal levels

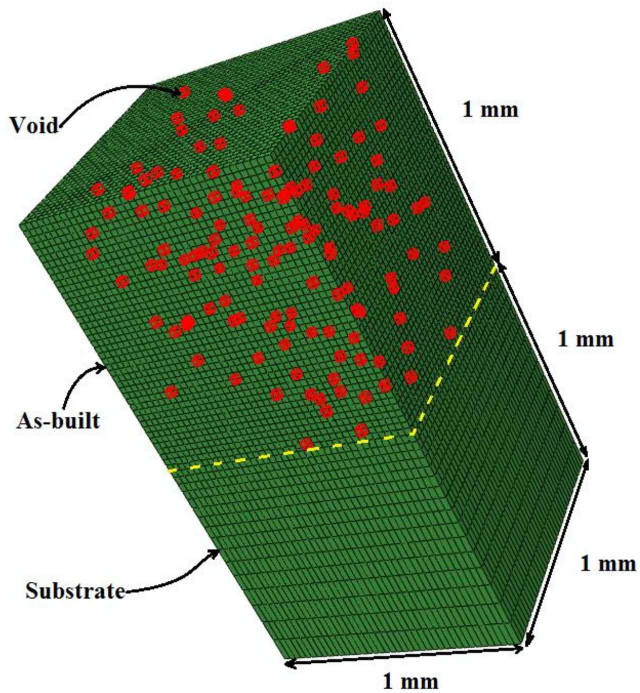

Figure 3.5 Geometrical model of as-built sample with embedded defects.

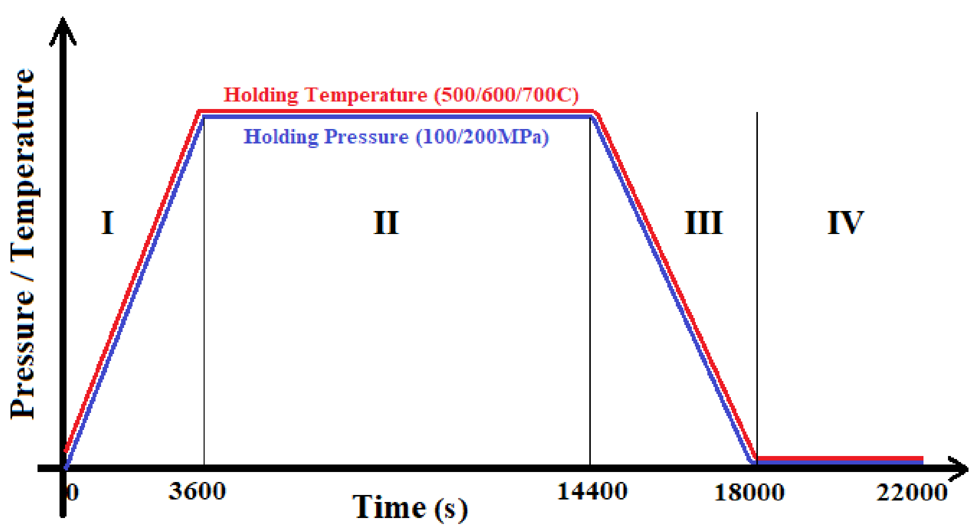

Figure 3.6 Temperature and pressure cycle during HIP versus time.

3.1.3 Model Assumptions

Several assumptions were adopted to maintain a reasonable balance between computational cost and model fidelity. The LPBF process was simulated using a continuum finite element framework. The powder bed was represented using homogenized material properties, and the laser-material interaction was represented using Goldak's double-ellipsoidal heat source model. Temperature-dependent material properties were incorporated throughout the LPBF simulations. Complex melt-pool phenomena were not simulated. In addition, radiation and convection heat-transfer mechanisms were incorporated through equivalent boundary conditions.

For the HIP simulations, the hydrostatic pressure was assumed to be spatially uniform and applied hydrostatically to the external surfaces of the component. The solid material was assumed to be homogeneous and isotropic, while its high-temperature response was represented using a bilinear isotropic hardening model and a hyperbolic-sine creep law. Temperature-dependent material properties were incorporated throughout the HIP and furnace simulations, and internal defects were represented using simplified void geometries to facilitate systematic investigation of the effects of pore morphology, size, and volume fraction on residual stress relaxation.

3.2 Fundamental Principles Governing Stress Analysis

This section presents the fundamental mechanical principles that underpin the stress analysis employed throughout this study. While the previous section focused on the numerical implementation of the simulation framework, the purpose of the this section is to describe the laws that govern how the stresses are generated, redistributed, and relaxed during high-temperature processes. By outlining the underlying mechanics—elasticity, plasticity, and creep deformation—this section explains the origins of the simulated behavior and provides the theoretical context necessary to interpret the results with accuracy and clarity. The concepts introduced here establish a solid and coherent foundation that links the governing equations to the simulation outcomes discussed in the subsequent chapters.

3.2.1 Governing Principles of Stress Relaxation

3.2.1.1 Conceptual Description of Stress Relaxation

Stress relaxation is the gradual decrease in stress over time when a material is held under a constant strain, especially at elevated temperatures where creep or viscoplastic flow can occur

(Figure 3.7). Imagine stretching or compressing a material and keeping the material at that fixed length (without allowing it to return back to its original state). Initially, the material resists strongly, and the internal stress is high. However, if the temperature is high (or as time progresses), atoms and dislocations begin to move. The material slowly deforms internally to reduce the stored stress, even though its external shape does not change. This reduction in stress under constant strain is defined as stress relaxation.

In essence, the material relaxes its internal forces through slow, permanent deformation. This phenomenon occurs in metals at high temperatures due to dislocation creep, and in polymers at room temperature due to viscoelastic flow. During HIP, the component is simultaneously subjected to a high hydrostatic pressure and an elevated thermal cycle within an inert gas environment. Residual stresses that originate from previous processes, such as LPBF, are initially high. Over the holding period, creep deformation enables the stresses to redistribute and gradually decrease—this is the stress relaxation process. It explains why HIP is highly effective in reducing residual stresses and closing internal voids. The material does not spring back; instead, it creeps internally until a balanced stress state is achieved.

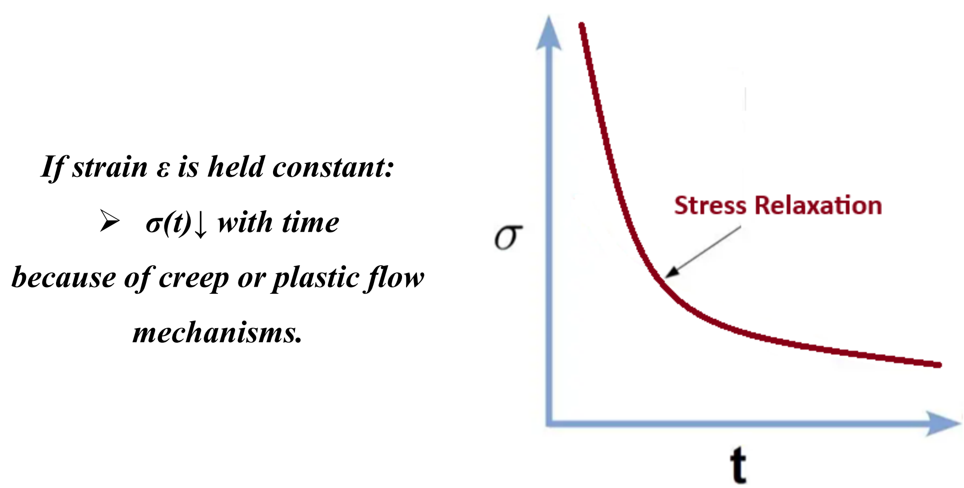

Figure 3.7 Stress relaxation.

3.2.1.2 Analytical Relationship Between Stress Relaxation and Plastic Strain

The relationship between stress relaxation and plastic deformation is obtained as follows. The total strain rate can be expressed as:

$$\dot{\varepsilon}_{total} = \dot{\varepsilon}_p + \dot{\varepsilon}_e \tag{3.15}$$

where $\dot{\varepsilon_p}$ and $\dot{\varepsilon_e}$ are the plastic and elastic strain rates, respectively. During a stress relaxation test, the total strain rate $\dot{\varepsilon_{total}}$ is zero because the total deformation is held constant. Substituting this condition into Equation (3.15) indicates that the plastic strain rate is equal in magnitude and opposite in sign to the elastic strain rate ($\dot{\varepsilon_p} = -\dot{\varepsilon_e}$). Since elastic strain rate is related to the stress rate by using Hooke's law, $\dot{\varepsilon_e} = \frac{\dot{\sigma}}{E}$, substituting into the above relation leads to:

$$\left.\begin{array}{r}\dot{\varepsilon_p} + \dot{\varepsilon_e} = 0\\ \dot{\varepsilon_e} = \dfrac{\dot{\sigma}}{E}\end{array}\right\} \rightarrow \dot{\sigma} = -E\dot{\varepsilon_p} \tag{3.16}$$

This fundamental relation indicates that, under a constant total-strain condition, the rate of stress reduction (stress relaxation rate) is directly related to the rate of time-dependent inelastic deformation. For the present analytical treatment, creep is considered as the governing time-dependent deformation mechanism. A commonly used relation for describing the dependence of creep strain rate on stress and temperature is the Norton power-law creep equation, expressed as:

$$\dot{\varepsilon_{cr}} = A\sigma^n e^{\frac{-Q}{RT}} \tag{3.17}$$

where $\dot{\varepsilon}_{cr}$ is the creep strain rate, σ is the applied (equivalent) stress, A and n are material constants, Q is the activation energy for creep, R is the universal gas constant, and T is the absolute temperature. By combining Equation (3.16) with the constitutive relation given in Equation (3.17), the stress-relaxation rate can be expressed as:

$$\dot{\sigma} = -E\dot{\varepsilon_{cr}} \rightarrow \frac{d\sigma}{dt} = -E\left(A\sigma^n \mathrm{e}^{\frac{-\mathrm{Q}}{\mathrm{RT}}}\right) \rightarrow \sigma^{-n} d\sigma = -E\left(A\mathrm{e}^{\frac{-\mathrm{Q}}{\mathrm{RT}}}\right) dt \tag{3.18}$$

For constant temperature and material properties, E, A, and exp(−Q/RT) can be treated as constants during the relaxation period. Therefore, stress relaxation curve as a function of time can then be obtained by integrating Equation (3.18), which yields:

$$\int_{\sigma_0}^{\sigma(t)} \sigma^{-n} d\sigma = \int_0^t -E\left(Ae^{\frac{-Q}{RT}}\right) dt \rightarrow \sigma(t) = ({\sigma_0}^{1-n} + (n-1)EAte^{\frac{-Q}{RT}})^{\frac{-1}{n-1}} \tag{3.19}$$

Equation (3.19) shows that, under the stated assumptions, stress decreases progressively with time as creep deformation accumulates. The derivation assumes a constant total strain, constant temperature during the relaxation period, constant material parameters at the specified temperature, and creep deformation governed by the Norton power-law relation. It also represents an idealized scalar stress-relaxation formulation rather than the complete multiaxial stress state.

Therefore, Equation (3.19) is used to describe the fundamental mechanism of creep-induced stress relaxation rather than to reproduce the complete thermo-mechanical response of the HIP cycle.

3.2.2 Fundamentals of Plastic Deformation and Stress Requirements

3.2.2.1 Conceptual Understanding of Plastic Deformation

Plastic deformation is a permanent, non-recoverable change in the shape of a material that occurs when the applied stress exceeds its elastic limit. Under loading, the material initially deforms elastically, and the deformation fully disappears once the load is removed. However, when the applied stress exceeds the yield point, the material enters the plastic region, where some of the deformation becomes permanent and remains even after unloading. In other words, when the applied load is removed, the material cannot fully revert back to its original shape, unlike in the elastic region.

3.2.2.2 Condition for the Onset of Plastic Deformation

Stress in a material usually acts in multiple directions (i.e., under a multiaxial stress state); therefore, a single stress component cannot be directly compared with the yield stress obtained from a simple uniaxial tensile test. For a general 3D stress state (i.e., multiaxial stress condition), yielding can be evaluated by using an equivalent stress criterion based on simple uniaxial tension tests. One of the most widely used criteria is the von Mises yield criterion, which is defined as:

$$\sigma_{eq} = \sqrt{\frac{1}{2}\left((\sigma_1 - \sigma_2)^2 + (\sigma_2 - \sigma_3)^2 + (\sigma_3 - \sigma_1)^2\right)} \tag{3.20}$$

Plastic deformation begins when the equivalent stress in the material equals or exceeds the yield stress, which is expressed as:

$$\sigma_{eq} \geq \sigma_Y \tag{3.21}$$

where σ_{eq} is the effective (equivalent) stress or von Mises stress, and σ_Y is the yield stress. Both depend on the temperature, strain rate, and material properties.

3.2.2.3 Role of Shear Stress in Plastic Deformation

In crystalline solids, plastic deformation occurs through the movement of dislocations along specific slip planes. Dislocations can only move under the action of shear stress. Hydrostatic stress, that is, equal pressure applied in all directions, cannot move dislocations and therefore cannot cause plastic deformation. Hence, the primary driving force for plastic deformation is shear stress, not hydrostatic (mean) stress. Shear stress promotes the movement of dislocations along crystallographic planes known as slip systems.

From the perspective of the dislocation theory, there is a critical resolved shear stress (τ_C), which is the minimum shear stress required to initiate slip on a specific slip system within a grain. When the resolved shear stress (τ_{RSS}) that is acting on the slip plane equals or exceeds this critical value, dislocation movement occurs, which leads to plastic deformation. However, if $\tau_{RSS} < \tau_C$, the dislocations remain locked, and the material behaves elastically. Also, if the applied stress only consists of hydrostatic components (equal in all directions), there is no preferred direction for shear, and thus no dislocation movement occurs. In such cases:

$$\sigma_1 = \sigma_2 = \sigma_3 = P \rightarrow \sigma_{eq} = 0 \tag{3.22}$$

Therefore, no plastic deformation takes place. The mathematical relationship between shear stress and equivalent (von Mises) stress also confirms this: if the shear stress is zero, then the equivalent stress is zero. For uniaxial loading (as in a tensile test):

$$\sigma_{eq} = \sigma_1 \tag{3.23}$$

and the maximum shear stress is:

$$\tau_{max} = \frac{\sigma_1}{2} = \frac{\sigma_{eq}}{2} \tag{3.24}$$

Thus, the equivalent stress and therefore yielding is directly proportional to shear stress. If $\tau = 0 \rightarrow \sigma_{eq} = 0$ → no yielding and no PEEQ.

This explains why, during processes such as HIP, even though high hydrostatic pressure is applied, the material does not undergo plastic deformation solely due to hydrostatic stress. Instead, plastic deformation or densification only occurs when a deviatoric (shear) stress component is present and exceeds a certain threshold. Under pure hydrostatic pressure, yielding does not occur, and the material remains completely elastic, although its volume may slightly decrease due to elastic compression.

3.2.3 Plasticity and Stress Response under Pure Hydrostatic Loading

3.2.3.1 Conceptual View of Hydrostatic Stress

Physically, when all normal stresses that act on a material are equal in magnitude, the stress state is said to be purely hydrostatic. Under such conditions, there is no difference between the principal stresses in any direction, which means that the material experiences no differential stress. As shear stress arises from differences in normal stresses in different directions, the absence of such differences implies that the shear stress components are zero. As a result, the material cannot undergo any distortional or shape changes, and the only possible deformation is a uniform volumetric change associated with elastic compression or expansion.

At the microscopic level, plastic deformation in crystalline solids occurs through the movement of dislocations along specific slip systems, which requires the presence of resolved shear stress on those planes. In a hydrostatic stress state, however, all directions are subjected to the same pressure, so no shear component acts on the slip planes. Consequently, dislocations remain immobile, and plastic deformation cannot be initiated. The deformation that does occur is entirely elastic and volumetric, governed by the bulk modulus of the material. Therefore, a fully dense material subjected to pure hydrostatic pressure experiences only elastic volumetric strain without any permanent changes to its shape or plastic flow.

3.2.3.2 Analytical Demonstration of Zero Shear Stress

In a continuous medium without voids, the normal stresses in all directions are equal and compressive under pure hydrostatic loading. Since all principal stresses are equal, there is no differential stress between the directions, and consequently, no shear stress component exists in the stress field. The maximum shear stress in a general 3D stress state is defined as:

$$\tau_{max} = \frac{\sigma_{max} - \sigma_{min}}{2} \tag{3.25}$$

For hydrostatic loading, $\sigma_{max} = \sigma_{min} = P$, and therefore the maximum shear stress is zero. If the shear stress (τ) is zero, the equivalent von Mises stress (σ_{eq}) must also be zero, since the equivalent stress is mathematically derived from the deviatoric (shear) components of the stress tensor. According to the von Mises yield criterion, yielding occurs when $\sigma_{eq} = \sigma_y$, where σ_y is the yield strength of the material. Thus, if $\sigma_{eq} = 0$, the yield condition cannot be satisfied, and the material remains entirely within the elastic regime, with no plastic deformation or irreversible strain. This conclusion can also be demonstrated analytically by using Cauchy stress decomposition. The total Cauchy stress tensor under hydrostatic loading is expressed as:

$$\sigma = \begin{bmatrix} P & 0 & 0 \\ 0 & P & 0 \\ 0 & 0 & P \end{bmatrix} = P\mathbf{I} \tag{3.26}$$

The stress tensor can be decomposed into hydrostatic and deviatoric parts as[169,170]:

$$\boldsymbol{\sigma} = \boldsymbol{s} + \sigma_{hyd}\mathbf{I} \tag{3.27}$$

where $\boldsymbol{s}$ is the deviatoric stress tensor and σ_{hyd} is the hydrostatic stress, defined by:

$$\sigma_{hyd} = \frac{1}{3}tr(\sigma) = \frac{1}{3}\left(\sigma_{xx} + \sigma_{yy} + \sigma_{zz}\right) = P \tag{3.28}$$

Substituting Equation (3.28) into Equation (3.27) shows that the deviatoric stress tensor becomes zero under hydrostatic loading. Therefore, the deviatoric (shear) stress is zero, and the von Mises equivalent stress, which only depends on the deviatoric component, is also zero:

$$\sigma_{eq} = \sqrt{\frac{3}{2}\,\boldsymbol{s}:\boldsymbol{s}} = 0 \tag{3.29}$$

Alternatively, using the definition of the von Mises stress based on the principal stresses (Equation (3.20)) and substituting the hydrostatic condition ($\sigma_1 = \sigma_2 = \sigma_3 = P$), the von Mises stress is zero.

Thus, both tensor decomposition and principal stress analyses confirm that under pure hydrostatic pressure, the equivalent von Mises stress becomes zero, thereby indicating the complete absence of any deviatoric (shear-producing) component in the stress state. As a result, a fully dense material under ideal hydrostatic loading experiences only elastic volumetric strain, with no possibility of plastic deformation or yielding.

In addition to the tensor-based demonstration presented above, the absence of shear stress under hydrostatic loading can also be verified through a stress transformation analysis on an arbitrarily inclined plane. By employing the classical stress transformation equations, the normal and shear stress components that act on any plane oriented at an angle θ can be expressed in terms of the original stress components. Figure 3.8 is a schematic illustration of the normal (σ_n) and shear (τ_n) stress components that are acting on an inclined plane oriented at an angle β with respect to a reference plane perpendicular to the direction of the applied normal stress σ_y.

The figure shows how externally applied stresses are transformed into normal and shear components on the inclined plane through stress transformation. To determine the normal (σ_n) and shear (τ_n) stress components that act on an inclined plane, the following are taken into consideration:

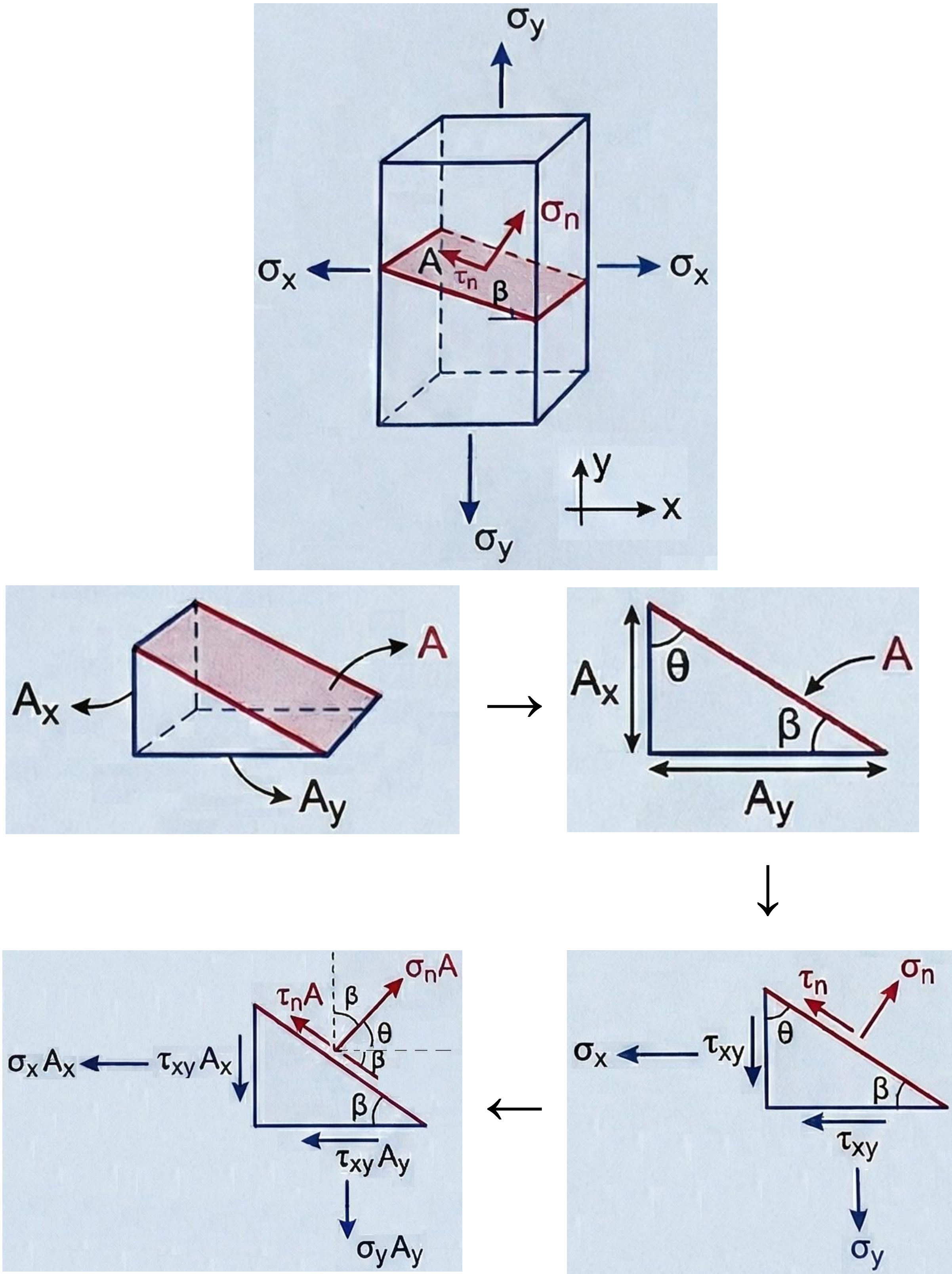

Figure 3.8 Schematic illustration of stress transformation on an inclined plane.

1-The projected areas of the inclined plane on the planes normal to x and y are:

$A_x = A\cos(\theta) = A\sin(\beta)$
$A_y = A\cos(\beta) = A\sin(\theta)$

These relations connect the forces that act on the faces normal to x and y to the forces that act on the inclined plane.

2- Forces that act on the projected faces are obtained by multiplying the stresses by the corresponding areas. The stresses σ_x and τ_{xy} act on the face with area A_x, while σ_y and τ_{xy} act on the face with area A_y. The traction on the inclined plane contributes to the σ_n and τ_n stress components. Writing force equilibrium in the x- and y- directions gives:

$$\sum F_x = 0 \tag{3.30}$$

$$\sum F_y = 0 \tag{3.31}$$

Applying Equations (3.30) and (3.31) and substituting the projected areas, the equilibrium equations can be written as:

$-\sigma_x A_x - \tau_{xy}\, A_y + \sigma_n\, A\cos(\theta) - \tau_n A\sin(\theta) = 0$
$-\sigma_y A_y - \tau_{xy}\, A_x + \sigma_n\, A\sin(\theta) + \tau_n A\cos(\theta) = 0$

$$\downarrow$$

$-\sigma_x A\, cos(\theta) - \tau_{xy} A\, sin(\theta) + \sigma_n\, A\cos(\theta) - \tau_n A\sin(\theta) = 0$
$-\sigma_y A\, sin(\theta) - \tau_{xy} A\, cos(\theta) + \sigma_n\, A\sin(\theta) + \tau_n A\cos(\theta) = 0$

$$\downarrow$$

$\sigma_n\, A\cos(\theta) - \tau_n A\sin(\theta) = \sigma_x A\, cos(\theta) + \tau_{xy} A\, sin(\theta)$
$\sigma_n\, A\sin(\theta) + \tau_n A\cos(\theta) = \sigma_y Asin\,(\theta) + \tau_{xy} A\, cos(\theta)$

Dividing both equations by A, the following simplified relations are obtained:

$\sigma_n\cos(\theta) - \tau_n\sin(\theta) = \sigma_x\, cos(\theta) + \tau_{xy}\, sin(\theta)$
$\sigma_n\sin(\theta) + \tau_n\cos(\theta) = \sigma_y sin\,(\theta) + \tau_{xy}\, cos(\theta)$

3- Solving the above system leads to classical stress transformation relations:

$$\cos(\theta) \times \{\sigma_n \cos(\theta) - \tau_n \sin(\theta) = \sigma_x\, cos(\theta) + \tau_{xy}\sin(\theta)\}$$
$$\sin(\theta) \times \{\sigma_n \sin(\theta) + \tau_n \cos(\theta) = \sigma_y sin\,(\theta) + \tau_{xy}\, cos(\theta)\}$$
$$\downarrow$$
$$\sigma_n \cos^2(\theta) - \tau_n \sin(\theta)\cos(\theta) = \sigma_x\, cos^2(\theta) + \tau_{xy}\, sin(\theta)\cos(\theta)$$
$$\sigma_n \sin^2(\theta) + \tau_n \cos(\theta)\sin(\theta) = \sigma_y sin^2\,(\theta) + \tau_{xy}\, cos(\theta)\sin(\theta)$$
$$\downarrow$$
$$\sigma_n(\cos^2(\theta) + sin^2\,(\theta)) = \sigma_y sin^2\,(\theta) + \sigma_x\, cos^2(\theta) + 2\tau_{xy}\, sin(\theta)\cos(\theta)$$

By applying standard trigonometric identities, the normal and shear stresses on an inclined plane can be expressed as:

$$\sigma_n = \frac{\sigma_x + \sigma_y}{2} + \frac{\sigma_x - \sigma_y}{2} cos2\theta + \tau_{xy} sin2\theta \tag{3.32}$$

$$\tau_n = -\frac{\sigma_x - \sigma_y}{2} sin2\theta + \tau_{xy} cos2\theta \tag{3.33}$$

These equations explicitly show that the normal and shear stresses on the inclined plane depend on the plane orientation (through 2θ) and the original stress state $(\sigma_x, \sigma_y, \tau_{xy})$. In a hydrostatic condition, the normal stresses are equal in all directions ($\sigma_x = \sigma_y = P$) and shear stress (τ_{xy}) is zero. Substituting these conditions into Equations (3.32) and (3.33) shows that normal stress (σ_n) remains equal to the applied pressure, whereas the shear stress (τ_n) is zero.

Hence, under hydrostatic loading, the shear stress on any plane is zero, and the stress state on every plane is purely normal with magnitude P. In other words, hydrostatic pressure does not produce a shear component regardless of the plane orientation. Therefore, both the tensor decomposition and stress transformation approaches consistently demonstrate that hydrostatic loading produces a purely normal stress state with no shear component.

3.2.4 Stress Analysis Around Voids and Plasticity

3.2.4.1 Conceptual View: Initiation of Plastic Deformation

When voids are present in a material, the stress state deviates locally from the ideal hydrostatic condition. Although the macroscopic stress field remains hydrostatic, the local stress distribution around each void becomes non-uniform due to the geometric mismatch between the solid matrix and pore surface. Mathematically, the local stress near a void can be expressed as:

$$\sigma_{ij}^{(local)} = P\delta_{ij} + s_{ij}^{(void)} \tag{3.34}$$

where P is the applied hydrostatic pressure and $s_{ij}^{(void)} \neq 0$ represents the local deviatoric stress that arises from the stress concentration and geometric constraints. This local deviatoric component produces a non-zero equivalent stress, given by:

$$\sigma_{eq}^{(local)} = \sqrt{\frac{3}{2} s_{ij}^{(void)} s_{ij}^{(void)}} > 0 \tag{3.35}$$

which enables localized plastic deformation and creep around the voids even under overall hydrostatic loading. As a result, plastic flow occurs in the vicinity of pores, thereby promoting void collapse and progressive densification during HIP.

In contrast, when the material is fully dense and homogeneous (i.e., void-free), the stress state is purely hydrostatic, which leads to $s_{ij} = 0$ and $\sigma_{eq} = 0$. In this case, there are no deviatoric or shear components to drive dislocation movement, and therefore no plastic deformation occurs—only a small elastic volumetric strain governed by the bulk modulus of the material. In summary, under pure hydrostatic loading, a void-free material experiences uniform elastic compression, whereas the presence of voids introduces local stress gradients and deviatoric components that facilitate plastic deformation and densification.

3.2.4.2 Analytical Stress Field for a Void in an Elastic Medium

If the component under consideration contains a void within an infinite elastic medium, the relationships derived for the ideal, void-free case undergo a fundamental change. Suppose that a spherical void of radius a exists at the center of the medium. Owing to the spherical symmetry of the problem, a spherical coordinate system (r, θ, ϕ) is adopted for the analysis (Figure 3.9). Under this symmetry, the principal normal stresses only depend on the radial coordinate r, and the non-zero stress components are expressed as functions of r:

$$\sigma_{rr} = \sigma_{rr}(r), \quad \sigma_{\theta\theta} = \sigma_{\varphi\varphi} = \sigma_{\theta\theta}(r) \tag{3.36}$$

where σ_{rr} represents the radial normal stress, $\sigma_{\theta\theta}$ denotes the hoop (tangential) stress in the θ direction or the polar normal stress, and $\sigma_{\phi\phi}$ corresponds to the hoop (tangential) stress in the φ direction or the circumferential normal stress. The shear stress components in the spherical coordinates, $\sigma_{r\theta}(r)$, $\sigma_{r\phi}(r)$, and $\sigma_{\theta\phi}(r)$, are zero due to the axisymmetric nature of the problem. The distribution of the normal and shear stress components in the spherical coordinates is shown schematically in Figure 3.10.

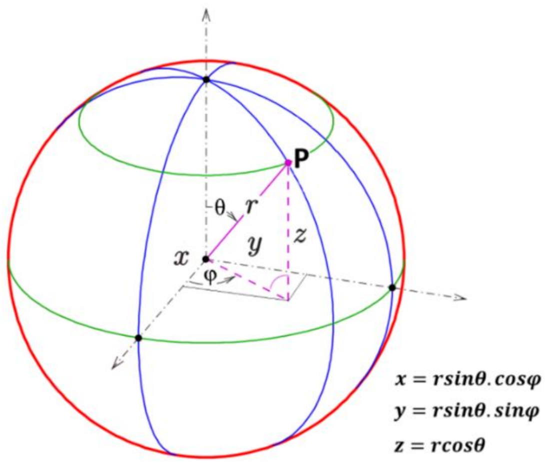

Figure 3.9 Spherical coordinate system (r, θ, ϕ).

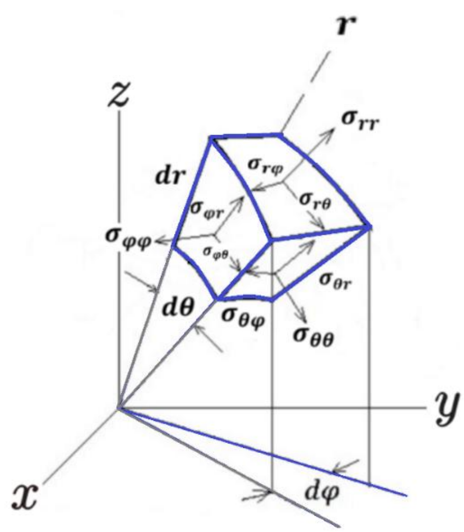

Figure 3.10 Schematic representation of stress components in a spherical coordinate system.

Therefore, only two unknown stress components remain to be determined. The stress equilibrium equation in the spherical coordinates is expressed as[171,172]:

$$\nabla . \sigma = 0 \tag{3.37}$$

For a general three-dimensional stress state in spherical coordinates, the radial equilibrium equation can be expressed as:

$$\frac{\partial\sigma_{rr}}{\sigma_r}+\frac{1}{r}\frac{\partial\sigma_{r\theta}}{\sigma_\theta}+\frac{1}{rsin\theta}\frac{\partial\sigma_{r\varphi}}{\sigma_\varphi}+\frac{2\sigma_{rr}-\sigma_{\theta\theta}-\sigma_{\varphi\varphi}}{r}+\frac{cot\theta}{r}\sigma_{r\theta}=0 \tag{3.38}$$

Due to the axisymmetric nature of the problem, the shear stress components vanish and the stress field is independent of the angular coordinates. Under these assumptions, Equation (3.38) reduces to:

$$\sigma_{r\theta}=\ \sigma_{r\varphi}=0,\quad \frac{\partial}{\partial\theta}=\frac{\partial}{\partial\varphi}=0\rightarrow\ \frac{d\sigma_{rr}}{dr}+\frac{2}{r}(\sigma_{rr}-\sigma_{\theta\theta})=0 \tag{3.39}$$

Solving this differential equation yields the general forms:

$$\sigma_{rr}(r)=A+\frac{B}{r^3} \tag{3.40}$$

$$\sigma_{\theta\theta}(r)=A-\frac{B}{2r^3} \tag{3.41}$$

where A and B are constants determined from the boundary conditions. Substituting Equations (3.40) and (3.41) into Equation (3.39) confirms that the assumed solution satisfies the governing equilibrium equation.

$$-3\frac{B}{r^4}+\frac{2}{r}\left(A+\frac{B}{r^3}-A+\frac{B}{2r^3}\right)=\ -3\frac{B}{r^4}+\frac{2}{r}\left(\frac{3B}{2r^3}\right)=-3\frac{B}{r^4}+3\frac{B}{r^4}=0$$

The constants A and B can be determined by applying appropriate boundary conditions. At large distances from the void, the radial stress approaches the external hydrostatic pressure (P_∞). Therefore:

$$\lim_{r\rightarrow\infty}\sigma_{rr}(r)=-P_\infty \tag{3.42}$$

From Equation (3.42), one of the constants is obtained as: Using Equation (3.42), the constant A is obtained as the negative of external hydrostatic pressure, i.e., $A=-P_\infty$. To evaluate the second constant, note that at the void surface ($r=a$), the radial stress equals the internal pressure (P_i) within the void:

$$\sigma_{rr}(a)=-P_i \tag{3.43}$$

Using these two boundary conditions, the second constant can be determined as follows:

$$\sigma_{rr}(a)=A+\frac{B}{a^3}=\ -P_i\ \Rightarrow-P_\infty+\frac{B}{a^3}=-P_i\ \Rightarrow\frac{B}{a^3}=P_\infty-P_i\Rightarrow B=a^3(P_\infty-P_i)$$

Substituting the constants A and B into the general solution, the stress field in spherical coordinates is obtained based on the formulation presented in the book Theory of Elasticity by Timoshenko and Goodier:

$$\sigma_{rr}(r) = -P_\infty + \frac{a^3}{r^3}\,(P_\infty - P_i) \tag{3.44}$$

$$\sigma_{\theta\theta}(r) = \sigma_{\varphi\varphi}(r) = -P_\infty - \frac{1}{2}\frac{a^3}{r^3}\,(P_\infty - P_i) \tag{3.45}$$

When the internal pressure inside the void is zero, the stress relations in the spherical coordinates can be expressed as follows:

$$\sigma_{rr}(r) = -P_\infty + \frac{a^3}{r^3}P_\infty = -P_\infty(1 - \frac{a^3}{r^3}) \tag{3.46}$$

$$\sigma_{\theta\theta}(r) = \sigma_{\varphi\varphi}(r) = -P_\infty - \frac{1}{2}\frac{a^3}{r^3}P_\infty = -P_\infty(1 + \frac{1}{2}\frac{a^3}{r^3}) \tag{3.47}$$

At the void surface, where the void radius is exactly equal to a, the stresses reduce to:

$$\sigma_{rr}(a) = -P_i \tag{3.48}$$

$$\sigma_{\theta\theta}(a) = \sigma_{\varphi\varphi}(a) = -P_\infty - \frac{1}{2}\,(P_\infty - P_i) = -\frac{3}{2}\,P_\infty + \frac{1}{2}P_i \tag{3.49}$$

The radial stress at the void wall (void surface) equals the internal pressure, while the tangential stresses depend on the difference in pressure between the inside and outside of the void. This imbalance between σ_{rr} and $\sigma_{\theta\theta}$ creates stress concentration at the void wall, which can exceed the yield stress of the material, thus leading to plastic deformation and void collapse[173–176]. From a mechanical perspective, this behavior can be interpreted in terms of the deviatoric nature of the stress field. Although the far-field loading may be purely hydrostatic, the local stress state around the void is no longer hydrostatic due to the geometric discontinuity. This result can be further explained by using the concept of stress transformation. In a general 3D state of stress, stress components that act on an infinitesimal element are represented by a Cauchy stress tensor:

$$[\sigma] = \begin{bmatrix} \sigma_x & \tau_{xy} & \tau_{xz} \\ \tau_{yx} & \sigma_y & \tau_{yz} \\ \tau_{zx} & \tau_{zy} & \sigma_z \end{bmatrix} \tag{3.50}$$

In general, the stress tensor can be expressed in terms of its principal components. When the coordinate axes coincide with the principal directions, the shear components vanish, and the stress tensor becomes diagonal:

$$[\sigma] = \begin{bmatrix} \sigma_1 & 0 & 0 \\ 0 & \sigma_2 & 0 \\ 0 & 0 & \sigma_3 \end{bmatrix} \tag{3.51}$$

If the coordinate system is rotated by using an arbitrary angle θ from the principal directions, both the normal and shear components on the rotated planes change according to the stress transformation relations. For a planar (2D) stress state, these relationships are given in Equations (3.32) and (3.33). When the coordinate axes coincide with the principal directions, the in-plane shear stress vanishes $\left(\tau_{xy} = 0\right)$. In this case, the shear stress on a rotated plane reduces to:

$$\tau_n = -\frac{\sigma_1 - \sigma_2}{2} sin2\theta \tag{3.52}$$

This expression shows that any difference between the principal stresses generates shear stresses on inclined planes. In contrast, when the normal stresses are equal in all directions ($\sigma_1 = \sigma_2 = \sigma_3 = \sigma$), the stress state becomes isotropic:

$$[\sigma] = \begin{bmatrix} \sigma & 0 & 0 \\ 0 & \sigma & 0 \\ 0 & 0 & \sigma \end{bmatrix} \tag{3.53}$$

Substituting this condition into Equations (3.32) and (3.33) demonstrates that, under this condition, the normal stress (σ_n) remains equal to the applied stress (σ), whereas the corresponding shear stress (τ_n) is zero. Therefore, no shear stress is generated under isotropic (hydrostatic) loading regardless of the plane orientation. Conversely, when the normal stresses are not equal ($\sigma_1 \neq \sigma_2$), shear stresses develop on inclined planes, indicating a non-hydrostatic stress state. This analytical result is fully consistent with the earlier conclusion that the difference between the radial and tangential stresses ($\sigma_{rr} \neq \sigma_{\theta\theta}$) around the void wall generates local shear components, which in turn promote plastic deformation and void collapse.

3.2.5 Stress Analysis of Void-Induced vs. Surface-Connected Defects

3.2.5.1 Stress State of Surface-Connected Defects

When a defect is fully embedded within a material, the stress field deviates from the ideal hydrostatic condition because the internal pressure (P_i) inside the void is not equal to the externally applied hydrostatic pressure (P_∞). This pressure difference generates directional stress variations that give rise to deviatoric components and local shear. The corresponding stress field for a spherical void in an infinite elastic medium has already been derived in Equations (3.44)–(3.49). The difference between the radial and tangential stresses at the void wall creates a local stress concentration. According to the von Mises criterion (Equation (3.20)), the equivalent stress is proportional to the pressure difference:

$$\sigma_{eq} = \frac{3}{2} \mid P_\infty - P_i \mid \tag{3.54}$$

Therefore, when $P_i < P_\infty$, a non-zero equivalent stress develops, which may exceed the yield strength of the material and promote localized plastic deformation and void collapse. Conversely, for open or surface-connected defects—such as through-thickness holes, surface recesses, or sharp re-entrant corners—where the internal pressure equals the external hydrostatic pressure ($P_i = P_\infty$), substitution into the same stress relations demonstrates that all principal stresses ($\sigma_{rr}, \sigma_{\theta\theta}, \sigma_{\phi\phi}$) become equal to the externally applied hydrostatic pressure (P_∞). Under these conditions, the stress tensor is purely hydrostatic and the deviatoric stress components vanish. Consequently, substitution into the von Mises criterion indicates that the equivalent stress is zero. Consequently, surface-connected defects do not induce yielding under purely hydrostatic loading, since the equivalent von Mises stress is zero. Therefore, no yielding or plastic deformation can occur. This distinction explains why HIP is highly effective in closing internal porosity, while surface-connected defects may remain largely unaffected.

The same conclusion can be reached through stress transformation. For a general two-dimensional stress state, the transformed shear stress on a plane inclined at an arbitrary angle θ is given by Equation (3.33). For a surface-connected defect under hydrostatic loading, the normal stresses are equal in all directions and the initial shear stress is zero. Substituting these conditions into Equation (3.33) demonstrates that the transformed shear stress remains zero for all plane orientations. Therefore, the stress state remains purely hydrostatic regardless of orientation, with no shear or deviatoric component. Consequently, no local yielding or plastic deformation is expected at surface-connected defects under purely hydrostatic loading.

3.2.6 Stress Influence of Void Characteristics

The effectiveness of an embedded void in generating shear stress—and consequently enabling plastic deformation— greatly depends on three key characteristics: void shape, void size, and void volume fraction (porosity). Each of these parameters modifies the local stress distribution and changes the equivalent von Mises stress differently. An understanding of their influence is crucial for predicting void collapse, densification, and stress relaxation during the HIP process. In the following sections, the influence of each characteristic is analyzed in two complementary ways: a conceptual view, which provides qualitative and physical interpretations, and an analytical view, which derives the corresponding mathematical relations.

3.2.6.1 Effect of Void Size

3.2.6.1.1 Conceptual View

The size of a void affects how far its stress field extends into the surrounding material. Larger voids influence a larger volume of material but do not necessarily change the magnitude of the stress at the void wall. This is because the surface stress is primarily governed by the pressure difference ($\Delta P = P_\infty - P_i$) rather than the absolute void radius. Thus, as the void size increases, the stress field expands outward self-similarly, while the stress at the void surface remains nearly constant. This self-similar scaling behavior explains why the collapse behavior of large and small voids follows similar patterns when normalized by their dimensions.

3.2.6.1.2 Analytical View

If the radius of the void changes from a to $2a$, the corresponding stress relations in the spherical coordinates are expressed as:

$$\sigma_{rr}(r) = -P_\infty + \frac{(2a)^3}{r^3}(P_\infty - P_i) \tag{3.55}$$

$$\sigma_{\theta\theta}(r) = \sigma_{\phi\phi}(r) = -P_\infty - \frac{1}{2}\frac{(2a)^3}{r^3}(P_\infty - P_i) \tag{3.56}$$

At the void surface, where the radial distance r equals the new void radius $2a$, the stresses are given by:

$$\sigma_{rr}(2a) = -P_i, \qquad \sigma_{\theta\theta}(2a) = \sigma_{\phi\phi}(2a) = -P_\infty - \frac{1}{2}(P_\infty - P_i) = -\frac{3}{2}P_\infty + \frac{1}{2}P_i.$$

It can be observed that doubling the void radius ($a \rightarrow 2a$) changes the stress distribution within the surrounding material as a function of the radial distance, yet the stresses at the void surface remain constant. This behavior is consistent with the theoretical formulation of elastic stress around spherical cavities under combined internal and external hydrostatic pressure.

During HIP, voids are subjected to both internal pressure (P_i) and external hydrostatic pressure (P_∞). The difference between these pressures produces a stress gradient in the surrounding material that governs the onset of plastic deformation. The highest stress concentration typically occurs at the void surface, where the mismatch between internal and external hydrostatic pressures is fully realized. Once this stress exceeds the yield strength of the material, localized plastic flow is initiated, thus leading to void shrinkage or collapse.

Even when the void radius changes, the equilibrium boundary condition requires that the radial stress at the void wall to be always equal to the internal void pressure ($\sigma_{rr}(a) = -P_i$). This condition is purely geometric and independent of the void size. Similarly, the tangential (hoop) stresses at the void surface only depend on the difference in pressure ($P_\infty - P_i$), not on the absolute value of the radius. Therefore, as the void expands, the surface stress remains constant while the stress field extends further into the surrounding material.

In other words, the stress field scales self-similarly with the void size, which means that as the void grows, the region of influence expands outward while the surface stress remains unchanged because they depend solely on the applied boundary pressures. This self-similar behavior arises from the fact that the stress field satisfies the same equilibrium and compatibility conditions for any void radius, provided that the ratio $\frac{a^3}{r^3}$ accurately represents the geometric decay of stress with distance from the void. The term $\frac{a^3}{r^3}$ in the analytical solution mathematically captures how the stress intensity diminishes with increasing radial distance, thus ensuring that the overall stress pattern retains the same spatial form, and simply scaled to the new void size. Consequently, while the stress magnitude at the void wall remains unchanged, the zone of influence that surrounds the void increases proportionally with its size[177].

Therefore, the self-similar nature of the stress field around voids plays a key role in their plastic response during HIP. When neighboring voids are close to each other, their stress fields may overlap, thus causing localized intensification and accelerating plastic deformation. The magnitude of stress concentration and the resulting densification rate are both strongly influenced by the void geometry, spacing, and spatial distribution. Consequently, accurate prediction and control of void shape, spacing, and pressure distribution are essential for optimizing HIP performance and minimizing residual porosity.

3.2.6.2 Effect of Void Shape

3.2.6.2.1 Conceptual View

The shape of a void has a decisive influence on the stress distribution in its vicinity. The geometry of a void plays a crucial role in determining how stress and strain are distributed in its vicinity. Spherical or nearly spherical voids generate smooth and symmetric stress fields that decay uniformly with distance, thus leading to homogeneous deformation around the pore. In contrast, non-spherical geometries, such as elongated, flattened, or sharp-edged cavities, induce stress concentrations due to the geometric discontinuities and curvature variations at their boundaries. These stress concentrations increase the local deviatoric stress, which promotes earlier plastic deformation and localized yielding. Hence, sharper void corners or larger aspect ratios result in greater tendency of localized plastic flow.

3.2.6.2.2 Analytical View

To investigate the influence of void shape on the surrounding stress and strain fields, it is necessary to review the inclusion theory in Eshelby[178], which provides the most fundamental analytical framework for studying the elastic fields associated with inclusions or cavities of various geometries. In the inclusion theory, there is the need for an ellipsoidal shaped inclusion or void to obtain a closed-form analytical solution. The reason is that the exact stress and strain solutions for a cubic or prismatic void in an infinite elastic medium are generally complex and often cannot be expressed in a simple form, except for certain specific geometries. However, for ellipsoidal cavities, Eshelby showed that stress and strain fields inside and around the void can be expressed analytically. Analytical solutions for ellipsoidal cavities show that both the internal and surrounding stresses are smooth and continuous.

For voids of arbitrary geometry, such as rectangular or irregular shapes, stress distribution cannot be obtained analytically, and numerical methods are required. In fact, an ellipsoidal shape is smooth and continuous, which distributes the stress concentration at the corners (as seen in a cubic shape) more uniformly. Therefore, for simplicity and to maintain analytical solvability, an ellipsoidal void is often approximated as a rectangular void with semi-axes a, b, and c along the x, y, and z directions, respectively. This approximation can estimate the internal and external stress states around the void.

In the following sections, the method for determining stress and strain fields is analytically presented by using the inclusion solution in Eshelby. For an ellipsoidal void embedded in an infinite isotropic elastic medium, the stress inside the ellipsoid is uniform. The uniformity of this stress arises from its mathematical properties and geometric symmetry. In the inclusion theory, it was shown that when a void with an ellipsoidal shape is embedded in an infinite elastic medium and subjected to uniform loading (such as external pressure or remote stress), the displacement field inside the ellipsoid varies linearly. This linearity of displacement causes the strain field, and consequently the stress field, within the void to be independent of position and maintain a constant value throughout its interior. The high degree of symmetry of the ellipsoidal shape, particularly the smoothness and continuity of the boundary curvature of the ellipsoid, is the main reason for this behavior, as every point inside the ellipsoid interacts with the boundaries and the surrounding medium in a geometrically symmetric manner. This is why the ellipsoid is the only geometry for which the internal stress within an infinite isotropic elastic medium remains uniform under uniform external loading. If the stress tensor in the ellipsoidal coordinate system is expressed as follows:

$$\sigma = \begin{bmatrix} \sigma_{xx} & 0 & 0 \\ 0 & \sigma_{yy} & 0 \\ 0 & 0 & \sigma_{zz} \end{bmatrix} \tag{3.57}$$

and if the cavity is subjected to a pressure difference between its interior and the surrounding medium ($\Delta P = P_{in} - P_\infty$), then the normal stresses along the principal axes of the ellipsoid, according to Eshelby[178], are given as follows:

$$\sigma_{ii} = -P_\infty + \Delta P \frac{1}{1 - S_i}, i = x, y, z \tag{3.58}$$

In Equation (3.58), ΔP represents the pressure difference, and S_i denotes the components of the tensor for the void (ellipsoid) along each principal direction in Eshelby. For an ellipsoidal cavity with semi-axes α, β, and γ, the components of the tensor in Eshelby are defined as follows:

$$S_x = \frac{\alpha\beta\gamma}{2} \int_0^\infty \frac{ds}{(s + \alpha^2)\sqrt{(s + \alpha^2)(s + \beta^2)(s + \gamma^2)}} \tag{3.59}$$

$$S_y = \frac{\alpha\beta\gamma}{2} \int_0^\infty \frac{ds}{(s + \beta^2)\sqrt{(s + \alpha^2)(s + \beta^2)(s + \gamma^2)}} \tag{3.60}$$

$$S_z = \frac{\alpha\beta\gamma}{2} \int_0^\infty \frac{ds}{(s + \gamma^2)\sqrt{(s + \alpha^2)(s + \beta^2)(s + \gamma^2)}} \tag{3.61}$$

These integrals are generally evaluated numerically. For a cavity, a simple relation holds:

$$S_x + S_y + S_z = 1 \tag{3.62}$$

Several common methods are available to equate or approximate a rectangular (cuboidal) cavity with dimensions a, b, and c to an ellipsoidal cavity with semi-axes α, β, and γ, which are described as follows.

(a) Simple Approximation

In this method, the semi-axes of the ellipsoid are taken as half of the length, width, and height of the rectangular cavity, respectively:

$$\alpha = \frac{a}{2}, \qquad \beta = \frac{b}{2}, \qquad \gamma = \frac{c}{2} \tag{3.63}$$

If only the overall geometric shape and relative proportions are of interest (and small volumetric discrepancies are acceptable), this approximation is sufficient. However, the volume of the ellipsoidal cavity obtained by this approach is not equal to that of the rectangular cavity as the volume of the ellipsoid is usually smaller.

(b) Volume-Equivalent Ellipsoid Approximation

In this approach, the volume of the ellipsoid is taken to be equal to the volume of the rectangular cavity, i.e.,

$$V_{ellipsoid} = V_{box} \tag{3.64}$$

Usually, the aspect ratios of the geometry are kept while introducing a single scaling factor k:

$$\alpha = k\frac{a}{2}, \qquad \beta = k\frac{b}{2}, \qquad \gamma = k\frac{c}{2} \tag{3.65}$$

Equating the volumes gets:

$$\frac{4}{3}\pi(k\frac{a}{2})(k\frac{b}{2})(k\frac{c}{2}) = abc$$

Simplifying gives:

$$\frac{4}{3}\pi\frac{k^3}{8}abc = abc$$

$$\frac{\pi}{6}k^3abc = abc$$

$$k^3 = \frac{6}{\pi}$$

and therefore:

$$\mathrm{k} = (\frac{6}{\pi})^{1/3} \tag{3.66}$$

Thus, the semi-axes of the volume-equivalent ellipsoid are:

$$\alpha = (\frac{6}{\pi})^{1/3}\frac{a}{2}, \qquad \beta = (\frac{6}{\pi})^{1/3}\frac{b}{2}, \qquad \gamma = (\frac{6}{\pi})^{1/3}\frac{c}{2} \tag{3.67}$$

This ensures that the ellipsoid has the same volume as the rectangular cavity while maintaining proportional geometric ratios among its axes.

(c) Equivalence Based on Second Moment of Inertia

In this method, the second moments of inertia with respect to the principal axes are considered to be equal for both the ellipsoid and the rectangular box. This approach effectively retains the "effective dimensions" in each direction and provides a more realistic basis for comparing stress and strain distributions. Therefore, for a rectangular cavity with dimensions $(a \times b \times c)$:

$$\frac{I_x{}^{box}}{V_{box}} = \frac{1}{12}(b^2 + c^2) \tag{3.68}$$

$$\frac{I_y{}^{box}}{V_{box}} = \frac{1}{12}(a^2 + c^2) \tag{3.69}$$

$$\frac{I_z{}^{box}}{V_{box}} = \frac{1}{12}(a^2 + b^2) \tag{3.70}$$

For the equivalent ellipsoid with semi-axes (α, β, γ):

$$\frac{I_x{}^{ell}}{V_{ell}} = \frac{1}{5}(\beta^2 + \gamma^2) \tag{3.71}$$

$$\frac{I_y{}^{ell}}{V_{ell}} = \frac{1}{5}(\alpha^2 + \gamma^2) \tag{3.72}$$

$$\frac{I_z{}^{ell}}{V_{ell}} = \frac{1}{5}(\alpha^2 + \beta^2) \tag{3.73}$$

By equating Equations (3.68)–(3.70) with Equations (3.71)–(3.73), a system of three equations is obtained for determining the semi-axes α, β, γ. Solving this system yields:

$$\alpha^2 = \frac{5}{12}a^2, \qquad \beta^2 = \frac{5}{12}b^2, \qquad \gamma^2 = \frac{5}{12}c^2 \tag{3.74}$$

Therefore, the semi-axes of the inertia-equivalent ellipsoid are:

$$\alpha = \sqrt{\frac{5}{12}}a, \qquad \beta = \sqrt{\frac{5}{12}}b, \qquad \gamma = \sqrt{\frac{5}{12}}c \tag{3.75}$$

This method maintains the geometric distribution of the lengths and provides a more realistic representation of bending or stress concentration behavior, since the geometric influence in each direction is maintained. It should be noted that in this approach, the ellipsoidal volume is not necessarily equal to the rectangular volume (the ellipsoidal cavity is usually slightly smaller), because the equivalence is based on the second moments (which correspond to geometric spreading relative to the axes), rather than the overall volume.

By calculating the Eshelby tensor components (S_i) based on the second moment of inertia equivalence method, the normal stresses in the three principal directions for the rectangular cavity can be determined, from which the equivalent von Mises stress can subsequently be evaluated. Using this method, the equivalent ellipsoidal geometries and the corresponding Eshelby tensor components were first determined for several representative void configurations with different aspect ratios. Subsequently, the resulting internal principal stresses and equivalent von Mises stresses were evaluated using the Eshelby inclusion solution. The analytical results are summarized in Tables 3.3 and 3.4.

The analytical results clearly demonstrate that as the void height increases from a to $3a$, the equivalent von Mises stress increases significantly. This indicates that the stress difference between the principal directions becomes more pronounced, thereby generating higher levels of deviatoric stress within the surrounding material. Since plastic deformation is governed by the magnitude of deviatoric (shear) stress, a larger von Mises stress implies that the material approaches its yield limit more readily. Consequently, increasing the void aspect ratio intensifies local stress concentration and enhances the likelihood of localized plastic flow and yielding, even though all other loading and material conditions remain unchanged.

It is important to distinguish between the uniform stress field obtained from the equivalent-ellipsoid approximation and the local stress field in the surrounding solid at the surface of a physical cavity. The values summarized in Table 3.4 correspond to the uniform field associated with the equivalent-ellipsoid representation and are used primarily to evaluate the effect of geometric anisotropy on the relative differences among the principal stress components. They should not be interpreted as the actual stresses in the surrounding matrix at the cavity wall. For the limiting case in which the equivalent ellipsoid becomes spherical ($a = b = c$), symmetry results in equal principal components in the uniform equivalent-ellipsoid field. Consequently, the von Mises stress calculated from those equal components is zero. This result explains the zero value reported for the cube/spherical-equivalent case in Table 3.4. However, it does not imply that the material surrounding an actual spherical cavity experiences zero deviatoric stress.

Table 3.3 Equivalent ellipsoidal semi-axes and tensor components for different void geometries

Void Geometry	**Equivalent Ellipsoidal Semi-Axes**	**Eshelby Tensor Components**
Cube ($a \times a \times a$)	$\alpha = \beta = \gamma = \sqrt{\frac{5}{12}}a$	$S_x = S_y = S_z = \frac{1}{3}$
Rectangular cuboid ($a \times a \times 2a$)	$\alpha = \beta = \sqrt{\frac{5}{12}}\,a, \gamma = \sqrt{\frac{5}{12}}\,(2a)$	$S_x = S_y = 0.413$ $S_z = 0.173$
Rectangular cuboid ($a \times a \times 3a$)	$\alpha = \beta = \sqrt{\frac{5}{12}}\,a, \gamma = \sqrt{\frac{5}{12}}\,(3a)$	$S_x = S_y = 0.445$ $S_z = 0.108$

Table 3.4 Uniform principal stresses and corresponding von Mises equivalent stresses obtained from the equivalent-ellipsoid approximation for different void geometries.

Void Geometry	**Uniform Principal Stresses from the Equivalent-Ellipsoid Approximation**	**Equivalent Stress of the Uniform Equivalent-Ellipsoid Field**
Cube ($a \times a \times a$)	$\sigma_{xx} = \sigma_{yy} = \sigma_{zz} = -P_\infty + \frac{3}{2}\Delta P$	0
Rectangular cuboid ($a \times a \times 2a$)	$\sigma_{xx} = \sigma_{yy} = -P_\infty + 1.704\Delta P$ $\sigma_{zz} = -P_\infty + 1.210\Delta P$	$0.494\Delta P$
Rectangular cuboid ($a \times a \times 3a$)	$\sigma_{xx} = \sigma_{yy} = -P_\infty + 1.803\Delta P$ $\sigma_{zz} = -P_\infty + 1.212\Delta P$	$0.681\Delta P$

A physical spherical cavity perturbs an otherwise hydrostatic stress field because the radial traction at the cavity boundary must satisfy the internal pore-pressure condition. Based on Equations. (3.44) and (3.45), and by substituting the radial and tangential stress components at the cavity wall into the von Mises equivalent-stress relation given in Equation. (3.20), the equivalent stress at the cavity wall is $\frac{3}{2}|\Delta P|$.

Therefore, even a perfectly spherical cavity generates a localized deviatoric stress in the surrounding material under hydrostatic far-field loading. The zero equivalent stress reported for the spherical-equivalent case in Table 3.4 refers only to the uniform field of the equivalent-ellipsoid approximation and not to the local matrix stress at the cavity surface. The Eshelby-based comparison is therefore used in the present study as a mechanistic indicator of the additional stress anisotropy associated with increasing void aspect ratio, rather than as an exact prediction of cavity-wall stress.

3.2.6.3 Effect of Void Volume Fraction

3.2.6.3.1 Conceptual View

Another key factor that plays a crucial role in determining the mechanical response of materials during the HIP process is the void volume fraction which represents the overall volume fraction of voids within a material. The number of voids significantly influences the overall stress–strain behavior, plastic deformation, and densification kinetics. Voids can be a source of stress concentration within a material, thus reducing the effective load-bearing area and facilitating localized plastic flow under hydrostatic pressure and temperature. As the void fraction increases, the material becomes less stiff and more prone to deformation under the same external stress. However, this effect has a physical limit. Therefore, understanding the quantitative relationships among voids, stress distribution, and yielding is essential for accurately predicting material behavior during HIP[129,179,180].

3.2.6.3.2 Analytical View

To analyze this effect, several analytical and empirical models have been developed to describe how void percentage alters the effective stress, yield strength, and PEEQ of a material. The following sections present these models. To study the influence of porosity on plastic deformation during HIP, several assumptions are made as follows:

(a) The porosity fraction, denoted as f, is assumed to vary between 0 and 1.

(b) The macroscopic stresses for a pure material that does not have any voids are denoted as $\sigma_0^1, \sigma_0^2,\ and\ \sigma_0^3$.

(c) In the presence of porosity within a material, the stress distribution during the HIP process will be naturally affected, thus leading to variations in the magnitude of the effective stress. To account for this behavior, several constitutive models have been proposed in the literature for calculating the effective stress as a function of porosity.

The most relevant of these models, which depends on the degree of porosity within the material, are described in the following section.

(1) When the porosity level is low, a simple model can be used to represent the increase in stress based on the reduction of the effective load-bearing area. This relationship is given as follows[181]:

$$\sigma = \frac{F}{A_{\text{eff}}} = \frac{F}{A(1-f)} = \frac{\sigma_0}{(1-f)} \tag{3.76}$$

(2) As porosity increases, the material ligaments begin to interact and coalesce, which lead to stress concentration within the surrounding matrix. Consequently, more advanced constitutive models are required to accurately describe the material behavior under these conditions. The Gurson–Tvergaard–Needleman (GTN) model[182,183] is one of the most comprehensive and widely used models for describing the behavior of ductile materials containing voids. This model is particularly applicable to materials with a relatively high porosity level, where simpler models become insufficient to capture the nonlinear behavior of the matrix–void interaction. The yield function of this model is expressed as follows:

$$\phi = (\frac{\sigma_{eq}}{\sigma_y})^2 + 2q_1 f^* \cosh(\frac{3q_2 p}{2\sigma_y}) - (1 + q_3(f^*)^2) = 0 \tag{3.77}$$

where:

- q_1, q_2, q_3: empirical constants related to the type of material,
- p: hydrostatic stress during the process,
- f^*: corrected (or effective) porosity,
- σ_y: yield stress of the matrix material, and
- σ_{eq}: equivalent von Mises stress.

The GTN model accounts for both the growth and coalescence of voids during plastic deformation. By introducing porosity as an internal variable into the yield function, the model effectively captures the progressive degradation of the load-bearing capacity of the material under increasing hydrostatic tension, which makes it particularly suitable for simulating the HIP process and void closure behavior. The most common applications of this model are in HIP processes, powder consolidation, densification of porous materials, and modeling ductile fractures in metallic components.

(3) The Eshelby–Mori–Tanaka model is a micromechanical approach that considers voids as embedded particles within a matrix and accounts for their distribution and mutual interactions. This model incorporates the effects of void shape and interaction between the inclusions and the surrounding matrix[182]. The effective modulus for spherical voids is expressed as:

$$E = E_0 \frac{1-f}{1+\alpha f} \tag{3.78}$$

where E_0 is the elastic modulus of the matrix material, and α is a parameter dependent on the Poisson's ratio of the matrix. The main advantage of this model is that it provides a direct analytical relationship between the matrix and voids. However, as discussed in previous sections, several alternative micromechanical models can also be employed to describe similar stress–strain behaviors in materials with voids or defects.

To better evaluate the effect of porosity on the magnitude of PEEQ during the HIP process, a simplified analytical model (Model 1) is employed. In this model, the equivalent von Mises stress is calculated according to Equation (3.20). As discussed earlier, the effective stress increases as the load-bearing area decreases. Therefore, the relationship previously introduced in Equation (3.76) is adopted.

Substituting Equation (3.76) into Equation (3.20), the effect of porosity on the equivalent stress can be evaluated. Accordingly, when the material contains a porosity fraction f, the equivalent von Mises stress becomes:

$$\sigma_{eq} = \frac{1}{1-f}\sqrt{\frac{1}{2}[(\sigma_1^0 - \sigma_2^0)^2 + (\sigma_2^0 - \sigma_3^0)^2 + (\sigma_3^0 - \sigma_1^0)^2]} \tag{3.79}$$

where σ_1^0, σ_2^0, and σ_3^0 are the principal stresses in the fully dense material ($f = 0$).This expression shows that the equivalent stress increases proportionally with the level of porosity, relative to the initial stress state in a fully dense material. The equivalent stress can be expressed in a simplified form relative to the initial stress state, as follows:

$$\sigma_{eq}(f) = \frac{{\sigma_{eq}}^0}{1-f} \tag{3.80}$$

where σ_{eq}^0 represents the equivalent von Mises stress in the fully dense material, that is, in the absence of any voids or porosity. It should be noted that the presence of porosity also changes the yield stress of the material, and this change will be explained in the following section.

It is well known that the yield strength of a material decreases with increasing voids. This relationship can be expressed empirically using the following power-law form[183]:

$$\sigma_Y(f) = \sigma_Y^0(1-f)^m \tag{3.81}$$

where σ_Y^0 is the yield stress of the fully dense material, and m is an empirical constant that depends on the type of material and pore geometry. The value of m typically ranges between 1 and 3. The condition for the onset of plastic deformation can be expressed as:

$$\sigma_{eq}(f) \geq \sigma_Y(f) \tag{3.82}$$

Substituting Equations (3.80) and (3.81) into Equation (3.82) gives:

$$\sigma_{eq}^0 \geq \sigma_Y^0(1-f)^{m+1} \tag{3.83}$$

This expression can be solved to determine the critical porosity beyond which plastic deformation begins:

$$\frac{\sigma_{eq}^0}{\sigma_Y^0} \geq (1-f)^{m+1} \;\rightarrow\; 1-f \leq \left(\frac{\sigma_{eq}^0}{\sigma_Y^0}\right)^{\frac{1}{1+m}} \;\rightarrow\; f_{cr} = 1-(\frac{\sigma_{eq}^0}{\sigma_Y^0})^{\frac{1}{1+m}} \tag{3.84}$$

An increase in porosity results in higher plastic deformation. However, this increase has a limit, as for each level of porosity, the above relationship and continuum-based models must remain valid.

3.2.7 Residual Stress Relaxation in Defect-Free Materials

3.2.7.1 Conceptual View

In a fully dense, defect-free material, HIP (or furnace heating) can relax the residual stresses. The key point is that stress relaxation requires plastic deformation or creep, which in turn needs a non-zero shear (deviatoric) stress (τ) or equivalent stress.

With only HIP loading, the stress state would be purely hydrostatic ($\sigma_1 = \sigma_2 = \sigma_3 = -P$) for a defect-free material with initially *no* residual stress and only loaded by a uniform hydrostatic pressure. In that case, the shear stress τ and von Mises equivalent stress σ_{eq} are both zero, so no plastic deformation would occur. One might argue that with HIP, if the material has no defects, τ should be zero under pure hydrostatic loading, and thus no plastic deformation should occur. However, in this scenario, the defect-free material already contains a residual stress field σ_{res} from the LPBF process. That residual stress is not purely hydrostatic; it typically has a deviatoric part, which means that inside the material, there are already non-zero shear stresses (τ) and a non-zero equivalent von Mises stress $\sigma_{eq,res}$. Therefore, the shear stress that enables plastic deformation during HIP in a defect-free material does not come from the applied hydrostatic pressure, but rather from the pre-existing residual stresses.

When the part is placed in a HIP chamber, the hydrostatic pressure simply adds a hydrostatic component to this existing residual stress field. The shear part of the stress – which is what drives yielding and creep – is still the same residual deviatoric stress that existed before loading. As temperature rises, the material's yield strength $\sigma_y(T)$ and creep resistance decrease. Wherever the local equivalent residual stress $\sigma_{eq,res}$ exceeds the reduced $\sigma_y(T)$, plastic flow and/or creep occur, and the residual stress is partially relaxed. Thus, the shear stress that causes stress relaxation in a defect-free component during HIP does not come from the applied hydrostatic pressure, but the pre-existing residual stresses themselves. HIP in this case behaves, from a stress-relaxation standpoint, essentially like a high-temperature furnace cycle: in both cases, the residual deviatoric stress is used as the driving force, and temperature (time-dependent creep plus reduced yield strength) as the enabling factor. The presence of pressure only changes the hydrostatic level, not the deviatoric driving force for plasticity.

3.2.7.2 Analytical View

Under HIP loading alone, a defect-free material with no initial residual stress experiences a purely hydrostatic stress state. As demonstrated previously in Equations (3.26)–(3.29), such a loading condition generates no deviatoric stress component and therefore produces zero von Mises equivalent stress. Consequently, no yielding or plastic deformation occurs, and the material undergoes only elastic volumetric compression.

However, in the present case, the defect-free material already contains a residual stress field σ_{res} from the LPBF process. Let the initial residual stress tensor in the solid be $\boldsymbol{\sigma}_{\mathrm{res}}$. During HIP, a uniform hydrostatic pressure $P > 0$ is applied, thus producing a hydrostatic Cauchy stress:

$$\boldsymbol{\sigma}_{hyd} = P\,\mathrm{I} \tag{3.85}$$

The total Cauchy stress during HIP is therefore the superposition of the applied hydrostatic pressure and the pre-existing residual stress field:

$$\boldsymbol{\sigma}_{\mathrm{tot}} = \boldsymbol{\sigma}_{hyd} + \boldsymbol{\sigma}_{\mathrm{res}} = P\,\mathbf{I} + \boldsymbol{\sigma}_{\mathrm{res}} \tag{3.86}$$

The residual stress tensor can be decomposed into hydrostatic and deviatoric parts as:

$$\boldsymbol{\sigma}_{\text{res}} = \boldsymbol{s}_{\text{res}} + \sigma_{hyd_{\text{res}}} \mathbf{I} \tag{3.87}$$

where the hydrostatic part of the residual stress is:

$$\sigma_{hyd_{\text{res}}} = \frac{1}{3}\,\text{tr}(\boldsymbol{\sigma}_{\text{res}}) \tag{3.88}$$

Accordingly, the hydrostatic part of the total stress becomes:

$$\sigma_{hyd_{\text{tot}}} = \frac{1}{3}\,\text{tr}(\boldsymbol{\sigma}_{\text{tot}}) = \frac{1}{3}\,\text{tr}(P\,\mathbf{I} + \boldsymbol{\sigma}_{\text{res}}) = P + \sigma_{hyd_{\text{res}}} \tag{3.89}$$

The deviatoric part of the total stress is obtained by subtracting the hydrostatic component of the total stress tensor from the total stress tensor:

$$\boldsymbol{s}_{\text{tot}} = \boldsymbol{\sigma}_{\text{tot}} - \sigma_{hyd_{\text{tot}}} \mathbf{I} \tag{3.90}$$

Substituting Equations (3.86) and (3.89) gives:

$$= (P\,\mathbf{I} + \boldsymbol{\sigma}_{\text{res}}) - (P + \sigma_{hyd_{\text{res}}})\,\mathbf{I} = \boldsymbol{\sigma}_{\text{res}} - \sigma_{hyd_{\text{res}}}\,\mathbf{I} = \boldsymbol{s}_{\text{res}}$$

where

$$s_{res} = \begin{bmatrix} s_{res,xx} & s_{res,xy} & s_{res,xz} \\ s_{res,yx} & s_{res,yy} & s_{res,yz} \\ s_{res,zx} & s_{res,zy} & s_{res,zz} \end{bmatrix} \tag{3.91}$$

Therefore, the deviatoric stress tensor does not change with the addition of the hydrostatic HIP stress:

$$\boldsymbol{s}_{\text{tot}} = \boldsymbol{s}_{\text{res}} \tag{3.92}$$

Therefore, the von Mises equivalent stress during HIP becomes:

$$\sigma_{\text{eq,tot}} = \sqrt{\frac{3}{2}\,\boldsymbol{s}_{\text{tot}}\!:\boldsymbol{s}_{\text{tot}}} = \sqrt{\frac{3}{2}\,\boldsymbol{s}_{\text{res}}\!:\boldsymbol{s}_{\text{res}}} = \sigma_{\text{eq,res}} \tag{3.93}$$

where

$$s_{res}\!:s_{res} = {s_{res,xx}}^2 + {s_{res,yy}}^2 + {s_{res,zz}}^2 + 2({s_{res,xy}}^2 + {s_{res,xz}}^2 + {s_{res,yz}}^2) \tag{3.94}$$

Thus, the equivalent stress that controls yielding and creep is the same before and after applying hydrostatic pressure. The HIP pressure changes only the hydrostatic part (P), not the deviatoric part. The yielding condition during heating may therefore be written as:

$$\sigma_{\text{eq,res}} \geq \sigma_y(T) \tag{3.95}$$

where $\sigma_y(T)$ is the temperature-dependent yield strength. As the temperature increases, $\sigma_y(T)$ decreases; and at some critical temperature T^*, $\sigma_{\text{eq, res}} \approx \sigma_y(T^*)$, and plastic flow/creep begins.

This causes stress redistribution and reduction of the residual stress tensor $\boldsymbol{\sigma}_{\mathrm{res}}$. After cooling back down, a new, smaller residual stress field remains. Crucially, the inequality above does not contain the HIP pressure P; only $\boldsymbol{\sigma}_{\mathrm{res}}$ and $\sigma_y(T)$ appear. Therefore, for a defect-free material, the amount of residual stress relaxation is governed by the initial residual deviatoric stress and the thermal history, and essentially the same whether the heat treatment is performed in a furnace or a HIP chamber with only hydrostatic pressure.

3.2.8 Stress Relaxation under Combined Residual and Applied Stresses

This section evaluates how stress relaxation can be increased and clarifies the relationships among creep rate, temperature, and the amount of deviatoric stress inside the material. Both a conceptual explanation and formal analytical derivation are provided.

3.2.8.1 Conceptual View

Stress relaxation occurs when internal stresses decrease over time under constrained deformation, and at elevated temperatures, this process is governed primarily by creep—a time-dependent form of plastic deformation. When the total strain is constrained—for example, when the part is clamped or when parts of the material are surrounded by stiffer adjacent zones—any CEEQ that develops must be accommodated by a reduction in elastic strain. As previously established in Equations (3.15) and (3.16), this reduction in elastic strain directly corresponds to a decrease in internal stress. Since elastic strain is directly related to stress, $\sigma = E\varepsilon_e$, any increase in CEEQ produces a corresponding decrease in stress. Therefore, any factor that increases the CEEQ rate will proportionally increase the rate of stress relaxation.

Creep in metals is primarily governed by temperature and the level of effective shear stress, both of which directly control the rate at which time-dependent plastic deformation occurs. Increasing the temperature enhances atomic mobility, dislocation activity, and diffusion-assisted mechanisms, thus resulting in a significantly higher creep rate and, consequently, higher stress relaxation within a given holding period. Likewise, a higher deviatoric stress—i.e., the shear-type component of the stress state rather than the purely hydrostatic part—provides a greater thermodynamic driving force for dislocation creep, thereby accelerating the rate at which CEEQ accumulate and allowing residual stresses to diminish more rapidly. Additionally, extending the holding time at elevated temperatures facilitates the development of more creep deformation, thus further increasing the total amount of stress relaxation achieved. Together, these factors dictate the overall efficiency of high-temperature processes such as HIP or furnace heat treatment in reducing residual stresses within metallic components.

Residual stresses inside a material inherently contain deviatoric components, even in the absence of external hydrostatic pressure. Thus, a fully dense material without defects can still relax stress during HIP, because residual stresses provide the deviatoric stress needed to activate creep. While only hydrostatic HIP pressure alone does not generate shear stress in defect-free regions, the situation changes when voids are present. HIP pressure that acts on these geometrical features produces additional deviatoric stresses that combine with the residual stresses. The residual and HIP-induced stress contributions must be combined in tensor form. Accordingly, the total deviatoric stress tensor can be expressed as:

$$\boldsymbol{S}_{\mathrm{tot}} = \boldsymbol{S}_{\mathrm{res}} + \boldsymbol{S}_{\mathrm{HIP}} \tag{3.96}$$

where $\boldsymbol{S}_{\mathrm{res}}$ is the deviatoric component of the initial residual stress tensor generated during LPBF, and $\boldsymbol{S}_{\mathrm{HIP}}$ is the local deviatoric stress tensor induced by the interaction of the externally applied HIP pressure with the void geometry. Since creep is highly sensitive to applied stress, even a modest increase in the deviatoric component of the total stress tensor ($\boldsymbol{S}_{\mathrm{tot}}$) can substantially increase the creep rate and, consequently, enhance stress relaxation. When only residual stresses are present, creep-driven relaxation does occur, but the rate of this relaxation is limited by the relatively small deviatoric (shear-type) stress available. However, when residual stresses are constructively supplemented by pressure-induced deviatoric stresses—such as those generated near pores or geometrical discontinuities during HIP—the total driving stress for creep increases, thus leading to a markedly accelerated relaxation response. This explains why the application of hydrostatic pressure can significantly assist with stress relaxation. Most importantly, this enhancement only occurs in regions where the externally applied hydrostatic pressure can generate shear components; in fully dense areas where the stress state remains purely hydrostatic, no additional deviatoric stress is produced, and creep-assisted relaxation remains minimal. Therefore, HIP can substantially accelerate stress relaxation in defect-affected regions, but not in perfectly dense regions where the pressure remains purely hydrostatic.

3.2.8.2 Analytical View

As previously introduced in Equation (3.14), the hyperbolic-sine creep law is adopted to describe the creep-controlled stress relaxation behavior during HIP and heat treatment. This constitutive model relates the equivalent creep strain rate to the applied deviatoric stress and temperature, and is particularly suitable for high-temperature and stress conditions where dislocation creep dominates.

For a constrained material element, the total strain remains constant during relaxation. Therefore, based on the strain decomposition previously established in Equations (3.15) and (3.16), any increase in creep strain must be balanced by an equal reduction in elastic strain, leading directly to a decrease in stress. Substituting Equation (3.14) into the stress-rate relationship gives:

$$\dot{\sigma} = -EA[\sinh(B\sigma_{eq})]^n \exp(-\frac{\Delta H}{R(T - T^Z)}) \tag{3.97}$$

where σ_{eq} represents the von Mises equivalent stress calculated from the current deviatoric stress tensor. This expression confirms that stress relaxation only occurs when the creep mechanism is active, and that relaxation proceeds more rapidly at higher temperatures and under higher deviatoric stresses. Let the von Mises equivalent stress that drives creep consist of two contributing factors:

$$\sigma_{eq,tot} = \sqrt{\frac{3}{2}\boldsymbol{s}_{tot}:\boldsymbol{s}_{tot}} = \sqrt{\frac{3}{2}(\boldsymbol{s}_{res} + \boldsymbol{s}_{HIP}):(\boldsymbol{s}_{res} + \boldsymbol{s}_{HIP})} \tag{3.98}$$

where $\boldsymbol{s}_{res}$ originates from the initial residual stresses generated during LPBF, and $\boldsymbol{s}_{HIP}$ arises from the local stress concentrations induced by pressure from HIP which acts on voids. Accordingly, the ratio between the creep strain rates with and without HIP-induced deviatoric stress at the same temperature becomes:

$$\frac{\dot{\varepsilon}^{cr}_{(\text{res+HIP})}}{\dot{\varepsilon}^{cr}_{(\text{res only})}} = [\frac{\sinh(B\sigma_{eq,tot})}{\sinh(B\sigma_{eq,res})}]^n \tag{3.99}$$

The hyperbolic-sine function increases rapidly with stress. Therefore, even a modest increase in the effective deviatoric stress (σ^{cr}) can produce a disproportionately large increase in the creep strain rate. Since $\sigma^{cr}_{\text{tot}} > \sigma^{cr}_{\text{res}}$ and $\sinh(x)$ is a strictly increasing, convex function, the numerator in the creep equation becomes much larger than the denominator—especially at higher stresses. Therefore:

$$\dot{\varepsilon}^{cr}_{(\mathrm{res+HIP})} > \dot{\varepsilon}^{cr}_{(\mathrm{res\ only})} \tag{3.100}$$

Furthermore, from the stress-relaxation relationship previously established in Equation (3.97), a higher creep rate directly produces a faster reduction in stress magnitude. Therefore:

$$|\ \dot{\sigma}_{(\mathrm{res+HIP})}\ | > |\ \dot{\sigma}_{(\mathrm{res\ only})}\ | \tag{3.101}$$

Thus, stress relaxation is significantly faster and more effective when HIP-induced deviatoric stress adds to the residual stress. Near voids, HIP pressure generates a local deviatoric stress $\sigma^{cr}_{\mathrm{HIP}} > 0$; when combined with $\sigma^{cr}_{\mathrm{res}}$, this increases $\sigma^{cr}_{\mathrm{tot}}$, amplifies the hyperbolic-sine term, raises the creep rate, and consequently enhances stress relaxation and void closure.

In contrast, in defect-free regions where the applied pressure is purely hydrostatic:

$$\sigma^{cr}_{H} = 0 \tag{3.102}$$

Under this condition, HIP pressure does not contribute to the deviatoric stress term in the creep law, and therefore cannot assist stress relaxation. Any relaxation that occurs in such regions is driven solely by the initial residual stress state together with elevated temperature.

CHAPTER FOUR: RESULTS AND DISCUSSION

This chapter presents and discusses the results obtained from the numerical simulations and analyses conducted in this research work. The findings are organized into two main sections, which correspond to the major components of the study. In the first part, the results and discussion related to the LPBF process are presented. This section focuses on the changes in temperature, stress, and strain fields during the LPBF process, as well as the development and distribution of residual stresses induced by the rapid thermal cycles characteristic of AM. The influence of key process parameters—such as laser power, scanning speed, and preheating temperature—on residual stress formation is analyzed and interpreted in detail.

In the second part, attention is directed toward the post-processing phase, where the effects of the HIP process and conventional furnace heat treatment on residual stress relaxation are investigated. The results of both post-processing methods are compared to evaluate the role of hydrostatic pressure in promoting densification and stress relief. Additionally, this section presents and discusses the influence of void morphology (shape and size) and void volume fraction on the efficiency of stress relaxation during HIP. Various void geometries and porosity levels are analyzed to assess their effects on local deformation behavior, pore closure mechanisms, and the resulting residual stress distribution. Through this analysis, HIP and furnace treatments show a comparative performance, thus providing insight into the mechanisms that govern stress reduction, defect elimination, and the enhancement of mechanical performance in LPBF-produced components.

4.1 Results and Discussion of LPBF Process

4.1.1 Temperature Evaluation During LPBF Process

The thermal history of the manufactured part determines the relationship between temperature and residual stress, as also discussed by Li et al.[155] and Sandmann et al.[184]. Figure 4.1 illustrates the temperature history at a centroid point in the first layer over time. The coordinates of the centroid point are X= 0.025 mm, Y= 0.100 mm, and Z= 0.050 mm. The total simulation time for the 20 layers is 400 sec. The plot shows rapid fluctuations in temperature, with each fluctuation representing a short heating process that lasts approximately 0.022 seconds, followed by a cooling process that takes about 20 seconds.

The temperature distributions of both time and space change rapidly during the LPBF process. As plotted in Figure 4.1, the nodal temperature is particularly high in the first and second layers because the laser heat source is in close proximity to the designated point. The maximum temperature of the melt pool is reached during the first peak fluctuation as the laser moves across the selected point. The information plotted in Figure 4.1 demonstrates the dynamic nature of temperature changes during the printing process, with rapid fluctuations and varying spatial distributions. This information is crucial in understanding the thermal behavior of the part during printing and its potential effect on residual stress formation. Ding et al.[185]reported that the maximum temperature of the melt pool has an immense impact on the generated residual stress. They showed that a large expansion in the material leads to a large deformation in the surrounding material. The sequential changes in temperature during the printing process are related to the effect of remelting due to printing the top layers, which can result in thermal gradients and internal stresses within the part. The impact of these fluctuations becomes less significant after the seventh layer since the laser heat source is far from the point mentioned above. Since the fluctuation becomes constant after the seventh layer, it is concluded that the newly deposited layers can affect the quality of the part and fatigue life of the component up to the seventh layer beneath this layer. Thus, better temperature control enhances dimensional accuracy, mechanical performance, and reliability of the final part.

The generation of residual stress is closely associated with the temperature distribution throughout the LPBF process. As the laser traverses the layer of powder, the powder particles at the focal point is rapidly heated, thus exceeding their melting point and resulting in the formation of a melt pool and a HAZ in the surrounding vicinity. The melt pool follows a defined trajectory during the laser scanning process, where it dissipates some of its heat through radiation and convection to the cooler environment. Simultaneously, a significant amount of the heat is transferred via conduction to the neighboring particles and substrates. Eventually, as the temperature of the melt pool decreases, a consolidated region is formed. The temperature distribution in each layer changes rapidly with time and space, as depicted in Figure 4.2 for the tenth layer at a laser speed of 600 mm/s and laser power of 120 W. When the laser heat source moves to the next track, the temperature field increases. In this figure, there are many thermal gradients near the laser spot, which results in the formation of internal thermal stress within the component.

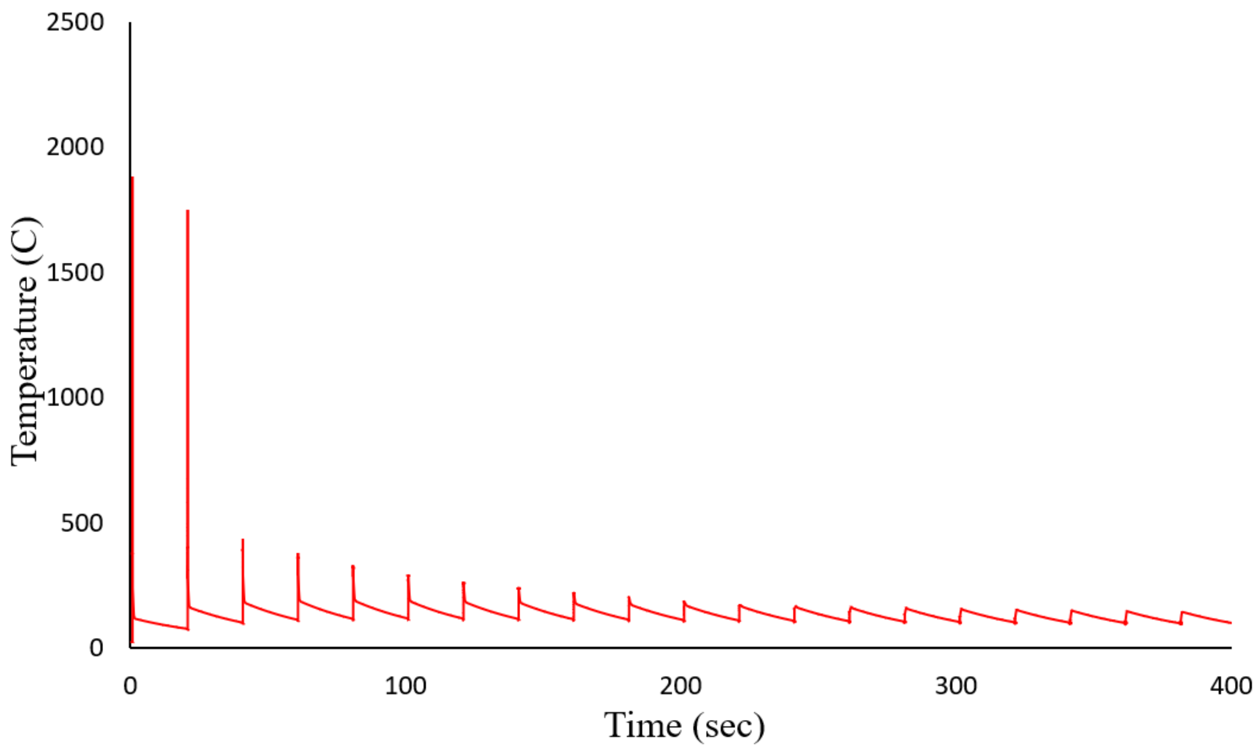

Figure 4.1 Transient temperature history during laser scanning of first layer with laser power of 120 W and laser speed of 600 mm/s.

Figure 4.3 shows that the melt pool and temperature profiles exhibit a comet-tail morphology. Similar thermal and melt-pool characteristics were reported by Patil and Yadava[52], He et al.[186], and Arısoy et al.[187] in their numerical studies of powder-bed fusion processes. The yellow area in Figures 4.2 and 4.3 shows that the thermal gradient in front of the moving laser beam is substantially steeper than that in the rear. This characteristic and the anisotropic shape of the melt pool result from the lower thermal conductivity of the powder material compared to that of the bulk metal.

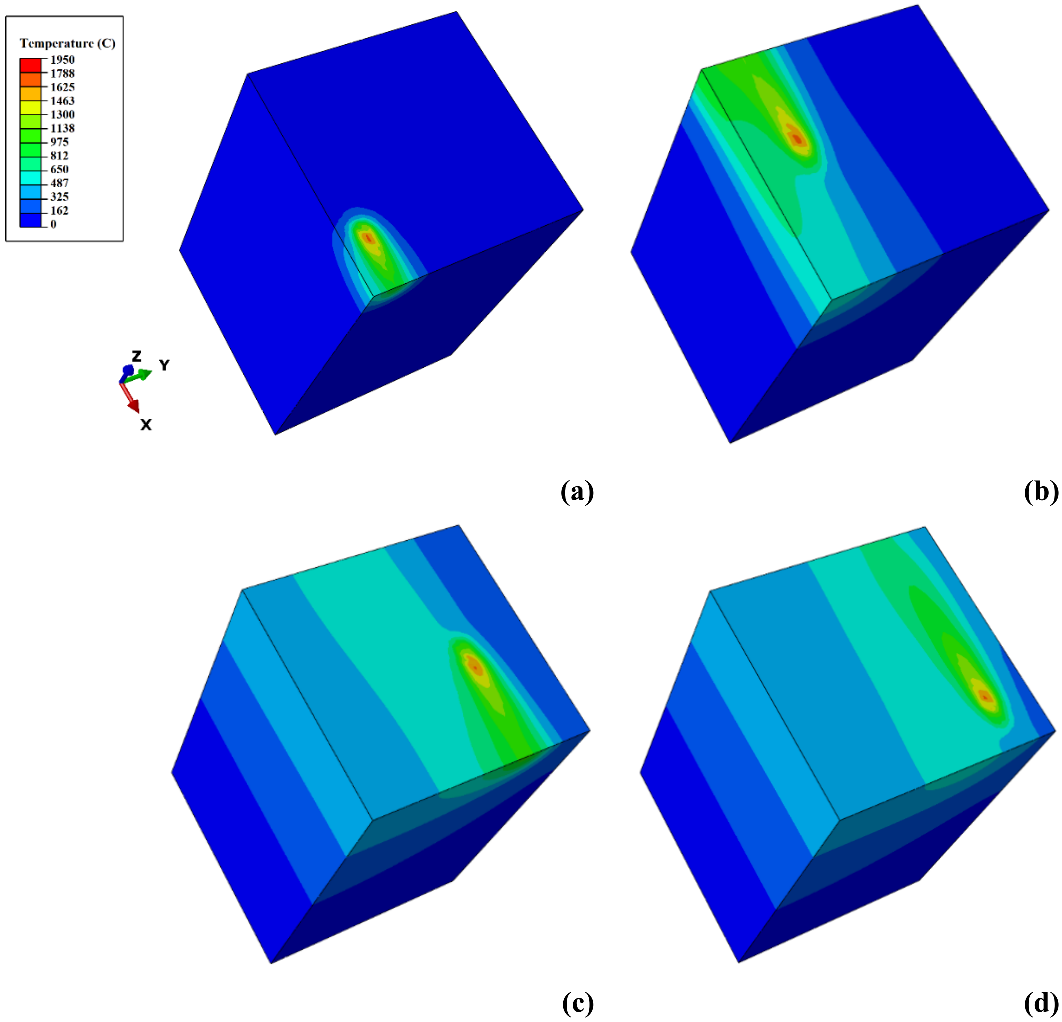

Figure 4.2 FE model snapshots of the temperature distribution (in °C) during LPBF process at the tenth layer using a zigzag pattern: a) 1st, b) 2nd, c) 7th, and d) 8th tracks. (Please refer to the online version of this article for the color legend and additional details).

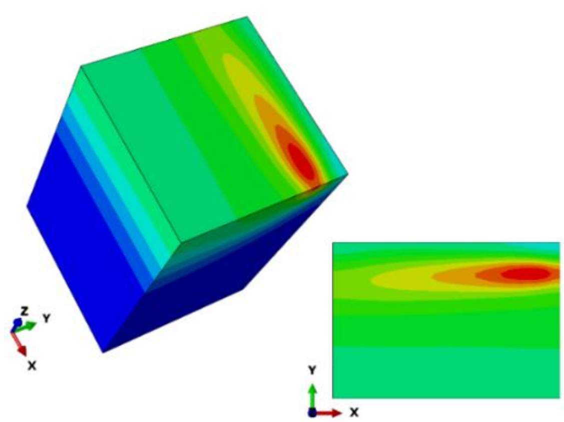

Figure 4.3 Shape of melt pool and heat-affected zone on tenth layer.

4.1.2 In-process Stress

Figure 4.4 shows the changes in the stress components S_{11}, S_{22}, and S_{33} as a function of time at a centroid point on the first layer. The coordinates of the centroid point are X= 0.025 mm, Y= 0.100 mm, and Z= 0.050 mm. The planar stress components S_{11} and S_{22} are subjected to both tensile and compressive stress at every fluctuation. The observed fluctuation is attributed to the thermal dynamics during the AM process. When the component is heated with a high-energy laser, the material undergoes expansion. However, this expansion is constrained by the cooler surrounding material, which leads to the formation of compressive stress in the heated zone. Upon cooling, the previously heated zone begins to cool and contract with the removal of the heat source. However, the contraction is limited by the PEEQ that formed during the heating phase. Consequently, tensile stress develops in the heated zone. Bayerlein et al.[188] conducted neutron diffraction measurements on a simple cuboid structure produced through laser beam melting. Their study revealed the changes in residual stresses at different stages of the build-up process. As new layers were added, tensile stresses were introduced into the material directly below, primarily within the build-up plane (longitudinal–transversal directions). Remarkably, this behavior was observed in the early stages of the build-up process.

S_{11} and S_{22} fluctuate as the nodal temperature for the selected point is under the direct influence of the laser beam-heat input up to the seventh layer. S_{11} and S_{22} converge towards zero after the seventh layer which shows that their impact on the quality of the part is reduced with the printing of new layers. S_{33} behaves differently than S_{11} and S_{22}. The latter two are influenced by the printed track directions as reported by Tangestani et al.[58,59]; however, S_{33} is influenced by the material deposition, constraint from the substrate, and printed geometry, as discussed by Chakraborty et al.[189]. S_{33} is almost zero up to the seventh layer built because the normal direction of the free surface is along a similar direction to S_{33} which leads to zero stress at the top surface. This observation is consistent with the findings of Li et al.[155]. By adding more material, the size of the printed geometry and distance of the selected point from the free surface increases during the process. As a result, S_{33} diverges from zero to the compressive stress. This trend continues up to the fifteenth layer where the created compressive stress is near the material yield stress, which becomes constant after the fifteenth layer. The stress recorded from a single node does not explain much about the laser parameters which is elaborated in the following section.

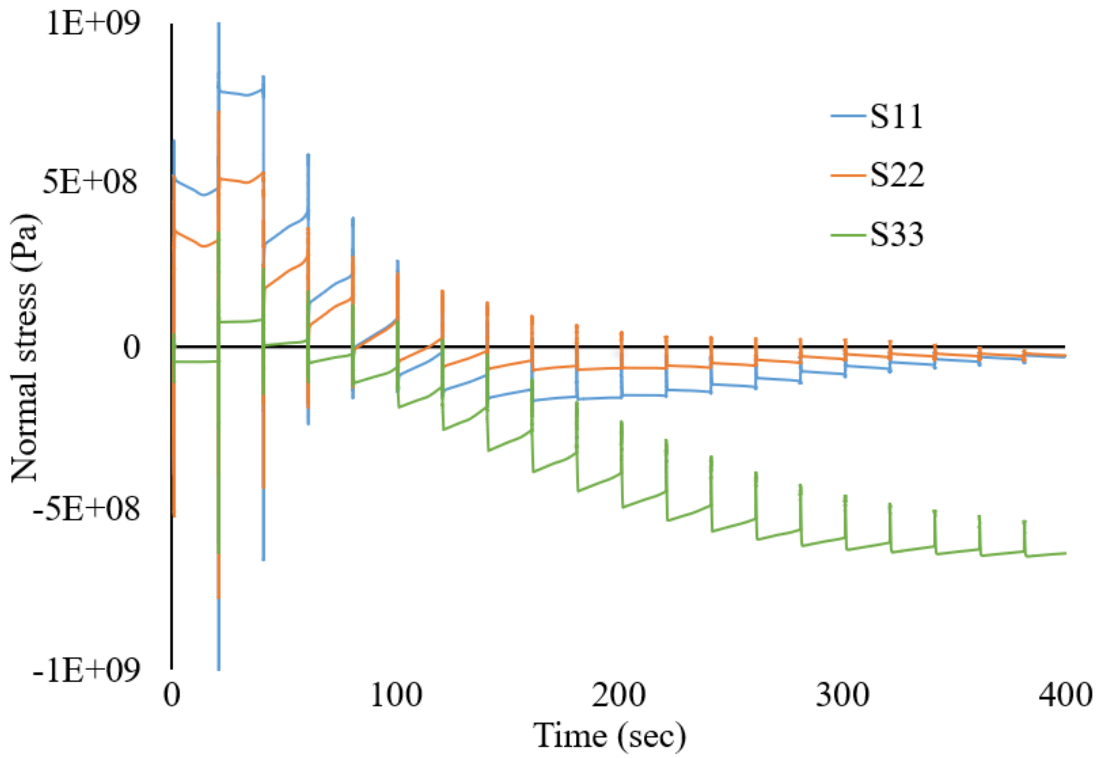

Figure 4.4 Residual stress history at centroid point in first layer at laser speed of 600 mm/s, and laser power of 120 W.

4.1.3 Stress Components

Heat input from the laser in the LPBF process is not uniformly distributed throughout the build area but concentrated along the laser path. Due to the uneven distribution of the heat input, thermal gradients develop, with hotter regions near the melt pool and cooler regions further away. These thermal gradients can create residual stresses in the part as it cools and solidifies. Figure 4.5 presents S_{11}, S_{22}, and S_{33} on Layers 1, 10, and 20 at the beginning of the cooling process, at a laser speed of 600 mm/s and laser power of 120 W. There is a strong correlation between the residual stresses and direction of the tracks. The green traces elongated in the X-direction in Figures 4.5(a), 4.5(b), and 4.5(c) represent larger residual stresses created along the track direction due to the greater distribution of heat input along this direction. As a result, a larger thermal gradient is generated in that direction, which results in the development of more stress. This observation is consistent with the findings reported by Tangestani et al.[58,59]. It is also important to note that the number of layers affects the distribution of the residual stresses in laser powder bed fused parts.

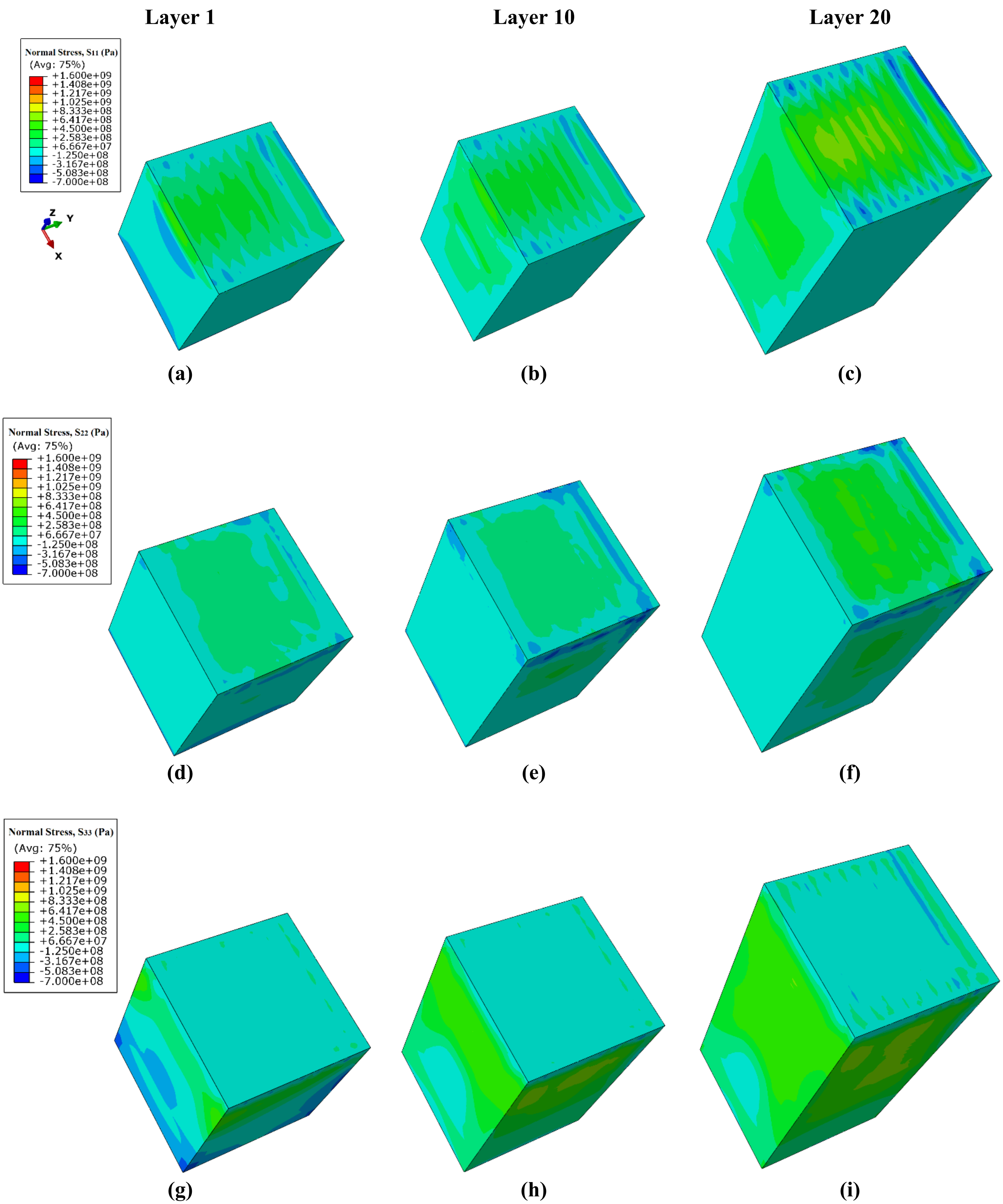

Figure 4.5 Residual stress distribution immediately after printing at laser speed of 600 mm/sec and laser power of 120 W for Layers 1, 10, and 20.

The yellow field on Layer 20 shows that this feature is more significant for the higher number layers. A larger thermal gradient could explain for this phenomenon as the thermal difference between the environment and the higher number layers is larger, which would create more stress. Also, the number of layers in a part can influence the residual stresses as the thermal history of each layer can influence the residual stresses in the subsequent layers. The heat input from the laser in LPBF is distributed more evenly in the perpendicular direction of the track, thus resulting in more uniform thermal gradients and lower residual stresses. S_{11} is larger in magnitude compared to S_{22} as shown in Figures 4.5(c), 4.5(d), and 4.5(e) as S_{22} is perpendicular to the direction of the track. However, since the laser changes direction near the edges for the zigzag pattern, S_{22} becomes larger than S_{11}. This can be seen as the sides of the components are in green for S_{22} and blue for S_{11}. Like S_{11}, the stress in the Y direction is increased for the higher number layers. S_{33} refers to the normal stress perpendicular to the surface of the component. Figures 4.5(g), 4.5(h), and 4.5(i) show that S_{33} is negligible on the top surface of a laser powder bed fused part since the surface is not attached to anything and can move freely without any external forces acting on it. Thus, there is no S_{33} on this surface, which results in an independent residual stress in the Z direction (perpendicular to the top surface) across the different deposited layers. However, it is essential to note that residual stresses in the S_{11} and S_{22} directions are found on the top surface, which can potentially affect the mechanical properties of the part.

4.1.4 Effect of Pre-heating on Residual Stress Distribution

The pre-heating temperatures in commercial LPBF systems are generally restricted to approximately 200°C due to limitations in machine design and operational challenges associated with higher temperatures, as reported by Ali et al.[190]. In this study, the influence of preheating temperature on residual stress evolution is investigated over a temperature range of 25–225°C. The effect of pre-heating temperature on the created residual stress in the X and Z directions are presented in Figures 4.6 and 4.7, respectively. There is an inverse relationship between the pre-heating temperature and internal residual stress. Figure 4.6(c) shows that increasing the pre-heating temperature to 225°C clearly results in a reduction in generated residual stress (S_{11}) between the center of the component and substrate compared with Figure 4.6(a), where the sample is modeled at a standard temperature of 25°C. Also, a comparison of Figures 4.7(a), 4.7(b), and 4.7(c) clearly shows that the internal residual stress (S_{33}) is reduced with increasing pre-heating temperatures.

When the substrate is pre-heated, a more favorable thermal gradient is created during the printing process. Specifically, pre-heating helps to reduce the thermal gradient between the heated material and substrate, thus minimizing the temperature difference and resulting in lower cooling rates during solidification. This reduces the development of thermal and residual stresses in the printed part, as the lower cooling rates allow for more uniform solidification and minimize the gradients in temperature and subsequent stress. As a result, increasing the pre-heating temperature can help to reduce the residual stresses in the LPBF process, therefore resulting in higher part quality and less distortion or cracking. These results are in good agreement with trends reported by Mirkoohi et al.[191], who observed that increasing preheating temperature can result in a larger melt pool width and greater melt volume. However, the reduction of residual stress cannot be entirely attributed to fewer thermal gradients. Vasinonta et al.[192] explained that increasing the pre-heating temperature leads to a reduction in generated residual stresses since a decrease in the yield stress of materials at higher temperatures is crucial for limiting the overall residual stress build-up. Also, they reported that the Young's modulus decreases at higher temperatures, which reduces the total residual stress build-up. Kruth et al.[38] reported that the stress state (tensile and compressive) in the build direction is different from the center to the surface. Thus, any change in the center would be opposite of that at the surface. The gap between the surface and center is reduced by increasing the pre-heating temperature, and the magnitude of the tensile and compressive stresses would converge to zero, which is beneficial to the fatigue life of parts. As discussed earlier, pre-heating does not influence S_{33} at the top surface since S_{33} is always zero near the free surface at the top.

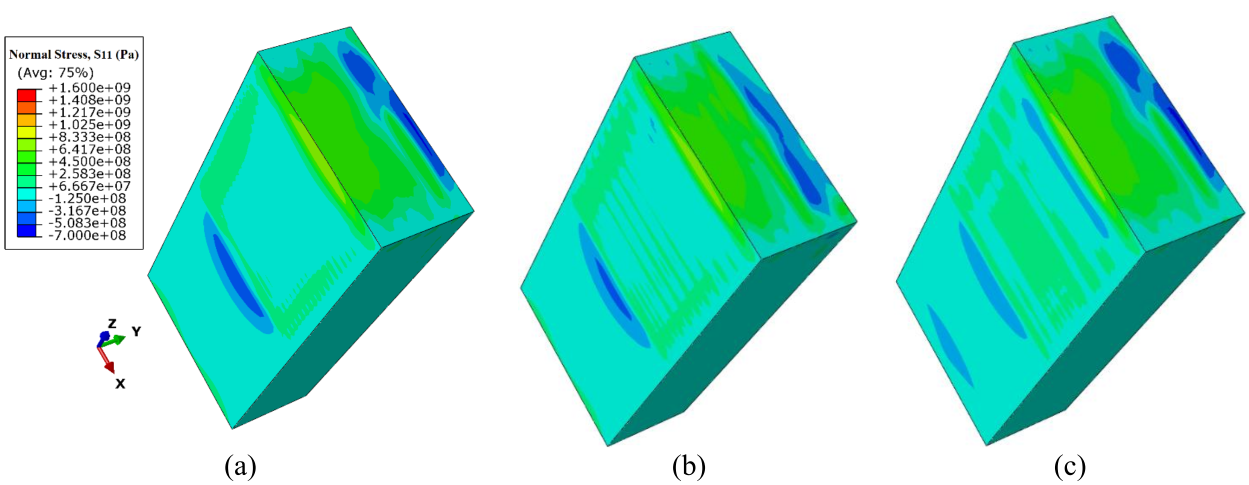

Figure 4.6 S_{11} at laser speed at 600 mm/sec and laser power of 120 W on Layer 20 with pre-heating temperatures of a) 25°C, b) 125°C, and c) 225°C. The components are cross sectioned from XZ plane.

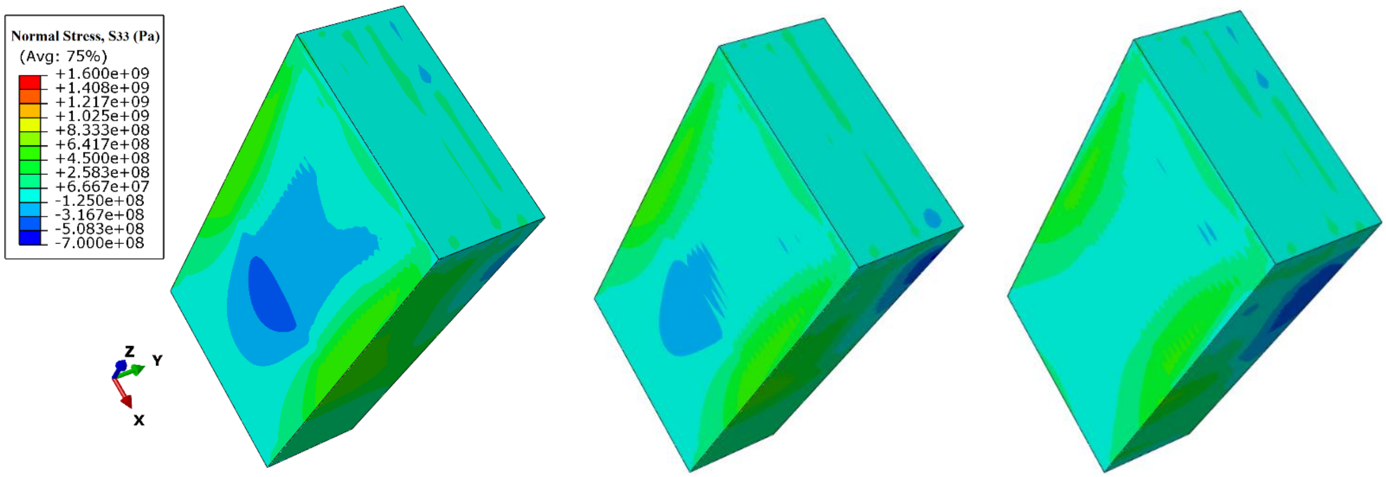

(a) (b) (c)

Figure 4.7 S_{33} at laser speed of 600 mm/sec and laser power of 120 W on Layer 20 with pre-heating temperatures of a) 25℃, b) 125℃ , and c) 225℃. The components are cross sectioned from XZ plane.

4.1.5 Effect of Laser Parameters on the Residual Stress

The predicted residual stresses in the longitudinal (S_{11}), transverse (S_{22}), and build (S_{33}) directions are illustrated in Figures 4.8, 4.9, and 4.10, respectively. The laser power is increased incrementally from 120 W to 180 W in the horizontal direction, while the laser speed is increased from 750 mm/s to 1050 mm/s in the vertical direction. These results were obtained immediately after printing Layer 20, which focus on the central stress field of the component. Figure 4.8 shows that there is a transition zone near the upper layers, where residual stress is higher due to insufficient reheating from the top-layer fusion, which is consistent with the findings reported by Mirkoohi et al.[191] and Simson et al.[193].

The main mechanism that causes the residual stresses in additively manufactured components is rapid solidification and the heat from the deposition of new layers. Laser power and speed significantly affect heat input and solidification conditions, including thermal gradients and cooling rates. Figure 4.8 shows that reduced laser speed and increased laser power can lead to lower residual stress. A slower laser speed extends the dwell time, thereby intensifying energy input, altering the material thermal history, and affecting the residual stress in the final printed part. Longer exposure to laser energy fosters uniform temperature distribution, fewer thermal gradients, and reduced thermal stress. In addition, a slower laser speed leads to longer solidification time, which in turn reduces the cooling rate, thus giving the material more time to relax and thereby lowering the stress during the solidification process. Manvatkar et al.[194] confirm that the cooling rate is reduced with a slower laser speed. Also, a slower laser speed results in fewer thermal gradients and deflection angles, which is the distortion produced by the bridge curvature technique used in geometrically similar bridge-shaped components, as reported by Kruth et al.[38]. Wu et al.[195]conducted an experimental investigation that examined the residual stresses induced by AM in 316L stainless steel. To gain deeper insight into the factors that influence residual stresses, they employed a dual approach. They utilized a destructive surface residual stress measurement technique, which involves digital image correlation combined with build plate removal and sectioning. In addition, a nondestructive volumetric evaluation method, namely neutron diffraction, was employed. The findings of their research revealed that an increase in applied energy per unit length (achieved by adjusting the laser power/speed) results in a reduction of residual stresses.

Adjusting the laser power during printing has a direct impact on the thermal history of a material, which in turn, influences residual stress. Higher laser power increases the energy transferred to the material, thus affecting both the melt pool temperature and size. This increase in laser power can concurrently reduce both the surface tensile stress and compressive stress near the substrate by elevating the melt pool temperature and enlarging the melt pool size. These larger, flatter melt pools facilitate a slower cooling rate, thereby diminishing residual stress. Additionally, increased laser power can result in more uniform temperature distribution and fewer thermal gradients, thus further mitigating residual stress. Moreover, the increased energy input from a higher laser power can lead to lower rates of solidification by providing more time for the material to relax and reduce stress during solidification, which potentially results in lower residual stress. Levkulich et al.[196] conducted a study to investigate the influence of processing parameters, such as laser speed and laser power, on residual stress in laser powder bed fused components, specifically focusing on Ti6Al4V. They employed various techniques, including hole drilling, contour analysis, and X-ray diffraction. Their findings revealed that increasing the laser power and reducing the laser speed both lead to less residual stress near the surface. Consequently, achieving lower residual stress while maintaining acceptable component density is possible by using a higher laser power and slower laser speed.

The results presented in Figure 4.8 clearly show that laser speed has a more significant impact on residual stress than laser power. This is because laser speed directly influences the thermal history of a material during the printing process, which in turn significantly affects the development of residual stress in the final printed part. In the LPBF process, the thermal history of a material is primarily determined by the laser speed. The effect of laser power on the thermal history of a material is generally considered to be secondary to laser speed. This is because the laser power determines the amount of energy delivered by the laser, while the laser speed controls the duration of exposure at each spot, thus having a more significant impact on the overall thermal history of the material. An analysis of the data in Figure 4.8 indicates higher tensile stress at the surface and compressive stress near the substrate. The surface of the part cools and solidifies faster due to its exposure to the cooler ambient environment, which leads to higher tensile stress as the material contracts upon solidification. Moving towards the interior of the part, the lower cooling and solidification rates result in the material remaining at higher temperatures for a longer period of time which causes compressive stress near the substrate. The outputs of the FE model agree with those of the experimental data reported in the literature. Shiomi et al[197]. conducted measurements of residual stress in a metallic model created by using LPBF. The experimental findings revealed a significant tensile stress that persists in the surface layer of the model. Mercelis and Kruth[198] investigated experimental methods designed to measure residual stress profiles in a series of test samples produced with varying processing parameters. To assess the residual stresses within the parts, they introduced an innovative experimental model that relies on measuring the deformation of the component when the stresses are released. This method is known as the "crack compliance method" (CCM). The results of their research revealed that residual stresses in parts manufactured by using LPBF are notably significant. The residual stress profile exhibits two distinct zones of substantial tensile stresses at the top of the part, with a large intermediate zone characterized by compressive stresses.

Figure 4.9 shows the stress is tensile on the surface and compressive near the substrate like S_{11} but at a smaller magnitude. This shows that the planar stresses S_{11} and S_{22} behave similarly, but the magnitude is dependent on the printing pattern. As explained in the previous section, the zigzag pattern has the strongest impact in the X-direction where most of the tracks are directed. Therefore, the stress is formed mostly in the X-direction, and the magnitude of S_{22} is smaller than that of S_{11}. Thus, the impact of the printing parameters, including laser speed and laser power, is smaller compared to the stress in the X-direction. During the printing process, there are no constraints on the top layer. Thus, only printing parameters such as the printing pattern, laser power, and laser speed influence the magnitude of the created residual stresses in the X and Y directions. On the other hand, the center of the geometry is always constrained by the substrate and has a lower temperature compared to the newly produced layer. This difference in temperature and boundary conditions exerts a cyclic thermal load onto the previously deposited layers. This cyclic process applies compressive and tensile loads to the previously deposited layers and leads to stress relaxation; thus, the central part of the components has less stress (in the X and Y directions) compared to the top layer.

Figure 4.10 shows the S_{33} values for different laser speeds and powers. In the surrounding areas, the surface is subjected to tensile stress, which has negative repercussions for fatigue life in printed components. On the other hand, there is evidence of compressive residual stresses in the center of the blocks that can be beneficial for enhancing fatigue life. The impact of laser power and laser speed on the magnitude of tensile stress at the sides of the component is relatively minor due to skywriting that is used to change the direction of the laser for each track. However, the most significant impact of these laser parameters is observed at the center of the component, where S_{33} increases with higher laser speed and greater laser power. Since the top surface is free and the normal vector of the surface is aligned with the stress direction, S_{33} is almost zero at the top surface. Therefore, it can be concluded that laser power and laser speed do not impact the magnitude of S_{33} at the top surface of the part.

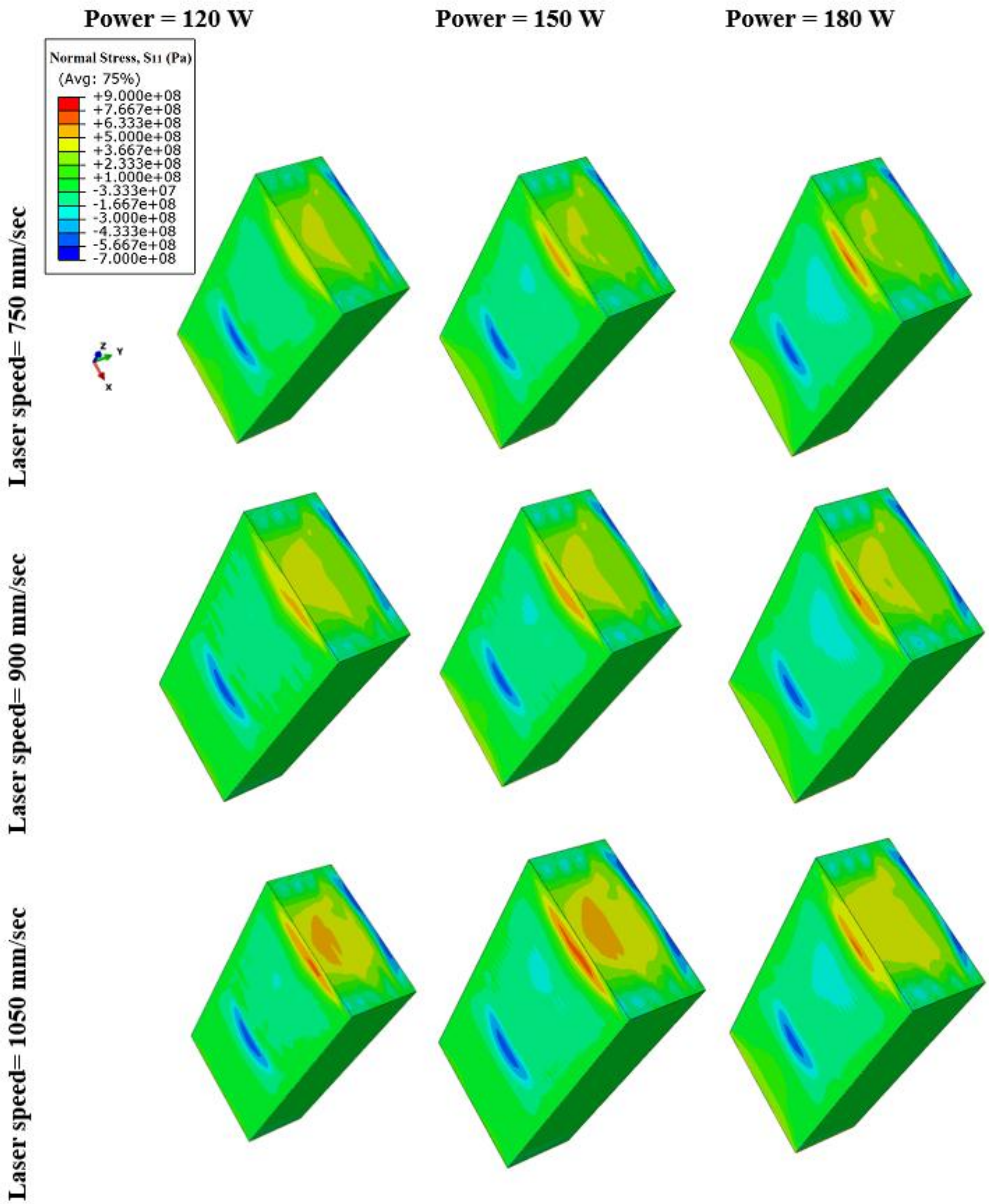

Figure 4.8 S_{11} immediately after printing at different laser speeds and powers on Layer 20. The components are cross sectioned from the XZ plane.

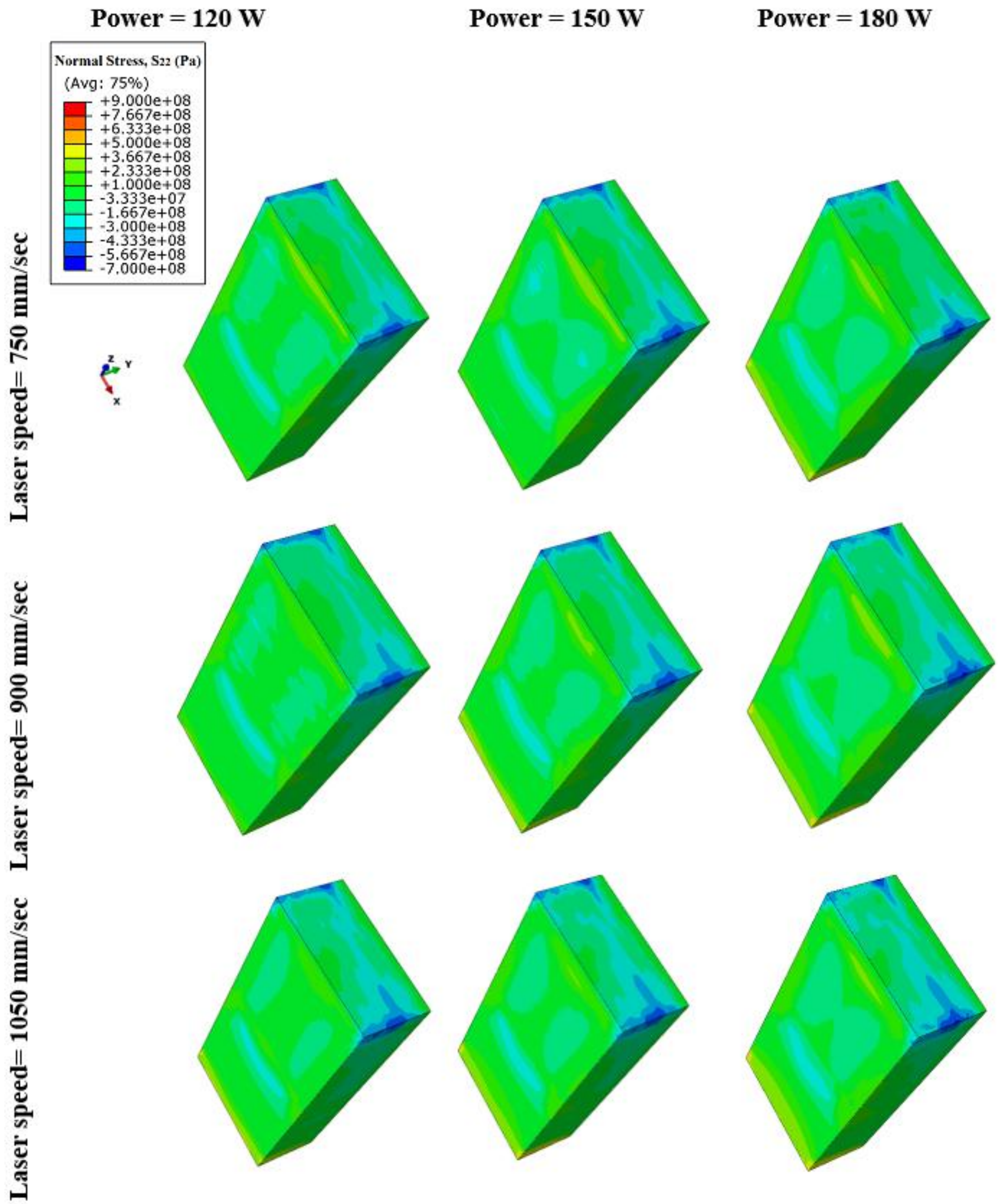

Figure 4.9 S_{22} immediately after printing at different laser speeds and powers on Layer 20. The components are cross sectioned from the XZ plane.

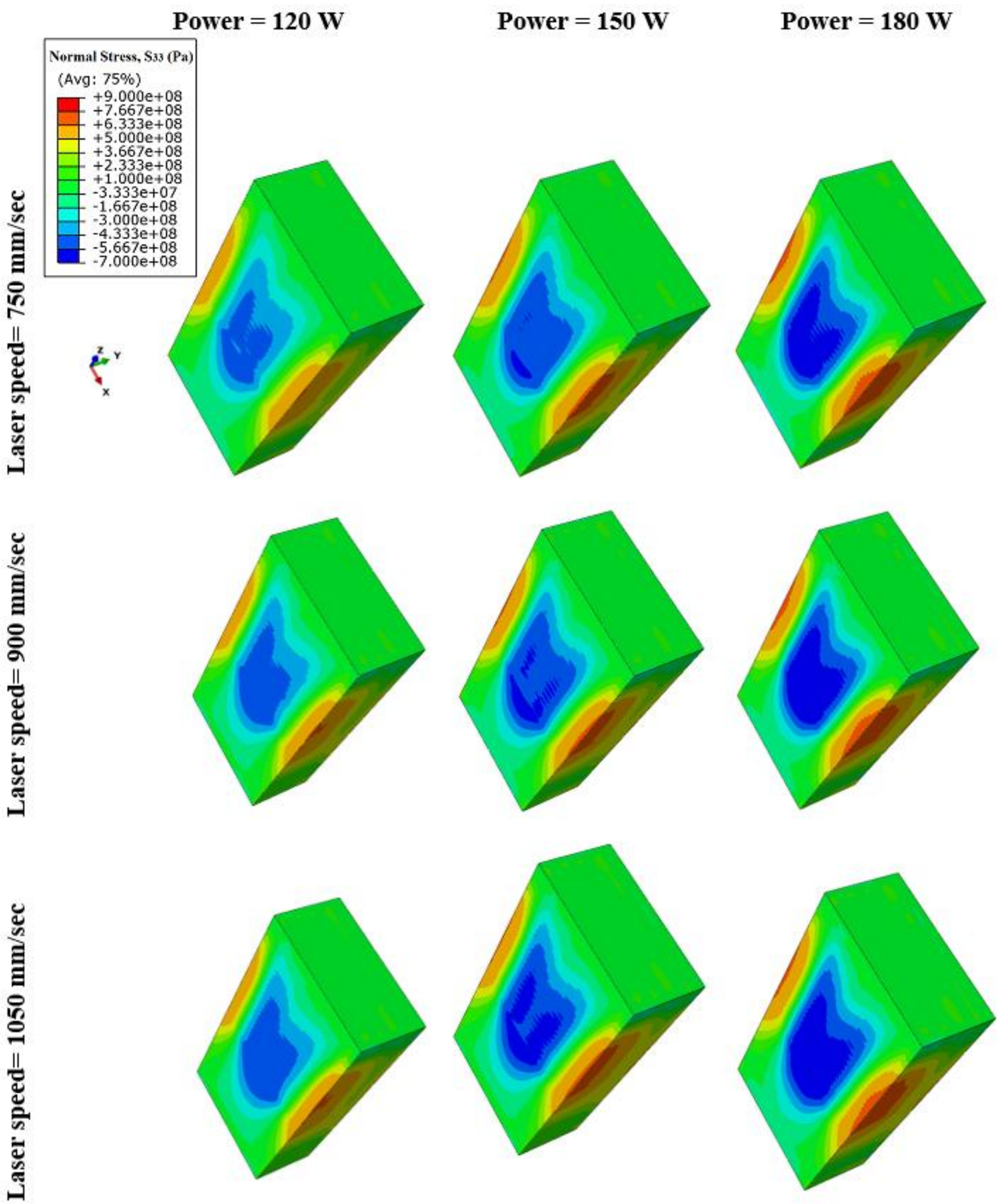

Figure 4.10 S_{33} immediately after printing at different laser speeds and powers on Layer 20. The components are cross sectioned from the XZ plane.

4.2 Results and Discussion of Post-Processing Treatments (HIP and Furnace)

Figure 4.11 provides the FE analysis results of a sample built by LPBF processing by using the FE model developed in the previous stage. The color coding represents the distribution of normal stress (S_{11}) within the material. In this figure, red, yellow, and green colors indicate areas of tensile stress, while blue color indicates areas of compressive stress. Figure 4.11 shows the voids within the material. In this study, two points, A and B, are examined, which are found on the surface of the as-built section shown in this figure. Point A is positioned on the surface of the yz plane, approximately 0.45 mm from the top edge in the z-direction and 0.4 mm from the left edge in the y-direction, directly in front of a void where the stress concentration is higher due to the proximity to this void. In contrast, Point B, also situated on the surface of the yz plane, is 0.05 mm from the top edge in the z-direction and 0.4 mm from the left edge in the y-direction, located far from any voids and, therefore, represents a region less influenced by void-induced stress concentration. Both Points A and B are under initial tensile residual stress.

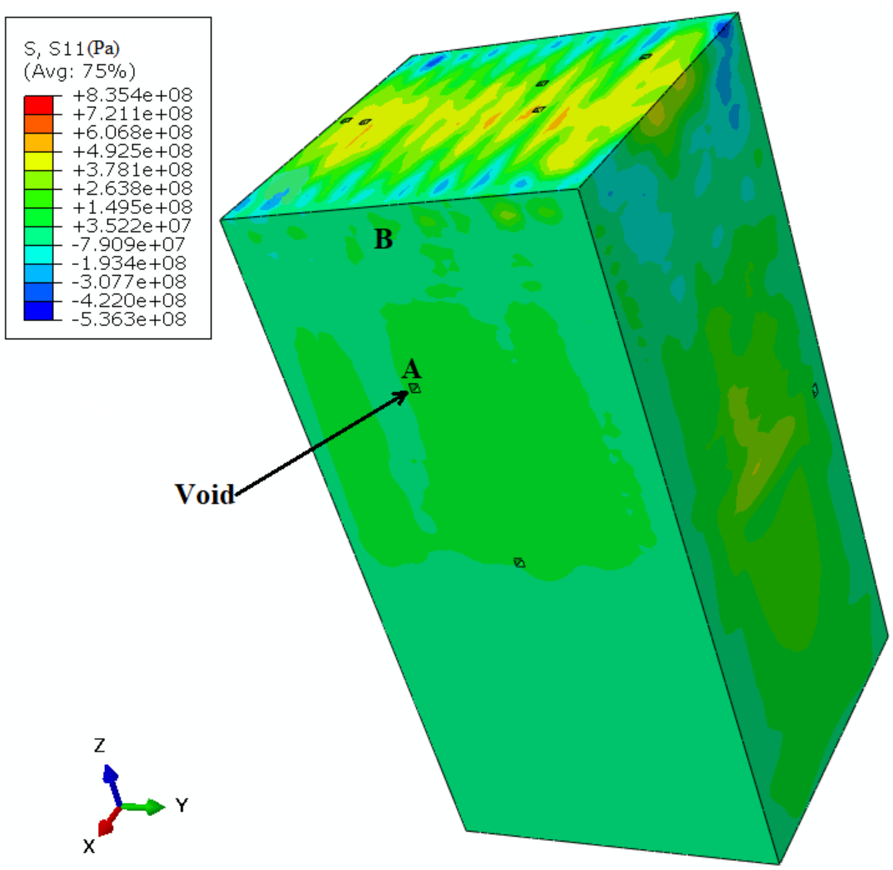

Figure 4.11 Normal stress (S_{11}) distribution of LPBF sample after printing.

4.2.1 Stress Analysis of Furnace Treatment

Figure 4.12 illustrates the changes in the strain over time at two distinct points – A (close to a pore) and B (further away from a pore) – within a material exposed to a temperature of 700°C in a regular furnace. During the heat treatment process, the material undergoes plastic deformation and creep due to prolonged exposure to high temperatures and the presence of initial residual stresses. The figure compares the equivalent CEEQ and equivalent PEEQ at Points A and B. As depicted, CEEQ at both points is significantly higher than PEEQ, thus indicating that creep is the dominant deformation mechanism. During Stage I of the heat treatment, CEEQ exhibits a gradual increase, whereas PEEQ experiences a rapid surge before stabilizing. The FE model results underscore substantial deformation driven primarily by creep, as CEEQ continues to increase until the end of Stage II, after which it stabilizes.

The results also reveal that both CEEQ and PEEQ are higher at Point A compared to Point B. This discrepancy may be attributed to stress concentration around the pore at Point A, as voids within materials typically amplify local stress fields, thereby accelerating deformation mechanisms. Specifically, at Point A, the equivalent CEEQ reaches 2.74%, while the PEEQ stabilizes at approximately 0.28%. In contrast, at Point B, located farther from the pore, the equivalent CEEQ and PEEQ stabilize at 0.16% and 0.078%, respectively. This indicates that materials located farther from voids experience lower strains, likely due to reduced stress concentration. When comparing the two points, the CEEQ at Point A is approximately 1612.5% higher than that at Point B, while the PEEQ (PEEQ) at Point A is about 250% higher than that at Point B. These differences further emphasize the significant influence of stress concentration near pores on both creep and plastic deformation.

Figure 4.13 depicts the equivalent von Mises stress at Points A and B during heat treatment at 700°C in a regular furnace. Initially, the residual stress decreases approximately linearly due to limited plastic deformation, as illustrated in Figure 4.12. This trend corresponds to the linear reduction in yield strength with temperature. As the yield stress decreases during heating, the capacity of the material to sustain elastic deformation diminishes, thus resulting in the transitioning from elastic strain to PEEQ (as the yield stress and Young's modulus decrease with temperature) and a subsequent reduction in residual stresses.

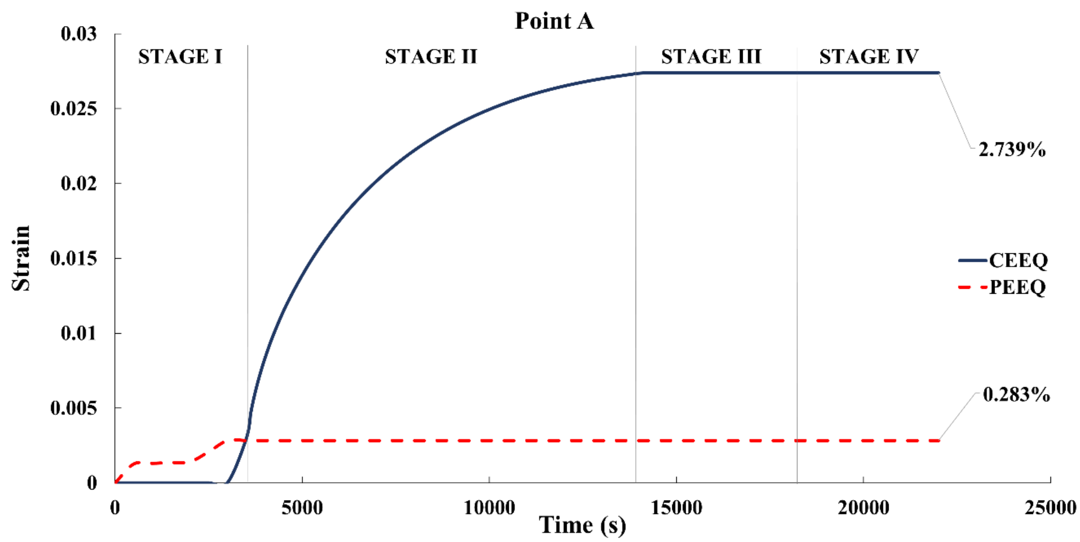

(a)

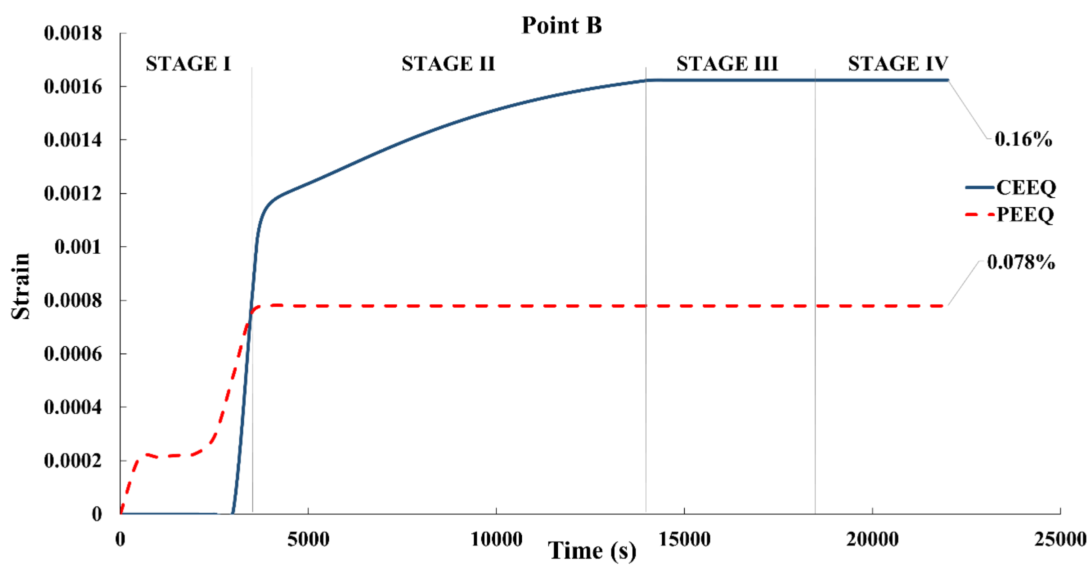

(b)

Figure 4.12 Comparison of CEEQ and PEEQ during heat treatment at 700°C, observed at (a) Point A and (b) Point B, as shown in Figure 4.11.

Approximately halfway through heating, there is a sharp drop in residual stress, which coincides with the rapid accumulation of CEEQ. This observation is consistent with the findings reported by Dong et al.[199], who highlighted the significant role of creep deformation in residual stress reduction during high-temperature processing. During the holding phase of HIP, the reduction in residual stress becomes less pronounced due to the limited development of CEEQ and absence of additional plastic deformation. At Point B, in particular, CEEQ stabilizes more quickly because the driving force for creep (i.e., stress) is significantly reduced following the sharp drop in stress in Stage I. Consequently, the creep process slows down over time, which leads to minimal changes in CEEQ. Since no substantial PEEQ develops during the holding phase, the reduction in residual stress is largely attributed to creep-induced stress relaxation. A comparison of the stress reduction at Points A and B reveals that the von Mises stress near the pore (Point A) decreases from 488 MPa to 118 MPa, while farther from the pore (Point B), the von Mises stress decreases from 414 MPa to 4 MPa. The reduction in residual stress observed under furnace heating aligns closely with the numerical results reported by De Baere et al.[157].

Figure 4.14 illustrates the effect of temperature on PEEQ at Points A and B during heat treatment for different temperatures (500°C, 600°C, and 700°C). Both plots show a rapid increase in the PEEQ during Stage I, followed by a stabilization phase that begins at the end of Stage I. The extent of PEEQ varies significantly between Points A and B. Near a pore (Point A), the plastic deformation reaches approximately 0.28% at 700°C, whereas far from the pore (Point B), it is only 0.078%. This indicates a substantial difference in strain response based on proximity to a pore, with plastic deformation near the pore being roughly three times greater than that farther away at the same temperature. This highlights the significant impact of localized stress concentration in regions close to pores.

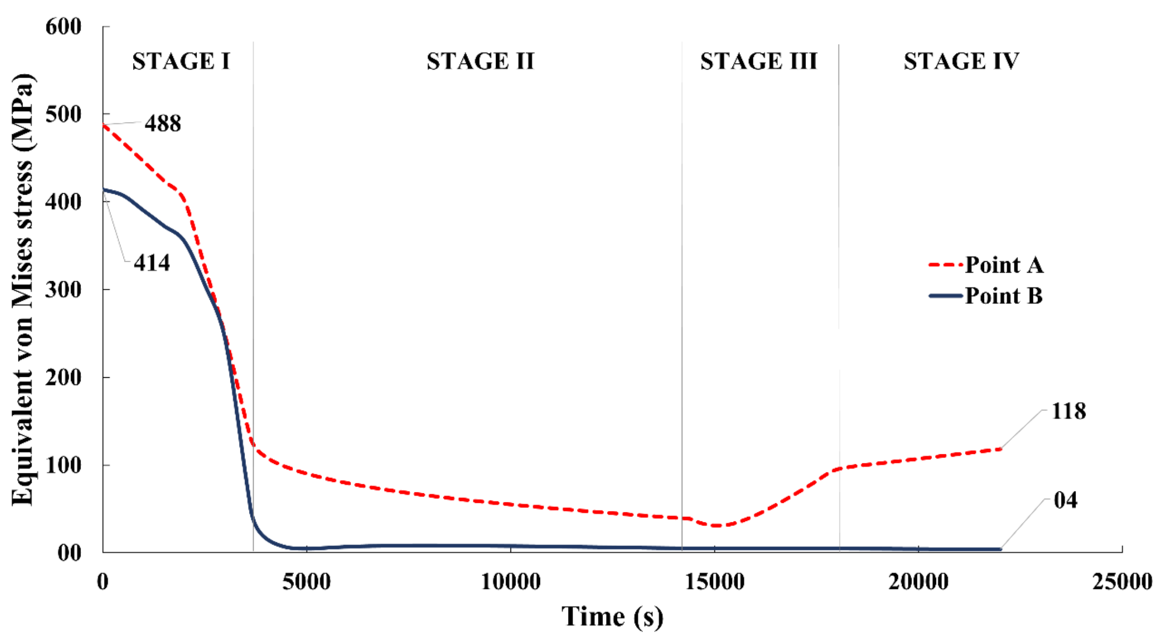

Figure 4.13 Equivalent von Mises stress during heat treatment at 700°C: Points A and B.

Temperature plays a crucial role in the variation of PEEQ. Higher temperatures significantly reduce the yield strength (σ_y) and Young's modulus (E) of the material, thus facilitating greater plastic deformation with lower resistance. The degree of stress relaxation due to the reduction in yield strength and Young's modulus of a material during heating is closely linked to the proportion of elastic strain that transitions into PEEQ. This relationship can be explained through the principles of metal plasticity that was expressed in Equation (3.12). When CEEQ (ε^{cr}) is negligible ($\varepsilon^{cr} = 0$), the total strain (ε) equals the thermal strain (ε^{th}), as any point in the material under uniform heating can freely expand and contract. Consequently, the PEEQ (ε^{pl}) can be derived as:

$$\varepsilon^{pl} = -\varepsilon^{el} = \frac{\sigma_y}{E}\,(\text{Room temperature}) - \frac{\sigma_y}{E}\,(\text{Furnace temperature}) \tag{4.1}$$

The disparity in the ratios of yield stress to Young's modulus at room and elevated temperatures determines the amount of elastic strain that transitions into PEEQ. Greater differences in these ratios allow for more elastic strain to transition to PEEQ, resulting in increased stress relaxation. This mechanism explains the significant enhancement in plastic deformation observed at elevated temperatures, particularly in regions near features that concentrate stress, such as pores.

Figure 4.15 illustrates the evolution of CEEQ during heat treatment in a regular furnace at varying temperatures (500°C, 600°C, and 700°C), highlighting the effect of temperature on creep behavior. The data from Points A (near the pore) and B (far from the pore) show that equivalent CEEQ develops much more slowly and stabilizes at a lower plateau at 500°C and 600°C compared to 700°C, indicating reduced plastic deformation and stress relaxation at lower temperatures. At 700°C, CEEQ becomes significantly more pronounced as materials exposed to elevated temperatures experience enhanced plastic deformation over time due to an increased rate of creep. This occurs because higher temperatures supply more thermal energy, facilitating dislocation movement within the crystal lattice. Consequently, atomic mobility increases, dislocation barriers are lowered, and the material softens, all of which amplify creep deformation.

While the amount of creep is significantly higher near the pore than far from it, the distribution of creep across the stages varies due to the influence of location and localized stress concentrations. At 700°C near the pore (Point A), CEEQ rises gradually during Stage I, followed by a significant increase in Stage II, before stabilizing at approximately 2.74% by the end of the holding time. This indicates that substantial creep deformation primarily occurs during Stage II, as stress redistribution takes longer due to the high localized stress. Conversely, far from the pore (Point B), CEEQ increases rapidly during Stage I and gradually in Stage II, stabilizing at approximately 0.16%. Here, most creep deformation occurs during Stage I, where stress relaxation begins earlier and progresses more quickly due to the absence of concentrated stress and the lower initial stress levels.

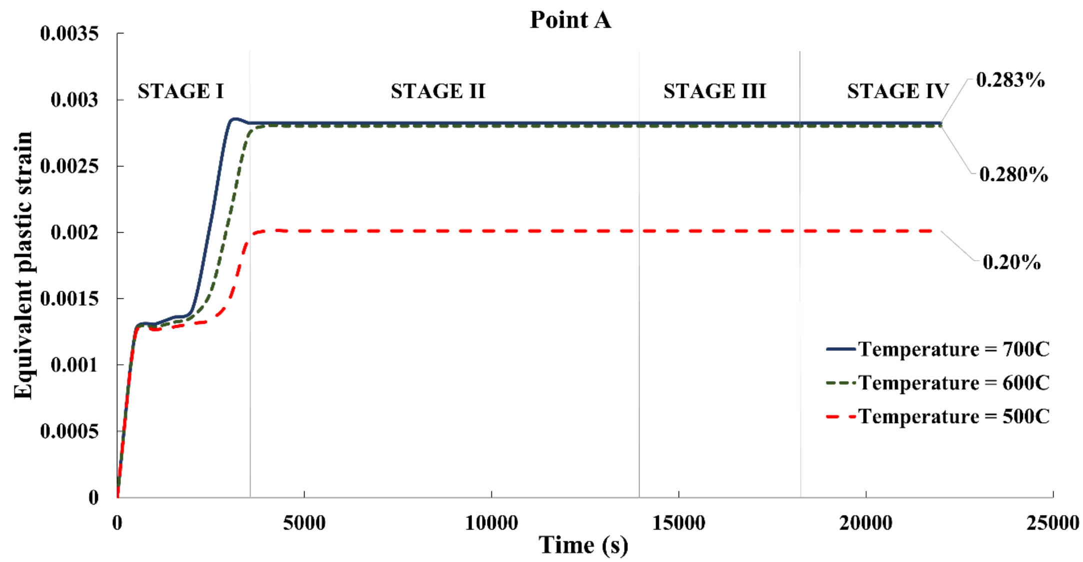

(a)

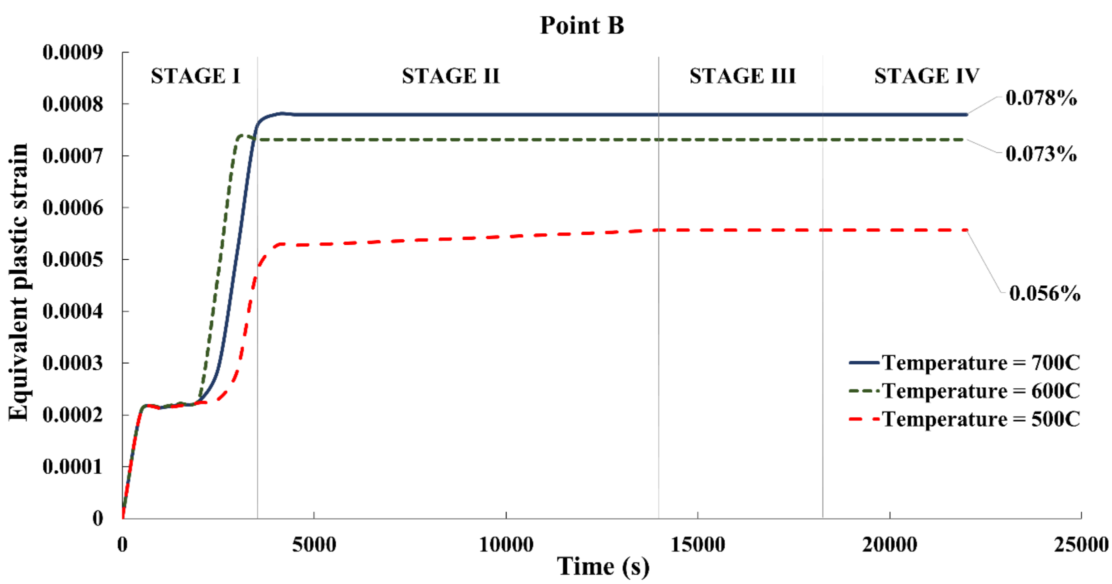

(b)

Figure 4.14 Comparison of PEEQ during heat treatment at points (a) A and (b) B under different temperatures.

The observed difference in behavior between Points A and B can be explained using the hyperbolic-sine creep law, which describes the non-linear relationship between stress, temperature, and creep rate. Near the pore, the local stress concentration is initially very high due to the presence of the void, causing elastic deformation to dominate during the early stage (Stage I). As creep progresses, the localized stress gradually decreases, delaying substantial creep deformation until Stage II, when the material undergoes a more prolonged relaxation process. In contrast, far from the pore (Point B), the initial stress levels are lower and more uniform, leading to a rapid onset of creep during Stage I, where stress relaxation occurs earlier and more quickly.

Figure 4.16 illustrates the variation in equivalent von Mises stress at points A and B during heat treatment under different temperature conditions (500°C, 600°C, and 700°C). The von Mises stress is a key measure of the ability of the material to sustain loads, and its reduction indicates stress relaxation caused by plastic deformation and creep. The trends in Figure 4.16 align well with the observations from Figures 4.14 and 4.15, where higher temperatures led to greater PEEQ and CEEQ.

At the onset of heat treatment, both points A and B show a sharp drop in von Mises stress, which reflects the material's immediate stress relaxation due to rapid plastic deformation. This initial behavior can be attributed to the high rate of PEEQ development observed in Figure 4.14 during Stage I, as well as the slight contribution of the creep mechanism outlined in Figure 4.15. The decline in stress is more pronounced at higher temperatures, as the material's yield strength and Young's modulus decrease significantly with temperature, increasing the proportion of elastic strain that transitions into PEEQ. Elevated temperatures also enhance atomic mobility and dislocation movement, facilitating stress relief.

At lower temperatures (500°C and 600°C), the von Mises stress stabilizes at higher levels compared to 700°C. For point A, stabilization occurs at approximately 305 MPa (500°C) and 190 MPa (600°C), whereas for point B, the values are around 383 MPa (500°C) and 257 MPa (600°C). These higher residual stress levels indicate that plastic deformation and creep are less effective at lower temperatures due to limited atomic mobility, reduced dislocation motion, and a smaller proportion of elastic strain converting to plastic deformation, as described in Figures 4.14 and 4.15. At 700°C, the von Mises stress stabilizes at significantly lower levels: 118 MPa at point A and 4 MPa at point B. This significant reduction in stress reflects the enhanced plastic deformation and CEEQ observed at this temperature. Near the pore (Point A), stress redistribution occurs more gradually, as CEEQ primarily develops during Stage II (Figure 4.15). Far from the pore (Point B), the stress stabilizes earlier due to rapid stress relaxation during Stage I, consistent with the observations of PEEQ and CEEQ in Figures 4.14 and 4.15.

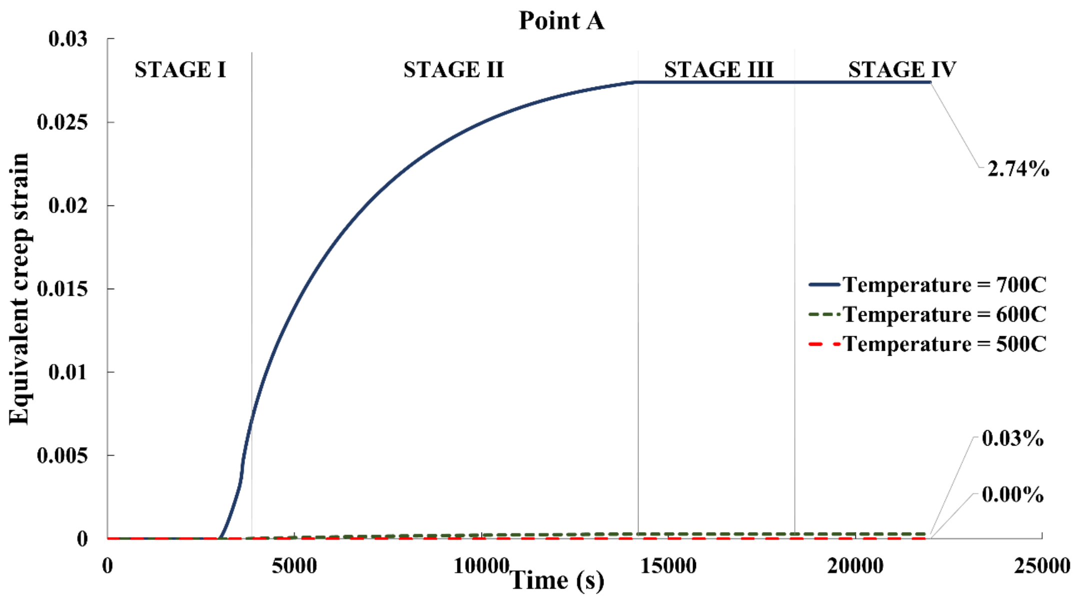

(a)

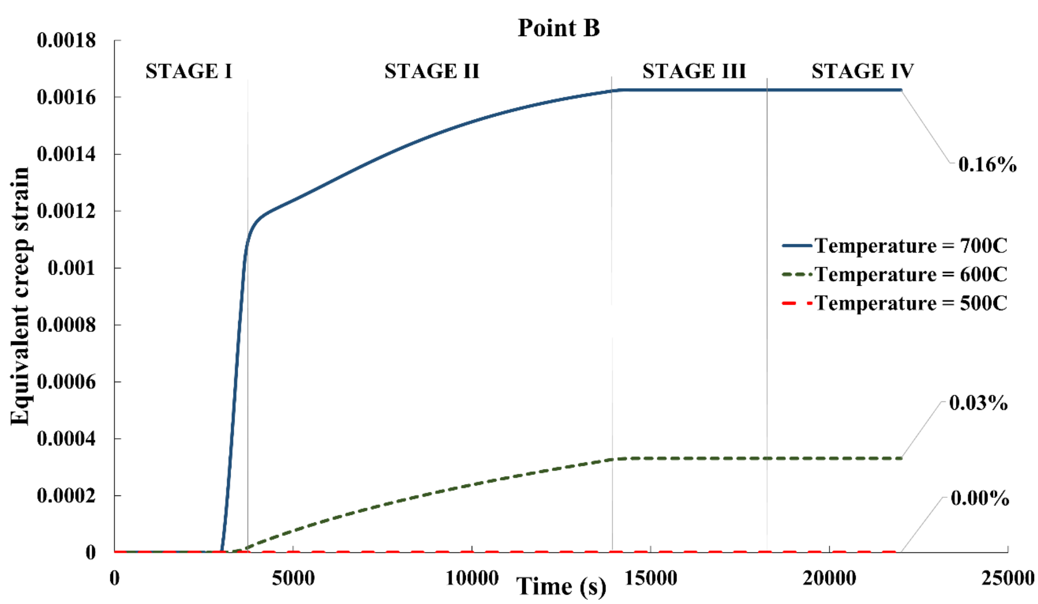

(b)

Figure 4.15 Comparison of CEEQ during heat treatment at points (a) A and (b) B under different temperatures.

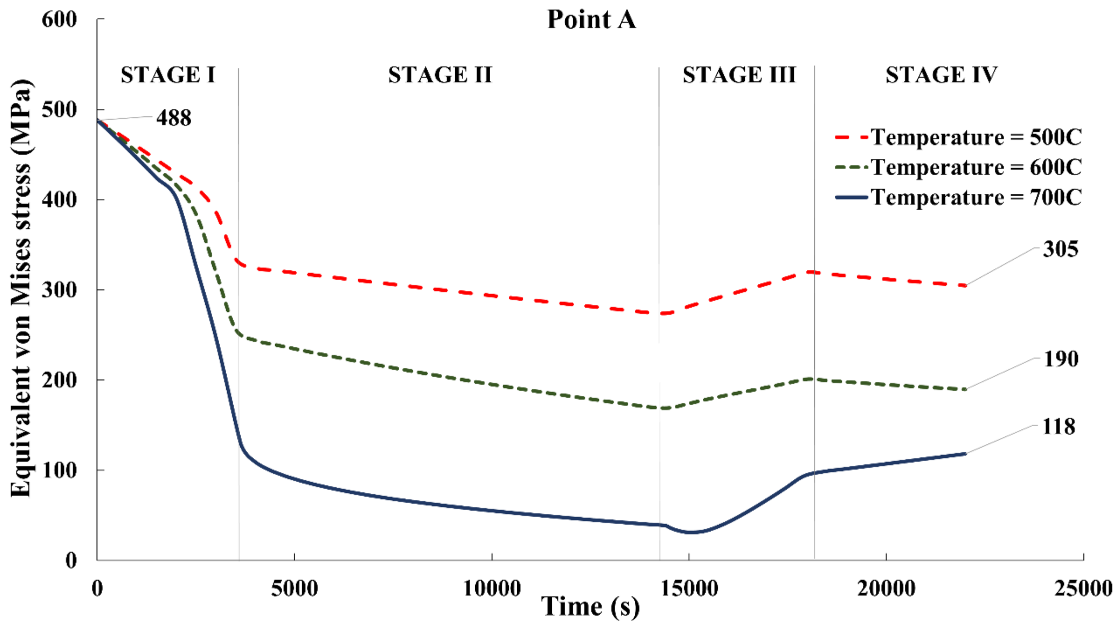

(a)

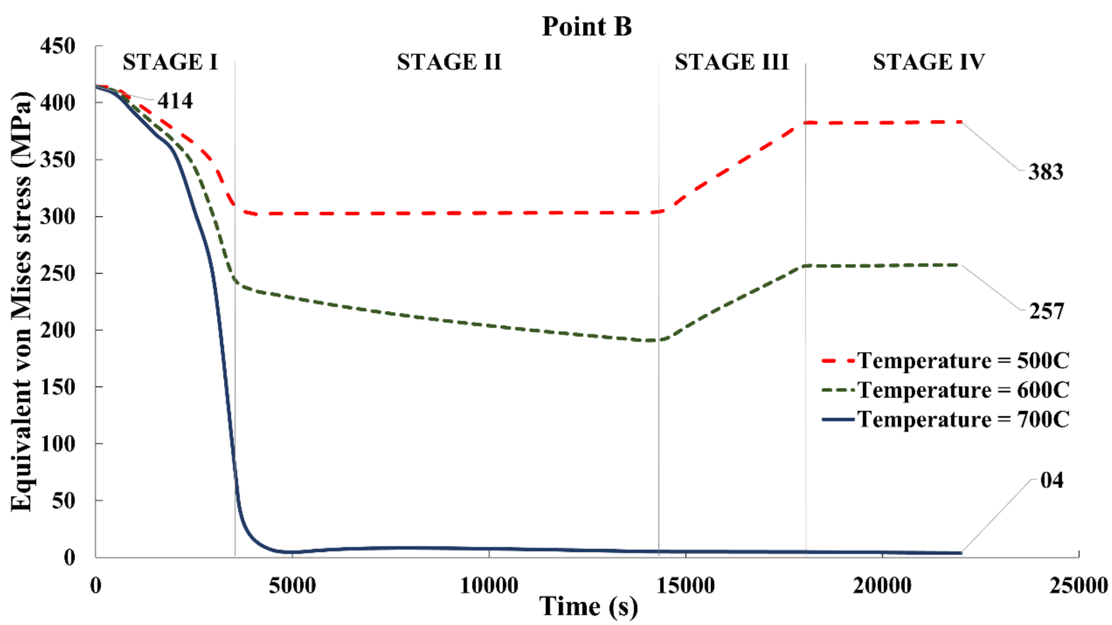

(b)

Figure 4.16 Comparison of equivalent von Mises stress during heat treatment at points (a) A and (b) B under different temperatures.

A notable difference at 700°C is the behavior of stress at the end of the holding stage (14,400 s). At Point B, the stress remains stable, while at Point A, a slight increase in stress is observed. This difference can be attributed to the localized stress concentrations near the pore at Point A, which may induce localized strain hardening after significant creep deformation in Stage II. In contrast, at Point B, the absence of such stress concentrations allows for continuous stress relaxation without any subsequent increase.

4.2.2 Stress Analysis under HIP

Figure 4.17 illustrates the evolution of CEEQ and PEEQ at Points A and B under HIP condition at 700°C and 100 MPa pressure. These results underscore the critical role of hydrostatic pressure in enhancing both creep and plastic deformation in additively manufactured materials. At Point A, which is near the pore, the CEEQ reaches 4.24%, indicating a significant increase in CEEQ compared to conditions without applied hydrostatic pressure. This represents a 55% enhancement in CEEQ compared to regular furnace heating. The PEEQ stabilizes at 0.34%, marking a 20% increase in plastic deformation compared to furnace conditions. The increase in strain near the pore is attributed to the amplified stress concentration caused by porosities, which act as stress raisers under hydrostatic pressure. These localized stress gradients generate shear stresses that promote dislocation motion, driving creep and plastic deformation. The large difference between CEEQ and PEEQ indicates that the dominant role of dislocation creep as the primary mechanism of deformation under HIP conditions. At Point B, located farther from the pore, the trends are similar, but the magnitudes are significantly lower due to reduced stress concentrations far from the pore. The CEEQ stabilizes at 0.25%, showing a 56.25% increase compared to furnace heating, while the PEEQ stabilizes at 0.08%, with negligible change. The smaller enhancement in PEEQ at Point B reflects the reduced stress concentration in regions far from porosities. However, the increase in CEEQ indicates that hydrostatic pressure still promotes significant deformation, even in areas with lower initial stress concentrations.

The presence of porosities in the material leads to non-uniform stress distribution under HIP conditions, with stress intensification around defects due to their irregular shapes. These elevated stress levels, coupled with high temperatures that reduce the material's yield strength, create stress gradients that drive plastic flow into voids. This process effectively closes voids and facilitates the relaxation of residual stresses. The summarized information for these findings is presented in Table 4.1 for ease of comparison and interpretation.

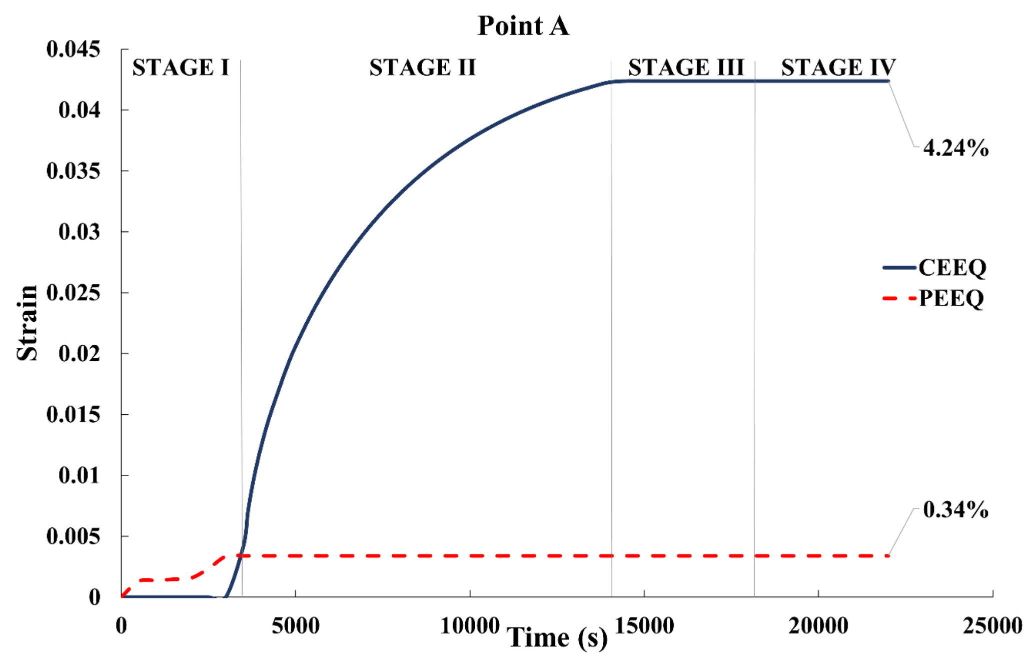

(a)

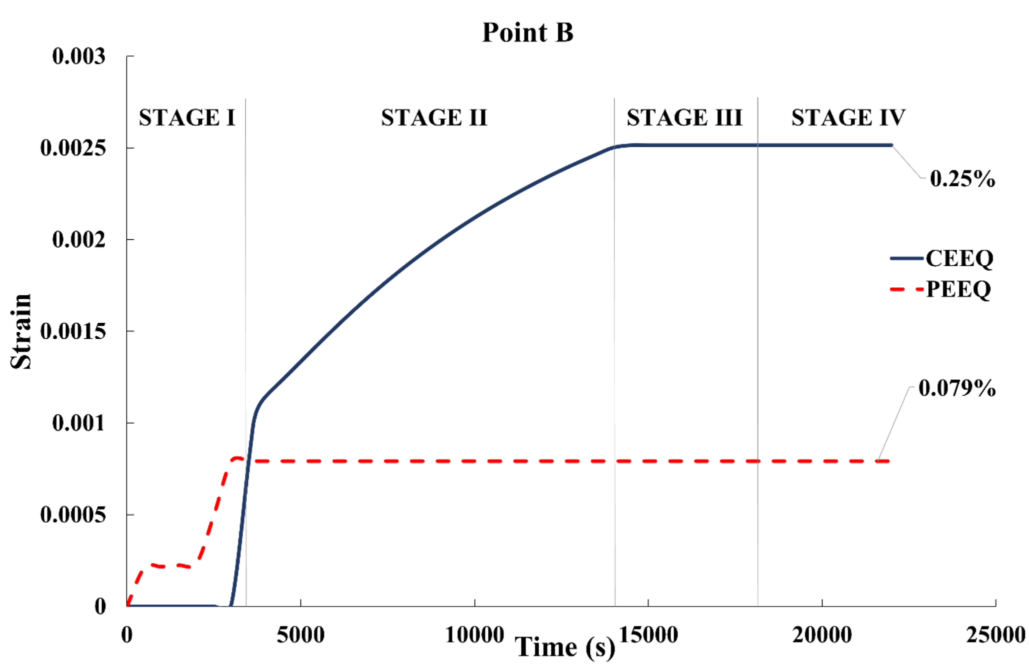

(b)

Figure 4.17 Comparison of CEEQ and PEEQ during HIP at 700°C and 100 MPa pressure, observed at (a) Point A and (b) Point B, as described in Figure 4.11.

Table 4.1 Comparison of CEEQ and PEEQ between furnace and HIP conditions

Point	**Condition**	**CEEQ (%)**	**PEEQ (%)**	**CEEQ Increase (%)**	**PEEQ Increase (%)**
A	Furnace	2.74	0.28	-	-
A	HIP (100 MPa)	4.24	0.34	54.82	20.14
B	Furnace	0.16	0.078	-	-
B	HIP (100 MPa)	0.25	0.079	56.25	1.27

Figure 4.18 illustrates the equivalent von Mises stress at Points A and B during HIP at a temperature of 700°C and an applied hydrostatic pressure of 100 MPa. The von Mises stress reduction during HIP is driven by the combined effects of creep and plastic deformation, which are enhanced under the synergistic action of elevated temperature and hydrostatic pressure. At the beginning of the HIP process (Stage I), both points exhibit a linear decline in von Mises stress, with greater reductions compared to the furnace condition. This reduction corresponds to the linear reduction in yield strength with temperature and mirrors the development of more plastic deformation intensified by hydrostatic pressure, as observed in Figure 4.17. By comparing PEEQ under furnace conditions (Figure 4.12) and HIP conditions (Figure 4.17), there is a 20.14% increase in PEEQ at Point A and a 1.27% increase at Point B. Approximately halfway through the heating phase, there is a sharp drop in residual stress, which coincides with the rapid accumulation of CEEQ, with creep playing a dominant role. By comparing CEEQ under furnace conditions (Figure 4.12) and HIP conditions (Figure 4.17), there is a 54.82% increase in CEEQ at Point A and a 56.25% increase at Point B. The greater plastic deformation and creep during the heating stage of HIP (Stage I) compared to furnace conditions is because they are intensified by the hydrostatic pressure. Hydrostatic pressure generates more stress gradients around the pores, which in turn generate more shear stress, the main cause of increased plastic deformation and creep.

During the holding stage (Stage II), the reduction in von Mises stress continues, but at a slower rate, particularly at Point A. The slower stress relaxation is attributed to the saturation of creep and plastic deformation mechanisms due to the limited development of CEEQ and the absence of additional plastic deformation. At Point B, in particular, CEEQ stabilizes faster because the driving force for creep (i.e., stress) is significantly reduced following the sharp stress drop in Stage I. At the end of Stage II, the stress at Point A stabilizes at 92 MPa, while Point B shows minimal residual stress of 3 MPa, highlighting the pronounced effect of hydrostatic pressure on stress homogenization. The stabilization during the later stages reflects the diminishing driving force for further creep as the residual stress is reduced.

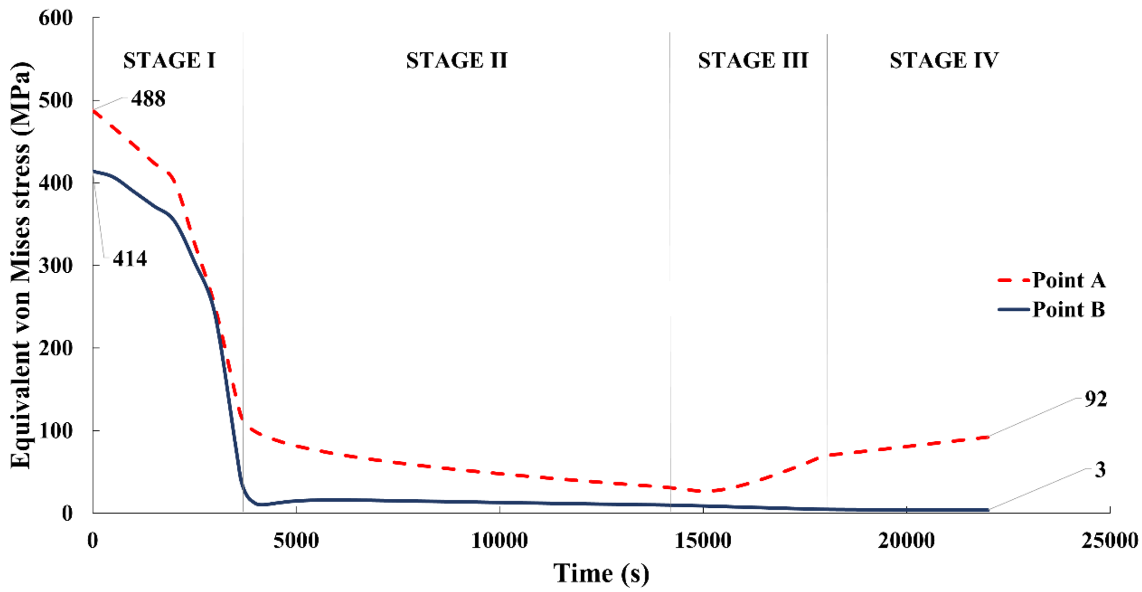

Figure 4.18 Equivalent von Mises stress during HIP at 700°C and 100 MPa pressure at points A and B.

Comparing Figure 4.18 (HIP) with Figure 4.13 (Furnace Heating) reveals the critical role of hydrostatic pressure in accelerating stress relaxation. Under furnace conditions, the stress reduction at Point A (near the pore) was limited to 118 MPa, and at Point B, it was 4 MPa. However, the application of pressure in HIP led to further stress relaxation, reducing the stress to 92 MPa at Point A and virtually eliminating it at Point B (3 MPa). This comparison demonstrates that the additional driving force provided by pressure in HIP is essential for enhanced plastic deformation and creep, resulting in more effective stress relaxation.

Table 4.2 compares the von Mises stress at Points A and B under furnace heating and HIP conditions. The comparison shows that HIP can enhance stress relaxation. Under furnace heating, the von Mises stress is decreased by 370 MPa, or a 75.82% reduction. During HIP, the stress reduction is increased to 396 MPa (81.15% reduction), thus demonstrating the added effect of hydrostatic pressure in facilitating stress relaxation and plastic deformation. The additional 6% reduction near the pore is attributed to the intensified stress gradients generated by hydrostatic pressure, which enhances dislocation movement and material flow into voids. At Point B, the von Mises stress under furnace heating is reduced by 410 MPa (99.04% reduction). During HIP, this reduction is slightly increased to 411 MPa (99.28% reduction). Although the change is smaller compared to Point A, it highlights the effectiveness of hydrostatic pressure in achieving near-complete stress relaxation even in regions with minimal initial stress concentrations.

The data in Table 4.2 underscore that hydrostatic pressure is a critical factor in enhancing both plastic deformation and creep, particularly in regions near defects. The elevated stress levels around porosities, combined with the applied hydrostatic pressure, generate significant shear stresses that accelerate dislocation movement. This process allows the material to flow into voids and close them effectively, which is not achievable with furnace heating alone. At Point B, the uniform stress distribution during HIP further facilitates near-complete stress relaxation, thus leading to exceptional material properties.

Table 4.2 Comparison of von Mises stress: furnace vs. HIP conditions

Point	Condition	Initial Stress (MPa)	Final Stress (MPa)	Stress Reduction (MPa)	Percentage of Reduction (%)
A	Furnace	488	118	370	75.82
A	HIP (100 MPa)	488	92	396	81.15
B	Furnace	414	4	410	99.04
B	HIP (100 MPa)	414	3	411	99.28

Plastic deformation drives stress relaxation. Both the experimental data reported in the literature and the FE simulations performed in the present study demonstrate that voids close during HIP but remain intact after conventional furnace heating. This comparison indicates that the hydrostatic pressure applied during HIP generates greater plastic deformation and, consequently, more effective residual stress relaxation. This trend agrees with the observations of Atabay et al.[200], who did not find pore closure in furnace-treated laser powder bed fused Inconel 718, and Osman et al.[201], who showed that standalone heat treatments applied after LPBF processing do not change the porosity. Song et al.[108] reported contradictory experimental findings and suggested that these discrepancies could be related to experimental sampling limitations in correlative imaging. They recommended μCT scanning of the exact same region of interest before (as-built) and after heat treatment. Unlike in a regular furnace where the amount of creep and plastic deformation are not sufficient to close voids in additively manufactured materials, the application of hydrostatic pressure during HIP introduces an additional driving force to enhance both mechanisms. The enhanced plastic deformation and creep in the HIP-treated sample are driven by the increased equivalent stress that acts on the material. The hydrostatic pressure intensifies the local stress gradients, thereby increasing shear stress, enhancing dislocation mobility, and promoting material flow into the voids. This effectiveness of HIP in closing internal voids was demonstrated in an experimental study by Atabay et al.[202] where an X-ray micro-CT distinctly revealed a wide array of internal gas pores remnant in both horizontally- and vertically-built LPBF processed samples and their absence in these parts after post-processing with a combination of high temperature and hydrostatic pressure.

The closure of voids results in the redistribution and relaxation of the residual stresses, as shown in Figure 4.19. This figure compares the pore morphology of a HIP-treated sample to that of a furnace-heated sample at Point A. The HIP-treated sample shows significant transformations in pore shape, thus reflecting the combined effects of high temperature and hydrostatic pressure. Under HIP conditions, the initial flat surface of the micropore transforms into a convex shape as the material flows into the void due to creep and plastic deformation. FE simulations show that pore closure begins during Stage I, accelerates during Stage II, and is completed by the end of Stage II. During Stage III or the temperature and hydrostatic pressure reduction stage, the closed pore retains its shape without further changes. The FE modeling results, particularly regarding pore closure during HIP, align well with the findings reported by Cegan et al.[139], Fryé et al.[203], Hirata et al.[204], Nudelis and Mayr[135], and Plessis et al.[205]. In contrast, the furnace-heated sample shows minimal changes in pore morphology, as the absence of hydrostatic pressure limits the ability of the material to deform and fill the void. This behavior is also consistent with the observations reported by Cegan et al.[139].

Figure 4.20 compares the changes of the PEEQ at Points A and B under varying hydrostatic pressure conditions with pressures of 0 MPa (furnace), 100 MPa, and 200 MPa. At Point A, the PEEQ increases with pressure, and stabilizes at 0.28%, 0.34%, and 0.55% for furnace, 100 MPa, and 200 MPa, respectively. The addition of pressure enhances plastic deformation, as higher equivalent stress enables more plastic deformation. At Point B, the effect of hydrostatic pressure is less pronounced, as indicated by very low change in PEEQ from 0.078% (furnace) to 0.079% (100 MPa) and 0.082% (200 MPa). This shows that plastic deformation is more sensitive to pressure near pores, where localized stress concentrations have more impact.

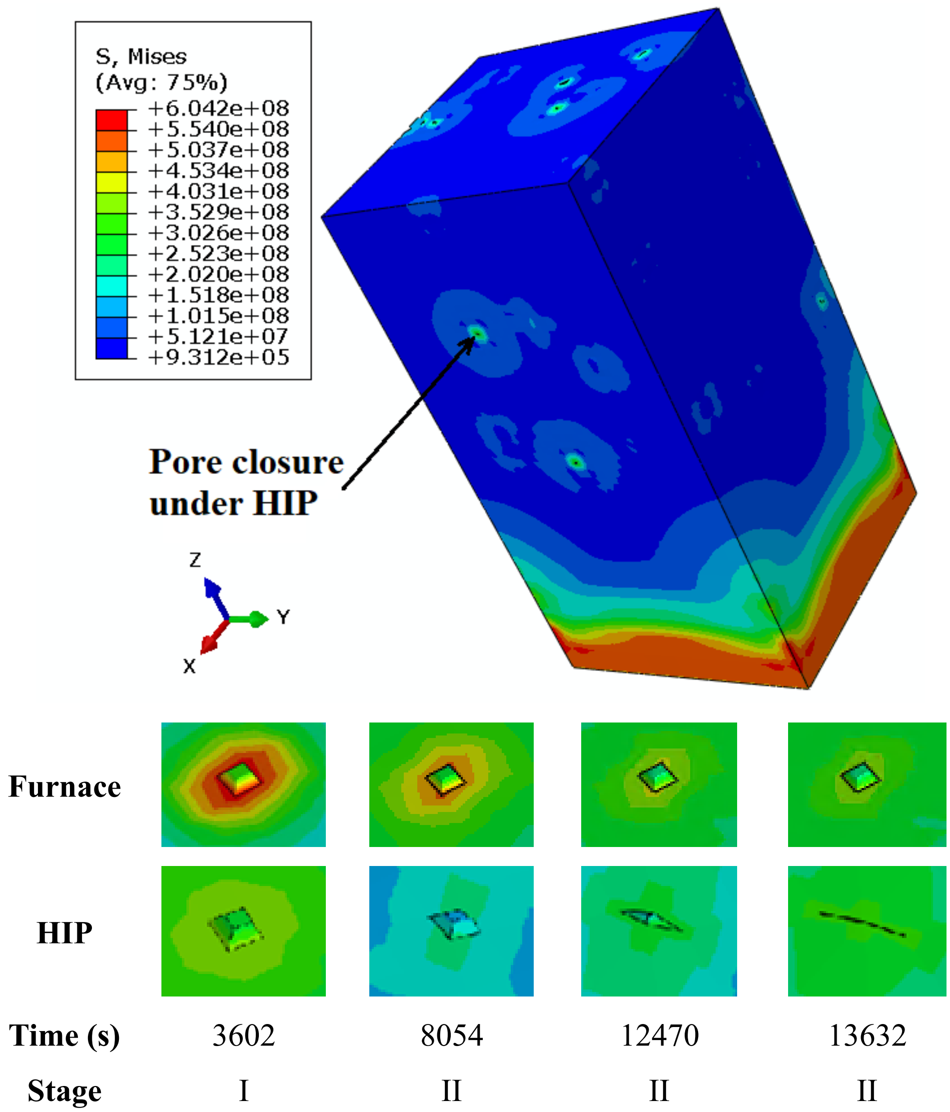

Figure 4.19 Pore morphology changes of HIP-treated sample (200 MPa, 700°C) compared to furnace-heated sample (700°C).

Figure 4.21 illustrates the changes in the CEEQ at Points A and B under varying hydrostatic pressure conditions at a temperature of 700°C. The results show that pressure during HIP accelerates creep deformation at both locations. At Point A, the CEEQ significantly increases with increasing pressure, and stabilizes at 2.74% (furnace), 4.24% (100 MPa), and 5.89% (200 MPa). This substantial increase highlights the role of hydrostatic pressure in enhancing creep, as higher equivalent stress generated by pressure reduces the energy barriers for dislocation movement, thereby accelerating dislocation activity. This process assists in the closure of defects, which results in a denser material. The resulting densification alleviates stress concentration around defects, thus enabling a more uniform stress distribution and reducing the residual stress. At Point B, the CEEQ also increases with pressure but to a lesser extent, and stabilizes at 0.16% (furnace), 0.25% (100 MPa), and 0.43% (200 MPa). These results indicate that although creep deformation is less pronounced with distance from the pores, the addition of hydrostatic pressure still promotes deformation. The observations align with the hyperbolic-sine creep law, which describes the non-linear dependence of creep rate on stress. These findings are consistent with those reported in previous experimental and numerical studies. For example, Prasad et al.[97] and Tammas-Williams et al.[100] demonstrated that increasing the applied hydrostatic pressure during HIP promotes pore closure and enhances porosity reduction. Similar trends have also been reported in other studies[135,137,139,167,206,207].

The von Mises stress reduction at Points A and B is shown under three conditions: furnace heating (0 MPa), HIP at 100 MPa, and HIP at 200 MPa. The results highlight the critical role of hydrostatic pressure in accelerating stress relaxation through the mechanisms of creep and plastic deformation. At Point A, near the pore, the initial von Mises stress starts at 488 MPa. Under furnace conditions, the stress is reduced to 118 MPa. However, when hydrostatic pressure is applied, the stress is further reduced to 92 MPa at 100 MPa and 66 MPa at 200 MPa. This reduction corresponds to a 22.03% improvement in stress relaxation at 100 MPa compared to the furnace condition, and a 44.06% improvement at 200 MPa. The pronounced effect of hydrostatic pressure at Point A is attributed to localized stress concentration around the pore. The application of hydrostatic pressure amplifies the stress gradients and enhances both plastic deformation and creep, thus leading to significant material flow into the voids.

At Point B, which is farther from the pore, the initial stress starts at 414 MPa. Under furnace heating, the von Mises stress is reduced to 4.03 MPa. With the application of hydrostatic pressure, the stress is further reduced to 3.83 MPa at 100 MPa and to 3.29 MPa at 200 MPa. These reductions represent a 4.96% decrease at 100 MPa and an 18.35% decrease at 200 MPa compared to the furnace condition. Although the overall stress reduction is less dramatic at Point B compared to

Point A, it shows the homogenizing effect of pressure in regions farther from stress concentrations. The nearly complete relaxation at Point B reflects the uniform stress distribution promoted by hydrostatic pressure. A summary of the von Mises stress reduction at Points A and B under varying pressure conditions is provided in Table 4.3.

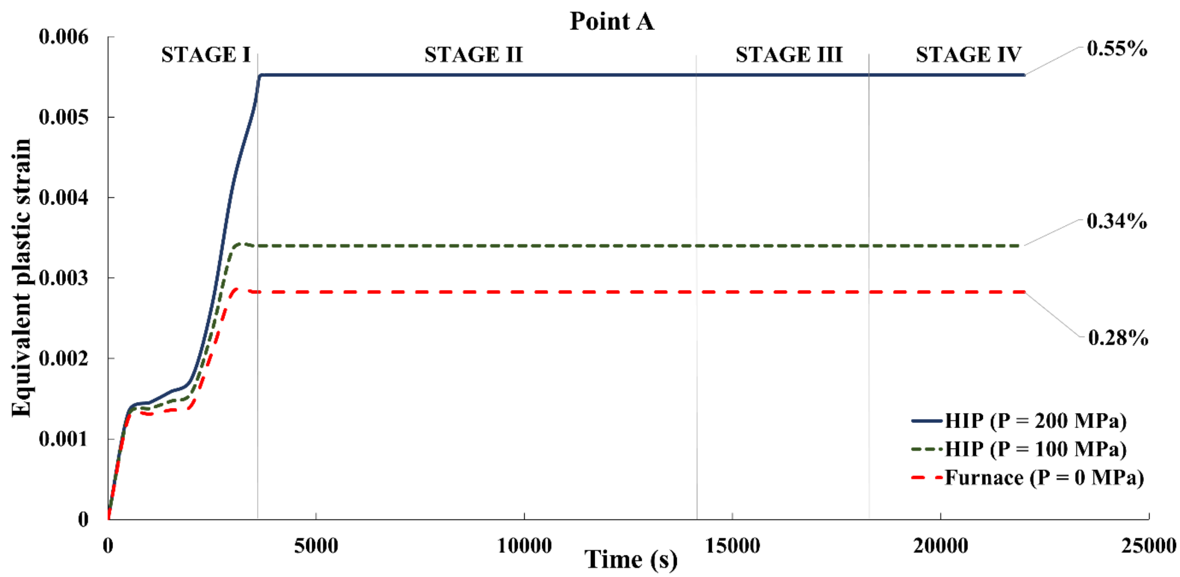

(a)

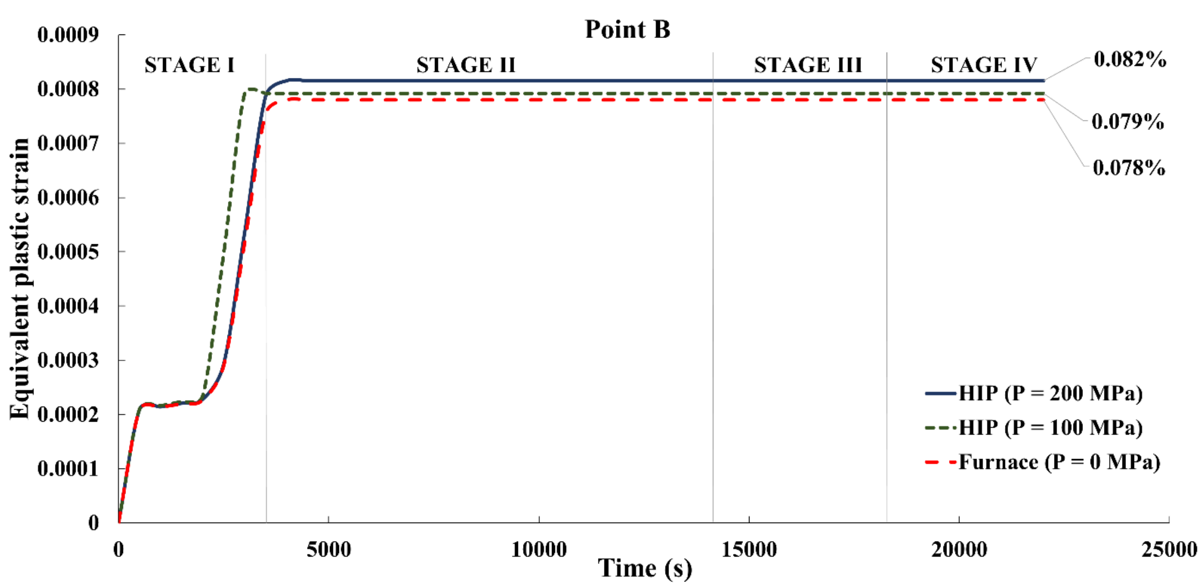

(b)

Figure 4.20 Comparison of PEEQ during HIP at 700°C at Points (a) A and (b) B under varying pressure conditions.

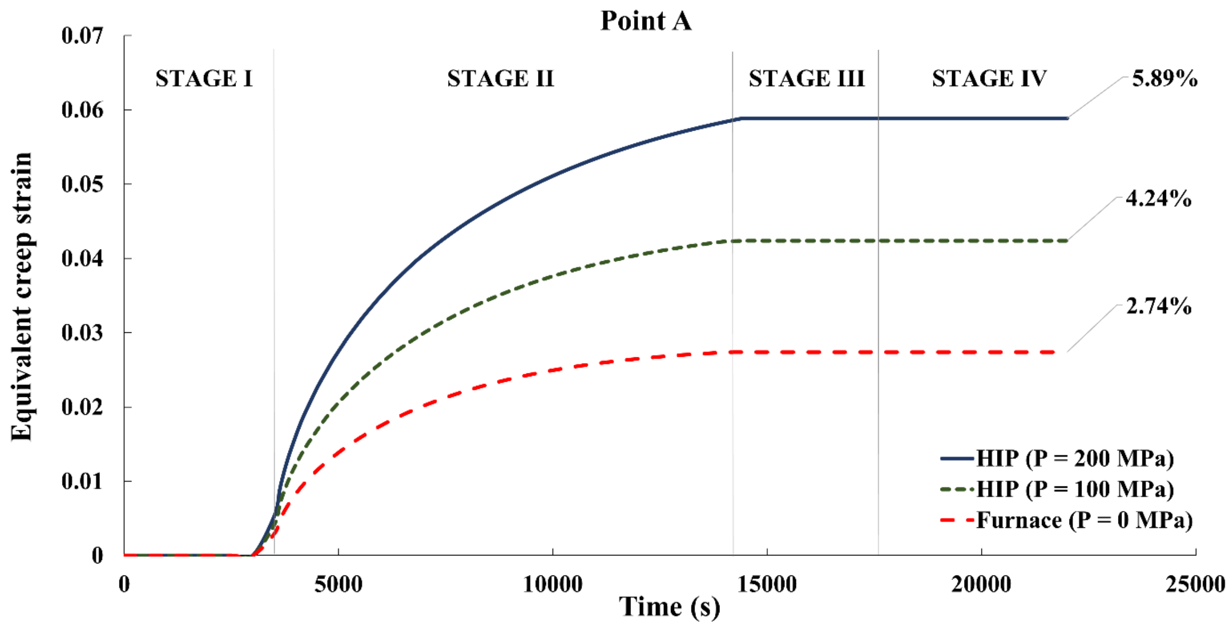

(a)

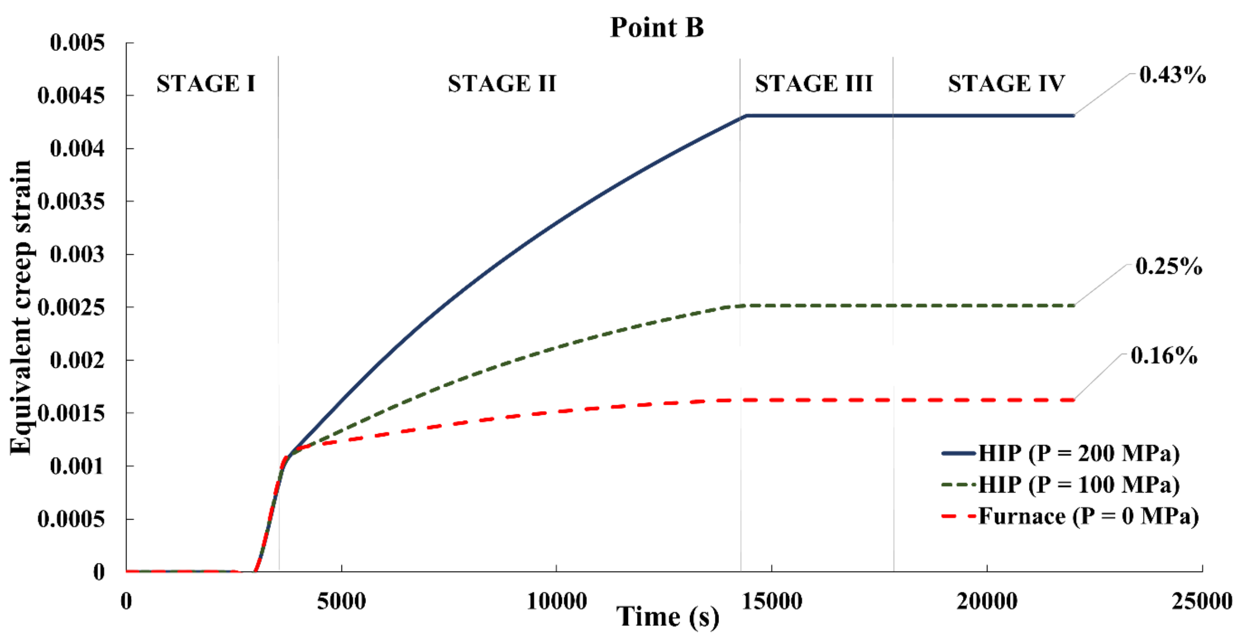

(b)

Figure 4.21 Comparison of CEEQ during HIP at 700°C at Points (a) A and (b) B under varying pressure conditions.

Table 4.3 Comparison of von Mises stress reduction at Points A and B under different pressure conditions

Point	Condition	Initial Stress (MPa)	Final Stress (MPa)	Improvement Over Furnace (%)
A	**Furnace**	488	118	-
A	**HIP (100 MPa)**	488	92	22.03
A	**HIP (200 MPa)**	488	66	44.06
B	**Furnace**	414	4.03	-
B	**HIP (100 MPa)**	414	3.83	4.69
B	**HIP (200 MPa)**	414	3.29	18.35

Figure 4.22 illustrates the evolution of PEEQ at Points A and B under HIP conditions with a pressure of 200 MPa, comparing three temperatures: 500°C, 600°C, and 700°C. At Point A, the PEEQ increases significantly as the temperature rises. At 500°C, the PEEQ stabilizes at 0.29%, at 600°C, 0.45% and at 700°C, 0.55%. This indicates that higher temperatures enhance plastic deformation by lowering the yield strength, which facilitates material flow into voids. At Point B, the PEEQ exhibits similar behavior, with stabilization values of 0.05% at 500°C, 0.07% at 600°C, and 0.08% at 700°C. Although the absolute values are smaller compared to Point A, the trends suggest that the temperature dependence of plastic deformation remains consistent. The differences between Points A and B are primarily due to stress concentration near the pore at Point A, which amplifies local deformation mechanisms. The observed trend across different temperatures confirms that the mechanism of plastic deformation under HIP is driven by temperature-dependent reduction in yield strength and stress gradient effects. The higher plastic deformation at elevated temperatures highlights the synergy between temperature and hydrostatic pressure in closing voids.

Figure 4.23 shows the development of CEEQ at Points A and B under the same HIP conditions and temperatures as in Figure 4.22. At Point A, the CEEQ increases significantly with temperature, and then stabilizes at negligible levels at 500°C, 0.29% at 600°C, and 5.89% at 700°C. The pronounced increase at 700°C indicates that higher thermal energy enhances dislocation mobility, which leads to accelerated creep deformation. At Point B, the CEEQ follows a similar pattern, with stabilization values of negligible levels at 500°C, 0.30% at 600°C, and

0.43% at 700°C. The lower CEEQ at Point B reflects the absence of stress concentration, which limits localized deformation compared to Point A. The results show that the creep mechanism during HIP is temperature-dependent, with higher temperatures driving more significant strain. This observation supports the conclusion that creep plays a dominant role in void closure during HIP, particularly at elevated temperatures.

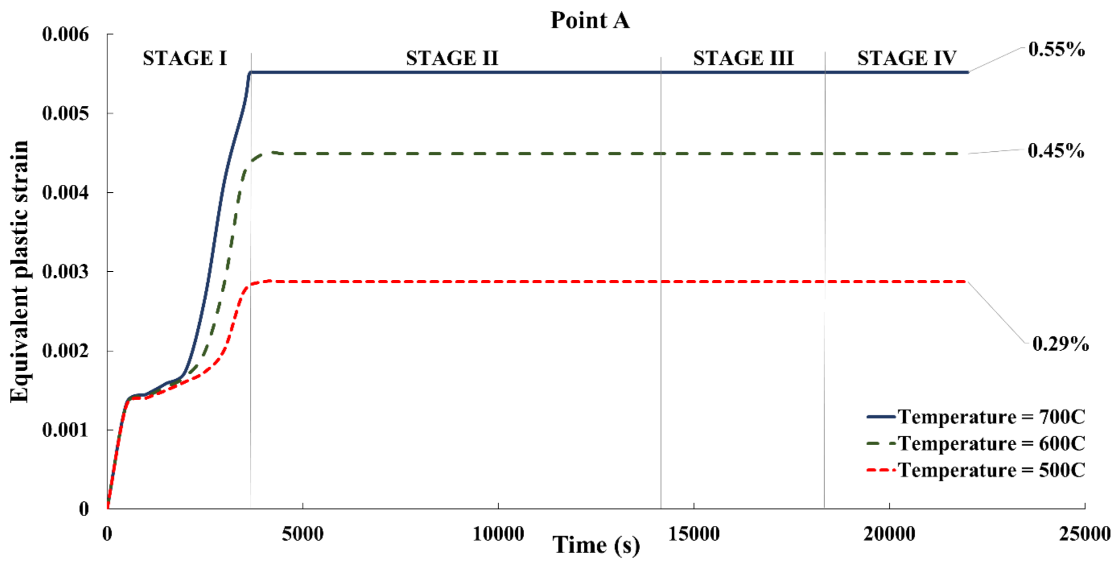

(a)

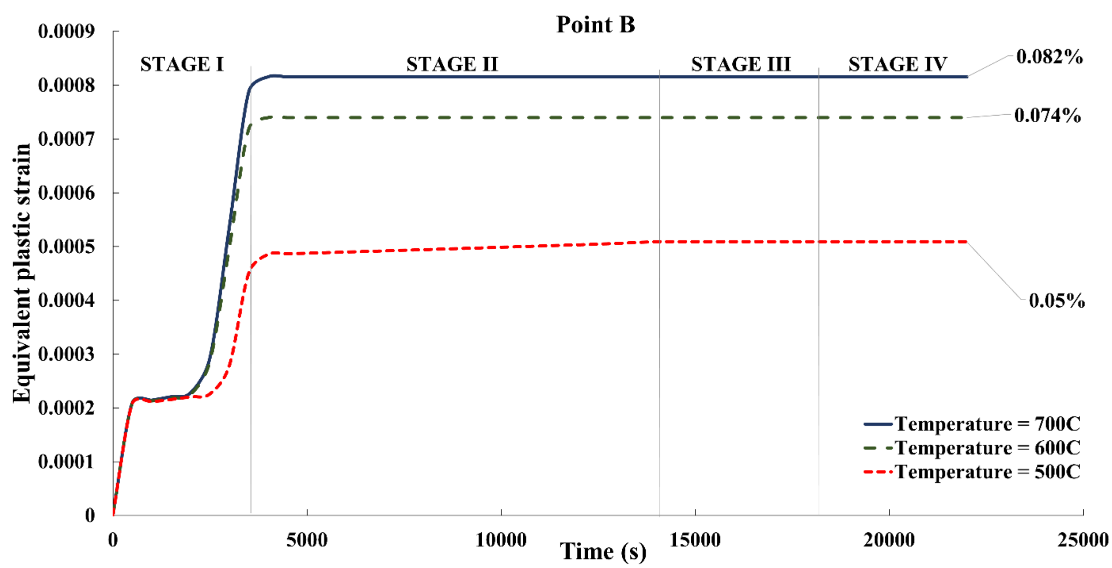

(b)

Figure 4.22 Comparison of equivalent plastic strain during HIP at 200 MPa at Points (a) A and (b) B under varying temperatures.

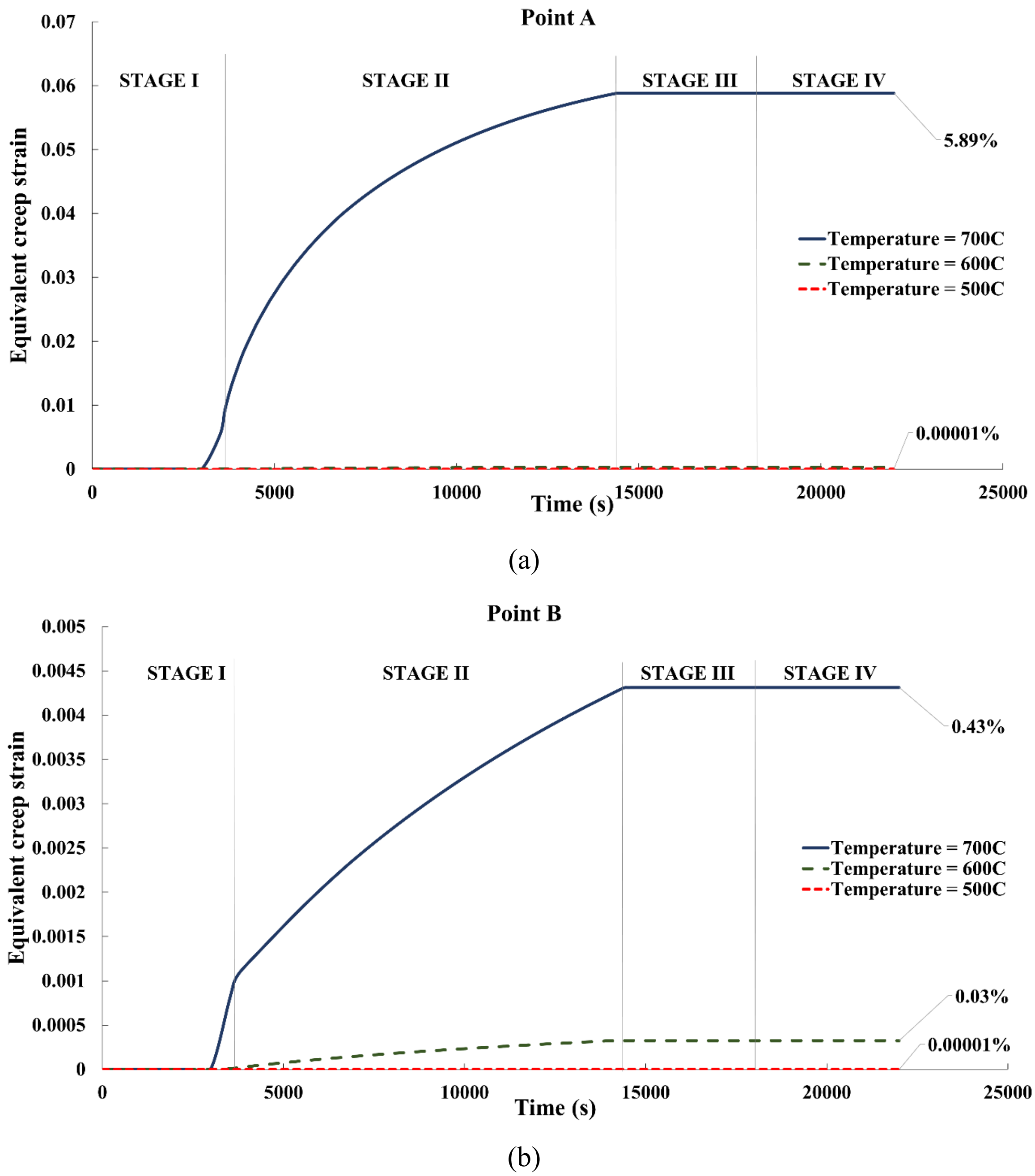

Figure 4.23 Comparison of equivalent creep strain during HIP at 200 MPa at Points (a) A and (b) B under varying temperatures.

A comparison of the effects of temperature (Figure 4.23) and hydrostatic pressure (Figure 4.21) on the CEEQ reveals that temperature has more influence than hydrostatic pressure. Figure 4.23 shows that at a constant hydrostatic pressure of 200 MPa, increasing the temperature from 500°C to 700°C increases the CEEQ from 0.00001% to 0.43% at Point B, thus representing a change of nearly five orders of magnitude and indicating significantly more pronounced creep deformation at higher temperatures. In contrast, Figure 4.21 shows that at a constant temperature of 700°C, increasing the hydrostatic pressure from 0 MPa to 200 MPa increases the CEEQ from 0.16% to 0.43% at Point B, which is less than one order of magnitude. While temperature has the greatest impact on the CEEQ, hydrostatic pressure still plays a significant role, albeit not to the same extent as temperature.

The FE modeling results align with the fundamental behavior described by the hyperbolic-sine creep law. In this law, the exponential term $\exp(-\frac{Q}{RT})$ captures the profound influence of temperature on the creep rate. This is because temperature provides the thermal activation energy required for dislocation movement. At lower temperatures, dislocations remain thermally locked and unable to effectively overcome the energy barriers. However, at higher temperatures, thermal energy increases exponentially, thus facilitating dislocation movement, which accelerates creep deformation. The FE model results in Figure 4.23 show this exponential effect, which is consistent with the strong dependence of temperature described by the hyperbolic-sine law.

On the other hand, the equivalent-stress term in the hyperbolic-sine creep law has a less pronounced but still significant influence on the creep rate. The stress dependence enters the constitutive relation through the dimensionless quantity $B\sigma_{eq}$, where B has units reciprocal to those used for stress. At sufficiently large positive values of $B\sigma_{eq}$, the hyperbolic-sine function approaches its exponential asymptote:

$$\sinh\left(B\sigma_{eq}\right) \approx \frac{1}{2}\exp\left(B\sigma_{eq}\right) \qquad B\sigma_{eq} \gg 1 \qquad (4.2)$$

This form is dimensionally consistent because the arguments of both the hyperbolic-sine and exponential functions are dimensionless. Under this high-stress condition, the creep rate therefore exhibits an approximately exponential dependence on equivalent stress. Consequently, a local increase in equivalent stress can substantially increase the creep strain rate. In the present HIP simulations, this effect is particularly relevant near internal voids, where the applied hydrostatic pressure perturbs the local stress state and generates additional deviatoric stress components.

While this leads to an exponential increase in the creep rate with stress, the effect remains less dramatic than the temperature-driven exponential increase. Hydrostatic pressure contributes to creep deformation primarily by increasing the stress gradients and driving shear stress, thus enhancing dislocation movement. However, its overall effect on the creep rate, as observed in Figure 4.21, is comparatively smaller than the exponential increase driven by temperature.

The observed results are summarized in Table 4.4. Increasing the temperature exponentially accelerates the creep rate due to the thermal activation energy that drives dislocation movement. At higher temperatures, atomic mobility increases, and dislocations overcome energy barriers more readily, thus resulting in significant creep deformation. Conversely, increasing hydrostatic pressure contributes to the equivalent stress, which enhances creep through stress-driven dislocation movement. However, the effect of hydrostatic pressure follows a slower, non-linear relationship compared to the exponential effect of temperature. This interpretation is further supported by Prasad et al.[97], who reported that, in void closure during HIP, temperature plays a more dominant role than both applied hydrostatic pressure and holding time.

Figure 4.24 illustrates the reduction in von Mises stress at Points A and B under the same HIP conditions (200 MPa) and the three temperatures shown in Figure 4.22. At Point A, the stress decreases from 488 MPa to 249 MPa at 500°C, to 150 MPa at 600°C, and to 66 MPa at 700°C. Similarly, at Point B, the stress decreases from 414 MPa to 384 MPa at 500°C, to 257 MPa at 600°C, and to 3 MPa at 700°C. According to Figures 4.22 and 4.23, lower temperatures result in less stress reduction due to the reduced activation of creep and plastic deformation mechanisms. In contrast, higher temperatures significantly amplify these mechanisms by lowering the yield strength and increasing dislocation mobility, which enhance stress relaxation. This comparison underscores the critical role of temperature in facilitating stress relaxation under a constant pressure. The results confirm that the mechanism of stress relaxation remains consistent across different temperatures, with higher temperatures intensifying these effects. This consistent behavior across a range of temperatures shows the effectiveness of HIP in improving material properties, particularly for additively manufactured materials with inherent porosities.

Table 4.4 Comparison of effects of temperature and pressure on CEEQ and their corresponding mechanisms

Factor	Impact on CEEQ	Mechanism
Temperature (T)	Exponential increase (dominant)	Provides thermal energy for atomic mobility and dislocation movement.
Pressure ($\boldsymbol{\sigma_{eq}}$)	Non-linear increase (weaker)	Generates stress gradients that enhance dislocation movement.

We discussed how LPBF induces residual stresses in additively manufactured materials, particularly the development of tensile residual stresses near the surface of components[131]. These tensile stresses can significantly affect the fatigue life of a material, as they are often the primary cause of fatigue failures due to their crack-opening nature. Figure 4.25 shows the normal stress (S_{11}) after AM and HIP under a hydrostatic pressure of 200 MPa and at a temperature of 700°C, with stress values expressed in MPa. This figure shows how the hydrostatic pressure applied during HIP effectively transforms tensile stresses into compressive stresses, which is in close agreement with the experimental results reported by Zhang et al.[113]. The shift from tensile to compressive surface stresses is advantageous for the fatigue life of the material, as compressive stresses help to close micropores, which are potential initiation and propagation sites for cracks. By applying high hydrostatic pressure at elevated temperatures, HIP mitigates crack initiation and growth, thereby enhancing the fatigue life of the material.

The data presented in Table 4.5 provides a detailed analysis of the normal stresses (S_{11}, S_{22}, and S_{33}) in three orthogonal directions (X, Y, and Z) at Points A and B during AM, furnace heating, and HIP at pressures of 100 MPa and 200 MPa. The results emphasize the transformative effect of HIP in converting the tensile stresses generated during the LPBF process into compressive stresses. During AM, all stresses at both Points A and B exhibit tensile behavior, as shown by the positive values under the AM column. For instance, at Point A, S_{11}, S_{22}, and S_{33} are 48 MPa, 243 MPa, and 6 MPa, respectively, while at Point B, they are 94 MPa, 15.8 MPa, and 30 MPa. These tensile stresses arise due to the rapid solidification and cooling inherent to the LPBF process, which results in the accumulation of residual stresses. Such tensile stresses are detrimental as they promote crack initiation and propagation, thus reducing the fatigue life of the material.

The transition from tensile to compressive stresses begins with furnace heating. At Point A, furnace heating reduces S_{11} from 48 MPa to -83 MPa, S_{22} from 243 MPa to -60 MPa, and S_{33} from 6 MPa to -130 MPa. A similar trend is observed at Point B, where S_{11}, S_{22}, and S_{33} are reduced to -3.8 MPa, -0.3 MPa, and -2.8 MPa, respectively. This reduction highlights the role of thermal energy in facilitating stress relaxation and redistribution. However, the furnace condition alone does not fully utilize the mechanisms of plastic deformation and creep, and the resulting compressive stresses are limited in magnitude.

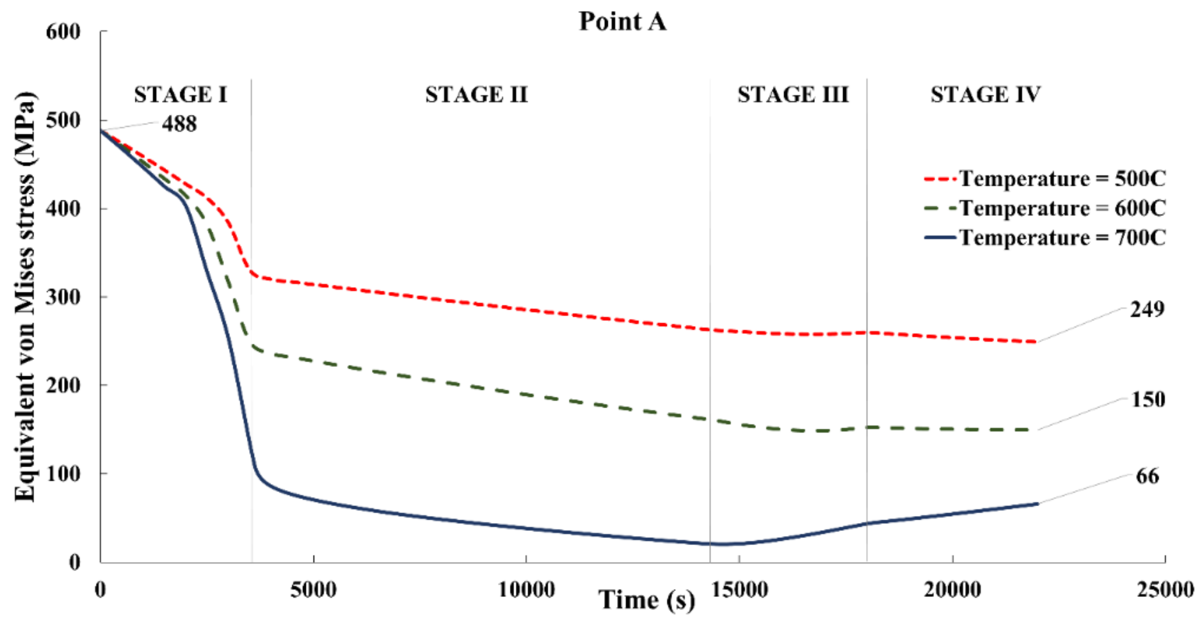

(a)

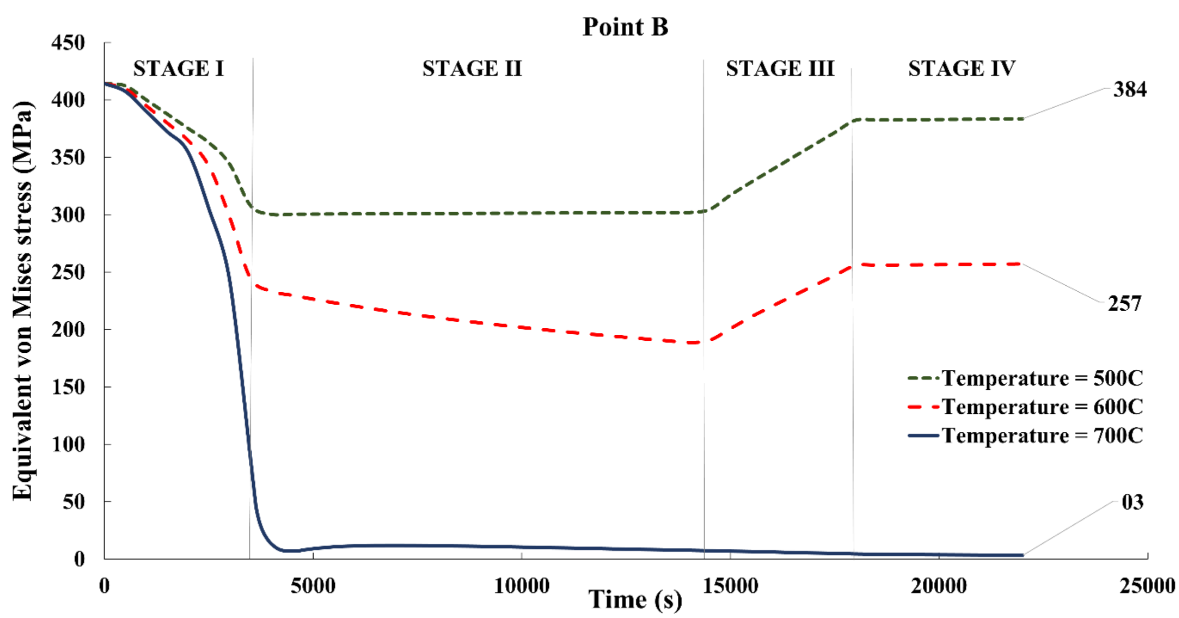

(b)

Figure 4.24 Comparison of equivalent von Mises stress during HIP at 200 MPa at Points (a) A and (b) B under varying temperatures.

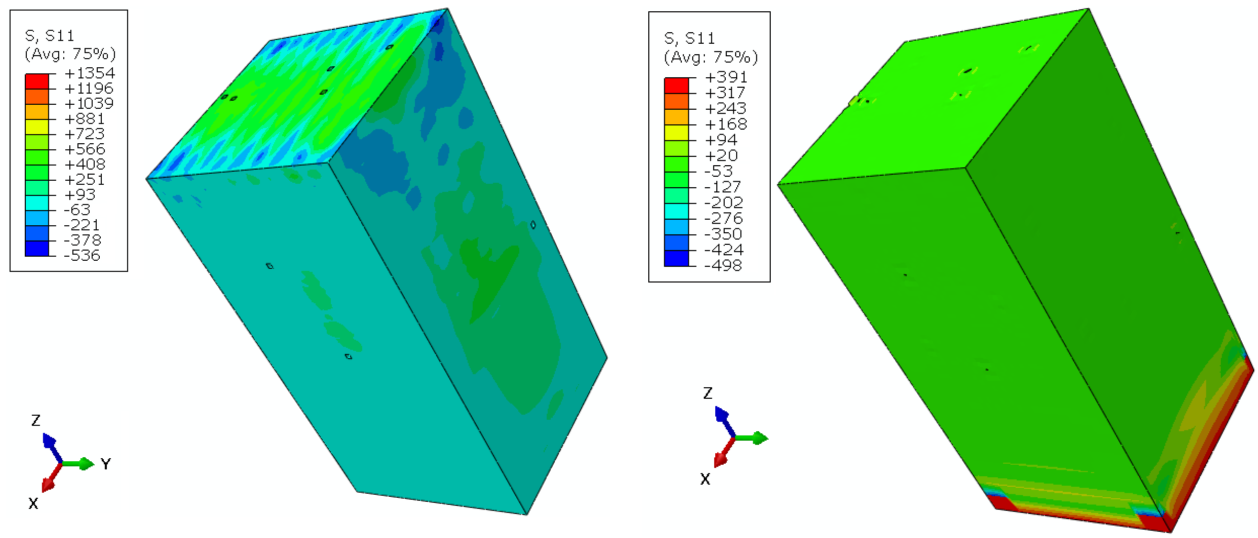

(a) (b)

Figure 4.25 Influence of HIP process conducted under pressure of 200 MPa and temperature of 700°C on normal stress (S_{11}): (a) After LPBF processing and (b) after HIP.

Under HIP conditions, the application of hydrostatic pressure significantly amplifies stress relaxation, thus converting tensile stresses into more substantial compressive stresses. At Point A, S_{11} decreases to -126 MPa at 100 MPa and further to -169 MPa at 200 MPa. Similarly, S_{22} decreases to -92 MPa and -126 MPa, while S_{33} decreases to -190 MPa and -250 MPa at 100 MPa and 200 MPa, respectively. At Point B, even though the stress magnitudes are lower due to reduced stress concentration further away from the pore, HIP still promotes substantial compressive stress. For example, S_{11} is reduced to -14.4 MPa and -28 MPa, S_{22} to -10.8 MPa and -25 MPa, and S_{33} to -13 MPa and -27 MPa under hydrostatic pressures of 100 MPa and 200 MPa, respectively.

The transition from tensile to compressive stresses is driven by the synergistic effects of high temperature and hydrostatic pressure during HIP. Elevated temperature reduces the yield strength of the material, thus enabling plastic deformation, while the pressure produces stress gradients that amplify the shear stress. This combination facilitates dislocation movement, creep, and material flow into voids, thereby leading to stress redistribution. As a result, tensile stress concentrations are eliminated, and the material experiences uniform compressive stress, which is highly beneficial to fatigue life.

A comparison between the furnace and HIP conditions highlights the superior effectiveness of HIP. At Point A, the furnace treatment reduces S_{11} to -83 MPa, while HIP reduces it further to -

126 MPa at 100 MPa and -169 MPa at 200 MPa. At Point B, the furnace treatment reduces S_{33} to -2.8 MPa, while HIP reduces S_{33} -13 MPa at 100 MPa and -27 MPa at 200 MPa. This underscores the critical role of hydrostatic pressure in enhancing stress relaxation and redistribution beyond what can be achieved through furnace heating alone.

The increasing magnitude of compressive stresses with higher pressure during HIP further shows the role of hydrostatic pressure in amplifying the stress relaxation mechanisms. For instance, at Point A, S_{33} transitions from -190 MPa at 100 MPa to -250 MPa at 200 MPa, thus indicating that higher hydrostatic pressure drives more significant plastic deformation and creep. This effect is consistent across all the stress components and both Points A and B, thereby underscoring the robustness of HIP in improving the mechanical properties of additively manufactured materials.

Table 4.5 Changes in normal stresses (S_{11}, S_{22}, and S_{33}) with AM, furnace treatment and HIP at Points A and B

Condition	**AM**		**Furnace**		**HIP (100 MPa)**		**HIP (200 MPa)**	
Location	**A**	**B**	**A**	**B**	**A**	**B**	**A**	**B**
S_{11} (MPa)	48	94	-83	-3.8	-126	-14.4	-169	-28
S_{22} (MPa)	243	15.8	-60	-0.3	-92	-10.8	-126	-25
S_{33} (MPa)	6	30	-130	-2.8	-190	-13	-250	-27

4.2.2.1 Effect of Void Morphology on Stress Distribution & Plastic Deformation

Porosity formation in LPBF is strongly influenced by the processing parameters such as laser power, scanning speed, hatch spacing, and scanning strategy, all of which govern the energy input and melt pool stability. Kasperovich et al.[12] and Nudelis et al.[135,136] discussed the influence of processing parameters on melt pool behavior and defect formation, while similar observations have been reported in other studies[141–143]. Read et al.[140] showed that porosity is significantly affected by the laser power, scanning speed, and their interaction. Likewise, Hasmuni et al.[208] emphasized that hatch spacing—controlling the overlap between adjacent scan tracks—also plays a crucial role in pore formation. Furthermore, Cegan et al.[139] showed that scanning speed significantly governs both the morphology and spatial distribution of pores. At scanning speeds below 1200 mm/s, rounded porosity is predominantly observed, mainly localized near the specimen edges. These pores comprise both large keyhole-type defects and smaller gas-type pores. Conversely, higher scanning speeds (~1200 mm/s) promote the formation of irregular LOF porosity distributed throughout the bulk material. This highlights the strong sensitivity of pore characteristics to variations in the scanning speed.

In LPBF, three types of pores are typically observed: gas, keyhole, and LOF pores, as documented in previous studies[100,143,209–214]. These defects differ in morphology, size, and formation mechanism and can appear in a broad range of metallic materials processed by LPBF. Gas pores are generally small (typically below 100 μm) and nearly spherical. Their formation is associated with the protective gas used during processing and the difference in gas solubility between the liquid and solid phases of the material. During solidification, the solubility of dissolved gas markedly decreases. Consequently, gas accumulates at the solidification front and may nucleate into spherical pores when its concentration exceeds the solubility limit in the solid phase[31]. Keyhole pores develop when the process transitions to keyhole-mode melting due to excessively high laser power density. Intense localized evaporation produces a deep vapor cavity within the melt pool. If this cavity becomes unstable and collapses, process gas can be entrapped in the molten material, thus forming relatively large pores that are often located near the bottom of the melt pool[36]. LOF pores arise when the supplied laser energy is insufficient to completely melt the powder bed. These defects are typically large, irregular in shape, and may contain partially unmelted powder particles. LOF pores can originate from inadequate scan track overlap, excessive hatch spacing, large spatter agglomerates, or oxide layers that prevent proper melting and metallurgical bonding[215].

As pore morphology varies significantly based on the processing conditions, the geometric characteristics of voids—particularly their size, shape, and aspect ratio—are expected to strongly influence local stress distribution and plastic deformation behavior, especially under high temperature and hydrostatic pressure conditions such as those found during HIP. While the formation mechanisms of porosity have been widely investigated, less attention has been given to the direct mechanical implications of different void morphologies under combined thermal and pressure loadings. To systematically isolate and quantify the influence of void geometry, a controlled numerical framework was developed.

To begin the investigation, the effect of the aspect ratio—a key parameter that influences the mechanical response of porous materials during HIP—was first analyzed. In this context, the aspect ratio is defined as AR = Longest Dimension / Shortest Dimension, and four void shapes with the same cross-sectional areas (25 μm × 25 μm) but varying lengths were considered to isolate the role of elongation. These configurations ranged from a compact cube to increasingly elongated rectangular voids, with aspect ratios of 1.0, 2.0, 3.0, and 4.0, respectively. This preliminary geometric assessment provides the basis for the following numerical simulations and highlights how increased aspect ratio can amplify local stress concentrations and deformation. The detailed results and their implications are discussed in the subsequent sections.

Four simulations were conducted at 200 MPa and 500°C to examine the influence of void shape—particularly the aspect ratio of voids—on the mechanical response of the material. As illustrated in Figure 4.26, four distinct void geometries are considered: a single cube (25 μm × 25 μm × 25 μm, AR = 1.0), two adjacent cubes (25 μm × 25 μm × 50 μm, AR = 2.0), three adjacent cubes (25 μm × 25 μm × 75 μm, AR = 3.0), and four adjacent cubes (25 μm × 25 μm × 100 μm, AR = 4.0). While all of the configurations share the same cross-sectional area (25 μm × 25 μm), they vary in length—specifically 25, 50, 75, and 100 μm—thereby resulting in different aspect ratios and shapes which range from near-spherical to elongated forms. The red regions indicate the distributed voids embedded within the matrix. The first geometry (25 μm × 25 μm × 25 μm) is more representative of a spherical void, whereas the last one (25 μm × 25 μm × 100 μm) resembles a non-spherical or irregularly shaped void. In each simulation, two groups of points were selected for analysis: one group located near the voids, and another positioned at the four corners of the top surface—the farthest from the voids (Points A, B, C, and D).

Tables 4.6 to 4.9 present the detailed simulation results for each void configuration. Each table includes the values for the accumulated CEEQ, PEEQ, initial and final von Mises stresses, and the corresponding stress reduction at the selected points after the HIP process. Table 4.6 presents the post-HIP mechanical response of the material that contains the four adjacent cubic voids (25 μm × 25 μm × 100 μm), as illustrated in Figure 4.26(d). The selected evaluation points are categorized based on their proximity to the voids: Points 1–3 are near the voids, and Points A–D are far from them. The data clearly show that the mechanical behavior significantly depends on the location relative to the voids.

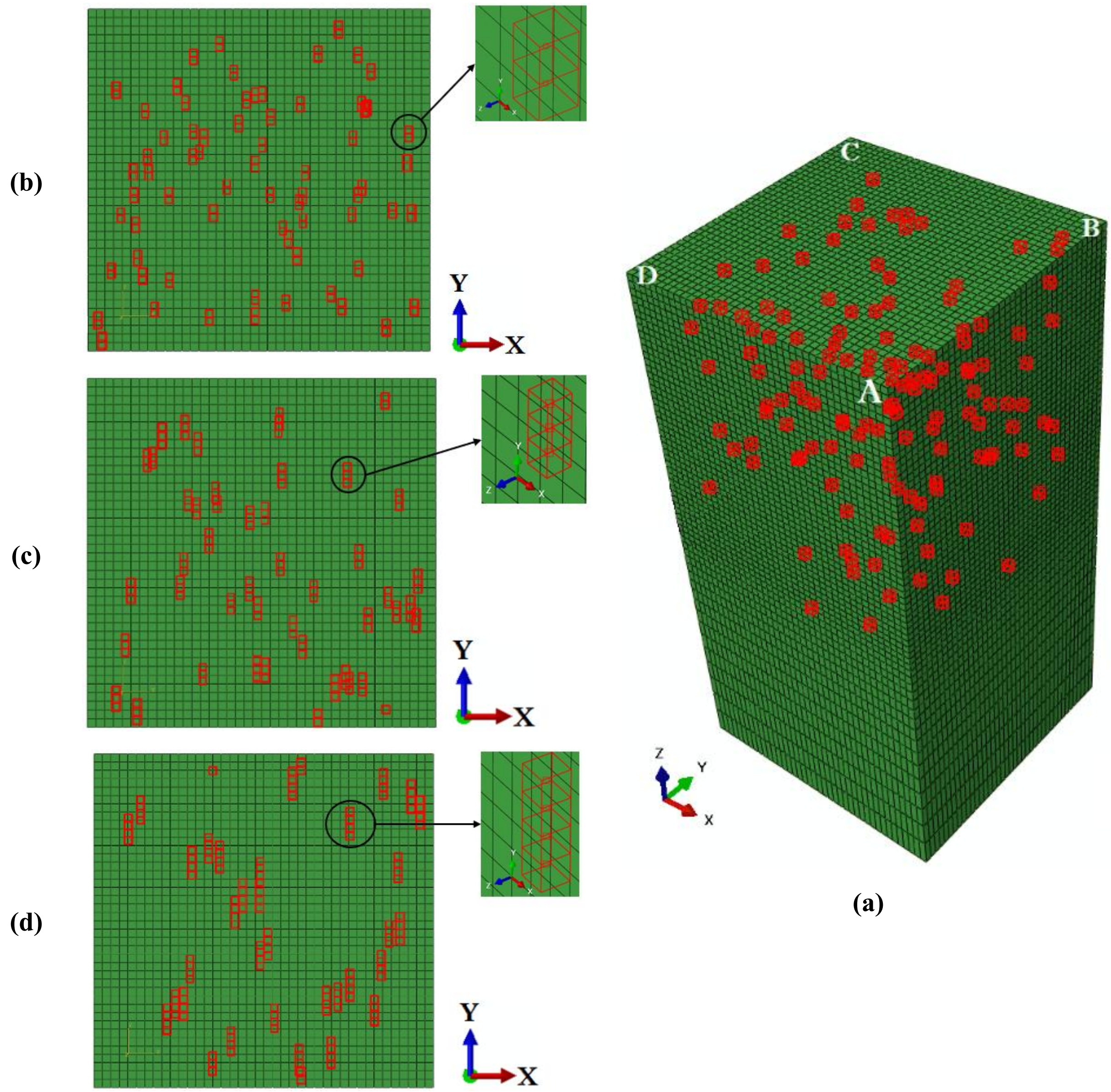

Figure 4.26 Schematic representations of four different void morphologies analyzed in this study: (a) a single cubic void, and (b) two, (c) three, and (d) four adjacent cubic voids.

At Points 1–3, which are closest to the void cluster, there is a substantial accumulation of both PEEQ and CEEQs. For instance, Point 1 exhibits the highest CEEQ value of 8.78×10^{-3} and a corresponding PEEQ of 8.40×10^{-3}, thus indicating intense local deformation due to the high stress concentration near the elongated void. Similarly, Points 2 and 3 show higher CEEQ values of 6.72×10^{-3} and 4.49×10^{-3} along with PEEQ values of 6.19×10^{-3} and 5.62×10^{-3} respectively.

These localized deformations correspond to significant stress relaxation. The initial von Mises stress at Point 1, which was 530.5 MPa, is reduced to 213.5 MPa, thus resulting in a stress drop (ΔStress) of 317 MPa or a 59.75% reduction. Similar reductions are observed at Points 2 and 3, with stress reductions of 56.52% and 54.21%, respectively. This substantial stress relief is clearly the result of the active creep and plastic mechanisms promoted by both the applied HIP conditions and the local geometry-induced stress concentrations.

In contrast, Points A–D, which are positioned far from the voids (near the top corners of the sample), exhibit negligible CEEQ and PEEQ. For instance, Point A shows a very low CEEQ of 2.35×10^{-6} and zero PEEQ. Consequently, the stress relaxation is also minimal, with a ΔStress of 16.7 MPa, which corresponds to only a 16.51% reduction. Similarly, Point B shows the lowest stress change of all points—only 6 MPa—despite a small CEEQ of 1.94×10^{-7}, thus highlighting that the material in these regions remain largely elastic.

Table 4.6 Effect of void morphology (four adjacent cubes) on equivalent creep and plastic strains, and residual stress reduction during HIP

Location Relative to Void	**Point**	**PEEQ (post-HIP)**	**CEEQ (post-HIP)**	**Initial von Mises stress (Pre-HIP)**	**Final von Mises stress (Post-HIP)**	**ΔStress (MPa)**	**Stress Reduction (%)**
Near the void	1	8.40×10^{-3}	8.78×10^{-3}	530.5	213.5	317	59.75
	2	6.19×10^{-3}	6.72×10^{-3}	486.6	211.6	275	56.52
	3	5.62×10^{-3}	4.49×10^{-3}	501.7	229.7	272	54.21
Far from the void	A	0	2.35×10^{-6}	101.1	84.4	16.7	16.51
	B	0	1.94×10^{-7}	55.6	49	6.6	11.87
	C	0	8.25×10^{-7}	70.1	60.96	9.14	13.04
	D	0	3.24×10^{-7}	124.7	109.81	14.89	11.94

Table 4.7 presents the results for the void configuration which consists of three adjacent cubic voids (25 µm × 25 µm × 75 µm). Similar to the four-cube case, deformation and stress relaxation are notably higher near the voids (Points 1–3). The CEEQ values in this region range from 2.60×10^{-3} to 3.43×10^{-3}, while PEEQ varies from 1.14×10^{-3} to 1.87×10^{-3}, thus indicating significant accumulation of PEEQ and CEEQ. The highest creep activity is observed at Point 2,

which exhibits the highest CEEQ (3.43×10^{-3}). The initial von Mises stresses at these points exceed 530 MPa, with Point 2 reaching the highest stress (666.1 MPa), which is later reduced to 433 MPa, thus resulting in a stress decline of 233.1 MPa (35%). Point 1, with a ΔStress of 175.2 MPa, shows a stress reduction of 29.17%, while Point 3 shows the smallest decline (133.9 MPa, or 24.98%) despite having a high initial stress. These values highlight strong localized stress relaxation near the voids.

In contrast, Points A–D, located far from the voids, show minimal deformation and stress changes. The CEEQ values range from 1.17×10^{-6} to 1.75×10^{-7}, and PEEQ is zero at all points. Stress reductions are small, between 4.1 MPa (7.37%) and 16.1 MPa (15.92%), thus reinforcing the observation that the mechanical influence of voids remains highly localized.

Table 4.7 Effect of void morphology (three adjacent cubes) on equivalent creep and plastic strains, and residual stress reduction during HIP

Location Relative to Void	Point	PEEQ (Post-HIP)	CEEQ (Post-HIP)	Initial von Mises stress (Pre-HIP)	Final von Mises stress (Post-HIP)	ΔStress (MPa)	Stress Reduction (%)
Near the void	1	1.46×10^{-3}	2.82×10^{-3}	600.8	425.6	175.2	29.17
	2	1.87×10^{-3}	3.43×10^{-3}	666.1	433	233.1	35
	3	1.14×10^{-3}	2.60×10^{-3}	535.9	402	133.9	24.98
Far from the void	A	0	1.17×10^{-6}	101.1	85	16.1	15.92
	B	0	4.44×10^{-8}	55.6	51.5	4.1	7.37
	C	0	8.24×10^{-7}	70.1	60.98	9.12	13.01
	D	0	1.75×10^{-7}	124.7	111.3	13.4	10.75

Table 4.8 summarizes the mechanical response for a configuration with two adjacent cubic voids (25 µm × 25 µm × 50 µm). Compared to the three- and four-void cases, this geometry results in moderately less deformation near the voids. At Points 1–3, the PEEQ ranges from 1.229×10^{-3} to 1.689×10^{-3}, while CEEQ varies between 1.546×10^{-3} and 2.039×10^{-3}. Point 3 exhibits the highest accumulation of both PEEQ and CEEQ. The corresponding von Mises stress reductions are significant but somewhat less than those observed in more elongated void geometries. Specifically, Point 3 shows the highest ΔStress of 214.7 MPa (33.75%), followed by Point 1 with

149.1 MPa (26.28%) and Point 2 with 130 MPa (23.99%). Despite high initial von Mises stresses—up to 637.3 MPa—the stress relief is less efficient compared to the longer void cases. At far-field locations (Points A–D), the mechanical response is minimal. CEEQ values remain low (ranging from 1.983×10^{-8} to 1.091×10^{-6}) and PEEQ remains zero. Stress reductions in these regions are minor, particularly at Point B (2.2 MPa; 3.95%), thus confirming that regions far from the voids experience negligible mechanical activity during HIP.

Table 4.8 Effect of void morphology (two adjacent cubes) on equivalent creep and plastic strains, and residual stress reduction during HIP

Location Relative to Void	Point	PEEQ (Post-HIP)	CEEQ (Post-HIP)	Initial von Mises Stress (Pre-HIP)	Final von Mises Stress (Post-HIP)	ΔStress (MPa)	Stress Reduction (%)
Near the void	1	1.31×10^{-3}	1.54×10^{-3}	567.4	418.3	149.1	26.28
	2	1.22×10^{-3}	1.57×10^{-3}	541.9	411.9	130	23.99
	3	1.68×10^{-3}	2.03×10^{-3}	637.3	422.6	214.7	33.75
Far from the void	A	0	1.09×10^{-6}	101.1	85.2	15.9	15.72
	B	0	1.98×10^{-8}	55.6	53.4	2.2	3.95
	C	0	8.22×10^{-7}	70.1	61	9.11	12.98
	D	0	1.27×10^{-7}	124.7	112.1	12.6	10.1

Table 4.9 presents the response for a single cubic void (25 μm × 25 μm × 25 μm), which is the most compact void morphology. The deformation in the near-void region (Points 1–3) is significantly less than that in the other configurations. For instance, CEEQ ranges from 1.25×10^{-3} to 3.61×10^{-4} and PEEQ varies from 0 to 1.82×10^{-3}. Only Point 1 shows relatively large deformation, while Point 3 has zero PEEQ and limited creep. Stress reduction follows the same trend—lower than in elongated voids. Point 1 has a ΔStress of 134 MPa (25.02%), while Point 2 is 66.3 MPa (19.12%). At Point 3, a 69.5 MPa stress decline translates to a decrease of 15.46%, despite no plastic activity. These results underscore the limited relaxation efficiency associated with a single, compact void. At locations further away (Points A–D), the behavior is consistent with previous configurations—minimal strain, no plasticity, and modest stress relief (approximately 10–15%), which are indicative of a primarily elastic response.

The collective analysis of Tables 4.6 through to 4.9 clearly shows that void shape has a significant influence on localized plastic deformation and stress relaxation during HIP. Among the four configurations, the four-cube geometry (100 µm length) shows the most pronounced plastic and creep behavior near the voids, with the highest Δσ value reaching 317 MPa and a stress reduction of 59.75%. This indicates a highly effective stress relaxation mechanism near the elongated voids. In comparison, the three-cube (75 µm) configuration exhibits slightly reduced strain accumulation and stress relaxation, with a maximum Δσ of 233.1 MPa and stress reduction up to 35%. The two-cube (50 µm) case shows a further decrease, with the highest Δσ of 214.7 MPa and a maximum stress reduction of 33.75%. The single-cube configuration (25 µm), which is the most compact void geometry, shows the least effective response, with Δσ values not exceeding 134 MPa and a maximum stress reduction of only 25.02%, accompanied by low CEEQ and PEEQ values, particularly at points with negligible plastic activity.

Table 4.9 Effect of void morphology (single cube) on equivalent creep strain, equivalent plastic strain, and residual stress reduction during HIP

Location Relative to Void	**Point**	**PEEQ (Post-HIP)**	**CEEQ (Post-HIP)**	**Initial von Mises Stress (Pre-HIP)**	**Final von Mises Stress (Post-HIP)**	**ΔStress (MPa)**	**Stress Reduction (%)**
Near the void	1	1.82×10^{-3}	1.25×10^{-3}	533.5	400	134	25.02
	2	6.14×10^{-4}	6.81×10^{-4}	346.8	280.4	66.3	19.12
	3	0	3.61×10^{-4}	449.5	380	69.5	15.46
Far from the void	A	0	1.00×10^{-6}	101.1	85.4	15.7	15.52
	B	0	1.94×10^{-8}	55.6	53.42	2.18	3.92
	C	0	8.20×10^{-7}	70.1	61.1	9	12.83
	D	0	1.26×10^{-7}	124.7	112.1	12.6	10.1

Across all void configurations, the far-field regions (Points A–D) consistently show minimal PEEQ and CEEQ and modest stress relief, typically below 16%, irrespective of the void shape. These findings affirm that the mechanical response during HIP is highly localized around voids and strongly governed by the void geometry. Notably, increasing the void length—and hence the aspect ratio—leads to elevated stress concentration and intensified creep and plastic flow near the void, thus promoting a more efficient redistribution of residual stress under the applied high-pressure and high-temperature conditions.

This trend is further corroborated in Table 4.10, which summarizes the near-void mechanical response across the four geometries. As shown, the average von Mises stress reduction ($\Delta\sigma$) increases systematically with void length—from 89.5 MPa (19.2%) for a single-cube void to 288 MPa (56.83%) for the four-cube case. Likewise, the average CEEQ rises notably with increasing void length, reaching up to 6.66×10^{-3} in the most elongated configuration. Interestingly, although the two-cube and three-cube geometries exhibit nearly the same PEEQ values (PEEQ $\approx 1.4\text{–}1.5 \times 10^{-3}$), the three-cube configuration shows nearly double the CEEQ and higher stress relief, indicating a transition point beyond which further elongation leads to significantly enhanced time-dependent deformation and stress redistribution. This underscores the critical role of void aspect ratio in driving localized creep activity under HIP conditions.

Table 4.10 Average plastic and creep strains, and stress relaxation ($\Delta\sigma$ and %) for different void configurations

Void morphology	Avg PEEQ	Avg CEEQ	Avg $\Delta\sigma$ (MPa)	Avg $\Delta\sigma$ (%)
4 cubes (100 µm)	6.74×10^{-3}	6.66×10^{-3}	288	56.83
3 cubes (75 µm)	1.49×10^{-3}	3.05×10^{-3}	180.8	29.72
2 cubes (50 µm)	1.41×10^{-3}	1.72×10^{-3}	164	28.34
1 cube (25 µm)	0.813×10^{-3}	7.67×10^{-4}	89.5	19.20

Notes: PEEQ denotes plastic strain, CEEQ denotes creep strain.

Figures 4.27 and 4.28 visually reinforce the quantitative patterns reported in Tables 4.6 through to 4.10. In Figure 4.27, the bar chart illustrates the average CEEQ accumulation in the near-void region for each void morphology. The data clearly show that as voids become more elongated—from a single cube (25 µm) to four adjacent cubes (100 µm)—the average post-HIP CEEQ rises substantially. Specifically, the four-cube configuration reaches the highest CEEQ value of 0.006, whereas the single-cube case yields only 0.000642, thus reflecting minimal creep activity. This trend supports the notion that longer voids introduce more higher local deviatoric stresses and stress concentrations, which intensify the creep response under HIP conditions.

Figure 4.28 complements this by presenting the average residual stress reduction (%) for the same void geometries. As observed, more elongated voids result in more residual stress relaxation. The four-cube geometry achieves the highest average stress reduction of 56.2%, followed by the three-cube and two-cube configurations at 29.7% and 28.7%, respectively. The single-cube case remains the least effective, with an average stress reduction of only 19.9%. These results align well with the data in Table 4.10, thus affirming that the void aspect ratio plays a key role in driving local plastic deformation and promoting efficient stress redistribution. Taken together, these figures provide a strong graphical visual that confirms the conclusion that longer and more irregular voids significantly enhance local plasticity, creep, and stress redistribution, thus validating the effectiveness of HIP in healing defects with complex morphologies.

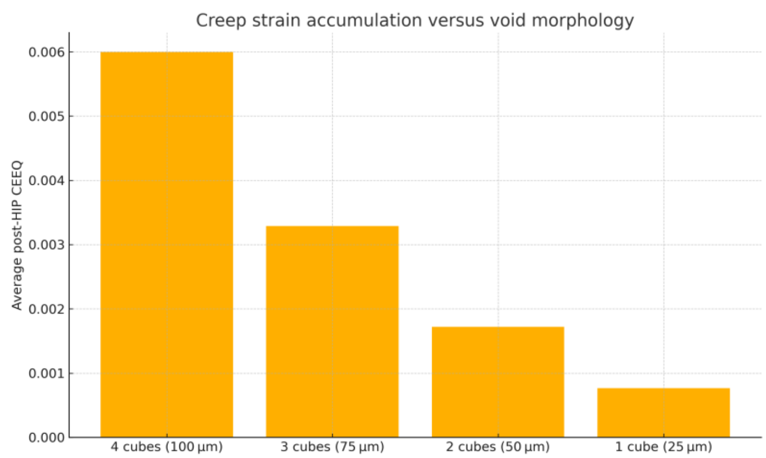

Figure 4.27 Creep-strain accumulation versus void morphology.

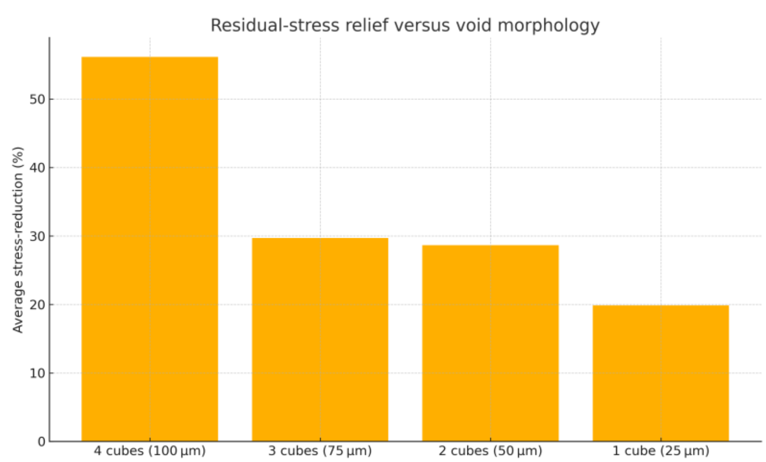

Figure 4.28 Residual stress relief versus void morphology.

The results obtained in this study showed that creep-dominated deformation, intensified by hydrostatic pressure, plays a dominant role in residual stress relaxation in laser powder bed fused materials. It should be noted that a portion of these findings has previously been published in Ref.[114]. In this study, the CEEQ remains an order of magnitude greater than the PEEQ, thus highlighting the dominant role of dislocation creep in stress redistribution during HIP. Notably, the current simulations, conducted under the same peak HIP conditions (500°C, 200 MPa), reproduce the same mechanistic hierarchy, thereby further supporting the consistency of the observed trends. Furthermore, the trend revealed in the present study—that more elongated voids (i.e., higher aspect ratio pores) promote faster closure of the voids and more stress relief—aligns closely with the experimental data reported in the literature for HIP-treated laser powder bed fused alloys. For example, Qin et al.[82] and Prasad et al.[97] reported that crack-like or elliptical pores tend to close more rapidly than near-spherical pores because of the higher local stress concentrations and enhanced deformation around elongated defects. Similar observations have also been reported in other experimental and numerical studies[135,136,138]. These studies consistently report that crack-like or elliptical pores close more efficiently than quasi-spherical voids, owing to the higher local deviatoric stresses that they induce, which in turn, drive more pronounced creep and plastic deformation. Together, these findings reaffirm the effectiveness of HIP in targeting critical defect morphologies and achieving exceptional residual stress relaxation.

Thus far, the analysis has focused on the influence of void shape on the CEEQ, PEEQ, and von Mises stress, which shows that more elongated voids enhance stress redistribution during HIP. Building on these findings, the next phase of the study shifts to the role of void size, while keeping the aspect ratio constant. This allows for a more focused investigation on how increasing the absolute void volume affects local deformation and stress relaxation.

Figure 4.29 illustrates the FE model geometry used to examine this effect, which features two large cubic voids embedded within the specimen. The red regions represent the voids, each with a significantly larger volume than those used in prior configurations. Positioned near the middle of the sample, these voids are intended to induce localized stress concentrations under HIP conditions, thereby amplifying the mechanical response and allowing for a more clear assessment of the size-driven effects.

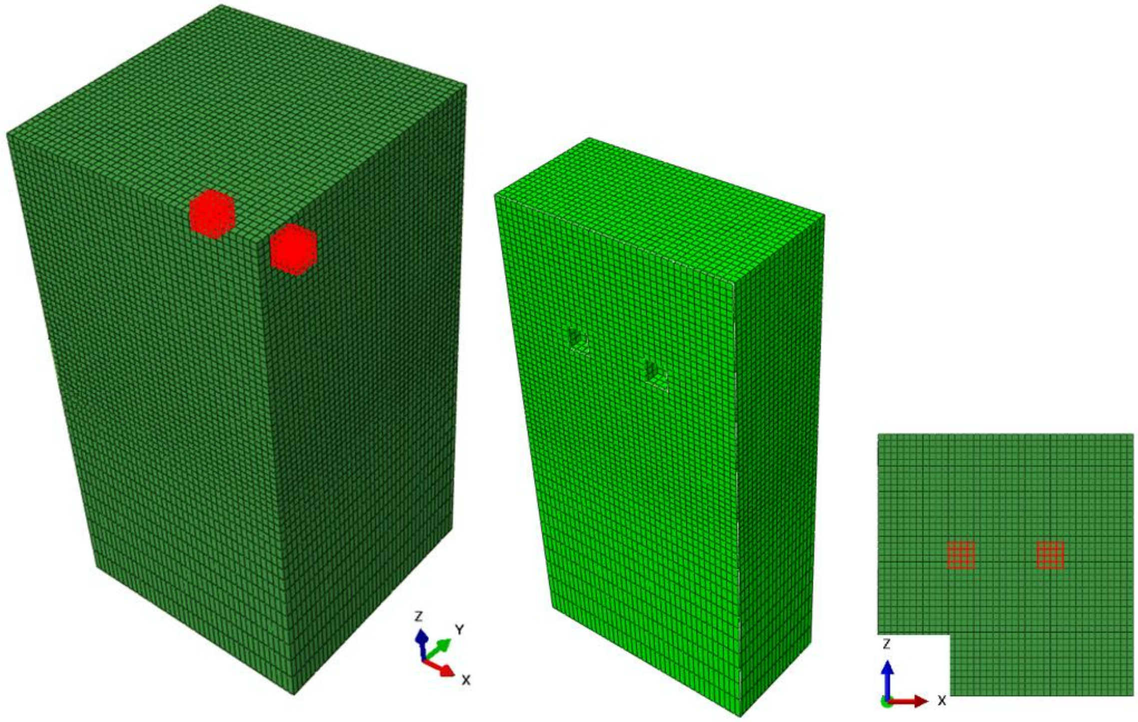

Figure 4.29 Finite element model geometry illustrating two large cubic voids configuration.

Table 4.11 Effect of void morphology (two big cubes) on equivalent creep strain, equivalent plastic strain, and residual stress reduction during HIP

Location Relative to Void	**Point**	**PEEQ (Post-HIP)**	**CEEQ (Post-HIP)**	**Initial von Mises Stress (Pre-HIP)[MPa]**	**Final von Mises Stress (Post-HIP)[MPa]**	**ΔStress (MPa)**	**Stress Reduction (%)**
Near the void	1	2.58×10^{-4}	3.78×10^{-3}	319.68	238.28	81.48	25.49
	2	5.11×10^{-4}	4.99×10^{-3}	450.28	318.28	132.02	29.32
	3	2.38×10^{-4}	3.41×10^{-4}	287.28	248.38	39	13.57
	4	1.73×10^{-4}	5.97×10^{-4}	295.78	247.98	47.8	16.15
Far from the void	A	0	1.46×10^{-6}	101.1	84.8	16.3	16.12
	B	0	1.99×10^{-8}	55.6	53.39	2.2	3.96
	C	0	8.21×10^{-7}	70.1	61.05	9.05	12.91
	D	0	1.06×10^{-7}	124.7	112.2	12.5	10.02

Table 4.11 presents the simulation results for the model with two large cubic voids, and its geometry is provided in Figure 4.29. The voids are embedded in the middle of the part and characterized by a regular, nearly spherical shape with a low aspect ratio, as clearly visible in the

model. These voids induce local stress concentrations during HIP at 500°C and 200 MPa, which are examined through accumulated CEEQ, PEEQ, and stress reduction. The table includes results for eight points, divided into two categories: Points 1–4 near the voids, and Points A–D further away from the voids.

The results for Points 1–4 reveal moderate levels of PEEQ, which range from 1.73×10^{-4} to 5.11×10^{-4}, and CEEQ values between 4.99×10^{-3} and 5.97×10^{-4}. The maximum CEEQ is recorded at Point 2, with 4.99×10^{-3}, while the largest ΔStress (132.02 MPa) is observed at Point 2 as well. Stress reduction percentages vary from 13.57% to 29.32%, confirming that deformation is concentrated around the voids. Points farther from the voids (Points A–D), as expected, exhibit negligible PEEQ and very low CEEQ—in the order of 10^{-7} to 10^{-6}—alongside modest stress relaxation (ΔStress below 17 MPa and stress reduction below 16.2%).

Interestingly, when compared to the single-cube configuration in Table 4.9, the two-void model in Table 4.11 produces a very similar mechanical response. Although the voids in Table 4.11 are larger in size, their shape remains highly regular and quasi-spherical, just like the single void in Table 4.9. This similarity leads to comparable values of CEEQ, PEEQ, and stress reduction near the voids. In both tables, the absence of significant geometric irregularities or elongation results in a limited stress redistribution, as creep and plastic flow are less activated than in cases with a high-aspect-ratio or elongated voids. This comparison highlights a key insight: void morphology (irregularity and aspect ratio) plays a more dominant role in stress relaxation during HIP than void size alone. As shown in Figure 4.29, the regular, compact voids in this model do not generate sufficient deviatoric stress to promote extensive creep deformation. Therefore, the results of Table 4.11 reinforce the conclusion that shape irregularity, rather than volume, governs the severity of local plasticity and stress relief in HIP-processed components.

Up to this point, the analysis has examined the impact of void morphology—particularly aspect ratio and size—on the CEEQ, PEEQ, and von Mises stress. Building on these insights, the next phase of the study shifts attention to the role of void irregularity, allowing for a more focused investigation into how increasing geometric complexity affects local deformation and stress relaxation. For this phase, an L-shaped void with an aspect ratio (AR) of 2.0 but with pronounced irregularity is considered. This void maintains the same square cross-section of 25 µm × 25 µm but differs in structural complexity. Unlike the two-cube void configuration with AR = 2.0 (as shown in Figure 4.26(b)), the selected void features a distinct L-shaped morphology, thus introducing internal corners and geometric irregularity. These features can significantly increase localized deformation and stress concentrations. Figure 4.30 shows the FE model of a specimen containing randomly distributed voids with this L-shaped morphology. Each void maintains a cross-section of 25 µm × 25 µm and extends 50 µm in two perpendicular directions, thus creating the characteristic L-shape. The voids exhibit a clustered distribution with notable shape irregularity, which make this configuration ideal for assessing the impact of irregular geometries on the HIP response.

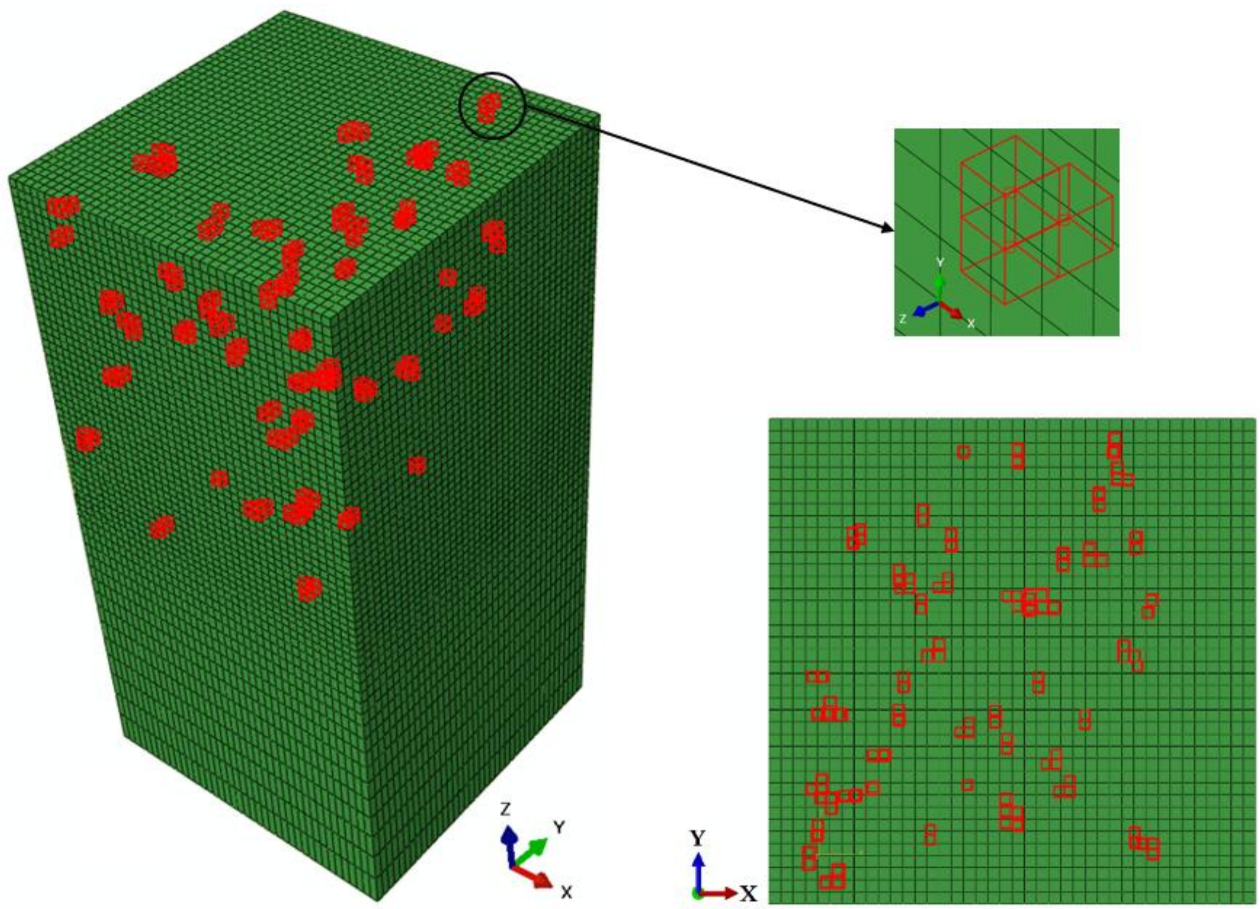

Figure 4.30 Finite element model of a specimen containing randomly distributed L-shaped voids (25 µm × 25 µm cross-section; 50 µm legs in two perpendicular directions).

Table 4.12 provides the post-HIP response results for the specimens with L-shaped voids. At Points 1–4, the deformation is highly localized: CEEQ = 3.23×10^{-2}–6.35×10^{-2} and PEEQ =

5.48×10^{-4}–7.00×10^{-4}. Most of the creep occurs at Point 3 (CEEQ = 6.35×10^{-2}), while most of the stress relief is found at Point 4 ($\Delta\sigma$ = 263.5 MPa, 64%). Points 1–2 also show substantial relaxation ($\Delta\sigma \approx$ 199.7–250.5 MPa, 51–56%). In contrast, the far-field points, Points A–D, show no PEEQ, very small CEEQ ($\approx10^{-7}$–10^{-6}), and modest declines in stress ($\Delta\sigma \approx$ 6–16 MPa, 10–16%), thereby confirming a strongly localized response.

Table 4.12 Effect of void morphology of L-shaped voids on equivalent creep and plastic strains, and residual stress reduction during HIP

Location Relative to Void	**Point**	**PEEQ (Post-HIP)**	**CEEQ (Post-HIP)**	**Initial von Mises Stress (Pre-HIP)[MPa]**	**Final von Mises Stress (Post-HIP)[MPa]**	**ΔStress (MPa)**	**Stress Reduction (%)**
Near the void	1	5.48×10^{-4}	3.23×10^{-2}	387.9	188.2	199.7	51.48
	2	7.00×10^{-4}	3.27×10^{-2}	451.9	201.4	250.5	55.43
	3	1.55×10^{-4}	6.35×10^{-2}	667.1	283.9	383.2	57.44
	4	6.76×10^{-4}	5.23×10^{-2}	411.3	147.8	263.5	64.06
Far from the void	A	0	1.37×10^{-6}	101.1	84.93	16.17	15.99
	B	0	6.99×10^{-8}	55.6	49.54	6.06	10.89
	C	0	8.21×10^{-7}	70.1	61.06	9.04	12.89
	D	0	2.24×10^{-7}	124.7	111.05	13.65	10.94

Although the aspect ratio is the same (AR = 2.0), the irregular geometry of the L-shaped voids produces a markedly stronger response than the usual two-cube configuration in Table 4.8. The CEEQ near the void for the two-cube case is only 1.54×10^{-3}–2.03×10^{-3} and the maximum amount stress relief is 214.7 MPa (33.75%). By contrast, the L-shape yields a CEEQ that is one to two orders of magnitude higher (up to 6.35×10^{-2}) and larger stress reductions (up to 263.5 MPa, 64%). On the other hand, the PEEQ for the L-shaped voids (10^{-3}–10^{-4} range) is lower than for the two-cube case ($\approx1.22\times10^{-3}$–1.68×10^{-3}), and the much larger CEEQ confirms creep-dominated relaxation, driven by the sharp internal corners and load-path turns that enhance the local deviatoric stresses.

The L-shaped configuration of the voids is also similar to the case with the largest aspect-ratio (four cubes) in overall effectiveness. Table 4.6 shows that the $\Delta\sigma$ values reach 317 MPa with an approximately 60% stress reduction and CEEQ near the voids of up to 8.78×10^{-3}, whereas Table 4.12 shows comparable or a higher percentage stress relief (up to 64%) and significantly increased creep accumulated (up to 6.35×10^{-2}). These comparisons highlight that void irregularity can be as influential as, and in some metrics more influential than, the aspect ratio in increasing local creep and enhancing residual stress relaxation during HIP. The present simulation results are consistent with the observations reported by Prasad et al.[97].

4.2.2.2 Effect of Void Percentage on Plastic Flow and Stress Reduction

To investigate the effect of the initial void percentage, a series of FE simulations were performed on a representative additively manufactured component subjected to a standard HIP cycle. Different initial levels of porosity were assigned to the sample to study the effect of the void content on the mechanical response during HIP. Microporosity was introduced to the FE model by using an element deletion technique, where a specific fraction of elements was randomly deactivated in the mesh to simulate voids. These deactivated elements do not contribute to the stiffness or load-carrying capacity of the structure, thus effectively acting as embedded pores. A Python script was employed to randomly distribute these voids throughout the sample while maintaining control over the total void volume fraction. Figure 4.31 illustrates the spatial distribution of the voids (in red) in two representative cases; for an initial porosity of (a) 0.25% and (b) 0.65%. As shown, the voids are randomly dispersed in the upper volume of the sample to replicate realistic as-built porosity patterns. This setup allows for controlled variation of six different initial porosities: 0.25%, 0.35%, 0.40%, 0.50%, 0.65%, and 0.80%. These values span from nearly fully dense (0.25%), which is representative of well-optimized LPBF builds, to moderately porous (0.80%), which is characteristic of less-refined printing conditions. Such porosity levels are consistent with the typical range found in as-built laser powder bed fused components by Cegan et al.[139]. All of the other material properties, including the elastic modulus, yield strength, and creep parameters, were kept constant across these cases. Therefore, any observed differences in stress relaxation, PEEQ, or creep behavior during HIP can be directly attributed to variations in the initial void content.

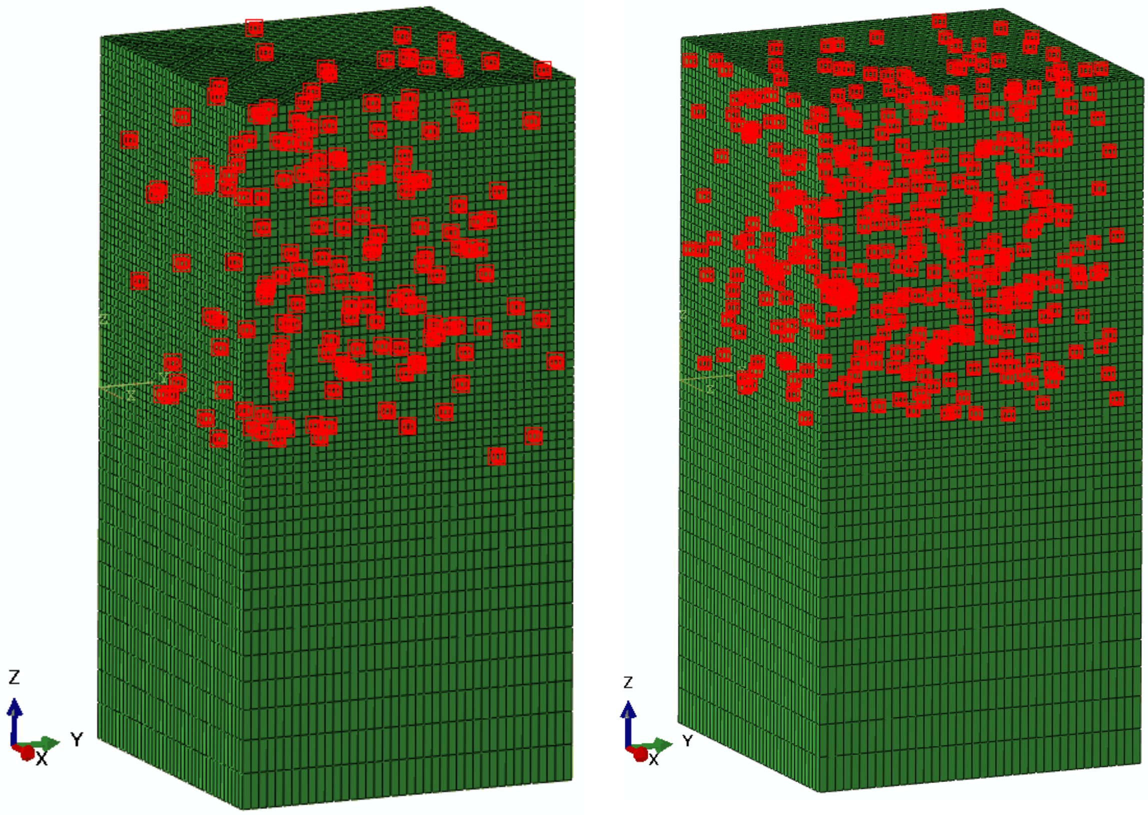

(a) **(b)**

Figure 4.31 Spatial distribution of randomly generated voids (red) in finite element model for two different initial porosities: (a) 0.25% and (b) 0.65%.

After initializing the stress state and porosity, the HIP cycle was simulated. A temperature of 700°C and an hydrostatic pressure of 200 MPa were applied to the part. The pressure was applied uniformly on all of the external surfaces, and the temperature was raised uniformly throughout the part to the target holding temperature. Both the hydrostatic pressure and temperature were ramped up over the course of one hour, then held constant for a sustained dwell time of 180 min. This prolonged hold at an elevated temperature under hydrostatic pressure provides sufficient time for creep deformation to occur, thereby complementing the instantaneous plastic compression that occurs during the pressurization phase. After holding, the pressure was released, and the part was cooled back to room temperature in the simulation. Thermal contraction during cooling, combined with permanent deformations from the HIP cycle, leads to the final residual stress state within the material.

To evaluate the outcomes for each initial porosity, the simulation results were analyzed with a focus on the PEEQ, CEEQ, and von Mises residual stress. The analysis examined the surface of the part, as surface stresses are critical for fatigue performance and often govern the overall residual stress behavior of the component. The top of the cubic sample was selected as a representative cross-section for a detailed analysis, since this region typically retains high tensile residual stresses in many additively manufactured components prior to HIP and is therefore a key target area for improvement.

To evaluate the mechanical response near the surface, the top layer of FEs were isolated in each simulation. From this layer, the nodal values of the PEEQ, CEEQ, and von Mises stress were extracted. This facilitated the generation of spatial maps that show the distribution of inelastic strain and residual stress on the surface after HIP for each initial porosity. This process is shown in Figure 4.32 with the sample that has an initial porosity of 0.1%. Figure 4.32(a) shows the distribution of equivalent von Mises stress throughout the LPBF-printed sample after HIP. To allow a more focused analysis of the surface behavior, a single top-surface layer of elements is extracted, as shown in Figure 4.32(b). The extracted PEEQ, CEEQ, and von Mises values were then plotted across the X–Y spatial coordinates of the surface, which resulted in the contour map shown in Figure 4.32(c). This approach enables a detailed, location-specific analysis of the surface deformation and stress characteristics, which are especially important in assessing residual stress behavior relevant to the fatigue performance.

Due to the presence of discrete pores, some very localized regions can exhibit abnormally high stress (for example, a sharp corner of a collapsing void might momentarily show a spike in von Mises stress). Including these extreme values in an average value could skew the comparison. Therefore, a filtering criterion was applied: any surface element with a von Mises stress that exceeds the mean by more than 2 standard deviations was flagged as an outlier and removed from the averaging. These outliers typically correspond to isolated stress hot-spots directly adjacent to the remaining pore sites. After removing the outliers, the average von Mises stress on the surface was calculated for each case. This average residual stress provides a single representative measure to compare the effectiveness of HIP on relieving stresses for different initial porosities.

Table 4.13 summarizes the filtered average PEEQ, CEEQ, and von Mises stress at the top surface for each initial porosity. The expected trend is that a higher initial porosity leads to greater overall deformation (since more void volume must be compacted). Indeed, the results show that as the initial void fraction increases, the inelastic strain (especially CEEQ) in the material increases. However, the trends are not strictly monotonic for the amount of strain: the CEEQ increases fairly consistently with porosity, but the PEEQ first increases and then declines at the highest initial porosities. Additionally, the residual von Mises stress on the surface, rather than decreasing with more plastic relaxation, increases markedly for the higher initial porosities (0.5–0.8%) after removing the outliers. The following discussion elaborates on these patterns in detail and explains the physical mechanisms responsible for the observed behavior.

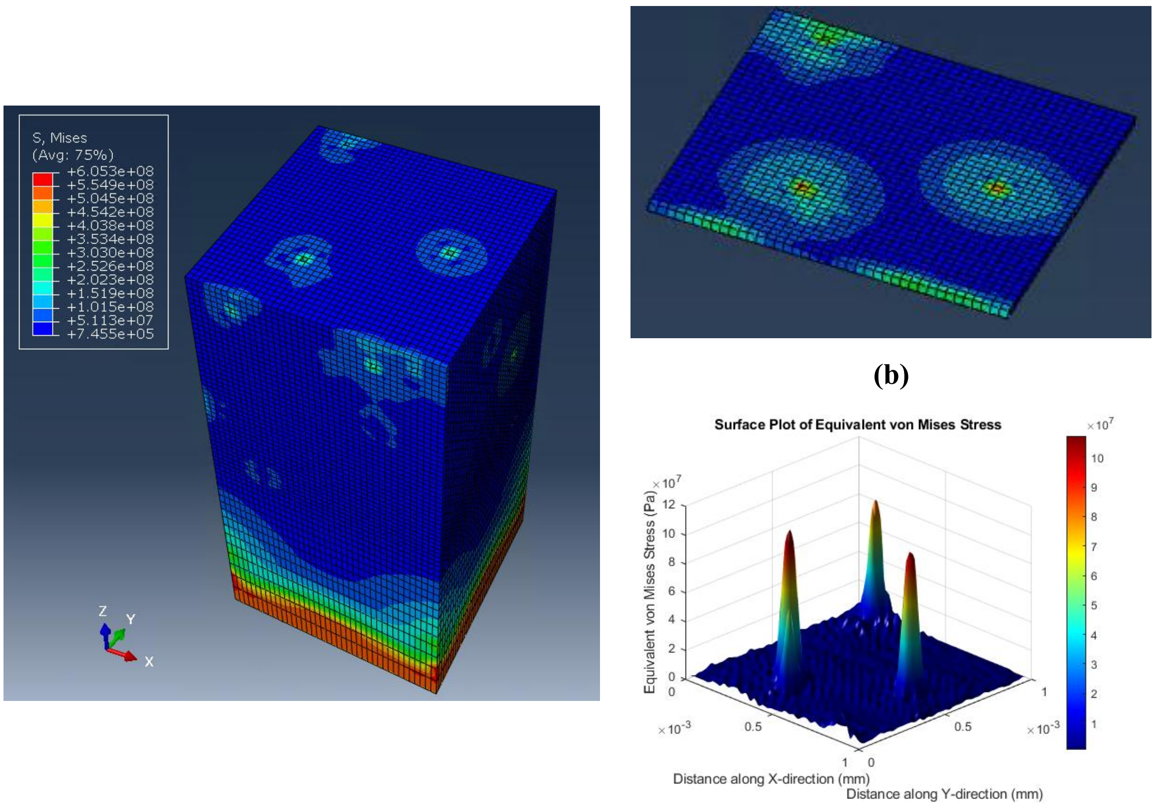

(a) (b) (c)

Figure 4.32 (a) Equivalent von Mises stress distribution in laser powder bed fused sample with 0.1% porosity after HIP (700°C, 200 MPa), (b) isolated single layer of finite elements at the top of component, and (c) surface plot of equivalent von Mise stress for single layer.

Table 4.13 Average values of PEEQ, CEEQ, and equivalent von Mises stress at end of HIP process (P=200 MPa, T=700ºC) under different void percentages

Void (%)	PEEQ	CEEQ	Post-HIP surface von Mises (MPa)	ΔStress = 352–Post (MPa)	Stress reduction (%)
0.25	2.41×10^{-4}	2.21×10^{-3}	5.24	346.76	98.51
0.35	2.53×10^{-4}	3.38×10^{-3}	5.19	346.81	98.53
0.40	2.61×10^{-4}	2.49×10^{-3}	4.47	347.53	98.73
0.50	2.26×10^{-4}	5.16×10^{-3}	7.46	344.54	97.88
0.65	2.16×10^{-4}	6.33×10^{-3}	9.12	342.88	97.41
0.80	1.47×10^{-4}	8.23×10^{-3}	11.8	340.20	96.65

According to Table 4.13, the CEEQ on the surface increases with initial porosity, as expected. Quantitatively, the average surface CEEQ increases from $\sim2.2\times10^{-3}$ at an initial porosity of 0.25% to $\sim8.2\times10^{-3}$ at 0.80%, which is roughly a fourfold increase. In other words, the top layer experienced about a 0.2% CEEQ at the lowest initial porosity, which increases to ~0.8% at the highest initial porosity. This pattern makes sense because creep deformation is the primary mechanism by which pores are eliminated in HIP conditions. A higher void volume means the material must undergo more time-dependent viscoplastic flow to collapse and heal those pores within the given holding time.

Unlike the CEEQ, the PEEQ on the surface does not simply increase with porosity – the data in Table 4.13 reveal that the PEEQ first peaks at a moderate porosity then declines at higher porosity. For instance, the average surface PEEQ is about 2.6×10^{-4} (0.026%) at an initial porosity of 0.4%, which is higher than the $\sim2.4\times10^{-4}$ at 0.25%, but with an initial porosity of 0.8%, the PEEQ is reduced to $\sim1.47\times10^{-4}$ (0.015%). In other words, a small amount of porosity (up to ~0.4%) increases the extent of plastic deformation, but further increases to 0.8% on average result in less PEEQ on the surface. Several factors related to the mechanics of void closure and material behavior explain for this non-monotonic pattern.

Under an applied hydrostatic pressure of 200 MPa at 700°C, the material will plastically yield in the immediate vicinity of the pores early in the HIP cycle. A void acts like a stress concentrator – the surrounding material is subjected to a deviatoric stress sufficient to cause yielding at the pore surface. This localized plastic flow helps to initiate pore collapse by slightly reducing the void volume. At low overall porosity, only a few such yielding events occur (around the few pores present). Much of the surface does not have any PEEQ at all because those regions are far from any void. Thus, the average PEEQ for a very low porosity sample is low. As the porosity increases, more pores are present to trigger more widespread plastic zones. Between an initial porosity of 0.25% and 0.4%, the average PEEQ rose slightly (from ~2.4×10^{-4} to ~2.6×10^{-4}) because more surface area was affected by plastic yielding near the pores. Essentially, the initial addition of porosity involves new regions in plastic deformation that were previously elastic.

Plastic strain around each void is limited by the hardening behavior of the material. Once the material at a pore edge yields and deforms, it undergoes strain hardening, which increases the local yield strength. Under a fixed external pressure, there is a limit to the amount of accumulated PEEQ. After a certain amount of plastic flow, the material strength increases to the point that further yielding becomes difficult without additional load. In the simulations, the PEEQ near the pores showed the tendency to reach a maximum in the order of a few tenths of a percent (e.g., ~0.28–0.5% PEEQ locally by the end of the holding). More importantly, once the material that surrounds a pore has yielded to this extent, additional void closure occurs mainly through creep rather than further plastic stretching. Therefore, there is effective saturation of PEEQ around each pore.

With a larger initial porosity (0.5–0.8%), one might expect many more plastic zones and thus a higher total PEEQ. However, the presence of more or larger pores does not produce proportionally more PEEQ; instead, the material yields in more regions but to a similarly limited extent. The average PEEQ actually decreases at the highest initial porosity because the pores are closer together and much of the surface has already undergone plastic yielding. As a result, their deformation zones can interfere or overlap, thus altering the distribution of PEEQ. When two pores are in proximity, the material between them is compressed from both sides. This increased constraint makes it harder for the material to yield as freely as it would around an isolated pore—there is less space for plastic flow because the neighboring pores are trying to collapse simultaneously. In effect, the plastic zones around the adjacent pores may merge or constrain one another, which causes the material to yield once to accommodate both pores rather than yielding independently for each. This interaction reduces the incremental PEEQ contributed by each additional pore at high pore densities. Consequently, the average PEEQ does not continue to increase; it can even decline if most of the new voids interact with the existing ones instead of generating new, independent yield regions.

Starting from an average as-built surface stress of ~352 MPa, HIP reduces the surface residual stress by roughly 97–99% across all porosities, which decreases the stress down to a range of 5–12 MPa. The least amount of surface stress post-HIP is found at an approximate initial porosity of 0.40% (~4.47 MPa), which correspond to the largest absolute decline (≈347.5 MPa; 98.7%). Beyond this point, the surface stress increases with porosity, reaching ~11.8 MPa at 0.80% (a 96.7% reduction). Thus, while HIP consistently delivers a very large stress relief relative to the initial state, the residual surface stress after HIP varies non-linearly with porosity — dipping near 0.4% and then increasing from 0.5% to 0.8% (Table 4.13; Figure 4.33). This behavior is explained in the following paragraphs.

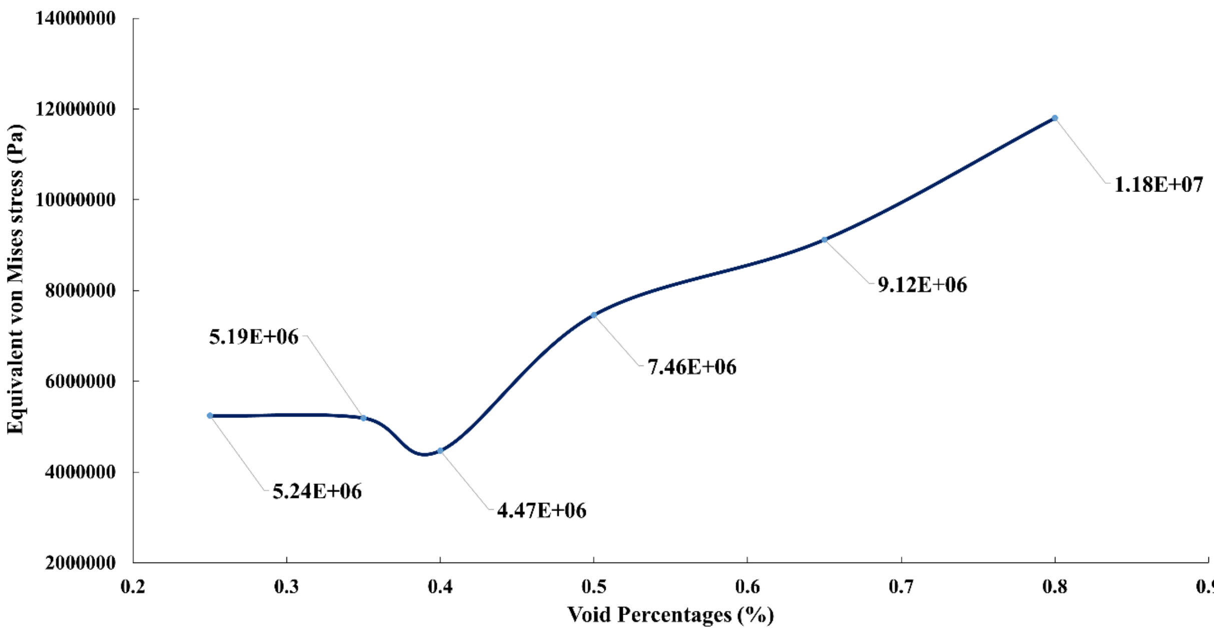

Figure 4.33 Average equivalent von Mises stress at top surface of sample after HIP as a function of initial void percentage.

The residual stress after HIP is primarily from the differential plastic and creep deformations—different regions deform to varying extents, and upon unloading and cooling, some zones pull against others. At low porosity, deformation is highly localized near isolated pores, and the remaining material deforms mostly elastically. These localized plastic zones effectively relieve stress, while the surrounding elastic material can largely equilibrate without large internal stress gradients after unloading. Therefore, a mostly homogeneous, fully dense solid with one or two healed pores will cool down with minimal residual mismatch. This is why the sample with an initial porosity of 0.25% has a very low average residual stress (~5 MPa) – apart from a couple of tiny regions near pores, the entire surface was essentially stress-free after HIP.

As porosity increases, deformation becomes more widespread but non-uniform. Different surface regions undergo different amounts of deformation: some areas (near the pores) have compressed and crept significantly, while others (perhaps between pores or near fewer pores) deformed less. Once the HIP pressure is removed, these regions cannot all return to a stress-free state because they have permanent strain differences. The result is a patchwork of residual stresses. Notably, the material that underwent significant plastic collapse of pores becomes surrounded by material that did not deform as much, thus leading to internal stress as they are bonded together. As porosity increases, this heterogeneity in strain is more pronounced, so there is overall more residual stress in the surface layer. Furthermore, when the pores are close together (as in higher-porosity samples), the material between them experiences multiaxial compression during HIP. This stress state is less effective at producing plastic flow than a uniaxial or simple shear state, as the material is constrained from all sides by the opposing pressure of the neighboring pore collapses. As a result, some of the inter-pore ligaments may not yield fully during the HIP cycle and instead carry high compressive stresses throughout the holding period. When the external hydrostatic pressure is removed, these ligaments rebound elastically, thus potentially inducing tensile residual stresses in themselves or the adjacent regions. In essence, closely spaced pores can trap stress within the material because deformation cannot occur freely in all directions. This effect can lead to higher residual stress concentration in high-porosity samples compared to those with isolated pores, which allow the surrounding material more freedom to deform. Paradoxically, while isolated pores (as in low-porosity cases) generate very high local stresses during HIP, they also allow the material to yield and creep sufficiently, thereby relaxing most of that stress by the end of the cycle. In contrast, clusters of pores (high porosity) form a stiffer, more constrained network that cannot fully relax, thus resulting in a higher residual stress after HIP.

Additionally, strain hardening plays a crucial role in limiting stress relief at higher porosities. When a pore closes under hydrostatic pressure, the surrounding material undergoes yielding and creep, which reduces the local stress during high-temperature holding. However, as the material strain-hardens and creep slows down while approaching equilibrium, the stress is not fully eliminated around the pore. In fact, after significant creep deformation, a localized increase in stress can occur near a pore, toward the end of the holding which is attributed to strain hardening in regions that have experienced substantial deformation. This means that by the end of the HIP cycle, the material that surrounds the pores may increase in strength (with higher yield strength due to accumulated PEEQ) while still retaining some residual stress. In contrast, such effects do not occur with distance from the pores, and the surface stress drops to nearly zero by the end of the process. In high-porosity samples, there are many regions adjacent to the pores where strain hardening has locked in stress—these areas can no longer yield to fully relieve the pressure-induced stresses. Upon cooling and unloading, these hardened regions retain a portion of the residual stress. At low porosity, such regions are sparse, and once the pressure is removed, most of the surface relaxes to a nearly stress-free state. At high porosity, however, the entire surface is populated by hardened, deformed zones that collectively hold residual stress, thus leading to a higher average von Mises stress.

The results of the present simulations are consistent with the findings reported by Tammas-Williams et al.[100] and Cegan et al.[139]. In particular, Cegan et al.[139] reported that the reduction in void volume fraction after HIP in 316L stainless steel fabricated by LPBF (analyzed by using XCT) does not follow a monotonic relationship with the initial porosity. Within an initial porosity range of 0.13–0.69, the percentage of void reduction first increases and then decreases with increase in porosity. A similar non-monotonic trend is observed in Williams et al.[100] for titanium produced by selective electron beam melting. In that study, complete (100%) void reduction occurs up to an initial porosity of 0.202, whereas for higher porosity levels (0.225–0.625), the reduction percentage decreases with increasing initial porosity. These findings support the non-monotonic relationship between initial porosity and densification efficiency through HIP.

4.2.2.3 Effect of Void Geometry Type (Through-Hole, Surface Void, Sharp-Cornered Defects) on Plastic Flow and Stress Reduction

Understanding the influence of the type of defect on local stress distribution is essential for explaining why only certain imperfections lead to plastic deformation during HIP. As illustrated in Figure 4.34, the geometry includes three distinct surface features: a through-thickness hole, surface recess (shallow circular cavity), and sharp re-entrant corner represented by the letter R. These geometries are often mistaken for voids; however, under HIP conditions, their stress response differs fundamentally from that of an embedded void.

During HIP, the external gas applies a uniform hydrostatic pressure P_∞ on all exposed surfaces. For both the through-hole and surface recess, the internal surfaces of these features are directly in contact with the same gas environment. Consequently, the internal pressure that acts on these surfaces equals the external hydrostatic pressure, i.e. $P_i = P_\infty$. Under this condition, no pressure differential exists across the defect boundary, and therefore no additional local stress concentration is generated in the surrounding solid. The resulting stress state remains purely hydrostatic and is identical to the hydrostatic tensor previously defined in Equation (3.26). As established earlier in Equations (3.26)–(3.29), a purely hydrostatic stress field produces zero deviatoric stress and zero von Mises equivalent stress.

Since all three principal stresses are equal ($\sigma_1 = \sigma_2 = \sigma_3 = P_\infty$), there is no differential stress and thus no shear component on any plane within the material. According to stress-transformation relations, when the normal stresses are equal in all directions, the shear stress (τ) is zero for any orientation of the plane, and the von Mises equivalent stress (σ_{eq}) also vanishes. Therefore, neither the through-hole, surface recess, nor sharp tip of the "R" feature can induce plastic flow during HIP, even though they appear geometrically discontinuous. The applied hydrostatic pressure merely causes uniform elastic volumetric compression. This concept highlights that only closed or embedded voids, where the internal pressure (P_i) is lower than the external hydrostatic pressure (P_∞), can generate non-uniform stresses that lead to local shear and plastic deformation.

As presented in Table 4.14, the FE results clearly show that the von Mises stress reduction at Points A, B, and C is nearly the same under both furnace and HIP conditions. This finding confirms that when the defect is fully open to the external surface, such as a through-holes, surface recesses, or sharp corners, the application of external HIP pressure does not provide any additional benefit compared to simple furnace heating. In such geometries, the internal surfaces of these openings are directly exposed to the surrounding gas pressure, thus leading to a uniform hydrostatic stress field with no differential or deviatoric component. Consequently, no plastic flow or shear stress can develop within the material that surrounds these features, and the von Mises equivalent stress effectively vanishes.

Table 4.14 Von Mises stress at 600°C: furnace vs HIP conditions

Point	Condition	Initial Stress (MPa)	Final Stress (MPa)	Stress Reduction (MPa)
A	Furnace	478	47	431
A	HIP (100 MPa)	478	47	431
B	Furnace	425	43	382
B	HIP (100 MPa)	425	43	382
C	Furnace	359	51	308
C	HIP (100 MPa)	359	51	308

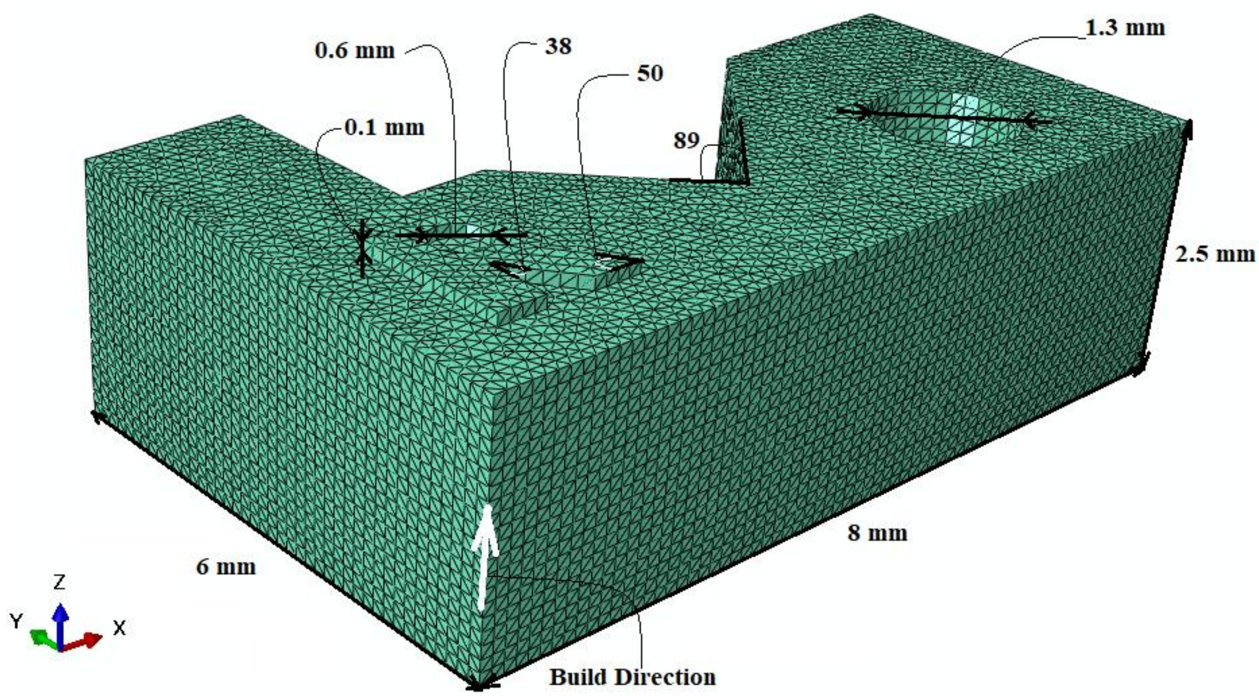

Figure 4.34 Schematic mesh of R-feature model showing through-hole, surface recess, and sharp re-entrant corner under uniform HIP pressure.

At all three representative points—Points A (sharp R edge), B (center of the circular recess), and C (top of the through-hole surface)—the stress relaxation is governed solely by thermal effects and material softening, not by pressure-induced deformation. Both HIP (100 MPa) and furnace treatments at 600°C yield the same reductions of approximately 308–431 MPa, thus confirming that the external hydrostatic pressure cannot influence stress relaxation in surface-connected defects. This behavior aligns with the theoretical explanation and previous reports. For example, Tammas-Williams et al.[100] and Cegan et al.[139] emphasized that HIP is effective primarily for enclosed or internal voids, where the externally applied pressure is transmitted hydrostatically through the material. Similar observations have also been reported in other studies[31,137,205,209,216,217], which indicated that external hydrostatic pressure has no mechanical influence on open or surface-connected defects.

4.3 Validation and Limitations of the Developed Framework

The finite element frameworks developed in this thesis were validated through comparison with experimental observations and previously validated numerical results reported in the literature[38,82,97,100,108,113,135–139,157,167,191,192,197–207,209,216,217]. It should be emphasized that no direct experimental work was conducted as part of this PhD study. Therefore, the validation process relied on published studies related to residual stress generation during LPBF, stress relaxation during furnace treatment, and HIP-induced stress relaxation.

The primary objective of the validation exercise was not to achieve exact quantitative agreement with experimental studies, but rather to determine whether the developed models could reproduce the qualitative trends and governing mechanisms reported in the literature. Particular attention was given to residual stress generation during LPBF, stress relaxation during furnace treatment and HIP, pore closure during HIP, and the influence of processing parameters such as temperature, hydrostatic pressure, and defect characteristics. The following sections compare the present simulation results with published experimental observations and numerical investigations to assess the capability of the developed framework to capture the dominant physical behavior associated with LPBF and HIP processing.

4.3.1 Validation of LPBF Residual Stress Predictions

The LPBF residual stress predictions were evaluated by examining whether the developed finite element framework could reproduce the dominant thermal and mechanical trends reported in experimental and numerical studies on laser powder bed fused components. The validation presented in this section is based on comparison with the published studies listed in Refs[38,52,58,59,155,184–198], which include both experimental measurements and previously validated numerical investigations. The validation was not based solely on comparing final stress magnitudes, but also on assessing whether the model captured the sequence of physical events responsible for residual stress formation during LPBF. These events include rapid local heating by the moving laser, formation of a small melt pool and heat-affected zone, steep spatial and temporal thermal gradients, constrained thermal expansion during heating, contraction during cooling, and the accumulation of tensile and compressive residual stresses after solidification.

The first indication of model reliability is its ability to reproduce the transient thermal behavior of the LPBF process. The predicted temperature history at the selected point showed repeated rapid heating and cooling cycles as successive layers were deposited. This behavior is physically consistent with the layer-by-layer nature of LPBF, where the heat source directly affects a material point only when the laser passes near that location and then affects it indirectly through reheating from subsequent layers. The fact that the temperature fluctuations became less significant after several layers is also reasonable because the selected point becomes progressively farther from the active heat source. This trend supports the physical validity of the thermal model, since residual stress generation in LPBF is governed by the same repeated thermal cycling and reheating behavior.

The predicted melt-pool and heat-affected-zone profiles further support the validity of the LPBF thermal model. The simulations produced a localized melt pool with an elongated comet-tail-shaped temperature distribution behind the moving laser. This behavior is consistent with the expected asymmetry of heat flow during LPBF, where heat is concentrated near the laser spot and is then conducted into the surrounding powder, solidified material, and substrate. The steeper thermal gradient ahead of the laser compared with the rear region is also physically reasonable because the material in front of the laser remains relatively cold, whereas the material behind the laser has already been heated. Therefore, the agreement in melt-pool shape and thermal-gradient distribution indicates that the Goldak heat source representation used in the model captured the main features of laser-material interaction sufficiently well for residual stress prediction.

The predicted in-process stress evolution also agrees with the experimentally observed mechanism of residual stress formation in LPBF. During laser heating, the material attempts to expand but is constrained by the colder surrounding material, leading to compressive stress in the heated zone. During subsequent cooling, contraction is restricted by the surrounding solidified material and by the plastic strain accumulated during heating, which leads to tensile stress development. This alternating compressive–tensile response explains the stress fluctuations predicted in S_{11} and S_{22} during the early layers. Experimental studies have shown that tensile stresses are introduced into the material beneath newly deposited layers during the build-up process, particularly within the build plane. The present simulations reproduced the same physical trend, which suggests that the model captured the constrained thermal expansion and contraction mechanisms responsible for residual stress accumulation.

The spatial distribution of the predicted stress components provides an additional level of validation. The simulations showed that S_{11} and S_{22} were strongly influenced by the scan-track direction, whereas S_{33} behaved differently because it was governed more strongly by material deposition, substrate constraint, and evolving build geometry. This distinction is physically meaningful. In LPBF, heat input is concentrated along the laser path, producing stronger thermal gradients and higher stresses along the scan direction. Therefore, the larger residual stresses predicted along the track direction are consistent with the expected directional nature of thermal loading in LPBF. In contrast, the low value of S_{33} near the free top surface is also reasonable because the surface is not mechanically constrained in the build direction. As more layers are added, the selected material point becomes embedded within the component, and the build-direction stress evolves because the local constraint state changes. This behavior explains why S_{33} becomes more significant away from the free surface and supports the ability of the model to capture geometry- and constraint-dependent stress evolution.

The model also reproduced the commonly reported residual stress distribution in LPBF components, where tensile stresses are formed near the surface and lower or compressive stresses are developed in interior or substrate-adjacent regions. This trend occurs because the surface layers cool more rapidly due to their exposure to the surrounding environment, producing contraction and tensile residual stress. In contrast, interior regions experience slower cooling and stronger constraint from the surrounding material, which can lead to compressive stress development. The present simulations reproduced this surface-to-interior stress variation, which is consistent with experimental observations reported using residual stress measurement techniques such as neutron diffraction, X-ray diffraction, contour analysis, and hole-drilling methods. This agreement is important because it shows that the model does not only reproduce local thermal histories, but also captures the larger stress redistribution pattern produced by thermal gradients and mechanical constraints during LPBF.

The predicted influence of process parameters further supports the validity of the model. The simulations showed that laser speed had a stronger influence on residual stress than laser power. This trend is physically reasonable because laser speed directly controls the exposure time of the material to the heat source, thereby strongly affecting cooling rate, thermal-gradient development, and the time available for stress relaxation during solidification. A slower laser speed increases dwell time and can promote a more uniform temperature distribution, reducing thermal gradients and lowering residual stress. This interpretation is consistent with studies reporting that lower cooling rates and higher energy input per unit length can reduce residual stress in LPBF components when adequate density is maintained. Similarly, the predicted effect of increasing laser power is consistent with the idea that higher energy input can enlarge and flatten the melt pool, reduce cooling rate, and reduce the magnitude of surface tensile stress under appropriate processing conditions.

The strongest agreement with the literature was observed for the effect of preheating. The simulations showed that increasing the preheating temperature substantially reduced the magnitude of residual stresses. This trend is expected because preheating reduces the temperature difference between the melt pool, the substrate, and the previously solidified material. As a result, thermal gradients and cooling rates are reduced, which decreases the driving force for residual stress formation. In addition, elevated preheating temperatures reduce the effective yield strength and elastic modulus of the material, making it easier for thermal stresses to relax during fabrication. Therefore, the reduction in residual stress caused by preheating is not only a numerical outcome of the model, but also follows directly from the thermal and mechanical response of the material at elevated temperatures. The agreement between this predicted trend and published experimental and numerical observations provides confidence that the model captured the dominant mechanisms by which preheating mitigates LPBF-induced residual stresses.

Overall, the LPBF validation demonstrates that the developed finite element framework is capable of reproducing the main qualitative trends and physical mechanisms governing residual stress formation during LPBF. The model captured the transient thermal cycles, melt-pool shape, scan-direction-dependent stress distribution, surface tensile stress formation, interior compressive stress development, and the relative influence of laser speed, laser power, and preheating temperature. Although exact quantitative agreement with any single experimental study was not the objective of this work, the consistency between the present simulations and published experimental and numerical observations indicates that the predicted LPBF residual stress field is physically reasonable and suitable for use as the initial stress state in the subsequent furnace and HIP simulations.

4.3.2 Validation of HIP-Induced Stress Relaxation and Porosity Closure

The HIP-induced stress relaxation and pore-closure predictions were validated by examining whether the developed numerical framework could reproduce the experimentally reported differences between conventional furnace treatment and HIP. The discussions presented in this section are based on comparisons with the experimental observations and numerical investigations reported in Refs[12,31,36,82,97,100,108,113,135–143,157,167,199–217]. The comparison is important because both treatments involve elevated temperature, but only HIP introduces externally applied hydrostatic pressure. Therefore, agreement with published observations requires the model to reproduce not only temperature-driven stress relaxation, but also the additional deformation mechanisms activated by pressure in the presence of internal defects.

The furnace simulations showed that residual stress relaxation can occur under temperature alone, mainly through temperature-driven creep. This trend is physically reasonable because increasing temperature reduces the yield strength and elastic modulus of the material, allowing part of the elastic strain to transform into plastic strain and promoting creep deformation over time. However, the furnace simulations also showed that, although residual stress was reduced, the internal pores remained largely unchanged. This behavior agrees with experimental observations reported for furnace-treated LPBF components, where standalone heat treatment reduces residual stress but does not provide sufficient mechanical driving force for pore closure. Therefore, the furnace results validate the temperature-driven portion of the model while also demonstrating the limitation of temperature alone in eliminating enclosed porosity.

In contrast, the HIP simulations reproduced the experimentally observed trend that combined temperature and hydrostatic pressure produces greater residual stress relaxation and promotes pore closure. This behavior is consistent with experimental studies reporting that HIP can reduce porosity, close internal defects, and transform tensile residual stresses into lower tensile or compressive stress states. The present simulations captured the same qualitative response: under HIP conditions, the residual stress decreased more than under furnace treatment, and the material near enclosed pores underwent greater plastic and creep deformation. This agreement supports the physical validity of the HIP model because it reproduces the key experimental distinction between furnace treatment and HIP: temperature reduces residual stress, whereas hydrostatic pressure enables additional defect-assisted deformation and densification.

The reason HIP produces a stronger response than furnace treatment can be understood from the analytical framework presented in Chapter 3. Under purely hydrostatic loading in a fully dense material, the principal stresses are equal, the deviatoric stress vanishes, and the von Mises equivalent stress remains zero. Therefore, externally applied hydrostatic pressure alone cannot induce additional plastic deformation in a defect-free material. This explains why hydrostatic pressure should not be expected to enhance stress relaxation simply by being applied uniformly to a fully dense body. However, enclosed internal voids disrupt the hydrostatic stress state. Around an enclosed defect, the externally applied hydrostatic pressure is not transmitted uniformly through the missing material inside the void, and this creates local stress gradients and deviatoric stress components around the void surface. These localized deviatoric stresses generate shear stresses that can activate plastic deformation and accelerate creep. Thus, the numerical results are consistent with the analytical prediction that the beneficial effect of HIP is controlled by the interaction between pressure and enclosed internal defects, rather than by hydrostatic pressure acting alone.

This mechanism also explains why the difference between HIP and furnace treatment was more pronounced in regions located near pores than in regions farther away from pores. In the simulations, locations in the vicinity of pores exhibited substantially greater creep and plastic deformation than regions farther from the defects. Under furnace conditions, this difference was caused mainly by the initial stress concentration around the pore. Under HIP conditions, the difference became more significant because the applied hydrostatic pressure intensified the local stress gradients around the enclosed defect. As a result, the near-pore region experienced higher equivalent stress, greater dislocation creep, and more localized plastic deformation. This behavior is consistent with the expected response of porous materials during HIP, where deformation is concentrated around defects and material flow into the void drives pore closure.

The comparison between CEEQ and PEEQ further validates the constitutive response of the model. In both furnace and HIP simulations, the equivalent creep strain was significantly larger than the equivalent plastic strain, indicating that creep-dominated deformation governs residual stress relaxation during elevated-temperature post-processing. This trend is consistent with the hyperbolic-sine creep law used in the model, which predicts a strong non-linear dependence of creep rate on stress and temperature. The increase in CEEQ with increasing pressure is therefore physically meaningful: pressure increases the local equivalent stress around enclosed voids, and the creep law consequently predicts faster creep deformation. This explains why HIP produced greater stress relaxation than furnace treatment even when both treatments were conducted under the same thermal cycle.

The pressure-dependence of the predicted response provides further validation. Increasing the applied pressure from furnace conditions to 100 MPa and then to 200 MPa increased both creep deformation and stress relaxation, particularly near the pore. This trend is consistent with the physical role of hydrostatic pressure during HIP. Higher hydrostatic pressure increases the local stress concentration around enclosed defects, thereby increasing the equivalent stress available to drive creep and plastic flow. This pressure-assisted deformation allows the surrounding material to move into the void, which reduces pore volume and redistributes the local stress field. The fact that the effect of hydrostatic pressure was strongest near the pore and weaker far from the pore supports the conclusion that pressure is effective primarily through defect-mediated stress amplification, not through uniform hydrostatic compression of the entire component.

The model also reproduced the experimentally reported difference in pore evolution between furnace treatment and HIP. During furnace heating, the absence of external hydrostatic pressure limited material flow into the voids, so the pore morphology remained nearly unchanged. During HIP, however, pore closure began during the heating stage, accelerated during the holding stage, and was largely completed before the end of the high-temperature and high-pressure hold. This sequence is physically reasonable because temperature reduces flow resistance and activates creep, while hydrostatic pressure provides the mechanical driving force required for void collapse. The predicted pore-shape evolution therefore supports the validity of the model in capturing the coupled role of temperature and hydrostatic pressure in HIP-induced densification.

The influence of void morphology also agrees with the analytical framework developed in Chapter 3. Based on the void-geometry-dependent stress amplification analysis, more elongated or irregular voids are expected to generate higher local deviatoric stresses than near-spherical pores under external hydrostatic pressure. This is because non-spherical defects disturb the surrounding stress field more strongly and create larger stress concentrations around sharp or elongated regions. The simulations confirmed this trend: elongated and irregular voids promoted greater localized deformation, faster pore closure, and larger residual stress reduction than more compact void geometries. Therefore, the morphology-dependent numerical results are consistent with the analytical expectation that aspect ratio and geometric irregularity control the magnitude of local stress amplification during HIP.

The validation of the HIP model is therefore not limited to reproducing isolated experimental trends. Rather, the simulations reproduce a connected sequence of experimentally observed and analytically predicted behavior: furnace treatment reduces residual stress through temperature-driven creep but does not close pores; HIP produces additional stress relaxation because pressure interacts with enclosed defects; creep deformation dominates over plastic deformation during high-temperature exposure; higher hydrostatic pressure increases local deformation and pore closure; and elongated or irregular pores generate stronger localized deformation than near-spherical pores. This consistency between the analytical framework, numerical results, and experimental observations reported in the literature provides confidence that the developed model captures the dominant mechanisms governing HIP-induced stress relaxation and porosity closure in LPBF-manufactured components.

4.3.3 Limitations of the Present Numerical Framework

Although good qualitative agreement was obtained between the present simulations and the experimental data reported in the literature and previously validated numerical results, several limitations of the developed numerical framework should be acknowledged.

In the current model, stress relaxation is primarily described through plastic deformation and a stress- and temperature-dependent dislocation-creep mechanism. This level of modeling is sufficient for the primary mechanistic objective of the present study, particularly to investigate how internal voids modify the local stress state under externally applied hydrostatic pressure and generate non-zero equivalent stresses capable of promoting creep and plastic deformation. However, high-temperature stress relaxation may involve additional deformation and microstructural mechanisms that were not explicitly incorporated into the present framework.

A more comprehensive model would therefore require the progressive incorporation of additional levels of physics. At the deformation-mechanism level, these may include diffusional creep mechanisms, such as Nabarro–Herring and Coble creep, as well as grain-boundary sliding and grain-size-dependent deformation. At the microstructural level, mechanisms such as recrystallization and grain growth could be incorporated to account for their influence on the evolving material response during high-temperature exposure. At the pore scale, additional physics, including internal gas pressure, opposing-surface contact, and interfacial bonding, could provide a more complete representation of void evolution during HIP. Accordingly, the present framework does not explicitly account for the full range of deformation, microstructural, and pore-scale mechanisms that may influence residual-stress relaxation during HIP.

Additional simplifications are associated with the LPBF simulation itself. Melt-pool phenomena such as the Marangoni effect, vaporization, and keyhole instability were not explicitly simulated. Furthermore, the ABAQUS finite element formulation is based on continuum mechanics and therefore does not explicitly represent material heterogeneity.

Internal defects were represented using simplified idealized geometries to enable systematic investigation of the effects of pore size, aspect ratio, irregularity, and volume fraction. Consequently, local stress concentrations in real LPBF components may differ from those predicted by the idealized models. Although mesh-sensitivity and time-step convergence studies were conducted, local stress concentrations near void surfaces may still be influenced by mesh refinement. In addition, explicit self-contact between opposing void surfaces was not incorporated; therefore, the predicted void-collapse behavior should be interpreted up to near-closure rather than as a representation of post-contact consolidation or metallurgical healing.

Validation was performed through comparison with experimental data reported in the literature and previously validated numerical studies rather than direct experimental measurements conducted as part of the present work. Therefore, some discrepancies may arise from differences in material composition, processing parameters, specimen geometry, measurement techniques, and post-processing conditions. In some cases, increasing the processing temperature beyond a certain limit resulted in numerical convergence difficulties as the opposing void surfaces approached contact; therefore, the analysis was restricted to temperature ranges for which stable and converged solutions could be obtained.

As a result, the present framework should not yet be interpreted as a fully quantitative process-design tool for direct industrial application. For example, determining the specific combination of pressure, temperature, and holding time required to reduce an initial residual stress to a prescribed target value would require a more comprehensive multiphysics model incorporating the relevant deformation and microstructural mechanisms, together with appropriate material-specific calibration and experimental validation. The present work therefore provides a mechanistic foundation toward such a comprehensive model rather than a complete industrial predictive framework.

Despite these limitations, the developed framework successfully reproduced the dominant trends reported in the literature, including residual stress generation during LPBF, stress relaxation during furnace treatment and HIP, progressive void collapse up to near-closure, and the influence of hydrostatic pressure and defect morphology on deformation behavior. Therefore, the model is considered particularly suitable for mechanistic investigations, comparative studies, and parametric analyses aimed at improving the understanding of residual stress relaxation in LPBF-manufactured materials. Future incorporation of additional levels of physical fidelity could progressively extend the present mechanistic framework toward a more comprehensive and quantitatively predictive model.

CHAPTER FIVE: SUMMARY AND CONCLUSIONS

5.1 Summary of PhD Work

5.1.1 Residual Stress Generation in LPBF Components

This PhD research investigated the generation and mitigation of residual stresses in LPBF components, with particular emphasis on the role of HIP as a post-processing technique. LPBF inherently produces high residual stresses due to rapid localized heating and cooling during layer-by-layer fabrication. These stresses can approach the material yield strength and may lead to distortion, cracking, and reduced fatigue performance. In addition, LPBF components often contain internal porosity caused by trapped gas and lack-of-fusion defects.

To study these phenomena, a high-fidelity thermo-mechanical finite element (FE) framework based on the representative volume (RV) approach was developed to simulate the LPBF process and predict the resulting residual stress field. The model incorporated a moving laser heat source and fully coupled thermal-mechanical analyses to capture the rapid thermal cycles and stress evolution during fabrication. The predicted residual stress distributions showed good agreement with experimental data reported in the literature.

The effects of key LPBF processing parameters, including laser power, scan speed, and base-plate preheating temperature, were systematically investigated. The results demonstrated that lower scan speeds and higher laser power reduced cooling rates and thermal gradients, thereby decreasing residual stress levels. Among all parameters, base-plate preheating was found to be the most effective strategy for residual stress reduction because it moderated thermal gradients and reduced the material yield strength during fabrication. Nevertheless, even under optimized LPBF conditions, significant residual stresses remained, indicating the need for post-processing treatments.

5.1.2 Mechanisms of Stress Relaxation During HIP

The central objective of this research was to determine the additional role of hydrostatic pressure in HIP-assisted stress relaxation compared to conventional furnace heat treatment. An analytical investigation confirmed that hydrostatic pressure alone cannot produce yielding or plastic deformation in a fully dense material because it does not generate deviatoric stress. Consequently, pressure-assisted stress relaxation requires internal defects or geometric discontinuities capable of breaking hydrostatic symmetry.

Using the LPBF-generated residual stress field as the initial condition, both furnace and HIP simulations were performed under identical thermal cycles. For fully dense components without internal porosity, HIP and furnace treatments produced nearly identical levels of stress relaxation. Since the applied HIP pressure remained purely hydrostatic, no additional plastic deformation was generated beyond temperature-driven creep. Similar behavior was also observed for surface-connected features such as holes, cavities, and notches, where pressure remained symmetrically balanced.

A fundamentally different response was observed when fully enclosed internal voids were introduced into the material. Under HIP conditions, the hydrostatic pressure generated localized deviatoric stresses around the void boundaries, thereby promoting creep deformation and plastic flow. This accelerated void collapse and enhanced residual stress relaxation beyond that achieved through furnace treatment alone. These findings confirmed the central hypothesis of this work: HIP becomes more effective than furnace annealing only when internal voids are present to convert hydrostatic pressure into localized shear-driven deformation.

The combined influence of temperature and hydrostatic pressure was also investigated. Higher temperatures significantly accelerated creep kinetics, while increased hydrostatic pressure enhanced localized deformation around voids. The results demonstrated the complementary roles of temperature and hydrostatic pressure in residual stress relaxation during HIP.

5.1.3 Effect of Void Characteristics on Stress Relaxation

The final stage of the research focused on the influence of void morphology and porosity volume fraction on HIP effectiveness. Different defect geometries, including cubic, elongated, crack-like, and L-shaped voids, were examined through systematic FE simulations.

The results showed that void morphology strongly influences pressure-assisted stress relaxation. Small and near-spherical pores generated limited localized deformation and modest stress reduction, whereas elongated and irregular defects produced significantly higher stress concentrations and greater plastic deformation around the voids. In particular, crack-like and L-shaped geometries amplified pressure-induced deformation and resulted in substantially greater stress relaxation.

The porosity volume fraction was also found to affect HIP performance. Increasing porosity initially enhanced stress relaxation by providing additional sites for pressure-assisted deformation. However, excessively high porosity caused interactions between neighboring voids, restricting deformation and reducing the efficiency of stress relaxation. This behavior indicated the existence of an optimal porosity range for maximizing HIP effectiveness.

Overall, this PhD work provides valuable insight into residual stress generation and mitigation in laser powder bed fused components by using advanced simulations to link the as-built condition to the post-processed outcome. The research demonstrates that HIP is not universally superior to conventional furnace treatment; rather, its effectiveness strongly depends on the existence and characteristics of internal voids. By integrating LPBF process simulation with HIP modeling within a unified framework, this study establishes an important link between as-built defect states and post-processing behavior.

To further contextualize the findings of this research and to outline potential avenues for extending the current work, several recommendations for future research are presented in Chapter 6. These recommendations are derived directly from the limitations and insights of the present study and aim to guide both experimental validation and advanced computational developments in the field of residual stress relaxation in additively manufactured materials.

5.2 Conclusion

This PhD research developed a thermo-mechanical framework to investigate residual stress generation and relaxation in LPBF components, with particular emphasis on the mechanistic role of HIP as a post-processing technique. By integrating FE modeling, analytical formulations, and systematic parametric investigations, the study established a fundamental understanding of the relationship between internal defects, pressure-assisted deformation, and residual stress relaxation. The major conclusions of this research are summarized as follows:

1. A computationally efficient thermo-mechanical finite element framework based on the representative volume (RV) approach was developed to generate LPBF-induced residual-stress fields while reducing computational time and maintaining sufficient predictive accuracy. The

framework provides a fast tool for generating different initial residual-stress states that can be transferred to subsequent furnace and HIP simulations.

2. Residual stresses in LPBF components are primarily generated by steep thermal gradients and cyclic heating/cooling during layer-wise fabrication. Tensile stresses approaching the material yield strength were mainly concentrated near the top layers, while lower or compressive stresses developed in constrained interior regions.
3. Among the investigated LPBF process parameters, base-plate preheating was identified as the most effective method for reducing residual stresses during fabrication. Scan speed and laser power also influenced stress evolution; however, significant residual stresses still remained after processing, highlighting the necessity of post-processing treatments.
4. A key mechanistic contribution of this work is the clarification of how hydrostatic pressure can generate the non-zero equivalent stress necessary to drive dislocation motion and the associated creep and plastic deformation that contribute to residual-stress relaxation. Pure hydrostatic pressure acting on a defect-free material does not itself generate equivalent stress. Accordingly, in the absence of internal voids, HIP and equivalent furnace treatment produced comparable stress-relaxation responses because hydrostatic pressure alone could not provide the additional deviatoric stress required to activate pressure-assisted deformation.
5. The presence of internal voids fundamentally changed this response. Under externally applied hydrostatic pressure, internal voids disrupted the purely hydrostatic stress state and generated non-zero local equivalent stress in the material surrounding the void. This localized deviatoric stress promoted dislocation motion and the associated creep and plastic deformation, providing the mechanistic basis through which hydrostatic pressure can contribute to enhanced residual-stress relaxation during HIP.
6. HIP was shown to simultaneously reduce residual stresses and promote closure of internal porosity, which cannot be achieved through thermal treatment alone. The simulations demonstrated progressive void collapse under combined temperature and hydrostatic pressure, together with the associated redistribution of the local stress field. Moreover, the combined effects of high temperature and hydrostatic pressure promote a transition in the residual stress state from tensile to compressive in certain regions, which is beneficial for fatigue performance and crack resistance.

7. Void morphology was found to play a critical role in HIP efficiency. Elongated and irregular voids generated higher localized deformation and more effective stress relaxation compared to near-spherical pores. In particular, irregular geometries such as L-shaped voids produced significantly greater pressure-assisted deformation.
8. The influence of porosity volume fraction on stress relaxation was found to be non-monotonic. Moderate porosity levels enhanced pressure-induced deformation and stress reduction, whereas excessively high porosity constrained deformation due to void interaction effects.
9. Temperature and hydrostatic pressure were found to play distinct but complementary roles during HIP. Temperature controlled creep kinetics and deformation rate, while the contribution of hydrostatic pressure became significant in the presence of internal voids, where the applied hydrostatic pressure generated localized non-zero equivalent stresses around the defects. The interaction between these mechanisms governed the overall stress-relaxation response during HIP.
10. The findings demonstrate that enhanced residual-stress relaxation during HIP is not caused by hydrostatic pressure acting directly on a fully dense material. Rather, it arises from the interaction between hydrostatic pressure and internal voids, which transforms the local stress state surrounding the void and activates deformation mechanisms that contribute to additional stress relaxation. Therefore, the effectiveness of HIP relative to equivalent furnace treatment depends strongly on the presence and characteristics of internal defects.

Overall, this research advances the fundamental understanding of pressure-assisted stress relaxation in additively manufactured metals and contributes to the broader implementation of LPBF technologies through improved prediction and mechanistic understanding of post-processing behavior.

CHAPTER SIX: RECOMMENDATIONS FOR FUTURE RESEARCH

Future research should focus on both experimental validation and advanced computational modeling to further improve the understanding of HIP in LPBF-manufactured materials.

Experimentally, advanced characterization techniques such as EBSD, SEM, and X-ray computed tomography (XCT) are recommended to investigate microstructural evolution, recrystallization, and pore closure after HIP treatment. Controlled studies under varying hydrostatic pressure conditions would also help clarify the influence of hydrostatic pressure on grain evolution, dislocation recovery, and residual stress relaxation. In addition, in-situ HIP observations using synchrotron X-ray or neutron diffraction techniques could provide valuable real-time insight into pore collapse and stress-relaxation mechanisms. Future studies should also evaluate different alloy systems and LPBF process parameters to determine the general applicability of the present findings and identify material-specific HIP responses.

From a computational perspective, future work should focus on multiscale modeling approaches that couple microstructural evolution with macroscale stress-relaxation behavior. Incorporating recrystallization and phase transformation models into finite element simulations would improve prediction accuracy and strengthen comparison with experimental results. Furthermore, machine learning techniques could be used to develop efficient surrogate models for rapid prediction of HIP-induced stress-relaxation behavior.

Artificial intelligence (AI)-assisted finite element modeling provides an additional promising pathway for further increasing the computational efficiency of the framework developed in this thesis. Rather than replacing the physics-based finite element model, AI could be integrated with the validated FE framework as a computational accelerator. High-fidelity FE simulations could be used to train AI-based models that relate processing conditions, initial residual-stress states, and defect characteristics to quantities of interest such as residual-stress reduction, creep strain, plastic strain, and local equivalent stress. Once sufficiently trained and validated, these models could provide rapid predictions for new parameter combinations without requiring a complete finite element simulation for every case.

AI-assisted adaptive sampling could further reduce computational cost by identifying the most informative combinations of temperature, hydrostatic pressure, holding time, and defect characteristics for subsequent high-fidelity FE simulations. This capability would become increasingly valuable as additional physical mechanisms are incorporated into the framework, including diffusional creep, microstructural evolution, and more detailed pore-scale behavior, because these extensions would substantially increase the computational cost of the simulations. Hybrid AI–FE approaches could therefore retain the mechanistic and physics-based foundation of the present model while enabling faster parametric investigations and more efficient exploration of increasingly complex multiphysics formulations.

Overall, these future research directions will enhance the understanding of HIP-induced stress relaxation, pore closure, and microstructural evolution in additively manufactured materials.

PUBLICATIONS AND CONFERENCE PRESENTATIONS

Peer-Reviewed Journal Publications:

- **R. Mokhtari Homami**, O. Ojo, An Analytical and Numerical Investigation of the Effect of Void Morphology, Size, and Volume Fraction on Residual Stress Relaxation during Hot Isostatic Pressing of LPBF Components, ***Under Review.***
- **R. Mokhtari Homami**, O. Ojo, An Analytical and Numerical Investigation of Residual Stress Relaxation in LPBF Components during Hot Isostatic Pressing: The Critical Role of Internal Voids, ***Under Review.***
- **R. Mokhtari Homami**, P. Wanjara, J. Gholipour, G. Asala, B. Akinrinlola, O. Ojo, Numerical analysis of residual stress in a material produced by additive manufacturing and hot isostatic pressing, ***Journal of Manufacturing Processes*** 150 (2025) 1018–1039.
- **R. Mokhtari Homami,** O. Ojo, Residual Stress Analysis through Numerical Simulation in Powder Bed Additive Manufacturing using the Representative Volume Approach, The ***International Journal of Advanced Manufacturing Technology***, 129 (2023) 5581–5599.

Conference oral presentations:

- **R. Mokhtari Homami**, O. Ojo, Simulation of laser powder bed fusion process for nickel alloy Inconel 718 using representative volume. ***34th Canadian Materials Science Conference (CMSC)***, 2023.

Conference poster presentations:

- **R. Mokhtari Homami**, P. Wanjara, J. Gholipour, G. Asala, B. Akinrinlola, O. Ojo, "Numerical Characterization of Residual Stress Evolution in Additively Manufactured Materials During Hot Isostatic Pressing Under Varying Void Percentages". ***Manitoba Materials Conference (MMC), 2025***.
- **R. Mokhtari Homami**, P. Wanjara, J. Gholipour, G. Asala, B. Akinrinlola, O. Ojo, "Numerical Modeling of Residual Stress in Additively Manufactured Material During Hot Isostatic Pressing". ***36th Canadian Materials Science Conference (CMSC)***, **2025.** Best Poster Award.
- **R. Mokhtari Homami**, P. Wanjara, J. Gholipour, G. Asala, B. Akinrinlola, O. Ojo, "Numerical Analysis of Residual Stress in a Material Produced by Additive Manufacturing and Hot Isostatic Pressing". ***Manitoba Materials Conference (MMC), 2024***.

- **R. Mokhtari Homami**, O. Ojo, Finite Element Numerical Simulation of Powder Bed Fusion 3D Printing process, ***Manitoba Materials Conference (MMC), 2023***.

REFERENCES

1. Gibson, I. *et al. Additive Manufacturing Technologies*. vol. 17 (Springer, 2021).
2. Xu, J., Kontis, P., Peng, R. L. & Moverare, J. Modelling of additive manufacturability of nickel-based superalloys for laser powder bed fusion. *Acta Mater.* **240**, (2022).
3. Rezaei, A. *et al.* Contribution of hot isostatic pressing on densification, microstructure evolution, and mechanical anisotropy of additively manufactured IN718 Ni-based superalloy. *Materials Science and Engineering: A* **823**, (2021).
4. Cao, L. Mesoscopic-scale numerical investigation including the influence of scanning strategy on selective laser melting process. *Comput. Mater. Sci.* **189**, (2021).
5. Ding, X. & Wang, L. Heat transfer and fluid flow of molten pool during selective laser melting of AlSi10Mg powder: Simulation and experiment. *J. Manuf. Process.* **26**, (2017).
6. Jia, H., Sun, H., Wang, H., Wu, Y. & Wang, H. Scanning strategy in selective laser melting (SLM): a review. *International Journal of Advanced Manufacturing Technology* vol. 113 Preprint at https://doi.org/10.1007/s00170-021-06810-3 (2021).
7. Yin, J. *et al.* Vaporization of alloying elements and explosion behavior during laser powder bed fusion of Cu–10Zn alloy. *Int. J. Mach. Tools Manuf.* **161**, (2021).
8. Yadroitsev, I., Bertrand, P. & Smurov, I. Parametric analysis of the selective laser melting process. *Appl. Surf. Sci.* **253**, (2007).
9. Anwar, A. Bin & Pham, Q. C. Study of the spatter distribution on the powder bed during selective laser melting. *Addit. Manuf.* **22**, (2018).
10. Khairallah, S. A., Anderson, A. T., Rubenchik, A. & King, W. E. Laser powder-bed fusion additive manufacturing: Physics of complex melt flow and formation mechanisms of pores, spatter, and denudation zones. *Acta Mater.* **108**, (2016).
11. Guo, Q. *et al.* Transient dynamics of powder spattering in laser powder bed fusion additive manufacturing process revealed by in-situ high-speed high-energy x-ray imaging. *Acta Mater.* **151**, (2018).
12. Kasperovich, G., Haubrich, J., Gussone, J. & Requena, G. Correlation between porosity and processing parameters in TiAl6V4 produced by selective laser melting. *Mater. Des.* **105**, (2016).
13. Kok, Y. *et al.* Anisotropy and heterogeneity of microstructure and mechanical properties in metal additive manufacturing: A critical review. *Mater. Des.* **139**, (2018).

14. Fu, Y. *et al.* Machine learning algorithms for defect detection in metal laser-based additive manufacturing: A review. *Journal of Manufacturing Processes* vol. 75 Preprint at https://doi.org/10.1016/j.jmapro.2021.12.061 (2022).
15. Xue, L. *et al.* Controlling martensitic transformation characteristics in defect-free NiTi shape memory alloys fabricated using laser powder bed fusion and a process optimization framework. *Acta Mater.* **215**, (2021).
16. Radhakrishnan, J., Kumar, P., Li, S., Zhao, Y. & Ramamurty, U. Unnotched fatigue of Inconel 718 produced by laser beam-powder bed fusion at 25 and 600°C. *Acta Mater.* **225**, (2022).
17. Olakanmi, E. O., Cochrane, R. F. & Dalgarno, K. W. A review on selective laser sintering/melting (SLS/SLM) of aluminium alloy powders: Processing, microstructure, and properties. *Progress in Materials Science* vol. 74 Preprint at https://doi.org/10.1016/j.pmatsci.2015.03.002 (2015).
18. Volpato, G. M., Tetzlaff, U. & Fredel, M. C. A comprehensive literature review on laser powder bed fusion of Inconel superalloys. *Additive Manufacturing* vol. 55 Preprint at https://doi.org/10.1016/j.addma.2022.102871 (2022).
19. Dryepondt, S. *et al.* High temperature high strength austenitic steel fabricated by laser powder-bed fusion. *Acta Mater.* **231**, (2022).
20. Yamashita, Y., Murakami, T., Mihara, R., Okada, M. & Murakami, Y. Defect analysis and fatigue design basis for Ni-based superalloy 718 manufactured by selective laser melting. *Int. J. Fatigue* **117**, (2018).
21. Becker, T. H., Dhansay, N. M., Haar, G. M. Ter & Vanmeensel, K. Near-threshold fatigue crack growth rates of laser powder bed fusion produced Ti-Aal-4V. *Acta Mater.* **197**, (2020).
22. Blakey-Milner, B. *et al.* Metal additive manufacturing in aerospace: A review. *Mater. Des.* **209**, (2021).
23. Zaeh, M. F. & Branner, G. Investigations on residual stresses and deformations in selective laser melting. *Production Engineering* **4**, (2010).
24. Shi, Q., Gu, D., Xia, M., Cao, S. & Rong, T. Effects of laser processing parameters on thermal behavior and melting/solidification mechanism during selective laser melting of TiC/Inconel 718 composites. *Opt. Laser Technol.* **84**, (2016).

25. Zhang, B., Li, Y. & Bai, Q. Defect Formation Mechanisms in Selective Laser Melting: A Review. *Chinese Journal of Mechanical Engineering (English Edition)* vol. 30 Preprint at https://doi.org/10.1007/s10033-017-0121-5 (2017).

26. Thijs, L., Verhaeghe, F., Craeghs, T., Humbeeck, J. Van & Kruth, J. P. A study of the microstructural evolution during selective laser melting of Ti-6Al-4V. *Acta Mater.* **58**, (2010).

27. Rombouts, M., Kruth, J. P., Froyen, L. & Mercelis, P. Fundamentals of selective laser melting of alloyed steel powders. *CIRP Ann. Manuf. Technol.* **55**, (2006).

28. Gu, D. D., Meiners, W., Wissenbach, K. & Poprawe, R. Laser additive manufacturing of metallic components: Materials, processes and mechanisms. *International Materials Reviews* vol. 57 Preprint at https://doi.org/10.1179/1743280411Y.0000000014 (2012).

29. Delgado, J., Ciurana, J. & Rodríguez, C. A. Influence of process parameters on part quality and mechanical properties for DMLS and SLM with iron-based materials. in *International Journal of Advanced Manufacturing Technology* vol. 60 (2012).

30. Yadroitsev, I. & Smurov, I. Selective laser melting technology: From the single laser melted track stability to 3D parts of complex shape. in *Physics Procedia* vol. 5 (2010).

31. Aboulkhair, N. T., Everitt, N. M., Ashcroft, I. & Tuck, C. Reducing porosity in AlSi10Mg parts processed by selective laser melting. *Addit. Manuf.* **1**, (2014).

32. Weingarten, C. *et al.* Formation and reduction of hydrogen porosity during selective laser melting of AlSi10Mg. *J. Mater. Process. Technol.* **221**, (2015).

33. Sames, W. J., Medina, F., Peter, W. H., Babu, S. S. & Dehoff, R. R. Effect of process control and powder quality on inconel 718 produced using electron beam melting. in *8th International Symposium on Superalloy 718 and Derivatives 2014* (2014). doi:10.1002/9781119016854.ch32.

34. Elmer, J. W., Vaja, J., Carlton, H. D. & Pong, R. The effect of Ar and N2 shielding gas on laser weld porosity in steel, stainless steels, and nickel. *Weld. J.* **94**, (2015).

35. Gong, H., Rafi, K., Gu, H., Starr, T. & Stucker, B. Analysis of defect generation in Ti-6Al-4V parts made using powder bed fusion additive manufacturing processes. *Addit. Manuf.* **1**, (2014).

36. King, W. E. *et al.* Observation of keyhole-mode laser melting in laser powder-bed fusion additive manufacturing. *J. Mater. Process. Technol.* **214**, (2014).

37. Qiu, C. *et al.* On the role of melt flow into the surface structure and porosity development during selective laser melting. *Acta Mater.* **96**, (2015).

38. Kruth, J. P., Deckers, J., Yasa, E. & Wauthlé, R. Assessing and comparing influencing factors of residual stresses in selective laser melting using a novel analysis method. *Proceedings of the Institution of Mechanical Engineers, Part B: Journal of Engineering Manufacture* vol. 226 Preprint at https://doi.org/10.1177/0954405412437085 (2012).

39. Sames, W. J., List, F. A., Pannala, S., Dehoff, R. R. & Babu, S. S. The metallurgy and processing science of metal additive manufacturing. *International Materials Reviews* vol. 61 Preprint at https://doi.org/10.1080/09506608.2015.1116649 (2016).

40. DebRoy, T. *et al.* Additive manufacturing of metallic components – Process, structure and properties. *Progress in Materials Science* vol. 92 Preprint at https://doi.org/10.1016/j.pmatsci.2017.10.001 (2018).

41. Song, X. *et al.* Advances in additive manufacturing process simulation: Residual stresses and distortion predictions in complex metallic components. *Mater. Des.* **193**, 108779 (2020).

42. Chen, H. & Yan, W. Spattering and denudation in laser powder bed fusion process: Multiphase flow modelling. *Acta Mater.* **196**, (2020).

43. Gokcekaya, O. *et al.* Unique crystallographic texture formation in Inconel 718 by laser powder bed fusion and its effect on mechanical anisotropy. *Acta Mater.* **212**, (2021).

44. Jia, Q. & Gu, D. Selective laser melting additive manufacturing of Inconel 718 superalloy parts: Densification, microstructure and properties. *J. Alloys Compd.* **585**, (2014).

45. Kwabena Adomako, N., Haghdadi, N. & Primig, S. Electron and laser-based additive manufacturing of Ni-based superalloys: A review of heterogeneities in microstructure and mechanical properties. *Materials and Design* vol. 223 Preprint at https://doi.org/10.1016/j.matdes.2022.111245 (2022).

46. Wei, C. *et al.* Understanding of process and material behaviours in additive manufacturing of Invar36/Cu10Sn multiple material components via laser-based powder bed fusion. *Addit. Manuf.* **37**, (2021).

47. Kruth, J.-P. *et al.* On-line monitoring and process control in selective laser melting and laser cutting. *Proceedings of the 5th Lane Conference, Laser Assisted Net Shape Engineering* **1**, (2007).

48. Tillmann, W. *et al.* Hot isostatic pressing of IN718 components manufactured by selective laser melting. *Addit. Manuf.* **13**, (2017).

49. Shen, F., Zhu, W., Zhou, K. & Ke, L. L. Modeling the temperature, crystallization, and residual stress for selective laser sintering of polymeric powder. *Acta Mech.* **232**, (2021).

50. Xiao, Z. *et al.* Study of residual stress in selective laser melting of Ti6Al4V. *Mater. Des.* **193**, (2020).

51. Matsumoto, M., Shiomi, M., Osakada, K. & Abe, F. Finite element analysis of single layer forming on metallic powder bed in rapid prototyping by selective laser processing. *Int. J. Mach. Tools Manuf.* **42**, (2002).

52. Patil, R. B. & Yadava, V. Finite element analysis of temperature distribution in single metallic powder layer during metal laser sintering. *Int. J. Mach. Tools Manuf.* **47**, (2007).

53. Hussein, A., Hao, L., Yan, C. & Everson, R. Finite element simulation of the temperature and stress fields in single layers built without-support in selective laser melting. *Mater. Des.* **52**, (2013).

54. Paul, R., Anand, S. & Gerner, F. Effect of thermal deformation on part errors in metal powder based additive manufacturing processes. *J. Manuf. Sci. Eng.* **136**, (2014).

55. Van Belle, L., Vansteenkiste, G. & Boyer, J. C. Comparisons of numerical modelling of the Selective Laser Melting. in *Key Engineering Materials* vols 504–506 (2012).

56. Price, S., Cheng, B., Lydon, J., Cooper, K. & Chou, K. On Process Temperature in Powder-Bed Electron Beam Additive Manufacturing: Process Parameter Effects. *Journal of Manufacturing Science and Engineering, Transactions of the ASME* **136**, (2014).

57. Hodge, N. E., Ferencz, R. M. & Vignes, R. M. Experimental comparison of residual stresses for a thermomechanical model for the simulation of selective laser melting. *Addit. Manuf.* **12**, (2016).

58. Tangestani, R. *et al.* An Efficient Track-Scale Model for Laser Powder Bed Fusion Additive Manufacturing: Part 1- Thermal Model. *Front. Mater.* **8**, (2021).

59. Tangestani, R. *et al.* An Efficient Track-Scale Model for Laser Powder Bed Fusion Additive Manufacturing: Part 2—Mechanical Model. *Front. Mater.* **8**, (2021).

60. Michaleris, P., Zhang, L., Bhide, S. R. & Marugabandhu, P. Evaluation of 2D, 3D and applied plastic strain methods for predicting buckling welding distortion and residual stress. *Science and Technology of Welding and Joining* **11**, (2006).

61. Bugatti, M. & Semeraro, Q. Limitations of the inherent strain method in simulating powder bed fusion processes. *Addit. Manuf.* **23**, (2018).
62. Peyre, P. & Charkaluk, É. *Additive Manufacturing of Metal Alloys 1: Processes, Raw Materials and Numerical Simulation*. *Additive Manufacturing of Metal Alloys 1: Processes, Raw Materials and Numerical Simulation* (2022). doi:10.1002/9781394163380.
63. Celebi, A. & Appavuravther, E. Z. Analyzing the Effect of Voxel-Based Surface Mesh Application on Residual Stress with Simufact Additive Software. *Duzce University Journal of Science and Technology* **6**, (2018).
64. Shaikh, A., Shinde, A., Chinchanikar, S. & Deshpande, T. Effect of Voxel-Based Surface Mesh Size on Process Simulation for Metal Additive Manufacturing of Ti6Al4V Impeller of Centrifugal Compressor. in *Lecture Notes in Mechanical Engineering* (2022). doi:10.1007/978-981-19-2890-1_25.
65. Galati, M. & Iuliano, L. A literature review of powder-based electron beam melting focusing on numerical simulations. *Additive Manufacturing* vol. 19 Preprint at https://doi.org/10.1016/j.addma.2017.11.001 (2018).
66. Chen, S., Ma, J., Gao, H., Wang, Y. & Chen, X. Research on Residual Stresses and Microstructures of Selective Laser Melted Ti6Al4V Treated by Thermal Vibration Stress Relief. *Micromachines (Basel).* **14**, (2023).
67. Mälzer, G., Hayes, R. W., Mack, T. & Eggeler, G. Miniature specimen assessment of creep of the single-crystal superalloy LEK 94 in the 1000 °C temperature range. *Metall. Mater. Trans. A Phys. Metall. Mater. Sci.* **38**, (2007).
68. Wangyao, P., Lothongkum, G., Krongtong, V., Homkrajai, W. & Chuankrerkkul, N. Microstructural restoration by hip and heat treatment processes in cast nickel based superalloy, IN-738. *Chiang Mai Journal of Science* **36**, (2009).
69. Bor, H. Y., Hsu, C. & Wei, C. N. Influence of hot isostatic pressing on the fracture transitions in the fine grain MAR-M247 superalloys. *Mater. Chem. Phys.* **84**, (2004).
70. Kim, M. T., Chang, S. Y. & Won, J. B. Effect of HIP process on the micro-structural evolution of a nickel-based superalloy. *Materials Science and Engineering: A* **441**, (2006).
71. Tammas-Williams, S., Withers, P. J., Todd, I. & Prangnell, P. B. Porosity regrowth during heat treatment of hot isostatically pressed additively manufactured titanium components. *Scr. Mater.* **122**, (2016).

72. Choi, J. P. *et al.* Densification and microstructural investigation of Inconel 718 parts fabricated by selective laser melting. *Powder Technol.* **310**, (2017).
73. Bassini, E. *et al.* Influence of solutioning on microstructure and hardness of hot isostatically pressed Astroloy. *J. Alloys Compd.* **723**, (2017).
74. Bassini, E. *et al.* Net shape HIPping of a Ni-superalloy: A study of the influence of an as-leached surface on mechanical properties. *J. Mater. Process. Technol.* **271**, (2019).
75. Ghorbanpour, S. *et al.* Additive manufacturing of functionally graded inconel 718: Effect of heat treatment and building orientation on microstructure and fatigue behaviour. *J. Mater. Process. Technol.* **306**, (2022).
76. Kreitcberg, A., Brailovski, V. & Turenne, S. Effect of heat treatment and hot isostatic pressing on the microstructure and mechanical properties of Inconel 625 alloy processed by laser powder bed fusion. *Materials Science and Engineering: A* **689**, (2017).
77. Hosseini, E. & Popovich, V. A. A review of mechanical properties of additively manufactured Inconel 718. *Additive Manufacturing* vol. 30 Preprint at https://doi.org/10.1016/j.addma.2019.100877 (2019).
78. Yap, C. Y. *et al.* Review of selective laser melting: Materials and applications. *Applied Physics Reviews* vol. 2 Preprint at https://doi.org/10.1063/1.4935926 (2015).
79. Kaletsch, A., Qin, S., Herzog, S. & Broeckmann, C. Influence of high initial porosity introduced by laser powder bed fusion on the fatigue strength of Inconel 718 after post-processing with hot isostatic pressing. *Addit. Manuf.* **47**, 102331 (2021).
80. Mishurova, T. *et al.* The Influence of the Support Structure on Residual Stress and Distortion in SLM Inconel 718 Parts. *Metall. Mater. Trans. A Phys. Metall. Mater. Sci.* **49**, (2018).
81. Lesyk, D. A., Martinez, S., Pedash, O. O., Dzhemelinskyi, V. V. & Lamikiz, A. Porosity and surface defects characterization of hot isostatically pressed Inconel 718 alloy turbine blades printed by 3D laser metal fusion technology. *MRS Adv.* **7**, (2022).
82. Qin, S., Herzog, S., Kaletsch, A. & Broeckmann, C. Effects of pressure on microstructure and residual stresses during hot isostatic pressing post treatment of aisi m50 produced by laser powder-bed fusion. *Metals (Basel).* **11**, (2021).
83. Chen, C. *et al.* Effect of hot isostatic pressing (HIP) on microstructure and mechanical properties of Ti6Al4V alloy fabricated by cold spray additive manufacturing. *Addit. Manuf.* **27**, (2019).

84. Wanjara, P. *et al.* Overview: Additive/Subtractive Hybrid Manufacturing of Heat Resisting Materials. in *Key Engineering Materials* vol. 964 (2023).
85. Wawrzyniak, N., Wanjara, P., Brochu, M. & Brochu, M. Measuring the tensile properties of Ti6Al4V fabricated by laser powder bed fusion: Influence of specimen dimensions. *Theoretical and Applied Fracture Mechanics* **131**, (2024).
86. Sarafan, S. *et al.* Benchmarking of 316L Stainless Steel Manufactured by a Hybrid Additive/Subtractive Technology. *Journal of Manufacturing and Materials Processing* **6**, (2022).
87. Sarafan, S. *et al.* Evaluation of maraging steel produced using hybrid additive/subtractive manufacturing. *Journal of Manufacturing and Materials Processing* **5**, (2021).
88. Aina, J. *et al.* Development of post-treatment for enhanced performance of an additively manufactured Alloy 718. *International Journal of Advanced Manufacturing Technology* **135**, (2024).
89. Mumtaz, K. A., Erasenthiran, P. & Hopkinson, N. High density selective laser melting of Waspaloy®. *J. Mater. Process. Technol.* **195**, (2008).
90. Nayak, S. K., Jinoop, A. N., Shiva, S. & Paul, C. P. Laser Additive Manufacturing of Nickel Superalloys for Aerospace Applications. in *Additive and Subtractive Manufacturing Processes* (2022). doi:10.1201/9781003327394-10.
91. Sanchez, S. *et al.* Powder Bed Fusion of nickel-based superalloys: A review. *International Journal of Machine Tools and Manufacture* vol. 165 Preprint at https://doi.org/10.1016/j.ijmachtools.2021.103729 (2021).
92. Zhang, J., Song, B., Wei, Q., Bourell, D. & Shi, Y. A review of selective laser melting of aluminum alloys: Processing, microstructure, property and developing trends. *Journal of Materials Science and Technology* vol. 35 Preprint at https://doi.org/10.1016/j.jmst.2018.09.004 (2019).
93. Du, D. *et al.* Influence of build orientation on microstructure, mechanical and corrosion behavior of Inconel 718 processed by selective laser melting. *Materials Science and Engineering: A* **760**, (2019).
94. Kunz, J. *et al.* Influence of hot isostatic pressing post-treatment on the microstructure and mechanical behavior of standard and super duplex stainless steel produced by laser powder bed fusion. *Materials Science and Engineering: A* **794**, (2020).

95. Xu, Q., Li, W., Yin, Y. & Zhou, J. Closure behavior of the artificial gas pore inside the as-cast ti6al4v alloy during hip: Constitutive modeling and numerical simulation. *Metals (Basel).* **11**, (2021).
96. Epishin, A., Fedelich, B., Link, T., Feldmann, T. & Svetlov, I. L. Pore annihilation in a single-crystal nickel-base superalloy during hot isostatic pressing: Experiment and modelling. *Materials Science and Engineering: A* **586**, (2013).
97. Prasad, M. R. G., Gao, S., Vajragupta, N. & Hartmaier, A. Influence of trapped gas on pore healing under hot isostatic pressing in nickel-base superalloys. *Crystals (Basel).* **10**, 1147 (2020).
98. Xu, Q. *et al.* Effects of hot isostatic pressing temperature on casting shrinkage densification and microstructure of Ti6Al4V alloy. *China Foundry* **14**, (2017).
99. Maj, P. *et al.* Influence of Hot Isostatic Pressing on the Microstructure and Mechanical Properties of Hastelloy X Samples Manufactured via Laser Powder Bed Fusion. *Applied Sciences (Switzerland)* **15**, (2025).
100. Tammas-Williams, S., Withers, P. J., Todd, I. & Prangnell, P. B. The effectiveness of hot isostatic pressing for closing porosity in titanium parts manufactured by selective electron beam melting. *Metallurgical and materials transactions A* **47**, 1939–1946 (2016).
101. Lee, S. C. Effects of Temperature of HIP Process on Characteristics of Inconel 718 Superalloy. *International Journal of Cast Metals Research* **19**, 175–180 (2006).
102. Chang, S.-H., Lee, S.-C., Tang, T.-P. & Ho, H.-H. Evaluation of HIP pressure on Inconel 718 superalloy. *International Journal of Cast Metals Research* **19**, 181–187 (2006).
103. du Plessis, A. & Rossouw, P. Investigation of porosity changes in cast Ti6Al4V rods after hot isostatic pressing. *J. Mater. Eng. Perform.* **24**, 3137–3141 (2015).
104. Sentyurina, Z. A. *et al.* The effect of hot isostatic pressing and heat treatment on the microstructure and properties of EP741NP nickel alloy manufactured by laser powder bed fusion. *Addit. Manuf.* **37**, 101629 (2021).
105. Åsberg, M., Fredriksson, G., Hatami, S., Fredriksson, W. & Krakhmalev, P. Influence of post treatment on microstructure, porosity and mechanical properties of additive manufactured H13 tool steel. *Materials Science and Engineering: A* **742**, 584–589 (2019).
106. Sun, X. *et al.* Hot isostatic pressing of MRI compatible Zr-1Mo components manufactured by laser powder bed fusion. *Mater. Charact.* **169**, 110657 (2020).

107. Molaei, R., Fatemi, A. & Phan, N. Significance of hot isostatic pressing (HIP) on multiaxial deformation and fatigue behaviors of additive manufactured Ti-6Al-4V including build orientation and surface roughness effects. *Int. J. Fatigue* **117**, 352–370 (2018).
108. Song, J. *et al.* Laser powder bed fusion of high-strength maraging steel with concurrently enhanced strength and ductility after heat treatments. *Materials Science and Engineering: A* **854**, 143818 (2022).
109. Liu, X., Liu, Y., Zhou, Z., Zhong, H. & Zhan, Q. A combination strategy for additive manufacturing of AA2024 high-strength aluminium alloys fabricated by laser powder bed fusion: Role of hot isostatic pressing. *Materials Science and Engineering: A* **850**, 143597 (2022).
110. Poulin, J.-R., Kreitcberg, A. & Brailovski, V. Effect of hot isostatic pressing of laser powder bed fused Inconel 625 with purposely induced defects on the residual porosity and fatigue crack propagation behavior. *Addit. Manuf.* **47**, 102324 (2021).
111. Poulin, J.-R., Brailovski, V. & Terriault, P. Long fatigue crack propagation behavior of Inconel 625 processed by laser powder bed fusion: Influence of build orientation and post-processing conditions. *Int. J. Fatigue* **116**, 634–647 (2018).
112. Teixeira, Ó., Silva, F. J. G., Ferreira, L. P. & Atzeni, E. A review of heat treatments on improving the quality and residual stresses of the Ti–6Al–4V parts produced by additive manufacturing. *Metals (Basel).* **10**, 1006 (2020).
113. Zhang, H., Li, C., Yao, G. & Zhang, Y. Hot isostatic pressing of laser powder-bed-fused 304L stainless steel under different temperatures. *Int. J. Mech. Sci.* **226**, 107413 (2022).
114. Homami, R. M. *et al.* Numerical analysis of residual stress in a material produced by additive manufacturing and hot isostatic pressing. *J. Manuf. Process.* **150**, 1018–1039 (2025).
115. Kashfi, M. & Tehrani, M. Effects of void content on flexural properties of additively manufactured polymer composites. *Composites Part C: Open Access* **6**, 100173 (2021).
116. Abdelhafeez, A. M. & Essa, K. E. A. Influences of powder compaction constitutive models on the finite element simulation of hot isostatic pressing. *Procedia CIRP* **55**, 188–193 (2016).
117. Buljak, V., Baivier-Romero, S. & Kallel, A. Calibration of Drucker–Prager cap constitutive model for ceramic powder compaction through inverse analysis. *Materials* **14**, 4044 (2021).

118. Zhou, W., Fan, Y., Zhang, P., Yin, Y. & Zhou, J. Numerical simulation and optimization of the hot isostatic pressure process of a part of aircraft structure. *Procedia Manuf.* **37**, 138–145 (2019).
119. Xue, Y., Lang, L. H., Bu, G. L. & Li, L. Densification modeling of titanium alloy powder during hot isostatic pressing. *Science of Sintering* **43**, 247–260 (2011).
120. Essa, K., Khan, R., Hassanin, H., Attallah, M. M. & Reed, R. An iterative approach of hot isostatic pressing tooling design for net-shape IN718 superalloy parts. *The International Journal of Advanced Manufacturing Technology* **83**, 1835–1845 (2016).
121. Vattur Sundaram, M., Khodaee, A., Andersson, M., Nyborg, L. & Melander, A. Experimental and finite element simulation study of capsule-free hot isostatic pressing of sintered gears. *The International Journal of Advanced Manufacturing Technology* **99**, 1725–1733 (2018).
122. Du, Y. Y., Chen, Y. & Zhu, C. Consolidation and Simulations of Hot Isostatic Pressing of Selective Laser Sintered Stainless Steel Parts. *Powder Metallurgy and Metal Ceramics* **58**, 249–256 (2019).
123. Abouaf, M., Chenot, J. L., Raisson, G. & Bauduin, P. Finite element simulation of hot isostatic pressing of metal powders. *Int. J. Numer. Methods Eng.* **25**, 191–212 (1988).
124. Abena, A., Aristizabal, M. & Essa, K. Comprehensive numerical modelling of the hot isostatic pressing of Ti-6Al-4V powder: From filling to consolidation. *Advanced Powder Technology* **30**, 2451–2463 (2019).
125. Kohar, C. P. *et al.* A new and efficient thermo-elasto-viscoplastic numerical implementation for implicit finite element simulations of powder metals: An application to hot isostatic pressing. *Int. J. Mech. Sci.* **155**, 222–234 (2019).
126. Jinka, A. G. K. & Lewis, R. W. Finite element simulation of hot isostatic pressing of metal powders. *Comput. Methods Appl. Mech. Eng.* **114**, 249–272 (1994).
127. Van Nguyen, C., Deng, Y., Bezold, A. & Broeckmann, C. A combined model to simulate the powder densification and shape changes during hot isostatic pressing. *Comput. Methods Appl. Mech. Eng.* **315**, 302–315 (2017).
128. Wikman, B., Svoboda, A. & Häggblad, H.-Å. A combined material model for numerical simulation of hot isostatic pressing. *Comput. Methods Appl. Mech. Eng.* **189**, 901–913 (2000).

129. Gurson, A. L. Continuum theory of ductile rupture by void nucleation and growth: Part I—Yield criteria and flow rules for porous ductile media. (1977).
130. Cui, J., Lv, X. & Fu, H. Numerical Simulation and Hot Isostatic Pressing Technology of Powder Titanium Alloys: A Review. *Metals (Basel).* **15**, 542 (2025).
131. Homami, R. M. & Ojo, O. Residual stress analysis through numerical simulation in powder bed additive manufacturing using the representative volume approach. *International Journal of Advanced Manufacturing Technology* **129**, (2023).
132. Wang, X., Niu, L., Cheng, K., Wang, B. & Zhang, Q. A Porosity Closure Model Under Hot Isostatic Pressing of an IN718 Alloy Manufactured by Powder Bed Fusion. *Materials* **18**, 1001 (2025).
133. Liverani, E., Lutey, A. H. A., Ascari, A. & Fortunato, A. The effects of hot isostatic pressing (HIP) and solubilization heat treatment on the density, mechanical properties, and microstructure of austenitic stainless steel parts produced by selective laser melting (SLM). *The International Journal of Advanced Manufacturing Technology* **107**, 109–122 (2020).
134. Dye, D. *et al.* Modeling and measurement of residual stresses in a forged IN718 superalloy disc. *Superalloys, TMS* **35**, 315–322 (2004).
135. Nudelis, N. & Mayr, P. Pore tracing in additive manufactured and hot isostatic pressed components. *J. Mater. Sci.* **58**, 14245–14253 (2023).
136. Nudelis, N. & Mayr, P. A novel classification method for pores in laser powder bed fusion. *Metals (Basel).* **11**, 1912 (2021).
137. Kellett, B. J. & Lange, F. F. Experiments on pore closure during hot isostatic pressing and forging. *Journal of the American Ceramic Society* **71**, 7–12 (1988).
138. Mishurova, T. *et al.* Understanding the hot isostatic pressing effectiveness of laser powder bed fusion Ti-6Al-4V by in-situ X-ray imaging and diffraction experiments. *Sci. Rep.* **13**, 18433 (2023).
139. Cegan, T. *et al.* Effect of hot isostatic pressing on porosity and mechanical properties of 316 l stainless steel prepared by the selective laser melting method. *Materials* **13**, 4377 (2020).
140. Read, N., Wang, W., Essa, K. & Attallah, M. M. Selective laser melting of AlSi10Mg alloy: Process optimisation and mechanical properties development. *Materials & Design (1980-2015)* **65**, 417–424 (2015).

141. de Terris, T. *et al.* Optimization and comparison of porosity rate measurement methods of Selective Laser Melted metallic parts. *Addit. Manuf.* **28**, 802–813 (2019).

142. Qi, T. *et al.* Selective laser melting of Al7050 powder: Melting mode transition and comparison of the characteristics between the keyhole and conduction mode. *Mater. Des.* **135**, 257–266 (2017).

143. Fabbro, R. Melt pool and keyhole behaviour analysis for deep penetration laser welding. *J. Phys. D Appl. Phys.* **43**, 445501 (2010).

144. Deev, A. A., Kuznetcov, P. A. & Petrov, S. N. Anisotropy of mechanical properties and its correlation with the structure of the stainless steel 316L produced by the SLM method. *Phys. Procedia* **83**, 789–796 (2016).

145. Yang, Y., Allen, M., London, T. & Oancea, V. Residual strain predictions for a powder bed fusion Inconel 625 single cantilever part. *Integr. Mater. Manuf. Innov.* **8**, 294–304 (2019).

146. Li, C., Denlinger, E. R., Gouge, M. F., Irwin, J. E. & Michaleris, P. Numerical verification of an Octree mesh coarsening strategy for simulating additive manufacturing processes. *Addit. Manuf.* **30**, 100903 (2019).

147. Tangestani, R. *et al.* Multi-scale model to simulate stress directionality in laser powder bed fusion: application to thin-wall part failure. *Mater. Des.* **232**, 112147 (2023).

148. Ukwattage, A. K. & Achuthan, A. Development of residual stress of parts fabricated via selective laser melting (SLM) techniques under di erent scanning strategies. in *2018 AIAA/ASCE/AHS/ASC Structures, Structural Dynamics, and Materials Conference* 0090 (2018).

149. Li, C., Gouge, M. F., Denlinger, E. R., Irwin, J. E. & Michaleris, P. Estimation of part-to-powder heat losses as surface convection in laser powder bed fusion. *Addit. Manuf.* **26**, 258–269 (2019).

150. Prabhakar, P., Sames, W. J., Dehoff, R. & Babu, S. S. Computational modeling of residual stress formation during the electron beam melting process for Inconel 718. *Addit. Manuf.* **7**, 83–91 (2015).

151. Li, C., Liu, J. F., Fang, X. Y. & Guo, Y. B. Efficient predictive model of part distortion and residual stress in selective laser melting. *Addit. Manuf.* **17**, 157–168 (2017).

152. Parry, L., Ashcroft, I. A. & Wildman, R. D. Understanding the effect of laser scan strategy on residual stress in selective laser melting through thermo-mechanical simulation. *Addit. Manuf.* **12**, 1–15 (2016).
153. Goldak, J., Chakravarti, A. & Bibby, M. A new finite element model for welding heat sources. *Metallurgical transactions B* **15**, 299–305 (1984).
154. Flynn, J. M., Shokrani, A., Newman, S. T. & Dhokia, V. Hybrid additive and subtractive machine tools–Research and industrial developments. *Int. J. Mach. Tools Manuf.* **101**, 79–101 (2016).
155. Li, C., Liu, Z. Y., Fang, X. Y. & Guo, Y. B. Residual stress in metal additive manufacturing. *Procedia CIRP* **71**, 348–353 (2018).
156. Bayat, M. *et al.* Part-scale thermo-mechanical modelling of distortions in laser powder bed fusion–analysis of the sequential flash heating method with experimental validation. *Addit. Manuf.* **36**, 101508 (2020).
157. De Baere, D. *et al.* Thermo-mechanical modelling of stress relief heat treatments after laser-based powder bed fusion. *Addit. Manuf.* **38**, 101818 (2021).
158. Syed, A. K. *et al.* An experimental study of residual stress and direction-dependence of fatigue crack growth behaviour in as-built and stress-relieved selective-laser-melted Ti6Al4V. *Materials Science and Engineering: A* **755**, 246–257 (2019).
159. Denlinger, E. R. & Michaleris, P. Effect of stress relaxation on distortion in additive manufacturing process modeling. *Addit. Manuf.* **12**, 51–59 (2016).
160. Williams, R. J. *et al.* Effects of heat treatment on residual stresses in the laser powder bed fusion of 316L stainless steel: Finite element predictions and neutron diffraction measurements. *J. Manuf. Process.* **57**, 641–653 (2020).
161. Ferreira, M. S. & Yanagihara, J. I. Unsteady heat conduction in 3D elliptical cylinders. *International communications in heat and mass transfer* **28**, 963–972 (2001).
162. Liu, W. Analysis of steady heat conduction for 3D axisymmetric functionally graded circular plate. *J. Cent. South Univ.* **20**, 1616–1622 (2013).
163. Jahed, H. & Roostaei, A. A. A. *Cyclic Plasticity of Metals: Modeling Fundamentals and Applications*. (Elsevier, 2021).

164. Gouge, M., Michaleris, P., Denlinger, E. & Irwin, J. The finite element method for the thermo-mechanical modeling of additive manufacturing processes. in *Thermo-mechanical modeling of additive manufacturing* 19–38 (Elsevier, 2018).

165. Pan, C., Zhao, C., Chang, Q., Zhou, J. & Wu, Q. Three-dimensional metal particle flow simulation during the whole rolling process for 60 kg/m heavy rail. *Advances in Mechanical Engineering* **9**, 1687814017720879 (2017).

166. Kassner, M. E. *Fundamentals of Creep in Metals and Alloys*. (Butterworth-Heinemann, 2015).

167. Li, W., Xu, Q., Yin, Y., Zhou, J. & Nan, H. Research on pore closure behavior and microstructure evolution during hot isostatic pressing of Ti6Al4V alloy casting. *Journal of Materials Research and Technology* **24**, 3628–3642 (2023).

168. Hill, R. *The Mathematical Theory of Plasticity*. vol. 11 (Oxford university press, 1998).

169. Fody, J. M. & Lang, C. G. *Hot Isostatic Pressing for Reduction of Defects in Additively Manufactured Inconel-718 Preliminary Simulation Approach and Results*. (2021).

170. Wang, J., Srivatsa, S., Wu, Z. & Huang, Z. Modeling of metal powder densification under hot isostatic pressing. *Materials* **17**, 1933 (2024).

171. Sadd, M. H. *Elasticity: Theory, Applications, and Numerics*. (Academic Press, 2009).

172. Buchely, M. & Marañon, A. Spherical cavity expansion approach for the study of rigid-penetrator's impact problems. *Applied Mechanics* **1**, 20–46 (2020).

173. Rice, J. R. & Tracey, D. M. On the ductile enlargement of voids in triaxial stress fields∗. *J. Mech. Phys. Solids* **17**, 201–217 (1969).

174. Abdelghani, M., Tewfik, G., Witek, M. & Djahida, D. Factors of Stress Concentration around Spherical Cavity Embedded in Cylinder Subjected to Internal Pressure. *Materials* **14**, 3057 (2021).

175. Sergeev, N. N. *et al.* Formation of plastic zones near spherical cavity in hardened low-carbon steels under conditions of hydrogen stress corrosion. *Inorganic materials: applied research* **9**, 663–669 (2018).

176. Lu, X., Barber, J. R. & Comninou, M. Stress concentration due to an array or hemispherical cavities at the surface of an elastic half-space. *J. Elast.* **28**, 111–122 (1992).

177. Mengsha, S., Chunyu, Z., Yuheng, C. & Biao, W. Experimental and theoretical evaluation of influence of hole size on deformation and fracture of elastic perforated plate. *Mechanics of Materials* **187**, 104841 (2023).
178. Eshelby, J. D. The determination of the elastic field of an ellipsoidal inclusion, and related problems. *Proc. R. Soc. Lond. A Math. Phys. Sci.* **241**, 376–396 (1957).
179. Liu, B. *et al.* The size effect on void growth in ductile materials. *J. Mech. Phys. Solids* **51**, 1171–1187 (2003).
180. Xu, W. & Jiao, Y. Theoretical framework for percolation threshold, tortuosity and transport properties of porous materials containing 3D non-spherical pores. *Int. J. Eng. Sci.* **134**, 31–46 (2019).
181. Phani, K. K. & Niyogi, S. K. Young's modulus of porous brittle solids. *J. Mater. Sci.* **22**, 257–263 (1987).
182. Mori, T. & Tanaka, K. Average stress in matrix and average elastic energy of materials with misfitting inclusions. *Acta metallurgica* **21**, 571–574 (1973).
183. Kováčik, J. Correlation between Young's modulus and porosity in porous materials. *J. Mater. Sci. Lett.* **18**, 1007–1010 (1999).
184. Sandmann, P. *et al.* Influence of laser shock peening on the residual stresses in additively manufactured 316L by Laser Powder Bed Fusion: A combined experimental–numerical study. *Addit. Manuf.* **60**, 103204 (2022).
185. Ding, J. *et al.* A computationally efficient finite element model of wire and arc additive manufacture. *The International Journal of Advanced Manufacturing Technology* **70**, 227–236 (2014).
186. He, P. *et al.* Fatigue and dynamic aging behavior of a high strength Al-5024 alloy fabricated by laser powder bed fusion additive manufacturing. *Acta Mater.* **220**, 117312 (2021).
187. Arısoy, Y. M., Criales, L. E. & Özel, T. Modeling and simulation of thermal field and solidification in laser powder bed fusion of nickel alloy IN625. *Opt. Laser Technol.* **109**, 278–292 (2019).
188. Bayerlein, F., Bodensteiner, F., Zeller, C., Hofmann, M. & Zaeh, M. F. Transient development of residual stresses in laser beam melting–A neutron diffraction study. *Addit. Manuf.* **24**, 587–594 (2018).

189. Chakraborty, A. *et al.* In-process failure analysis of thin-wall structures made by laser powder bed fusion additive manufacturing. *J. Mater. Sci. Technol.* **98**, 233–243 (2022).
190. Ali, H., Ma, L., Ghadbeigi, H. & Mumtaz, K. In-situ residual stress reduction, martensitic decomposition and mechanical properties enhancement through high temperature powder bed pre-heating of Selective Laser Melted Ti6Al4V. *Materials Science and Engineering: A* **695**, 211–220 (2017).
191. Mirkoohi, E. *et al.* Mechanics modeling of residual stress considering effect of preheating in laser powder bed fusion. *Journal of Manufacturing and Materials Processing* **5**, 46 (2021).
192. Vasinonta, A., Beuth, J. L. & Griffith, M. Process maps for predicting residual stress and melt pool size in the laser-based fabrication of thin-walled structures. (2007).
193. Simson, T., Emmel, A., Dwars, A. & Böhm, J. Residual stress measurements on AISI 316L samples manufactured by selective laser melting. *Addit. Manuf.* **17**, 183–189 (2017).
194. Manvatkar, V., De, A. & DebRoy, T. Spatial variation of melt pool geometry, peak temperature and solidification parameters during laser assisted additive manufacturing process. *Materials Science and Technology* **31**, 924–930 (2015).
195. Wu, A. S., Brown, D. W., Kumar, M., Gallegos, G. F. & King, W. E. An experimental investigation into additive manufacturing-induced residual stresses in 316L stainless steel. *Metallurgical and Materials Transactions A* **45**, 6260–6270 (2014).
196. Levkulich, N. C. *et al.* The effect of process parameters on residual stress evolution and distortion in the laser powder bed fusion of Ti-6Al-4V. *Addit. Manuf.* **28**, 475–484 (2019).
197. Shiomi, M., Osakada, K., Nakamura, K., Yamashita, T. & Abe, F. Residual stress within metallic model made by selective laser melting process. *CIRP annals* **53**, 195–198 (2004).
198. Mercelis, P. & Kruth, J. Residual stresses in selective laser sintering and selective laser melting. *Rapid Prototyp. J.* **12**, 254–265 (2006).
199. Dong, P., Song, S. & Zhang, J. Analysis of residual stress relief mechanisms in post-weld heat treatment. *International Journal of Pressure Vessels and Piping* **122**, 6–14 (2014).
200. Atabay, S. E. *et al.* In envelope additive/subtractive manufacturing and thermal post-processing of Inconel 718. *Materials* **16**, 1 (2022).

201. Osman, M. *et al.* Effect of heat treatment on the microstructure and mechanical properties of 18Ni-300 maraging steel produced by additive–subtractive hybrid manufacturing. *Materials* **16**, 4749 (2023).

202. Atabay, S. E. *et al.* Laser powder bed fusion printing of CoCrFeMnNi high entropy alloy: processing, microstructure, and mechanical properties. *High Entropy Alloys & Materials* **2**, 129–173 (2024).

203. Fryé, T., Strauss, J. T., Fischer-Bühner, J. & Klotz, U. E. The effects of hot isostatic pressing of platinum alloy castings on mechanical properties and microstructures. in *The Santa Fe Symposium on Jewelry Manufacturing Technology* 189–210 (2014).

204. Hirata, T., Kimura, T. & Nakamoto, T. Effects of hot isostatic pressing and internal porosity on the performance of selective laser melted AlSi10Mg alloys. *Materials Science and Engineering: A* **772**, 138713 (2020).

205. Du Plessis, A. & Macdonald, E. Hot isostatic pressing in metal additive manufacturing: X-ray tomography reveals details of pore closure. *Addit. Manuf.* **34**, 101191 (2020).

206. Puichaud, A.-H. *et al.* Microstructure and mechanical properties relationship of additively manufactured 316L stainless steel by selective laser melting. *EPJ Nuclear Sciences & Technologies* **5**, 23 (2019).

207. Atkinson, H. V & Davies, S. Fundamental aspects of hot isostatic pressing: An overview. *Metallurgical and materials transactions A* **31**, 2981–3000 (2000).

208. Hasmuni, N., Ibrahim, M., Raus, A. A., Wahab, M. S. & Kamarudin, K. Porosity effects of AlSi 10mg parts produced by selective laser melting. *Journal of Mechanical Engineering (JMechE)* 246–255 (2018).

209. Gaytan, S. M. *et al.* Advanced metal powder based manufacturing of complex components by electron beam melting. *Materials technology* **24**, 180–190 (2009).

210. Karlsson, J., Snis, A., Engqvist, H. & Lausmaa, J. Characterization and comparison of materials produced by Electron Beam Melting (EBM) of two different Ti–6Al–4V powder fractions. *J. Mater. Process. Technol.* **213**, 2109–2118 (2013).

211. Hrabe, N. & Quinn, T. Effects of processing on microstructure and mechanical properties of a titanium alloy (Ti–6Al–4V) fabricated using electron beam melting (EBM), Part 2: Energy input, orientation, and location. *Materials Science and Engineering: A* **573**, 271–277 (2013).

212. Tammas-Williams, S. *et al.* XCT analysis of the influence of melt strategies on defect population in Ti–6Al–4V components manufactured by Selective Electron Beam Melting. *Mater. Charact.* **102**, 47–61 (2015).

213. Puebla, K. *et al.* Effect of melt scan rate on microstructure and macrostructure for electron beam melting of Ti-6Al-4V. *Mater. Sci. Appl* **3**, 259–264 (2012).

214. Bauereiß, A., Scharowsky, T. & Körner, C. Defect generation and propagation mechanism during additive manufacturing by selective beam melting. *J. Mater. Process. Technol.* **214**, 2522–2528 (2014).

215. Haeckel, F., Meixlsperger, M. & Burkert, T. Technological challenges for automotive series production in laser beam melting. (2017).

216. Li, P. *et al.* Investigation of the mechanisms by which hot isostatic pressing improves the fatigue performance of powder bed fused Ti-6Al-4V. *Int. J. Fatigue* **120**, 342–352 (2019).

217. Zang, T. *et al.* Fatigue Crack Initiation and Growth Behaviors of Additively Manufactured Ti-6AI-4V Alloy After Hot Isostatic Pressing Post-Process. *Metals (Basel).* **14**, 1350 (2024).

APPENDIX A: Material Definitions and Constitutive Inputs Used in the FE Models

A.1 Material Assignment

Two nickel-based superalloy datasets were used at different stages of the sequential numerical framework developed in this thesis. The LPBF simulation employed Inconel 718 (IN718) for both the deposited material and the substrate. The subsequent furnace and hot isostatic pressing (HIP) simulations employed the elevated-temperature material properties of Astroloy.

A.2 Inconel 718 Properties Used in the LPBF Simulation

IN718 was used for both the printed region and substrate in the LPBF model. Because LPBF involves rapid heating and cooling over a wide temperature range, temperature-dependent thermal and mechanical properties were employed. The incorporated properties included thermal conductivity, specific heat, coefficient of thermal expansion, Young's modulus, Poisson's ratio, yield strength, and density. These properties govern different aspects of the coupled thermo-mechanical response. Thermal conductivity and specific heat control heat transfer and temperature evolution, while the coefficient of thermal expansion governs thermally induced expansion and contraction. Young’s modulus, Poisson’s ratio, and yield strength determine the corresponding elastic and plastic mechanical responses as the material undergoes repeated heating and cooling cycles. Table A.1 shows temperature-dependent material properties of IN718 used in the LPBF model. The individual properties were available at different temperature points because they were obtained from separate experimental datasets. Therefore, a common temperature grid was not artificially imposed.

Table A.1. Temperature-dependent material properties of IN718 used in the LPBF model[131]

Temperature (◦C)	**Thermal conductivity (W/m◦C)**	**Coefficient of thermal expansion (mm/mm◦C)**	**Poisson's ratio**	**Young's modulus (MPa)**	**Yield strength (MPa)**	**Specific Heat (J/kg °C)**
16					1209	
19.85						427.14
21	11	1.28E-05	0.294	199,947		
38			0.291	198,569		
87					1164	
93	13	1.32E−05	0.288	195,811		
99.85						441.74
149			0.280	193,053		
200					1120	
204	14	1.36E−05	0.280	190,295		
260			0.275	186,847		
299.85						481.74
308					1089	
316	16	1.39E−05	0.272	184,090		
371			0.273	180,642		
421					1065	
427	18	1.43E−05	0.271	177,884		
482			0.272	174,437		
499.85						521.74
538	20	1.46E−05	0.271	170,989	1067	
593			0.276	166,853		
649	22	1.51E−05	0.283	163,405	1023	
699.85						561.74
704			0.292	158,579		
710					969	
760	23	1.60E−05	0.306	153,753	875	
815			0.321	146,858	543	
871	25		0.331	139,274		
882					306	
899.85						601.74
927			0.334	129,621		
953					138	
982	27		0.341	119,968		
990					134	
1038			0.366	109,626		
1093	29		0.402	98,595	74	
1226	30					
1349.85						691.74

A.3 Astroloy Properties Used in the Furnace and HIP Simulations

The main furnace and HIP simulations employed the high-temperature thermo-mechanical properties of Astroloy[114]. The actual Abaqus material card used in the production model contained temperature-dependent definitions for thermal conductivity, density, elastic modulus, Poisson's ratio, thermal expansion, plasticity/hardening, specific heat, and creep.

A.4 Plasticity and Hardening Definition for Astroloy

Temperature-dependent plastic behavior was represented using an isotropic hardening formulation. For each temperature, two stress–equivalent-plastic-strain points were defined in Abaqus: the first corresponds to yielding at zero equivalent plastic strain, and the second defines the post-yield tangent response at an equivalent plastic strain of 0.01.

Table A.2. Temperature-dependent plasticity/hardening definition used for Astroloy

Temperature (°C)	**Yield stress at $\varepsilon^{pl} = 0$ (MPa)**	**Stress at $\varepsilon^{pl} = 0.01$(MPa)**	**Approx. tangent hardening modulus (GPa)**
20	489.0	499.9	1.09
200	449.0	458.96	0.996
400	403.0	411.39	0.839
650	206.0	209.69	0.369
800	101.0	102.51	0.151
1000	46.5	47.185	0.0685

A.5 Hyperbolic-Sine Creep Definition for Astroloy

Time-dependent deformation during furnace and HIP processing was represented using the built-in Abaqus hyperbolic-sine creep law:

$$\dot{\varepsilon}^{cr} = A[\sinh(B\sigma^{cr})]^n \exp[-\frac{\Delta H}{R(T - T^Z)}]$$

Table A.3. Material parameters for the hyperbolic sine creep law[114].

Power Law Multiplier (T^{-1})	**Hyperbolic Law Multiplier ($F^{-1}L^2$)**	**Eq Stress Order**	**Activation Energy (JM^{-1})**	**Universal Gas Constant ($JM^{-1}\theta^{-1}$)**
3.33E+25	0.86E-02	2.13	570066	8.31

The creep parameters were adopted from published material data and were not recalibrated against experimental measurements generated in the present PhD study. Thus, no inverse parameter identification or curve fitting was performed as part of this thesis. Instead, the constitutive parameters were adopted directly from published literature and implemented in Abaqus without additional recalibration or fitting in the present study.

A.6 Applicable Temperature Range

The Astroloy material card contains tabulated properties over a nominal range extending from 20°C to 1000°C. However, the principal post-processing simulations reported in this thesis were restricted to substantially lower temperatures, particularly the 400–700°C range investigated for furnace and HIP stress relaxation. As discussed in Section 4.3, simulations at temperatures above approximately 750°C under the investigated high-pressure conditions exhibited increasing numerical convergence difficulties and were therefore not used for the principal conclusions.

A.7 Temperature Interpolation and Extrapolation

Temperature-dependent properties were entered in Abaqus as discrete tabulated values. During the analysis, values required at temperatures between specified data points are obtained through the material-data interpolation procedures implemented internally by Abaqus. No user-defined interpolation algorithm or material subroutine was employed for these properties. No explicit extrapolation option was specified. Accordingly, the standard Abaqus material-data behavior applies. Outside the supplied range of an independent variable, Abaqus retains the property at the limiting tabulated value. Therefore, the temperature-dependent constitutive response within the investigated range was based on interpolation between literature-derived tabulated values rather than independent analytical fitting of each material property.

A.8 Sequential Numerical Workflow and Solver Implementation

The numerical framework developed in this thesis consisted of two sequential modeling stages: (i) simulation of residual-stress generation during LPBF and (ii) simulation of subsequent residual-stress relaxation during conventional furnace treatment and HIP. Different thermal–mechanical coupling strategies were employed in these two stages according to the physical processes being represented.

A.8.1 LPBF Thermal–Mechanical Workflow

The LPBF process was modeled using a sequentially coupled thermo-mechanical procedure. In the first analysis, the transient thermal response of the representative volume was calculated during layer-by-layer deposition and movement of the laser heat source. The thermal analysis accounted for the moving heat input, temperature-dependent material properties, conduction, convection, radiation, and progressive material deposition. The resulting transient temperature history was stored in the thermal output database (ODB). In the subsequent mechanical analysis, this temperature history was imported and used as the thermal loading history for calculation of thermal strain, plastic deformation, and the resulting residual-stress field. At the end of the mechanical LPBF analysis, the resulting stress tensor field was stored in the ODB and subsequently used to initialize the post-processing simulation.

A.8.2 Transfer of LPBF Residual Stress to the Post-Processing Model

The residual-stress field generated by the LPBF mechanical simulation was transferred to the furnace/HIP model as an initial stress condition. The stress tensor field was imported directly from the output database (ODB) of the preceding LPBF simulation using the Abaqus initial-condition capability. Thus, the residual-stress components stored at the final increment of the LPBF mechanical analysis were used to initialize the subsequent post-processing model. Only the stress tensor field was transferred from the LPBF ODB. The temperature field at the end of the LPBF simulation was not transferred to the furnace/HIP analysis. Similarly, no explicit ODB-based transfer of accumulated equivalent plastic strain, creep strain, or solution-dependent state variables was specified.

A.8.3 Initial-Stress Equilibration

Importing a residual-stress field from a preceding analysis can introduce a small numerical imbalance if the imported stresses are not in exact equilibrium with the geometry, constraints, or loading conditions of the new analysis. No explicit `UNBALANCED STRESS` option was specified in the production input file. Therefore, the Abaqus/Standard default treatment applies. Abaqus introduces an artificial balancing stress initially and ramps this contribution to zero as equilibrium is established.

A.8.4 Furnace and HIP Coupled Thermo-Mechanical Analysis

Unlike the LPBF simulation, the furnace and HIP stages were modeled using a fully coupled temperature–displacement analysis, in which the thermal and mechanical fields were solved simultaneously. The main input file contains:

```
*Step, name=Step-1, nlgeom=YES, inc=1000000
*Coupled Temperature-displacement,
```

The coupled temperature–displacement procedure simultaneously calculates temperature, displacement, stress, plastic deformation, and creep deformation. This treatment is particularly appropriate for HIP simulations because elevated temperature directly modifies the elastic, plastic, and creep responses during pressure application.

A.8.5 Element Deactivation and Introduction of Voids

In the main parametric HIP models, internal voids were generated by removing selected finite elements from the active continuum:

```
*Model Change, remove
```

The element sets were selected according to the desired void distribution and, for models containing numerous randomly distributed defects, Python-based procedures were employed to facilitate element selection. After deactivation, the removed elements no longer participate in the constitutive response of the solid domain.

A.8.6 Time Incrementation and Convergence Controls

Automatic time incrementation was used in the coupled post-processing simulation. The input definition

```
500., 22000., 1e-20, 500.
```

specifies an initial time increment of 500 s, a total step duration of 22,000 s, a minimum allowable increment of 1×10^{-20} s, and a maximum increment of 500 s. The very small permitted minimum increment allows Abaqus to reduce the increment substantially when strong nonlinearities arise from temperature-dependent material behavior, creep, plastic deformation, or large local deformation around defects. In addition,

```
deltmx=500.
```

limits the maximum allowable temperature change at a node during an increment to 500°C. Abaqus can therefore reduce the increment size if the temperature evolution becomes too rapid. The `DELTmx` option is part of the automatic time-incrementation control available in transient coupled temperature–displacement analysis.

A.8.7 Automatic Stabilization

Automatic stabilization was employed in coupled analysis as a numerical convergence aid for the strongly nonlinear problem. An initial dissipated-energy fraction of 0.0002 was specified, and adaptive stabilization was activated to allow Abaqus to adjust the damping factor according to the convergence behavior of the solution. The allowable ratio of stabilization energy to total strain energy was limited to 0.05. The stabilization parameters were determined independently for the principal coupled analysis step rather than being carried over from a preceding general step. Importantly, automatic stabilization was introduced solely to improve numerical convergence and does not represent a physical damping mechanism or part of the constitutive response of Astroloy**.**

A.8.8 Solver Strategy and Convergence Criterion

The numerical model was solved using Abaqus/Standard with a nonlinear fully coupled temperature–displacement procedure. No user-defined convergence tolerances, custom Newton schemes, or additional solver-control parameters were introduced. Except for the specified automatic time-incrementation settings, temperature-increment control (`DELTMX`), automatic stabilization, geometrical nonlinearity, and increment limits described above, the analysis relied on the default nonlinear convergence criteria available in Abaqus/Standard.

A.9 Boundary Conditions, Substrate Constraint, and Pressure Application

A.9.1 Attached Build-Plate Configuration

The LPBF-manufactured region was not separated from the build plate before the furnace and HIP simulations. Accordingly, the printed region and the underlying build plate were retained as a continuous assembly during post-processing, and a boundary condition similar to that used in the preceding LPBF simulation was maintained.

The lower surface of the build plate was constrained using an `ENCASTRE` boundary condition. This boundary condition was retained to preserve the constraint associated with the LPBF-generated residual-stress state transferred to the subsequent furnace and HIP simulations and to ensure consistency between the residual-stress-generation and post-processing stages. It also prevented rigid-body motion of the model during the subsequent thermo-mechanical analyses.

The `ENCASTRE` condition should nevertheless be regarded as a modeling idealization. A component resting freely on a support surface in an actual HIP chamber may not be restrained against all in-plane motion unless it is mechanically fixtured. Consequently, the present boundary condition represents a relatively restrictive support condition and may influence the absolute magnitude of thermal and residual stresses, particularly near the build plate. However, this limitation does not affect the consistency of the comparative analysis because the same substrate constraint was applied to the furnace and HIP simulations and to all investigated pressure cases. Therefore, the differences among these cases can be compared under the same boundary condition. A released-part configuration was not investigated in the present study and may be considered in future work to evaluate the influence of substrate release on the absolute stress magnitudes.

A.9.2 External HIP Pressure Application

In the principal element-deactivation model, the external HIP pressure was applied to the pressure-exposed exterior surfaces of the model using a distributed surface pressure load. The pressure magnitude and its variation throughout the HIP cycle were controlled through an amplitude definition corresponding to the heating/pressurization, holding, and depressurization stages. In Abaqus, the distributed pressure load acts normal to the defined element surfaces. Therefore, the selected exterior surfaces were subjected to the externally imposed HIP pressure as a compressive normal traction throughout the prescribed pressure cycle.

A.9.3 Enclosed Internal Voids

The internal voids used in the main parametric simulations were generated by deactivating selected elements within the model. The surfaces surrounding these enclosed regions were not included among the exterior surfaces subjected to the applied HIP pressure. Therefore, the HIP chamber pressure was applied only to the exterior surfaces of the component and was not applied directly to the internal surfaces of the enclosed voids.

No internal gas pressure was specified within the void regions. Accordingly, the internal pore pressure was assumed to be zero, and the pressure difference acting across the material surrounding the void was governed solely by the externally applied HIP pressure**.** This assumption was adopted deliberately to isolate the influence of externally applied hydrostatic pressure on the local stress state and deformation surrounding an enclosed defect.

A.9.4 Assumption of Zero Internal Pore Gas Pressure

Real LPBF pores may contain trapped gas. As an enclosed pore contracts during HIP, the pressure of trapped gas can increase and oppose further collapse. This gas-compression process was not modeled in the present numerical framework. Instead, the internal void was treated as an empty region with zero internal pressure. Consequently, simulations represent an idealized condition in which the entire external-to-internal pressure difference is available to drive deformation around the void.

This assumption is appropriate for the mechanistic objective of the present study because the primary research question concerns how externally applied pressure modifies the local stress field and residual-stress-relaxation response in the presence of internal defects. However, it may overestimate the mechanical driving force for complete pore collapse relative to a real sealed pore containing compressed gas. Accordingly, the assumption of $P_{void} = 0$ should be considered when interpreting quantitative pore-closure predictions, while its influence on the mechanistic comparison among defect geometries remains internally consistent because the same internal-pressure assumption was used in all corresponding simulations.

A.9.5 Enclosed, Through, and Surface-Connected Defects

The mechanical action of HIP pressure depends on whether a defect is isolated from or connected to the external pressure environment. For a fully enclosed void, the external HIP pressure acts on the exterior surfaces of the component, whereas no chamber pressure is applied directly to the internal void surface in the present model. Because the internal pressure was assumed to be zero, a pressure differential develops across the material surrounding the enclosed defect.

For a through-hole or surface-connected defect, the physical situation is different. Because the defect communicates directly with the HIP chamber, the pressurizing gas can access the internal defect surfaces. A physically representative model of such a defect should therefore apply the same chamber pressure to all gas-accessible surfaces, including the internal surfaces of the through-hole or surface-connected cavity. The pressure then acts on both the outer component surfaces and the exposed defect surfaces. Because Abaqus pressure is applied normal to each loaded surface, the resulting traction follows the local surface normal.

A.10 Finite Deformation, Pore Collapse, and Mesh Treatment

A.10.1 Finite-Deformation Formulation

Geometric nonlinearity was included in both the main element-deactivation simulations and the auxiliary explicit-cavity model using the `NLGEOM=YES` option in Abaqus/Standard. Therefore, changes in geometry associated with pressure-assisted creep, plastic deformation, and thermal deformation were included throughout the HIP cycle. Pore deformation was not prescribed through a pore-shrinkage law but developed naturally from the thermo-mechanical response of the surrounding material.

A.10.2 Cavity and Element-Deactivation Models

An auxiliary model with an explicitly represented geometrical cavity was initially examined to demonstrate pressure-assisted deformation toward an internal void. The model showed progressive inward deformation and reduction of the cavity dimensions during HIP.

For the main parametric investigation, however, internal voids were represented by deactivating selected elements. This approach enabled efficient generation of defects with different morphologies, distributions, and volume fractions while reducing preprocessing and computational requirements. The main simulations were developed primarily to investigate local stress redistribution, creep and plastic deformation, and residual-stress relaxation; pore shrinkage was an associated consequence of these mechanisms rather than the principal prediction objective.

A.10.3 Pore Closure and Mesh Treatment

The present simulations were primarily developed to investigate pressure-assisted deformation, local stress redistribution, and residual-stress relaxation around internal voids. Therefore, pore closure in this thesis refers to the progressive geometrical reduction of the void dimensions during HIP rather than complete pore elimination or metallurgical healing. The predicted void deformation should accordingly be interpreted as an indicator of the pressure-assisted deformation mechanism rather than as a detailed prediction of complete pore consolidation.

Adaptive remeshing was also not employed. Mesh quality was addressed through the initial mesh design and mesh-sensitivity assessment, with finer elements used around defect-containing regions. At higher temperatures and pressures, increased creep deformation may contribute to local mesh distortion and potential surface interpenetration. These effects, together with strong constitutive nonlinearity and time-increment reduction, may have contributed to the convergence difficulties observed under some conditions above approximately 750°C.